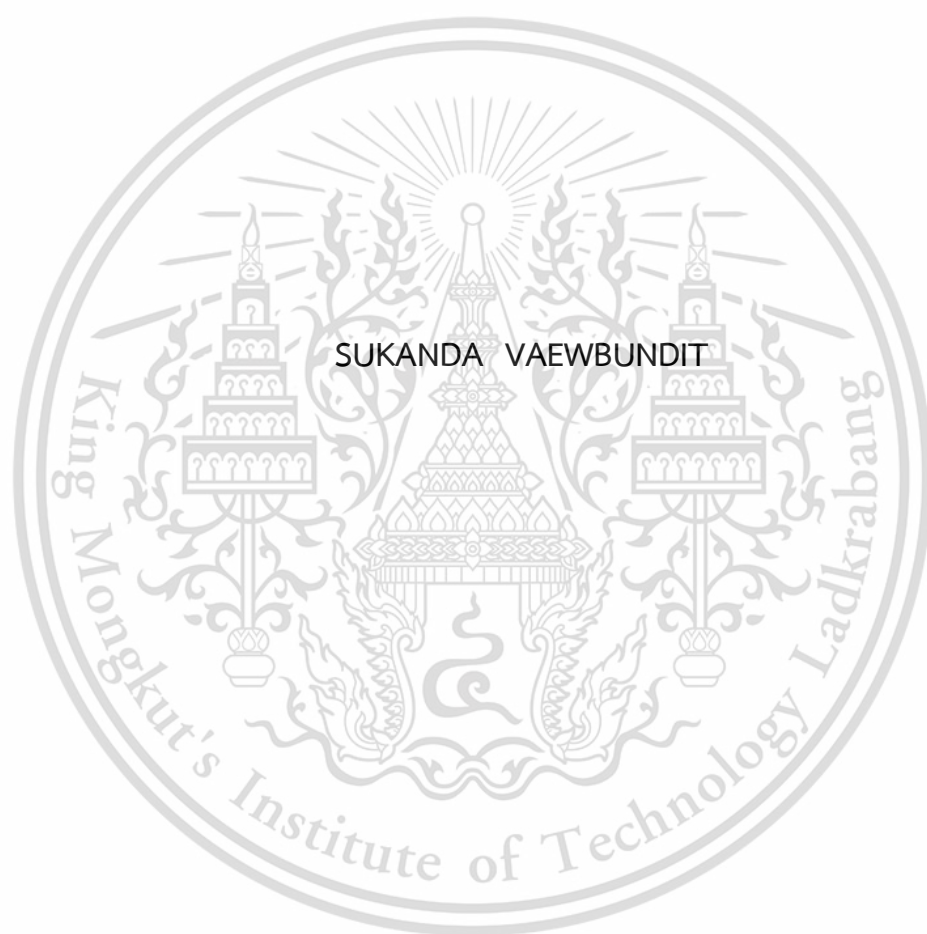


SYNTHESIS OF CHITOSAN/IRON OXIDE NANOCOMPOSITES BY
SOFT SOLUTION PROCESSING FOR MEDICAL APPLICATIONS



SUKANDA VAEWBUNDIT

A THESIS SUBMITTED IN PARTIAL FULFILLMENT OF THE REQUIREMENT FOR THE
DEGREE OF PHILOSOPHY IN APPLIED CHEMISTRY
DEPARTMENT OF CHEMISTRY SCHOOL OF SCIENCE
KING MONGKUT'S INSTITUTE OF TECHNOLOGY LADKRABANG
2022

KMITL-2022-SC-D-012-120

This material is reserved for educational use only, not allowed for commercial use.

Forbidden to modify the content, and cite the document when use.



COPYRIGHT 2022

SCHOOL OF SCIENCE

KING MONGKUT'S INSTITUTE OF TECHNOLOGY LADKRABANG

This material is reserved for educational use only, not allowed for commercial use.

Forbidden to modify the content, and cite the document when use.

Thesis Title	Synthesis of Chitosan/Iron Oxide Nanocomposites by Soft Solution Processing for Medical Applications
Student Name	Miss Sukanda Vaewbundit
Student ID	58605011
Degree	Doctor of Philosophy (Applied Chemistry)
Department	Chemistry
Year	2022
Thesis Advisor	Assoc.Prof.Dr.Punnama Siriphannon

Abstract

This research studied on synthesis of chitosan/iron oxide nanocomposites (CHI/IO) using two methods, i.e. the *in-situ* and adsorption systems, incorporating with the aqueous based systems at low reaction temperatures. In the *in-situ* synthesis, a chitosan solution was mixed with a mixture solution of iron(II) and iron(III), namely ammonium ferrous sulphate hexahydrate ((NH₄)₂SO₄FeSO₄•6H₂O) and ferric chloride hexahydrate (FeCl₃•6H₂O), with an initial Fe²⁺ : Fe³⁺ concentration of 0.625 : 1.25 M. After that, a solution of sodium tripolyphosphate (TPP) was added to the previous mixtures to crosslink chitosan, resulting in the chitosan network (CC) and the incorporation of Fe²⁺ and Fe³⁺ ions into the CC structure (CHI/Fe²⁺Fe³⁺). The TPP concentration was varied at 0.2, 0.3, 0.4, 0.5 and 0.6 %w/v. The CHI/Fe²⁺Fe³⁺ samples were then reacted in NaOH solution by hydrothermal and refluxing methods at 75, 100 and 125°C for 90 min, resulting in the CHI/IO nanocomposites. In the adsorption synthesis, the CC precipitates were soaked in the mixture solution of Fe²⁺Fe³⁺ with Fe²⁺ : Fe³⁺ concentration of 0.625 : 1.25 M, resulting in the adsorption of Fe²⁺ and Fe³⁺ ions into the CC templates (CC/Fe²⁺Fe³⁺). The CC/Fe²⁺Fe³⁺ samples were reacted in NaOH solution by hydrothermal and refluxing methods at 100°C, yielding the CHI/IO nanocomposites. When the CHI/IO nanocomposites prepared using both synthesis systems were analyzed by various techniques, it was discovered that CHI/IO nanocomposites synthesized at temperatures higher than 100°C were primarily composed of magnetite-maghemite nanocrystals embedded in the CC network. The iron oxide nanocrystals prepared by *in-situ* method had an irregular spherical shape with sizes ranging from 3.9 to 4.3 nm, and the iron oxide fraction in the nanocomposites was in the range of 70–75%. While the iron oxide nanocrystals prepared by adsorption synthesis were quadrilateral in shape, with sizes ranging from 10.3 to 13.5 nm, and the iron oxide fractions in the nanocomposites ranging from 28 to 35%. The increase of initial TPP concentration promoted the formation of non-uniform CC network. The iron oxide nanocrystals with broad particle size distribution were obtained in the nanocomposites when the non-uniform CC template was used as a template for crystal formation. The resultant CHI/IO nanocomposites exhibited superparamagnetic behavior, with maximum magnetization (M_{max}) values ranging from 8.6 to 15.2 emu/g. The nanocomposites were found to be extremely safe, with cell viability in the range from 57–96% after exposure to the CHI/IO nanocomposites, indicating their suitability for medical applications, particularly the hybrid material for hyperthermia applications.

Keywords : chitosan, superparamagnetic, reflux, iron oxide, hydrothermal

Acknowledgements

I would like to express my deepest appreciation to my advisor, Assoc.Prof.Dr.Punnama Siriphannon, for her invaluable instruction. Her patience and suggestion carried me through the difficulty of writing the international academic articles. I am extremely grateful to thesis's committee for the useful comments about this work. Additionally, this endeavor would not have been possible without the financial support from the Royal Golden Jubilee PhD program (RGJ) of the Thailand Research Fund (TRF) (PHD/0005/2558).

I am also thankful to the laboratory officers who facilitate the testing of my samples with various techniques as well as exchange knowledge about the testing with each other.

Lastly, I could not have undertaken this journey without understanding from my family. Many thanks for waiting patiently for my PhD study. Especially, my father, Somkiat Vaewbundit, who is my inspiration for PhD education and life that relied on own abilities for a better future. I would like to extend my sincere thanks to holy thing for allowing me to learn the truth of the world through the means of science.

Miss Sukanda Vaewbundit

Table of contents

	Page
Abstract in English	i
Acknowledgements	ii
Table of contents	iii
List of tables	vi
List of figures	vii
Abbreviations/ Symbols	xi
Chapter 1 Introduction	1
1.1 Research motivation	1
1.2 Objectives of the study	4
1.3 Scopes of the study	4
1.4 Benefits of the study	4
Chapter 2 Theory and literature reviews	6
2.1 Iron oxide nanoparticles (IO)	6
2.1.1 Iron oxides	6
2.1.2 Formation of IO nanoparticles	8
2.1.3 Toxicity of IO nanoparticles	9
2.2 Coating of IO nanoparticles	9
2.2.1 Types of coating	9
2.2.2 Advantages of coating	10
2.2.3 Chitosan	11
2.2.4 Sodium tripolyphosphate (TPP)	12
2.3 Synthesis methods of iron oxide nanoparticles (IO)	15
2.3.1 Soft solution processing	15
2.3.2 Hydrothermal method	16
2.3.3 Aqueous based refluxing method	18
2.4 Superparamagnetic properties	19
2.5 Magnetic hyperthermia	21

	Page
Chapter 3 Research methodology	33
3.1 Materials	33
3.2 Apparatus	33
3.3 Studied parameters	34
3.4 Experimental procedure	34
3.4.1 Preparation of iron oxide nanoparticles (IO)	34
3.4.2 Preparation of crosslinked chitosan precipitates (CC)	36
3.4.3 Preparation of chitosan/iron oxide nanocomposites (CS/IO) by <i>in-situ</i> method	37
3.4.4 Preparation of crosslinked chitosan/iron oxide nanocomposites (CC/IO) by adsorption method	39
3.4.5 Characterization and testing of CHI/IO nanocomposites	42
3.4.6 Cell viability assays	43
Chapter 4 Main results and discussion	44
4.1 Synthesis of IO nanoparticles	44
4.2 <i>In-situ</i> synthesis of CS/IO nanocomposites	47
4.2.1 Effect of hydrothermal temperature	47
4.2.2 Effect of synthesis method and the initial concentration of TPP solution	58
4.3 Adsorption synthesis of CC/IO nanocomposites	76
4.3.1 Effect of TPP concentration on CHI templates	77
4.3.2 Effect of synthesis method and the initial concentration of TPP solution on CC/IO nanocomposites	79
4.4 Comparison of <i>in-situ</i> and adsorption syntheses	99
4.5 Cell viability assays of CHI/IO nanocomposites	103
Chapter 5 Conclusions and suggestions	104
5.1 Conclusions	104
5.1.1 <i>In-situ</i> synthesis	104
5.1.2 Adsorption synthesis	105
5.1.3 Comparison of <i>in-situ</i> and adsorption syntheses	106
5.2 Suggestions	107

	Page
References	108
Appendices	116
Appendix A	117
Appendix B	135
Appendix C	145
Appendix D	163
Appendix E	181
Author biography	203



List of tables

Table	Page
2.1 Physical and magnetic properties of iron oxides	7
2.2 Crystallographic data of iron oxides	8
2.3 Comparing advantages of different methods for synthesis of inorganic oxide powders	17
3.1 Experimental conditions and abbreviations of the samples	41
4.1 Parameters used for <i>in-situ</i> synthesis of CS/IO nanocomposites and their XRD and TEM data	46
4.2 TGA, DSC, VSM and cell viability of CS/IO nanocomposites synthesized by <i>in-situ</i> synthesis	54
4.3 Parameters used for adsorption synthesis of CC/IO nanocomposites and their XRD and TEM data	82
4.4 TGA, DSC, VSM and cell viability of CC/IO nanocomposites synthesized by adsorption synthesis	91

List of figures

Figure	Page
2.1 Deacetylation of chitin	11
2.2 Sodium tripolyphosphate (TPP) structure	12
2.3 Relationship between nanoparticle radius (r) and coercivity (H_c)	19
2.4 Hysteresis curves that obtained from (a) superparamagnetic and (b) soft ferromagnetic materials	20
2.5 Hysteresis loop and magnetic properties of ferromagnetic materials	21
3.1 Preparation of iron oxide nanoparticles (IO)	35
3.2 Preparation of crosslinked chitosan precipitates (CC)	36
3.3 Preparation of CHI/IO nanocomposites by <i>in-situ</i> method, i.e. CS/IO-HT and CS/IO-R nanocomposites	38
3.4 Preparation of CHI/IO nanocomposites by adsorption method, i.e. CC/IO-HT and CC/IO-R nanocomposites	40
4.1 XRD pattern of IO-HT100 nanoparticles	45
4.2 XRD patterns of (a) CS0.3/IO-HT75, (b) CS0.3/IO-HT100 and (c) CS 0.3/IO-HT125 nanocomposites	48
4.3 TEM images of (a) CS0.3/IO-HT75 and (b) CS0.3/IO-HT100 nanocomposites	49
4.4 Schematic model of the formation of CS/IO nanocomposites prepared using <i>in-situ</i> synthesis	51
4.5 TGA and DTG thermograms of (a) CS0.3/IO-HT75, (b) CS0.3/IO-HT100 and (c) CS0.3/IO-HT125 nanocomposites under N_2 and air zero atmospheres	53
4.6 DSC thermograms of (a) CS0.3/IO-HT75, (b) CS0.3/IO-HT100 and (c) CS0.3/IO-HT125 nanocomposites	55
4.7 VSM curves of (a) CS0.3/IO-HT75, (b) CS0.3/IO-HT100 and (c) CS0.3/IO-HT125 nanocomposites	57
4.8 XRD patterns of (a) CS0.2/IO-HT100, (b) CS0.3/IO-HT100, (c) CS0.4/IO-HT100, (d) CS0.5/IO-HT100 and (e) CS0.6/IO-HT100 nanocomposites	59

Figure	Page
4.9 XRD patterns of (a) CS0.2/IO-R, (b) CS0.3/IO-R, (c) CS0.4/IO-R, (d) CS0.5/IO-R and (e) CS0.6/IO-R nanocomposites	60
4.10 Relationship between the average crystallite sizes of iron oxide (IO) nanocrystals in CS/IO nanocomposites synthesized using hydrothermal method (CS/IO-HT) and refluxing method (CS/IO-R) and TPP concentrations used in the synthesis	61
4.11 TEM images of (a) CS0.2/IO-HT100, (b) CS0.3/IO-HT100, (c) CS0.4/IO-HT100, (d) CS0.5/IO-HT100 and (e) CS0.6/IO-HT100 nanocomposites	62
4.12 TEM images of (a) CS0.2/IO-R, (b) CS0.3/IO-R, (c) CS0.4/IO-R, (d) CS0.5/IO-R and (e) CS0.6/IO-R nanocomposites	63
4.13 Relationship between the average particle sizes of iron oxide (IO) nanocrystals in CS/IO nanocomposites synthesized using hydrothermal method (CS/IO-HT) and refluxing method (CS/IO-R) and TPP concentrations used in the synthesis	65
4.14 Electron diffraction of CS0.6/IO-HT100	65
4.15 TGA and DTG thermograms of (a) CS0.2/IO-HT100, (b) CS0.3/IO-HT100, (c) CS0.4/IO-HT100, (d) CS0.5/IO-HT100 and (e) CS0.6/IO-HT100 nanocomposites under N ₂ and air zero atmospheres	67
4.16 TGA and DTG thermograms of (a) CS0.2/IO-R, (b) CS0.3/IO-R, (c) CS0.4/IO-R, (d) CS0.5/IO-R and (e) CS0.6/IO-R nanocomposites under N ₂ and air zero atmosphere	68
4.17 Relationship between the decomposition temperatures of chitosan (T _d) in CS/IO nanocomposites synthesized using hydrothermal method (CS/IO-HT) and refluxing method (CS/IO-R) and TPP concentrations used in the synthesis	69
4.18 DSC thermograms of (a) CS0.2/IO-HT100, (b) CS0.3/IO-HT100, (c) CS0.4/IO-HT100, (d) CS0.5/IO-HT100 and (e) CS0.6/IO-HT100 nanocomposites	70
4.19 DSC thermograms of (a) CS0.2/IO-R, (b) CS0.3/IO-R, (c) CS0.4/IO-R, (d) CS0.5/IO-R and (e) CS0.6/IO-R nanocomposites	72
4.20 VSM curves of (a) CS0.2/IO-HT100, (b) CS0.3/IO-HT100, (c) CS0.4/IO-HT100, (d) CS0.5/IO-HT100 and (e) CS0.6/IO-HT100 nanocomposites	73

This material is reserved for educational use only, not allowed for commercial use.

Forbidden to modify the content, and cite the document when use.

Figure	Page
4.21 VSM curves of (a) CS0.2/IO-R, (b) CS0.3/IO-R, (c) CS0.4/IO-R, (d) CS0.5/IO-R and (e) CS0.6/IO-R nanocomposites	74
4.22 Relationship between the average particle sizes of iron oxide (IO) nanocrystals in CS/IO nanocomposites synthesized using (a) hydrothermal and (b) refluxing methods and the highest maximum magnetization (M_{max}) of each size	75
4.23 The adsorption preparation of the chitosan/iron oxide nanocomposites	76
4.24 DSC thermograms of (a) CC0.3, (b) CC0.4, (c) CC0.5 and (d) CC0.6 templates	77
4.25 XRD patterns of (a) CC0.3/IO-HT100, (b) CC0.4/IO-HT100, (c) CC0.5/IO-HT100 and (d) CC0.6/IO-HT100 nanocomposites	80
4.26 XRD patterns of (a) CC0.3/IO-R, (b) CC0.4/IO-R, (c) CC0.5/IO-R and (d) CC0.6/IO-R nanocomposites	81
4.27 TEM patterns and particle size distribution (PSD) of (a) CC0.3/IO-HT100, (b) CC0.4/IO-HT100 and (c) CC0.5/IO-HT100 nanocomposites	83
4.28 TEM patterns and particle size distribution (PSD) of (a) CC0.3/IO-R, (b) CC0.4/IO-R and (c) CC0.5/IO-R nanocomposites	84
4.29 TGA and DTG thermograms of (a) CC0.3/IO-HT100, (b) CC0.4/IO-HT100 and (c) CC0.5/IO-HT100 nanocomposites under N_2 and air zero atmosphere	86
4.30 TGA and DTG thermograms of (a) CC0.3/IO-R, (b) CC0.4/IO-R and (c) CC0.5/IO-R nanocomposites under N_2 and air zero atmosphere	87
4.31 Relationship for the values of (a) the first decomposition temperature (T_{d1}) and (b) second decomposition temperature (T_{d2}) of CC templates in CC/IO nanocomposites and TPP concentration used in the hydrothermal synthesis	88
4.32 Relationship for the values of (a) the first decomposition temperature (T_{d1}) and (b) second decomposition temperature (T_{d2}) of CC templates in CC/IO nanocomposites and TPP concentration used in the refluxing synthesis	90

Figure	Page
4.33 DSC thermograms of (a) CC0.3/IO-HT100, (b) CC0.4/IO-HT100 and (c) CC0.6/IO-HT100 nanocomposites	92
4.34 DSC thermograms of (a) CC0.3/IO-R, (b) CC0.4/IO-R and (c) CC0.5/IO-R nanocomposites	94
4.35 VSM curves of (a) CC0.3/IO-HT100, (b) CC0.4/IO-HT100 and (c) CC0.5/IO-HT100 nanocomposites	95
4.36 VSM curves of (a) CC0.3/IO-R, (b) CC0.4/IO-R and (c) CC0.5/IO-R nanocomposites	96
4.37 Schematic diagrams of the crosslinking chitosan networks in the CHI/IO nanocomposites obtained by using different TPP concentrations	98
4.38 XRD patterns of (a) CC0.4/IO-R and (b) CS0.3/IO-HT100 nanocomposites	99
4.39 TEM images and particles size distributions of (a, b) CC0.4/IO-R and (c, d) CS0.3/IO-HT100 nanocomposites	100
4.40 VSM curves of (a) CC0.4/IO-R and (b) CS0.3/IO-HT100 nanocomposites	101
4.41 TGA thermograms of (a) CC0.4/IO-R and (b) CS0.3/IO-HT100 nanocomposites under N ₂ and air zero atmosphere	102

Abbreviations/Symbols

AFM	Atomic force microscopy
AMF	Alternating magnetic field
ATP	Adenosine triphosphate
CC	Crosslinked chitosan
CC/IO	Crosslinked chitosan/iron oxide nanocomposites synthesized by adsorption method
CHI/IO	Chitosan/iron oxide
C_{H_2O}	Specific heat capacity of water
C_M	Specific heat capacity of magnetic nanoparticles
CT	Computed tomography
CTAB	Cetyltrimethylammonium bromide
DLS	Dynamic light scattering
DMEM	Dulbecco's modified Eagle's medium
DMSO	Dimethyl sulfoxide
DNA	Deoxyribonucleic acid
DSC	Differential scanning calorimetry
dT/dt	The initial temperature rising rate
D_{XRD}	Average crystallite size
F	Field frequency
FBS	Fetal bovine serum
FESEM	Field emission scanning electron microscopy
FTIR	Fourier transform infrared spectroscopy
GRAS	Generally recognized as safe
H	Magnetic field
H_c	Coercivity
HCP	Hexagonal close packing
ΔH	Enthalpy of fusion
ΔH_d	Decomposition enthalpy
ΔH_m	Melting enthalpy
ICSD	Inorganic crystal structure database

This material is reserved for educational use only, not allowed for commercial use.

Forbidden to modify the content, and cite the document when use.

ILP	Intrinsic loss power
IO	Iron oxide
JCPDS	Joint committee on powder diffraction standards
M	Magnetization
M_{H_2O}	Mass of water
M_M	Mass of magnetic nanoparticles
M_{max}	Maximum magnetization
MNPs	Magnetic nanoparticles
M_r	Retentivity, Magnetic remanence
MRI	Magnetic resonance imaging
M_s	Saturation magnetization
MTT	(3-(4,5-dimethylthiazolyl-2)-2,5-diphenyltetrazolium bromide)
NMR	Fourier transform nuclear magnetic resonance spectrometry
NPs	Nanoparticles
OD	Optical density
PDI	Polydispersity index
PEG	Polyethylene glycol
PEI	Polyethyleimine
r_{sd}	The single domain critical radius
r_{sp}	The superparamagnetic critical radius
R&D	Research and development
SAR	Specific absorption rate
SCC7	Squamous cell carcinomas
SDS	Sodium dodecyl sulfate
SLP	Specific loss power
SPIONs	Superparamagnetic iron oxide nanoparticles
T_B	Blocking temperature
T_d	Decomposition temperature
TEM	Transmission electron microscopy
TGA	Thermogravimetric analysis
T_m	Melting temperature
TMAOH	Tetramethylammonium hydroxide
TPP	Sodium tripolyphosphate

This material is reserved for educational use only, not allowed for commercial use.

VSM	Vibrating sample magnetometry
WAXD	Wide-angle X-ray diffraction
XPS	X-ray photoelectron spectroscopy
XRD	X-ray diffractometry
ZFC/FC	Zero-field-cooling/field-cooling



Chapter 1

Introduction

1.1 Research Motivation

Cancer is the disease that causes many deaths. There were approximately 14 million people who were diagnosed with cancer each year and there were about 8 million people who died. In 2013, there were about 67,000 Thai people who died from cancer, accounting for 16% of all deaths. Moreover, the number of patients and deaths with cancer is on the rise every year [1].

Cancer occurs from the mutation of DNA within cells. Abnormal cells divide, grow and become malignant tumor known as cancer. Furthermore, they can spread to other organs and make those organs work abnormally. The treatment of cancer depends on the detection period. In Thailand, many types of cancer treatment, such as surgery, radiation therapy, chemotherapy, hormonal therapy and immunotherapy are used together. However, almost of cancer treatment make healthy tissues and healthy organs of human body get side effects. Therefore, the treatment that operates only cancerous tissues attracts the attention in order to reduce those side effects [2].

Local hyperthermia is the local cancer heat treatment using medium heat in the range of 39 to 45°C for damaging cancerous tissues. This level of heat treatment can cause some cancer cells die and the properties of all cancerous tissues are changed without affecting the normal tissues. Therefore, the response to radiation therapy and chemotherapy will be enhanced [3]. The local hyperthermia is generated by using the magnetic nanoparticles (MNPs) which have superparamagnetic properties. The magnetic dipole moments of MNPs are fluctuated by using an alternating magnetic field (AMF) generating localized heat for destroying cancerous tissues. The MNPs do not retain any magnetism after removal of the magnetic field [4]. Since the local hyperthermia treatment affects on specific area, it can reduce the side effects to the neighboring healthy tissues. Therefore, the local hyperthermia has potential to use for cancer treatment and the MNPs have been widely studied to develop their properties for enhancing the efficiency of local hyperthermia.

Cobalt ferrite (CoFe_2O_4) nanoparticles have attracted much attention in many studies because they have high magnetic properties. They have been prepared by various methods, such as conventional, coprecipitation, normal micelles and reverse micelles methods. Besides, various types of cations were used for substitution of Fe^{3+} site in order to increase the magnetic properties of cobalt compounds [5]. However, cytotoxicities of cobalt ion and cobalt metal have been concerned because they can induce apoptosis and at higher concentrations necrosis with inflammatory response. The cobalt metal and salts are genotoxic substances, inducing oxidative DNA damage and inhibition of DNA repair [6].

From the above mentioned drawbacks of cobalt compounds, iron oxide nanoparticles (IO), especially magnetite (Fe_3O_4), gradually play increasingly important role because they have lower toxicity than other magnetic nanomaterials including cobalt ferrite. Although the IO nanoparticles have been reported that they can accumulate in the liver, they will most likely be degraded and/or they can be reused by the human body. They can be metabolized through heme oxygenase-1 to form blood hemoglobin. From these merits, the IO nanoparticles have been synthesized in this study in order to develop the MNPs for hyperthermia applications [7].

Besides, one of the major problems of MNPs is agglomeration due to their high surface energy and magnetic interactions, resulting in the increase of MNPs cluster size. If the MNPs cluster size is higher than the critical value, the MNPs do not have superparamagnetic properties. In order to prevent the agglomeration of MNPs, synthetic polymers having long-chain molecules have been applied on the MNPs, such as sodium oleate and polyethylenimine (PEI) [8]. These synthetic polymers have wide range of chemical and physical properties; therefore, they were used for several applications including biomedical applications [9-11]. Although the synthetic polymers could effectively prevent the MNPs agglomeration, the important restriction of usage is about their biological properties. Therefore, biopolymers, which possess superior biodegradable, biocompatible and non-toxic properties, have been studied and used. For preventing the agglomeration of MNPs for hyperthermia application instead of synthetic polymers, the biopolymers, e.g. glycyrrhizic acid, dextran, hyaluronic acid, etc., have been studied [12-15].

Chitosan is one of the most attractive biopolymers because it possesses a linear polysaccharide of randomly distributed *N*-acetyl glucosamine and glucosamine

This material is reserved for educational use only, not allowed for commercial use.

units. The chitosan possesses several good biological properties, i.e. biocompatible, bacteriostatic, biodegradable, non-toxic and eatable natural polymer. In addition, it is a polyelectrolyte, being positive charge in acid environment; therefore, the negatively charged cell membrane has bioadhesivity with it. The chitosan is approved by Food and Drug Administration (USA) for wound dressing. Besides, the chitosan can bind materials, such as cholesterol, fats, proteins and tumor cells [15-16]. From various advantages of chitosan, it has been used as coating agent for MNPs in biomedical applications, such as drug delivery, magnetic resonance imaging (MRI) and computerized tomography (CT) imaging, hyperthermia therapy, etc. [17-20].

In this research, the chitosan/iron oxide nanocomposites have been synthesized by facile eco-friendly method in order to combine the advantages of these organic-inorganic hybrid materials. The IO nanoparticles which have superparamagnetic properties have been prepared within the ionically crosslinked chitosan network, in which the chitosan not only acts as biological template for growth of IO nanoparticles, but also as the coating agent for preventing the agglomeration. The formation and growth of IO nanoparticles in the nanocomposites have been prepared by using hydrothermal and refluxing methods. These two methods can perform using low temperature and pressure in an aqueous based system, in which they are easy, safe and environmentally friendly methods. The synthesized chitosan/iron oxide nanocomposites are biocompatible superparamagnetic materials which trend to degrade and reuse by the human body. Tripolyphosphate acting as crosslinking agent can be hydrolyzed into simpler phosphates and used as nutrient for human body like adenosine triphosphate (ATP). The IO nanoparticles can be metabolized to form blood hemoglobin. Therefore, these nanocomposites have the potential to further develop for medical applications, especially local hyperthermia treatment.

1.2 Objectives of the study

- 1) To study the effect of synthesis conditions on the structure and properties of chitosan/iron oxide nanocomposites
- 2) To study the cytotoxicity of synthesized chitosan/iron oxide nanocomposites
- 3) To study the superparamagnetic behavior of synthesized chitosan/iron oxide nanocomposites
- 4) To obtain the iron oxide nanoparticles which have the superparamagnetic properties with narrow size distribution thoroughly dispersed in the crosslinked chitosan network

1.3 Scopes of the study

- 1) Preparation of chitosan/iron oxide nanocomposites (CHI/IO) using various conditions as follows:
 - Precursor preparation method; i.e. adsorption and *in-situ* methods
 - Initial concentration of TPP solution; i.e. 0.2, 0.3, 0.4, 0.5 and 0.6 %w/v
 - Synthesis method; i.e. hydrothermal and refluxing methods
 - Hydrothermal reaction temperature; i.e. 75, 100 and 125°C
- 2) Characterization of synthesized composites by various techniques; i.e. X-ray diffractometry (XRD), differential scanning calorimetry (DSC), thermogravimetric analysis (TGA), vibrating sample magnetometry (VSM) and transmission electron microscopy (TEM)
- 3) Testing of synthesized composites by cell viability assays

1.4 Benefits of the study

This research developed a new method for the synthesis of IO nanoparticles with superparamagnetic properties by using the ionically crosslinked chitosan template for the formation and growth of IO nanoparticles. The crosslinked chitosan not only acts as biological template, but also as the coating agent for preventing the agglomeration of IO nanoparticles. Therefore, the crosslinked chitosan could improve the particle size, particle size distribution and the distribution of IO nanoparticles embedded in the chitosan matrix, leading to the enhancement of superparamagnetic properties. In order to reduce the usage of toxic organic solvent

This material is reserved for educational use only, not allowed for commercial use.

in the process of surface modification and coating of IO nanoparticles, the developed techniques use an aqueous system of low concentrations of non-hazardous chemicals. The synthesis temperature is not high, but it can effectively induce the formation of chitosan/iron oxide nanostructures. Therefore, the developed techniques are considered to be a soft solution processing which is safe and environmentally friendly process. In addition, the synthesized nanocomposites can be applied and further developed in medical field. The synthesized materials will be the tentative candidate for alternative cancer treatment.



Chapter 2

Theory and Literature Reviews

2.1 Iron oxide nanoparticles (IO)

2.1.1 Iron oxides

- Goethite (α -FeOOH)

Goethite originates from rock named follow Johann Wolfgang von Goethe, the German scientist. Its chemical composition has changed through the geological processes. Goethite is iron oxide that is thermodynamically most stable at ambient temperature, which has a diaspore structure which is hexagonal close packing of anions (hcp). The color of bulk goethite is dark brown or black but the color of goethite powders is yellow so the goethite powder is used as a pigment in several industrial works [21].

- Hematite (α -Fe₂O₃)

Hematite is widespread in rocks and soils, which is the oldest known iron oxide named from the Greek word 'haima' which means blood. The color of bulk hematite is blood-red, while the color of fine powders is black and coarse powders is grey. The hematite has a corundum structure which is hcp of anions. It is the most stable iron oxide like goethite. It is also used as an important pigment [21].

- Magnetite (Fe₃O₄)

Magnetite is in rocks as titanomagnetite form that shows the magnetic properties of rocks. Besides, the magnetite is naturally produced by various organisms, such as homing pigeon and marine mollusk named chiton. Magnetite contains both Fe(II) and Fe(III), in which it has a cubic inverse spinel structure. It has ferrimagnetic properties, having black color, then it is used as a pigment for cosmetics, polymer, rubber and magnetic inks [21-22]. Furthermore, the magnetite is also applied in biomedical field.

- Maghemite (γ -Fe₂O₃)

Maghemite is in soils, in which it changes from other iron oxides such as magnetite because of heat and organic matter. It has a cubic tetragonal structure and ferrimagnetic properties. Maghemite has red-brown color which is used as a

magnetic pigment in electronic recording media. It can be used in biomedical field because it is biocompatible and non-toxic to humans [21].

Iron oxides including goethite, hematite, magnetite and maghemite have the physical and magnetic properties as shown in Table 2.1 and have crystallographic data as shown in Table 2.2.

Table 2.1 Physical and magnetic properties of iron oxides [21, 23-24]

	Goethite	Hematite	Magnetite	Maghemite
Molecular formula	α -FeOOH	α -Fe ₂ O ₃	Fe ₃ O ₄	γ -Fe ₂ O ₃
Molecular weight (g/mol)	88.85	159.69	231.53	159.69
Color	Yellow-brown	Red	Black	Reddish-brown
Melting point (°C)	-	1350	1583–1597	-
Density (g/cm ³)	4.26	5.26	5.18	4.87
Hardness	5–5.5	6.5	5.5	5
Solubility in water	-	Insoluble	Insoluble	Insoluble
Solubility in HCl	-	Very little	Medium	Little
Type of magnetism	Antiferromagnetism	Weakly ferromagnetism or antiferromagnetism	Ferromagnetism	Ferromagnetism
M _s at 300 K (A·m ² /kg)	-	0.3	92–100	60–80
Néel (Curie) temperature (K)	400	(956)	(850)	(820–986)
Standard free energy of formation, ΔG_f° (kJ/mol)	-488.6	-742.7	-1012.6	-711.1

This material is reserved for educational use only, not allowed for commercial use.

Forbidden to modify the content, and cite the document when use.

Table 2.2 Crystallographic data of iron oxides [21, 23]

Compound	Crystallographic system (Structural type)	Space group	Stacking of closed packed anions	Lattice parameter (nm)			Z
				a	b	c	
Goethite	Orthorhombic	<i>Pnma</i>	ABAB [001]	0.9956	0.30215	0.4608	4
Hematite	Hexagonal	<i>R3c</i>	ABAB [001]	0.5034		1.3752	6
	Rhombohedral (Corundum)			0.5427			
Magnetite	Cubic (Inverse spinel)	<i>Fd3m</i>	ABCABC [111]	0.8396			8
Maghemite	Cubic	<i>P4₃32</i>	ABCABC	0.83474			8
	Tetragonal (Defect spinel)	<i>P4₁2₁2</i>	[111]	0.8347		2.501	24

2.1.2 Formation of IO nanoparticles

Magnetite can be formed by the addition of alkaline solution to a mixture of Fe^{3+} and Fe^{2+} solution in a molar ratio of 2:1.

The formation of magnetite can be described as follows:

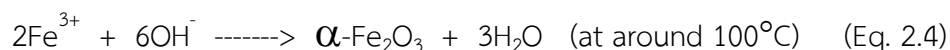
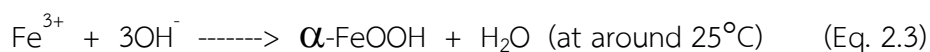


Whereas the maghemite is formed by the oxidation of magnetite as shown in Eq. 2.2.



The end product of the oxidation of small magnetite crystals that have size smaller than 30,000 nm is $\gamma\text{-Fe}_2\text{O}_3$; on the contrary, the end product of the oxidation of large crystals that have size larger than 30,000 nm is $\alpha\text{-Fe}_2\text{O}_3$ [25-26].

The goethite ($\alpha\text{-FeOOH}$) and hematite ($\alpha\text{-Fe}_2\text{O}_3$) are formed as the by-products of hydrolysis of Fe^{3+} as shown in Eq. 2.3 and 2.4.



This material is reserved for educational use only, not allowed for commercial use.

2.1.3 Toxicity of IO nanoparticles

Superparamagnetic iron oxide nanoparticles (SPIONs) such as magnetite and maghemite are widely used for magnetic hyperthermia applications because they can generate heat to damage the cancerous tumors without damaging healthy tissues. Moreover, they have superior biocompatibility that is metabolization through heme oxygenase-1 to form blood hemoglobin, ease of synthesis and long term stability [7]. The IO nanoparticles have no acute toxicity; however, the long term impact of using them cannot verify. The IO nanoparticles which accumulate in the liver will most likely be degraded and can potentially be reused by the human body. Besides, it has been reported that the magnetite particles loaded to solid core as a carrier were less toxic than nanoparticles of polysugars and the toxicity of IO nanoparticles also depended on the surface coating [27].

2.2 Coating of IO nanoparticles

2.2.1 Types of coating

Coating of IO nanoparticles with organic materials such as chitosan, dextran and polysugars or inorganic materials such as gold, carbon and silica is important for biomedical applications. The coating of nanoparticles can be divided into two main methods. Firstly, *in-situ* coating is the coating during synthesis of nanoparticles. Secondly, post-synthesis coating is the coating after obtaining the nanoparticles. The obtained nanoparticles from the latter method are known as core-shell MNPs. The *in-situ* method has several advantages over post-synthesis method, including reduction in agglomeration of nanoparticles because of immediate coating and fewer preparing procedures. It is however the presence of coating substances during synthesis can disturb the processes of nucleation and growth of crystals, in which the *in-situ* coating has effect on the crystal structure [28].

2.2.2 Advantages of coating

The coating of IO nanoparticles has several advantages for biomedical applications as follows.

- It can reduce agglomeration of IO nanoparticles. The agglomeration occurs because the IO nanoparticles have hydrophobic surfaces with large surface area to volume ratio, resulting in the hydrophobic interaction between each other. The agglomerated particles have poor dispersion and lose the superparamagnetic properties owing to the increasing of cluster size.

- It can prevent the IO nanoparticles from oxidation and corrosion. Although the IO nanoparticles are less sensitive to oxidation, the Fe_3O_4 nanoparticles will be oxidized and converted to $\alpha\text{-Fe}_2\text{O}_3$ due to the presence of vulnerable Fe^{2+} . The obtained IO nanoparticles have weak magnetic properties because $\alpha\text{-Fe}_2\text{O}_3$ displays no magnetism.

- It can improve biocompatibility and cell adhesion properties of IO nanoparticles. In case of the Fe_3O_4 nanoparticles, they have few hydroxyl groups on the surface hence it is difficult to bond with organic materials. When the Fe_3O_4 nanoparticles are coated with polymer, the amount of hydroxyl groups will be increased. Moreover, the polymer can be used as a matrix for drugs and genetic materials.

- It can enhance the circulation time of IO nanoparticles. In the event of using the IO nanoparticles in vivo, the IO nanoparticles must be prolonged their circulation time in blood to reach the target site. The coating of IO nanoparticles can resist the non-specific protein adsorption. The phagocytic cells can slowly recognize IO nanoparticles as foreign substances. Therefore, the IO nanoparticles can stay longer in blood circulation. Furthermore, the coated IO nanoparticles with slightly negatively charged substances can protect them from endocytic cells' uptake for the reason that the cell membrane is negatively charged.

- It can improve the physicochemical stability and biofunctionality of IO nanoparticles since the IO nanoparticles have relatively low colloidal stability in medium pH [28].

2.2.3 Chitosan

Chitosan is a linear polysaccharide of β -(1 \rightarrow 4) linked 2-acetamido-2-deoxy- β -D-glucopyranose or *N*-acetyl glucosamine units and 2-amino-2-deoxy- β -D-glucopyranose or glucosamine units. It is produced by treating chitin obtained from shrimp shells, crab shells and squid pens with an alkaline substance such as sodium hydroxide. This process is known as deacetylation of chitin [24]. In the deacetylation, the acetyl amine groups of chitin are converted into the amino groups as shown in Fig. 2.1. If the amino groups have more than sixty percent, they are known as chitosan [29].

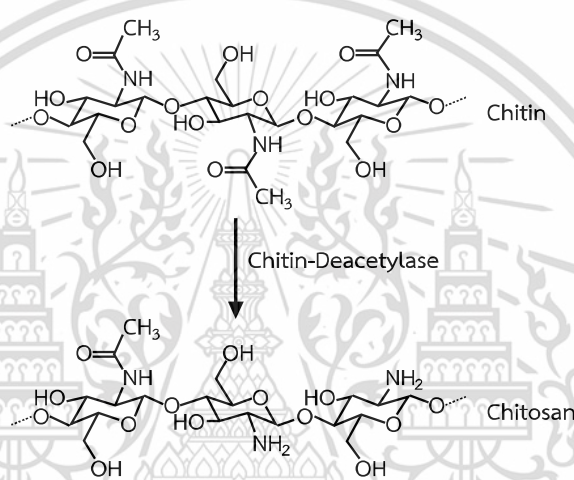


Figure 2.1 Deacetylation of chitin [29]

The chitosan has semi-crystalline structure, possessing several good biological properties. It is biocompatible, non-toxic, edible and biodegradable natural polymer. It can be metabolized by human enzymes, especially lysozyme. The chitosan has pH sensitivity. The amino group of chitosan has a pKa value of about 6.5; hence, chitosan is insoluble in neutral and basic environment but it is soluble in diluted acid. The chitosan is a polyelectrolyte, in which it possesses positive charges when dissolving in acid environment and its charge density depends on the environmental pH [30]. Since the cell membrane is negatively charged; therefore, the chitosan which is positively charged has bioadhesivity. In addition, the chitosan can combine with various organic materials, such as cholesterol, fats, proteins, tumor cells, etc. It has been report that fibroblasts which have negatively charged surface display higher adhesion to chitosan than keratinocytes which is the

cell type in the epidermis [31]. Besides, the chitosan has bacteriostatic effect. The amino groups of chitosan can be functionalized with other functional groups; therefore, the chitosan can be used for encapsulation of drugs, immobilization of enzymes and being a gene carrier [15-16]. From the above mentioned, the chitosan is considered to be suitable material for coating the MNPs in biomedical applications, such as drug delivery and hyperthermia.

2.2.4 Sodium tripolyphosphate (TPP)

Sodium tripolyphosphate (TPP) is an inorganic compound which has chemical formula of $\text{Na}_5\text{P}_3\text{O}_{10}$ as displayed in Fig. 2.2. TPP has low toxicity, in which it is classified as Generally Recognized As Safe (GRAS) by the Foods and Drugs Administration [32]. Besides, the polyphosphate units can be hydrolyzed into simpler phosphates and used as nutrient for human body like ATP and it has no effect on mutation and reproductive system.

The TPP has been widely used as a crosslinker for preparation of chitosan products. TPP links chitosan chains and change them into network which has a higher stability than chains. TPP is negatively charged so it can form with protonated amine of chitosan through ionic interaction. This preparation is known as ionotropic gelation which is the easiest synthesis because it is one-shot synthesis and uses the mild environment.

It was observed that the chitosan nanoparticles prepared by using the ionotropic gelation with TPP had a nanometric size, narrow size distribution and spherical shape, in which they were suitable for biomedical applications. Moreover, the chitosan crosslinked with TPP has amphoteric properties having both negatively charged and positively charged units; therefore, it can enhance the protein adhesion [15, 33-34].

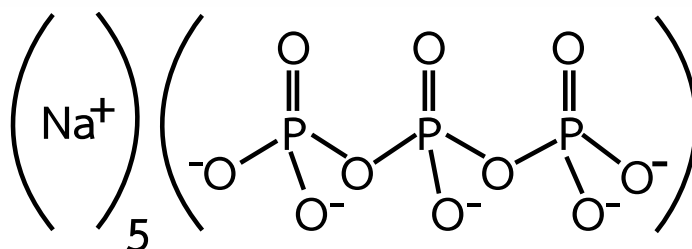


Figure 2.2 Sodium tripolyphosphate (TPP) structure [34]

Some literature reviews related to the chitosan crosslinked with TPP are shown below.

Gomathi, T. et al. [15] studied on the synthesis and size optimization of chitosan nanoparticles using the agitation. The samples were prepared by mixing 50 mg of chitosan with 10 mL of 2 %v/v acetic acid, The mixtures were agitated at 600 rpm for 20 min at room temperature. The agitation conditions were varied, i.e. agitating speed, time and temperature. TPP crosslinker was added to create the chitosan nanoparticles (CS NPs), in which they were dried in the open air and freeze drier. The molar ratio of chitosan:TPP was varied, i.e. 1:0.5, 1:0.8 and 1:1, in which the average particle size of synthesized CS NPs was 417, 242 and 295 nm, respectively. The CS NPs obtained from 1:0.8-chitosan:TPP was considered to be the optimum condition due to the complete crosslinking. The CS NPs synthesized by using different agitation speed of 200, 600 and 800 rpm resulted in the different average particle size of 210, 50 and 54 nm, respectively. The CS NPs synthesized with different agitation time of 30, 60 and 120 min created different the average particle size of 101, 78 and 50 nm, respectively. These results indicated that the average particle size was significantly reduced with increasing agitation time. Moreover, the CS NPs synthesized under different agitation temperature of 25, 40, 50 and 60°C displayed that the agglomeration of resultant NPs increased with increasing agitating temperature; therefore, the particle size and yield of CS NPs would increased. Hence, the optimum condition was the synthesis using the agitation at 600 rpm for 120 min at room temperature. The study of drying method of synthesized CS NPs indicated that the CS NPs obtained by drying under open air and freeze drier had the average particle size of 50 and 5.6 nm, respectively. This was probably because the drying under open air created the agglomeration of NPs. On the other hand, the effect of supercritical expansion of freeze drying could efficiently prevent the agglomeration, so the CS NPs dried using freeze drier had smaller particle size and narrow particle size distribution.

Rázga, F. et al. [35] studied on the synthesis of chitosan-tripolyphosphate (TPP) sub micron particles using dropwise adding method. The different concentrations of chitosan solution, i.e. 0.17, 0.22, 0.28, 0.33, 0.39, 0.56 and 0.67 mg/mL and TPP solutions, i.e. 0.42, 0.5, 0.72, 0.83, 1, 1.25 and 1.67 mg/mL were prepared by dissolving chitosan chlorhydrate and TPP in 0.9 %w/v of NaCl (saline). The pH of TPP solutions was then adjusted using HCl (pH=7.4). The samples were prepared by dropwise adding of 9 mL of chitosan solution into 1 mL of TPP solution. Then, the mixture was stirred under mild conditions at room temperature. The as-prepared chitosan-TPP particles were dialyzed using a dialysis SpectraPor tubing with molecular weight cut-off 3500 Da. The particles were prepared at pH=6, in which chitosan adopts the coiled conformation, corresponding to the increasing of molar ratio of TPP. The particle size and zeta potential of sample synthesizing at pH=6 was about 400 nm and 22 mV, respectively. The colloidal stability with the testing time of 24 h depends on the amount of TPP.

Pant, A. et al. [36] studied on the synthesis of chitosan-tripolyphosphate (TPP)-beta cyclodextrin (β -CD) using ultrasonic method. The sample was prepared by mixing β -CD solution with TPP solution with the molar ratio of β -CD:TPP of 1:1. Then, the mixture was treated by using ultrasonic bath for 1 h at room temperature. The as-prepared sample was filtered and dried. The FT-IR technique showed that the TPP molecule formed inclusion complex with β -CD. The size and zeta potential of chitosan nanoparticles based on TPP- β -CD inclusion complex was about 27 mV and 104 nm with the PDI value of 0.35, respectively. While those of chitosan nanoparticles based on TPP was about 48 mV and 169 nm with the PDI value of 0.67, respectively. Hence, TPP- β -CD inclusion complex can be used for the formation of chitosan nanoparticles with smaller and more uniform particle size in comparison to conventional TPP based chitosan nanoparticles.

Gierszewska, M. et al. [37] studied on the synthesis of chitosan membrane ionically crosslinked with pentasodium tripolyphosphate (TPP) using solution casting and solvent evaporation techniques. The sample was prepared by immersing a chitosan membrane in 100 mL of 1.3 %w/v aqueous TPP solution for 1 h at

temperature of 4°C. The pH value of initial TPP solution was varied, i.e. 9.0 and 5.5. The obtained membranes were thoroughly washed with deionized water and air-dried at 37°C, then dried under vacuum at 60°C for 24 h. The FT-IR technique confirmed the interaction between tripolyphosphate anionic groups of TPP and protonated amino groups ($-\text{NH}_3^+$) of chitosan, resulting in the forming of ionic crosslinking. The intensity of the phosphate band at $\sim 1215 \text{ cm}^{-1}$ for membrane crosslinked in TPP solution of pH 5.5 is higher than one of pH 9.0. This result indicated that membrane crosslinked at pH 5.5 has higher crosslinking density because $-\text{NH}_3^+$ of chitosan membrane are mostly deprotonated by OH^- ions at high pH value. The wide-angle X-ray diffraction (WAXD) technique showed that crystallinity of chitosan decreases after its crosslinking with TPP. The AFM technique confirmed that ionic crosslinking leads to an increase in the membrane roughness.

2.3 Synthesis methods of iron oxide nanoparticles (IO)

2.3.1 Soft solution processing

Soft solution processing is a wide group of synthesis processes of inorganic substances such as multicomponent oxide that uses an aqueous solution as precursors and/or reaction media. In addition, the soft solution processing has minimum steps and consumes low energy and materials. Due to using the aqueous media and low energy, the soft solution processing is environmentally friendly and economical process [38]. The solution treatment can be easily modified and/or combined with different methods, such as electrochemical method, hydrothermal method, refluxing method, microwave or ultrasonic-assisted methods, etc. Morphology and chemical composition of the desired materials can be controlled by adjusting the synthesis conditions [39].

Besides, the soft solution processing is capable of preparing iron oxides because the starting reactants can dissolve in water, while the iron oxides products aren't dissoluble in the aqueous solution. It was observed that the inorganic products obtained from the soft solution processing were also homogeneous and monodispersed particles [40].

2.3.2 Hydrothermal method

Hydrothermal method is the use of any heterogeneous chemical reaction in an aqueous solution under the condition above room temperature, typically more than 100°C and at pressure greater than 1 atm in a closed system for producing the desired materials such as inorganic oxides. The aqueous medium can be used as a catalyst of reaction by changing temperature and pressure. Besides, it is environmentally friendly and economical method.

When comparing the hydrothermal method with other methods for synthesis of inorganic oxide powders as shown in Table 2.3, the hydrothermal method has a good compositional control, good morphology control and good powder reactivity. It is because the hydrothermal method uses low temperature to create the crystalline products without calcination; therefore, it can avoid point defects of products and poor stoichiometric control owing to volatilization of components. The obtained particles have homogeneities of chemical composition and size. In addition, hydrothermal method is nonflammable, noncarcinogenic and nonmutagenic method. It also has thermodynamical stability.

Since size and morphology of particles which are synthesized via hydrothermal method can be controlled by reactions time and temperature, this method is beneficial to various industries because it can produce powder materials which have varieties of morphologies and sizes for desired applications. Besides, the hydrothermal method doesn't use any expensive catalysts, seeds or surfactants so it is capable for large-scale and low-cost production with high-quality crystals.

In case of producing of iron oxides via hydrothermal method, the formation of iron oxides occurs through two main routes including hydrolysis and oxidation and neutralization of mixed iron hydroxides. The first method typically uses ferrous salts as a precursor. The reaction conditions, such as temperature, time, starting concentration, ratio of reactants, nature of precursors and addition of seeds, strongly effect on the resultant products. It has been reported that the particle size of Fe_3O_4 increased with the increasing of reaction time. The precipitation of larger Fe_3O_4 particles will be obtained when the higher water content is used. The particle size of Fe_3O_4 is depended on the rate of nucleation and grain growth. Nucleation might be faster than grain growth at higher temperature as a result of decreasing in particle

size. On the contrary, the grain growth increases with an increasing of reaction time [41].

Hydrothermal method can also be combined with other methods such as electrochemistry, mechanochemistry, microwave and ultrasound to enhance the reaction kinetics and produce new advanced materials.

Table 2.3 Comparing advantages of different methods for synthesis of inorganic oxide powders [38]

	Solid state reaction	Coprecipitation	Polymerized complex	Sol-gel	Hydrothermal
Cost	Low-moderate	Moderate	High	High	Moderate
State of development	Commercial	Commercial/demonstration	R&D	R&D	Demonstration
Compositional control	Poor	Good	Excellent	Good-excellent	Good-excellent
Morphology control	Poor	Moderate	Moderate	Moderate	Good
Powder reactivity	Poor	Good	Good	Good	Good
Purity (%)	<99.5	>99.5	>99.9	>99.9	>99.5
Calcination step	Yes	Yes	Yes	Yes	No
Milling step	Yes	Yes	Yes	Yes	No

2.3.3 Aqueous based refluxing method

The aqueous based refluxing method is the heating the chemical reaction using aqueous medium for a specific time, while continually cooling the vapour produced back into liquid by a condenser. The thermal energy from heating mantle is the reaction energy of chemical reactants. The reactants can be solid and liquid, or both liquids. The temperature at which the reaction is heated depends on the boiling points of water which is 100°C. The aqueous based refluxing method plays an important role for green synthesis of various nanostructures, such as nanoparticles, nanowires, nanorods and core-shell nanostructures. The size, morphology and crystallinity of the nanostructures can be controlled by varying the parameters, such as the reaction time, cooling rate, order of addition of precursors and concentration of reactants. The aqueous based refluxing method has several advantages compared to traditional methods. This method provides a simple, low cost and environmentally friendly process and the possibility of being applied on a large scale [42].

- **Parameters**

- The reaction time: The nucleation occurs at the initial of reaction, then the nucleus grow in the original direction, forming grains. The grain growth and phase transformation simultaneously take place. The increase of reaction time effects on the grain growth and complete phase formation, resulting in the increase of crystal size and desired phase.

- The cooling rate: The reaction energy is supplied by the heat from heating mantle. The kinetic energies of molecules are high and the nucleation species rapidly move at high temperature. If the reaction cools down with slow cooling rate, the non-defective crystals were formed.

- The order of addition of precursors: The order of precursors is crucial for the chemical reaction which used various precursors because secondary phase could be formed if it is more stable than desired phase. Their reactivity and formation energies should be considered for the order of precursors [42].

2.4 Superparamagnetic properties

The MNPs for magnetic hyperthermia applications need to be superparamagnetic, in which it depended on the particle size of MNPs as shown in Fig. 2.3, that is the graph showing the relationship between nanoparticle radius (r) and coercivity (H_c). The coercivity is the resistance of MNP to demagnetism. A large magnetic particle has its multidomain structure. Magnetic dipole moments which have the same direction are separated by magnetic domain walls. The number of magnetic domains decreases when the particle size of magnetic particles decreases. When the particle size decreases toward the single domain critical radius (r_{sd}), the coercivity increases to maximum, resulting in the difficulty in magnetism removal. When the particle size is smaller than the r_{sd} , the particle becomes a single domain, in which it is about 19 nm for magnetite and 26 nm for maghemite. When the particle size is smaller than the superparamagnetic critical radius (r_{sp}), in which it is about 6 nm for magnetite and 10 nm for maghemite, the particle shows one magnetic dipole moment within one magnetic domain because of the fluctuated magnetic dipole moments, resulting in the magnetism removal of particle is easy; therefore, the coercivity value is zero and this particle has superparamagnetic properties [43-45].

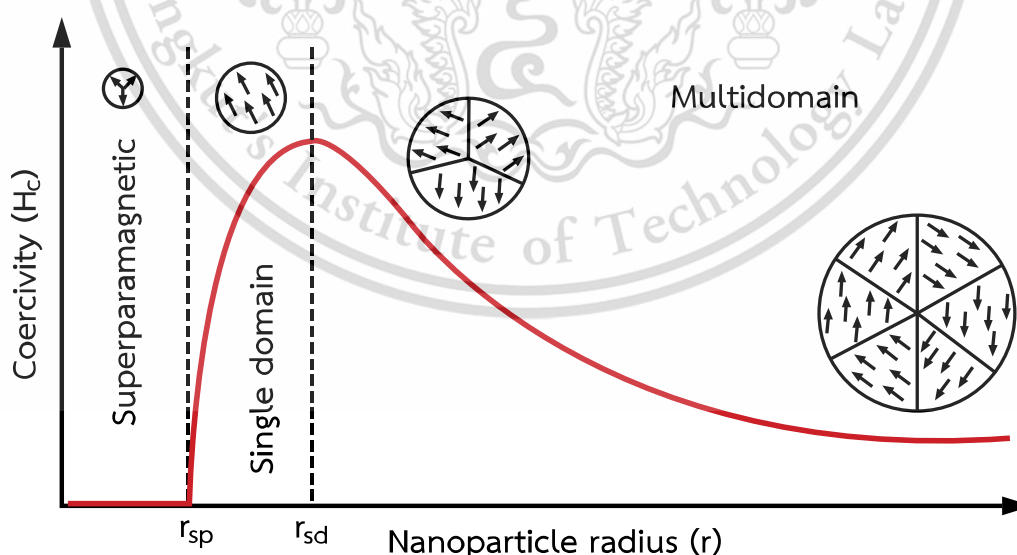


Figure 2.3 Relationship between nanoparticle radius (r) and coercivity (H_c) [43]

The superparamagnetic properties can be explained by hysteresis curves as shown in Fig. 2.4, showing the relationship between external or alternative magnetic field (H) and magnetization (M). In the ideal case, the superparamagnetic curve has no hysteresis loop, so it is observed as S-curve. This type of graph indicates that the MNPs response very fast to the external magnetic field when the magnetic field is applies. All magnetisms of MNPs disappear when the external magnetic field is removed as shown that the magnetization becomes zero in Fig. 2.5 (a). Therefore, the superparamagnetic particles are suitable for biomedical applications, such as magnetic hyperthermia, because they do not retain any magnetism after removal of external magnetic field. The graph with loop as shown in Fig. 2.5 (b) is similar to the data of soft ferromagnetic case. This case means the MNPs retain magnetism when the magnetic field is removed [43].

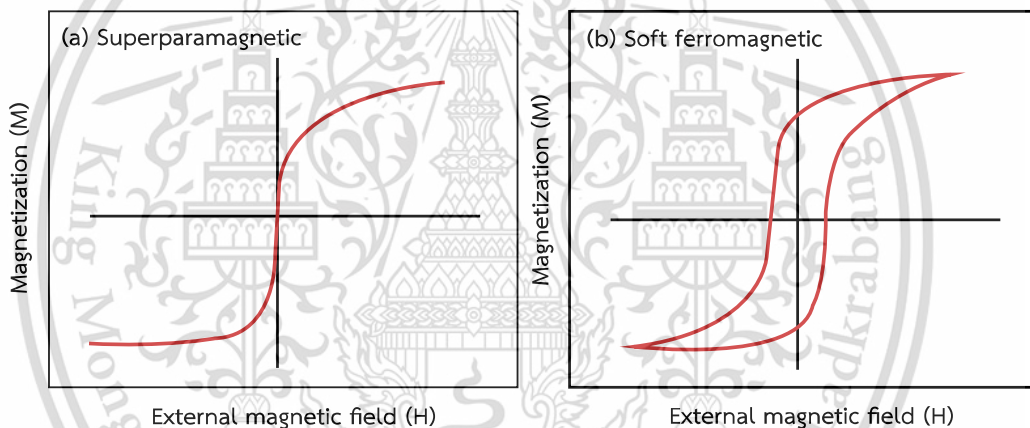


Figure 2.4 Hysteresis curves that obtained from (a) superparamagnetic and (b) soft ferromagnetic materials [43]

The hysteresis curves can show the magnetic properties as displayed in Fig. 2.5. The MNPs magnetize to saturate with alignment of every magnetic dipole moments known as saturation magnetization (M_s). When driving an external magnetic field drops to zero, the MNPs retain magnetization, in which this position is retentivity (M_r). With a further driving the external magnetic field, the magnetization value is zero and this position is coercivity (H_c). The external magnetic field is increased in the negative direction, the MNPs become magnetically saturated but they occur in the opposite direction [30].

This material is reserved for educational use only, not allowed for commercial use.

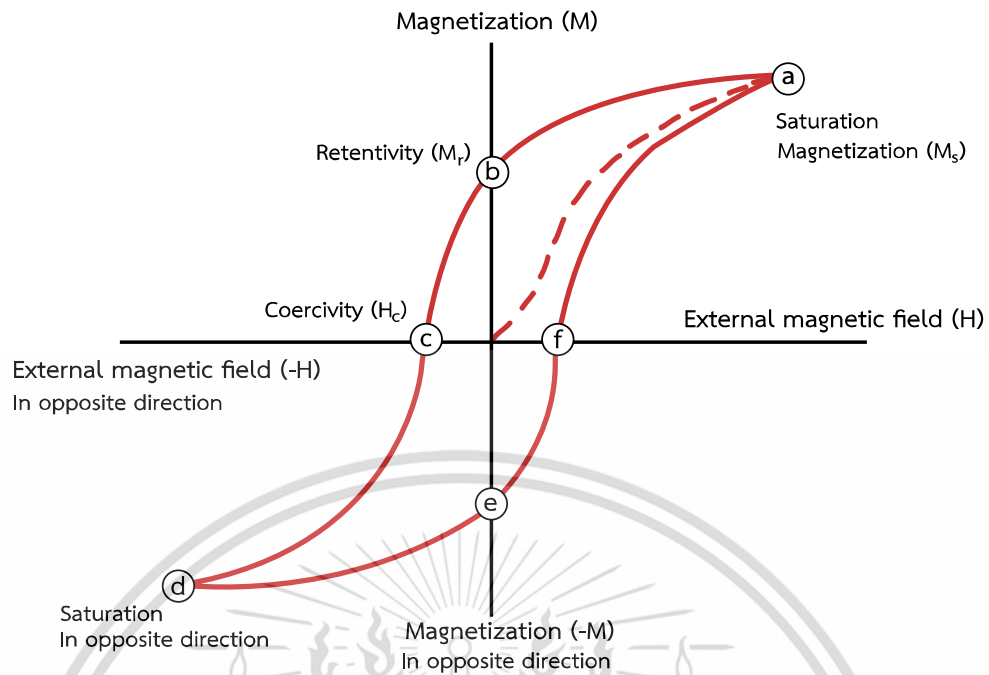


Figure 2.5 Hysteresis loop and magnetic properties of ferromagnetic materials [45]

2.5 Magnetic hyperthermia

Hyperthermia is a type of cancer treatment using heat to increase the temperature of cancerous tumors to the range of 42–46°C. This temperature range can change protein metabolism of the cancerous cells and finally lead to cellular degradation and apoptosis or a cell suicide mechanism [7]. Therefore, partial tumor tissues are dead and the properties of all tumor tissues are changed, meanwhile normal tissues are not injured because the normal tissues can transfer heat better than the cancerous tumors. The alteration of tumor tissues due to the hyperthermia can enhance the efficiency of other cancer therapies, such as chemotherapy, radiation therapy, immunotherapy, etc., because of a consequence of reducing the cancerous tumor size [3].

However the major problem of conventional hyperthermia is an inhomogeneity heat distribution which could create the partially unheated tumors, resulting in reduction of therapeutic efficiency. Furthermore, the increase of temperature in various spots of neighboring tissues could damage the healthy cells and nerves in vicinity of the treated area, resulting in the side effects to the neighboring tissues, such as burn, swell, blister, discomfort, and/or pain. Based on

the effects of conventional hyperthermia, magnetic hyperthermia has been developed as a new method for solving these problems.

Magnetic hyperthermia is a type of local hyperthermia using heat which is generated from magnetic nanoparticles (MNPs) under the alternating magnetic field (AMF). The AMF is a continuous magnetic field that periodically reverses direction, usually sinusoidally [14]. The AMF can change the magnetic dipole moment direction of MNPs and the magnetic dipole moment continuously reverses direction as a consequence, the MNPs can generate the heat to damage the cancerous tumors.

The efficiency of magnetic hyperthermia depends on the magnetic properties of MNPs. They are considered to be related to the heat generation from the MNPs and distribution to the cancerous tumors, in which they can improve the therapeutic efficiency and reduce the side effects to the neighboring tissues [46].

The heating efficiency of MNPs for magnetic hyperthermia is typically evaluated from the specific absorption rate (SAR) and intrinsic loss power (ILP) as shown in Eq. 2.5 and 2.6, respectively [43].

$$\text{Specific absorption rate (SAR; W/g)} = \frac{C_M m_M + C_{H_2O} m_{H_2O}}{m_M} \frac{dT}{dt} \quad (\text{Eq. 2.5})$$

Where C_M and m_M are the specific heat capacity and mass of MNPs,
 C_{H_2O} and m_{H_2O} are the specific heat capacity (4.18 J/gK) and mass of water,
 dT/dt is the initial temperature rising rate that was estimated by the Bekovic and Hamler method.

$$\text{Intrinsic loss power (ILP; nHm}^2/\text{kg)} = \frac{\text{SAR}}{H^2 f} \quad (\text{Eq. 2.6})$$

Where SAR (W/g) is the specific absorption rate,
 H (Oe) is the strength of magnetic field,
 f (Hz) is the field frequency.

Some literature reviews related to preparation of magnetic nanoparticles, their magnetic properties and hyperthermia applications are shown below.

Ristic, M. et al. [47] studied on the synthesis and magnetic properties of CoFe_2O_4 NPs. They were prepared by using 0.5 M cobalt(III) nitrate solution and 1 M ferric nitrate solution. The NaOH solution was added to adjust the pH value of 5.2, 5.3, 6.3, 7.2 and 11.4. The starting solutions were treated by ultrasonic or hydrothermal method at 160°C for the reaction time of 0, 1, 4, 24 and 72 h. The crystallite size of CoFe_2O_4 NPs increased with the increasing of pH value and heating time. All samples were mainly composed of CoFe_2O_4 crystalline phase; however, the samples synthesized at pH 7.2 and 11.4 showed the additional hematite ($\alpha\text{-Fe}_2\text{O}_3$) crystalline peaks in the XRD patterns. The study of magnetic properties displayed that the M_s and blocking temperature (T_B) increased with the increasing of the crystallite size. The CoFe_2O_4 NPs with the crystallite size of 8.7 and 18.1 nm had the M_s of 65.4 and 74 emu/g, respectively.

Amirabadizadeh, A. et al. [48] studied on the synthesis of ferrofluids based on CoFe_2O_4 NPs and the influence of reaction time on their structural, morphological and magnetic properties. In the preparation 1 M cobalt (II) nitrate solution was mixed with 2 M iron(III) nitrate solution and then 3 M NaOH solution was added. The mixture solutions were agitated at 90°C for various reaction times, i.e. 0.5, 2, 3.5, 5 and 6.5 h. The as-prepared CoFe_2O_4 NPs were treated by 2 M HNO_3 . Then the precipitates were dispersed in tetramethylammonium hydroxide (TMAOH), resulting in the ferrofluids. When the reaction time was increased, the average crystallite size and microstrain would increase to a maximum value at 3.5 h-reaction time and then they would decrease because of the decreasing and increasing of the surface tension of the crystallites, respectively. The FESEM showed that the synthesized nanoparticles were spherical shape. The nanoparticles synthesized at 3.5 and 5 h - reaction time were agglomeration; however, the nanoparticles synthesized at 0.5, 2, and 6.5 h-reaction time had smaller particle size, less agglomeration and more uniform distribution because the TMAOH surfactant well coated on the NPs surfaces. The study of magnetic properties indicated that the M_s and H_c values increased with the increasing of CoFe_2O_4 particle size because of the existence of larger particles

with higher ordered spines. Furthermore, the reduction in H_c of ferrofluids as compared to nanoparticles could be justified by the presence of water as carrier liquid and its effectiveness on Brownian rotation, resulting in the increasing of spin magnetization rotation. Besides, the M_s values of ferrofluids were lower than that of the nanoparticles due to the volume fraction of CoFe_2O_4 NPs in ferrofluids.

Cabuil, V. et al. [49] studied on the synthesis of ferrofluid based on CoFe_2O_4 NPs and the influence of hydrothermal treatment on size of nanoparticle. The CoFe_2O_4 NPs were prepared by using classical heating method (CH-NPs) and hydrothermal method (HT-NPs) at 100°C for 1 h. The hydrothermal treatment time was varied, i.e. 1, 2, 24 and 120 h. The CoFe_2O_4 NPs were dispersed in 0.2 M HCl. The XRD technique showed that the crystallite size of the HT-NPs was slightly larger than CH-NPs. The TEM results displayed that the HT-NPs are more spherical shape than that of CH-NPs. The spherical shape of HT-NPs was changed into cubic shape when the hydrothermal time was increased. It was because cubic shape is the most stable product.

Phong, P.T. et al. [43] studied on the sized-controlled heating ability of CoFe_2O_4 NPs for hyperthermia applications. The CoFe_2O_4 NPs with the particle size of 13.5 (Co1), 17.8 (Co2) and 24.2 (Co3) nm were prepared using microwave irradiation and hydrothermal methods. The study of magnetic properties using magnetic field of 80 Oe and frequency of 178 kHz showed that the M_s and H_c of increased with the increasing of their particle sizes. Because the effect of H_c was beyond the effect of M_s due to the low applied magnetic field, the SAR value which indicated that heating ability decreased with the increasing of H_c . This was probably because the H_c of the Co1 sample was smaller than the applied magnetic field strength. Thus, the magnetic moments of Co1 sample fully responded to magnetic field excitation. The Co1 sample could generate the highest amount of heat. On the other hand, the H_c of the Co2 and Co3 samples were larger than the applied magnetic field; therefore, the magnetic moments were unable to fully respond as a consequence, the samples generated the low amount of heat.

Briceño, S. et al. [50] studied on the solvothermal synthesis of cobalt ferrite hollow spheres with chitosan. The CoFe_2O_4 NPs coated with chitosan were prepared using *in-situ* coating (M1 sample) and post-synthesis coating (M2 sample) methods. The CoFe_2O_4 NPs obtained from post-synthesis coating were treated with oleic acid. In the synthesis, ethylene glycol was used as the solvent and the starting mixtures were treated in autoclave at 250°C for 13 h. The XRD technique revealed that the synthesized nanoparticles were mainly composed of CoFe_2O_4 crystalline phase and the M2 sample had sharper crystalline peaks than the M1 sample, corresponding to the greater degree of crystallinity. The TEM results displayed that the particle size of CoFe_2O_4 in M1 and M2 samples was 4 and 6 nm, respectively. The CoFe_2O_4 NPs in M1 sample had irregular shape, whereas those of M2 sample were uniform in size and morphology. Besides, the agglomeration was obtained in both M1 and M2 samples; however, the M2 sample had better dispersibility. The study of magnetic properties indicated that both M1 and M2 samples had narrow hysteresis loops, representing the soft ferromagnetic properties with a small response to the external magnetic field. The M1 and M2 samples exhibited the maximum magnetization of 15.6 and 28.9 emu/g, respectively. The greater degree of crystallinity and better dispersibility with more uniform shapes of CoFe_2O_4 NPs in the M2 sample resulted in the higher ordered magnetic vector and the stronger magnetic behavior.

de Lima, L.J. et al. [51] studied on the magnetic behavior of $\text{CoFe}_2\text{-CoFe}_2\text{O}_4$ nanocomposites obtained from colloidal synthesis using chitosan and borohydride reduction. The samples were prepared by mixing cobalt(II) chloride and iron(II) chloride solutions. Then the chitosan and sodium borohydride (NaBH_4) were added to create the precipitates. The precipitates were treated at 380°C for 2 h under N_2/H_2 atmosphere, resulting in the non-crosslinked sample (NPT1). The glutaraldehyde was used in order to crosslink NPT2 sample. The XRD technique presented that the NPT1 and NPT2 samples were metallic iron-cobalt alloy (CoFe_2) and cobalt ferrite (CoFe_2O_4), respectively. The proportion of CoFe_2 representing the soft ferromagnetic properties of the NPT1 was more than the NPT2. The average particle size of CoFe_2 was unchanged in both samples; however, the average particle size of CoFe_2O_4 increased from 3.9 nm of the NPT1 to 13.1 nm of the NPT2. The

addition of glutaraldehyde could modify the arrangement of the chitosan chains in the aqueous solution and thus enhanced the exposure of the nanoparticles to progressive oxidation. The study of magnetic properties at different temperatures of testing revealed that the H_c of NPT1 and NPT2 sample increased with the decreasing temperature of testing. The M_s of NPT1 sample was 192 emu/g which is similar to that $CoFe_2$ in bulk and the hysteresis curves showed the soft ferromagnetic properties at room temperature. These were because the effect of the soft magnetic phase of $CoFe_2$ was beyond the effect of the hard magnetic phase of $CoFe_2O_4$. For the NPT2, the hysteresis curves displayed a characteristic deformation at temperature below 100 K, resulting from an exchange-spring-like magnetic coupling which occurred between the soft and hard magnetic phases corresponding to a greater amount of $CoFe_2O_4$.

Fazio, E. et al. [52] studied on the synthesis of IO nanoparticles using laser ablation. The IO nanoparticles were prepared by using laser with frequency of 100 kHz, the pulse width of 6 to 8 ps and laser power of 0.1, 0.5 and 1.5 W in water and PVA aqueous solution. The Raman spectroscopy technique showed that the synthesized nanoparticles were mainly composed of hematite ($\alpha-Fe_2O_3$). The nanoparticles were spherical particles which their diameters were in the range of 20 to 100 nm, in which the particle size was directly proportional to the laser power used in the synthesis. The study of antibacterial activity on *Staphylococcus aureus* (*S. aureus*) found that the iron oxide nanoparticles in water showed a partial antibacterial effect, while those in PVA aqueous solution had slight effect.

Nemati, Z. et al. [11] studied on the synthesis of superparamagnetic iron oxide nanodiscs for hyperthermia therapy. The disc-shaped MNPs were synthesized via the soft template-assisted synthesis in a binary system of H_2O /Cetyltrimethylammonium bromide (CTAB) using refluxing method. Iron(III) acetylacetonate was used as the precursor. The resultant products obtained in disc-shaped MNPs were compared with the ones with spherical MNPs synthesized via refluxing method. The TEM results showed that the discs had average diameter around 11.5 nm. The thicknesses of disc-shaped MNPs obtained from AFM technique

was in between 2.5 and 3 nm. The XRD technique confirmed that both samples were either magnetite or maghemite. The study of magnetic properties presented that the blocking temperature (T_B) of the spherical MNPs was around 55 K, while that of the disc-shaped MNPs did not define because the zero-field-cooling/field-cooling (ZFC/FC) curve presented much broader maximum. The different in T_B between both samples, despite having a similar volume, could be related to an increase of anisotropy (K) values for the nanodiscs. The estimated anisotropy values of spherical MNPs and disc-shaped MNPs were 8.5×10^5 and 10.1×10^5 erg/cc, respectively. The increasing of anisotropy values could be associated with the shape (shape anisotropy) and the increase in surface area (surface anisotropy) of the nanodiscs. The study of magnetic hyperthermia exhibited that the specific loss power (SLP) value of nanodiscs was higher than spherical MNPs with a similar volume, especially at low magnetic fields. This confirmed that the disc-shaped MNPs showed advantages over the spherical MNPs for hyperthermia therapy. Besides, the size reduction of the nanodiscs hindered the heating capacity due to the loss of the vortex magnetic domain structure, despite the potential improvement of the circulation life time in the blood or the MNPs disaggregation. Therefore, the size of these nanodiscs should be carefully tuned in order to enhance their heating properties while conserving the in-vivo advantages associated with small superparamagnetic nanoparticles.

Das, H. et al. [53] studied on the superparamagnetic properties of magnesium ferrite nanoparticles (MgFe_2O_4 NPs) synthesized using ultrasonic spray pyrolysis technique for hyperthermia application. The nanoparticles were prepared using magnesium nitrate solution and iron(III) nitrate solution which molar ratio of Mg:Fe was 1:2. The mixture was treated by ultrasonic spray pyrolysis technique under various temperatures of 600, 700, 800 and 900°C. The XRD technique confirmed that the nanoparticles were magnesium ferrite. The MgFe_2O_4 NPs synthesized at 600, 700, 800 and 900°C had the crystallite size of 4.05, 9.6, 15.97 and 31.48 nm, respectively. The study of morphology found that the MgFe_2O_4 NPs had smooth spherical shape. When the pyrolysis temperature was increased, the agglomeration of nanoparticles would be decreased. MgFe_2O_4 NPs with the crystallite

size of 4.05 and 9.6 nm possessed the superparamagnetic properties, whereas the MgFe_2O_4 NPs with the crystallite size of 15.97 and 31.48 nm had the ferromagnetic properties. The M_s of MgFe_2O_4 NPs increased with the increasing of pyrolysis temperature. The study of heat generation displayed that the MgFe_2O_4 NPs with the crystallite size of 9.6 and 15.9 nm could generate heat, inducing the temperatures to 37 and 31°C, respectively. Therefore, the MgFe_2O_4 NPs synthesized at 700°C having crystallite size of 9.6 nm could generate the highest amount of heat, in which it was possible to develop for hyperthermia application.

Thomas, R.G. et al. [14] studied on the preparation of iron oxide nanoparticles and their hyperthermia and the magnetic resonance imaging (MRI) properties. The surfaces of iron oxide nanoparticles were modified with oleic acid and dopamine (HA-SPIONs) and oleic acid, dopamine and methoxy PEG succinimidyl succinate (HA-PEG10-SPIONs). The as-prepared nanoparticles were then conjugated with hyaluronic acid (HA) by using 1-ethyl-3-(3-dimethylaminopropyl) solution and N-hydroxy-succinimide solution. The DLS technique revealed that the HA-SPIONs and HA-PEG10-SPIONs had hydrodynamic sizes of 149 and 176 nm, respectively. From the study of the MRI properties, the obtained images after injection of the HA-SPIONs and HA-PEG10-SPIONs into SCC7 cells (Squamous cell carcinomas) for 3 h had T2 contrast of about 40 and 20%, respectively. The results of SAR measurement at 293 kHz and the magnetic field strength of 12.57 Oe showed that the specific absorption rate (SAR) values of the HA-SPIONs and HA-PEG10-SPIONs were 79.42 and 146.3 W/g, respectively. The study of the hyperthermia properties presented that both HA-SPIONs and HA-PEG10-SPIONs were less than 40% of live squamous cell carcinomas.

Lahiri, B.B. et al. [7] studied on the preparation of magnetite nanoparticles coated with phosphate and their hyperthermia properties. They were prepared using coprecipitation method from 0.2 M ferric chloride solution and 0.1 M ferrous sulphate solution. The mixture of starting solutions was diluted with water in order to obtain the concentrations of samples of 0.5 1.0 1.5 2.0 2.5 and 6.0 wt%. 25 mL of orthophosphoric acid was added into the diluted solution and the mixture was incubated for 1 h. The hyperthermia properties of the products were analyzed by

using various magnetic field strength, i.e. 0.36, 0.52, 0.64, 0.73 and 0.82 kAm⁻¹. The XRD and FTIR data confirmed that the synthesized nanoparticles were magnetite with the crystallite size of 7.75 nm. The VSM results showed that the uncoated and coated magnetite nanoparticles had the saturation magnetization (M_s) of 63.6 and 52 emu/g respectively, in which they had superparamagnetic properties. The TEM results displayed that the nanoparticles were spherical shape with the average particle size of 14 nm. The measurement of hydrodynamic size distribution presented that the size of magnetite nanoparticle was about 32 nm, which is four times greater than the crystallite size calculated from the XRD data, indicating the agglomeration of nanoparticles. In the hyperthermia study, all samples showed an intrinsic loss power (ILP) in the range of 158 to 125 nHm² kg⁻¹, indicating that all samples had high efficiency of heat generation. These ILP values were recorded at the product of magnetic field and frequency (H.f) = 0.92-1.03 × 10⁸ Am⁻¹ s⁻¹ which was lower than the specified threshold of 4.85 × 10⁸ Am⁻¹ s⁻¹, indicating that the samples were safe for hyperthermia application in the human body. The sample of the concentrations of 1.5 wt% with magnetic field strength of 0.82 kAm⁻¹ exhibited the highest value of heat generation.

Araújo-Neto, R.P. et al. [9] studied on the synthesis of magnetite nanoparticles and their surface modification with sodium oleate for hyperthermia application. The products were obtained by coprecipitation between iron(III) chloride hexahydrate and iron(II) sulphate heptahydrate. The XRD technique confirmed that the synthesized particles were magnetite and had an average crystallite size of 9.8 nm. In TEM images, it can be seen that the diameter of synthesized nanoparticles were in the range of 6 to 12 nm. From DLS technique, the hydrodynamic diameter of the nanoparticles was about 60.6 nm and polydispersity index (PDI) value was about 0.128. These result indicated that the agglomeration of nanoparticles when they were in the aqueous media. The VSM results presented that the M_s of the nanoparticles was 64 emu/g which accounted for 64% of unmodified nanoparticles. The study of hyperthermia properties displayed that the SAR value of the nanoparticles was 14 W/g at 62 kHz and a magnetic field strength of 15.9 kA/m, in

which the temperature could be increased to 42.5°C within 1.9 min when using the oleated coated magnetite nanoparticle density of 50 mg/mL.

Harraz, F.A. [54] studied on the synthesis of magnetite nanowires, in which they were modified surface with polyethylene glycol (PEG). Magnetite were prepared by mixing ferrous sulphate heptahydrate ($\text{FeSO}_4 \cdot 7\text{H}_2\text{O}$) with sodium thiosulphate pentahydrate ($\text{Na}_2\text{S}_2\text{O}_3 \cdot 5\text{H}_2\text{O}$). The obtained products were grinded and treated by hydrothermal method at 100, 125 and 150°C for 24, 48 and 72 h. The PEG aqueous solutions with the volume ratios of PEG:water, i.e. 0:4, 1:3, 1:2, 1:1, 3:1 and 4:0. were used as medium. It was found that synthesized nanowires obtained by using the volume ratio of PEG:water of 1:2 and hydrothermal treatment at 150°C for 24 h were magnetite crystalline phase without any impurities, having the crystallite sizes in the range of 30 to 45 nm. The TEM images displayed that those nanowires had the average diameter of 25 nm with the maximum length of 1.5 μm . Those nanowires were straight with smooth surface. The VSM technique showed that the M_s of those nanowires was about 90.94 emu/g. It is because the coexisting magnetite nanoparticles and their shape anisotropy.

Soares, P.I.P. et al. [17] studied on the synthesis of magnetite nanoparticles by chemical precipitation (Fe_3O_4 -CP NPs) and thermal decomposition (Fe_3O_4 -TD NPs). The magnetite nanoparticles were coated with chitosans having molecular weight of 38 (Cs 38 kDa) and 469 kDa (Cs 469 kDa) kDa for hyperthermia application. Iron(III) acetylacetonate ($\text{Fe}(\text{acac})_3$) was used as a reactant and TPP was a crosslinking agent. The TEM results showed that the average diameters of pristine Fe_3O_4 -CP NPs and Fe_3O_4 -TD NPs were 8.5 and 8 nm, respectively. The XRD technique confirmed that the crystalline phase of both synthesized pristine Fe_3O_4 -CP NPs and Fe_3O_4 -TD NPs was magnetite, having the same crystallite size of 9.7 nm. The VSM measurement indicated that the pristine Fe_3O_4 -CP NPs and Fe_3O_4 -TD NPs had the M_s of 58 emu/g and 61 emu/g, respectively. It can be concluded that the chemical precipitation and thermal decomposition methods did not significantly affect on the particle size and magnetic properties of the synthesized magnetite NPs. Besides, the SAR measurements revealed that the SAR value was inversely proportional to the

molecular weight of chitosan, in which the SAR values of Fe₃O₄-CP NPs and Fe₃O₄-TD NPs coated with Cs 469 kDa were respectively decreased by 1 and 7 times from those of Fe₃O₄-CP NPs and Fe₃O₄-TD NPs coated with Cs 38 kDa, respectively.

Tran, H.V. et al. [55] studied on the synthesis of chitosan/magnetite composite beads by hydrothermal treatment for removal of Pb(II) and Ni(II) from aqueous solution. Chitosan solution was prepared by mixing 0.5 g of chitosan, 5 mL of acetic acid and 45 mL of distilled water. Then ferrous chloride (FeCl₂) and ferric chloride (FeCl₃) with the molar ratio of 1:2 were dissolved in the chitosan solution. The mass ratio of chitosan to magnetite was varied, i.e. 1:2 and 4:1. Then, the as-prepared mixture was dropped into 30 wt.% NaOH solution. The suspension was kept at room temperature for 24 h. The obtained particles were separated, washed with distilled water and dried in vacuum at 70°C for 24 h. The synthesized chitosan/magnetite beads were studied for adsorption behaviors. They were investigated in aqueous solution at room temperature by using the different pH values, i.e. 4, 5 and 6. The XRD technique confirmed that the crystalline phase of all chitosan/magnetite beads were magnetite, having the same crystallite size of 35 nm. The TEM images showed that all chitosan/magnetite beads were spherical shape and their size were in the range of 25–30 nm. The VSM technique indicated that all chitosan/magnetite beads had superparamagnetic properties with the M_s of 55 emu/g. Moreover, the chitosan of chitosan/magnetite beads could coordinate with heavy metal ions at pH 4–6. Maximum adsorption capacities for Pb(II) and Ni(II) at pH 6 of chitosan/magnetite beads using the mass ratio of 4:1 were 63.33 and 52.55 mg/g, respectively. The adsorption capacity increases with the increase of pH value.

Unsoy, G. et al. [56] studied on the synthesis of chitosan-coated iron oxide nanoparticles (CS MNP) by chemical coprecipitation. Chitosan solution was prepared by dissolving 0.15 g of chitosan in 30 mL of 1% acetic acid and the pH was adjusted to 4.8 by 10 M NaOH. 1.34 g of Ferrous chloride tetrahydrate (FeCl₂·4H₂O) and 3.40 g of ferric chloride hexahydrate (FeCl₃·6H₂O) were dissolved in 30 mL of 0.5% chitosan solution. Then, the as-prepared solution was mixed with 10 mL of 7.5% TPP and 32% NH₄OH with vigorously stirring under N₂ gas flow at room temperature. The final

NH_4OH concentration was varied, i.e. 31% (CS MNP-S1), 33% (CS MNP-S2), 38.5% (CS MNP-S3) and 43% (CS MNP-S4). The ammonia solution was added to produce iron oxide nanoparticles, then the resulting mixture was stirred for 1 h. The CS MNP nanoparticles were washed with deionized water and separated by magnetic decantation for several times. The XRD technique confirmed the presence of the magnetite crystal in CS MNP nanoparticles, having an inverse cubic spinel structure. The crystal size of the bare magnetite and the CS MNP nanoparticles were about 18 and 8 nm, respectively. The XPS technique revealed that the photoelectron peaks at 711.7 and 725.2 eV were the characteristic doublet of $\text{Fe } 2p^{3/2}$ and $2p^{1/2}$ core-level spectra of iron oxide, respectively, corresponding to the oxidation state of Fe in magnetite. Additionally, the CS MNP nanoparticles expressed a new band for N1s at around 400 eV. This new band was assigned to chelation between the amino groups and iron ions ($\text{NH}_2\text{-Fe}$). The TEM images showed that the synthesized CS MNP nanoparticles were almost spherical and have uniform size distribution. The average diameters were in the range of 6–8 nm (CS MNP-S1), 5–7 nm (CS MNP-S2), 3–5 nm (CS MNP-S3) and 1–3 nm (CS MNP-S4). The sizes of the nanoparticles get smaller as the concentration of NH_4OH increases in the solution during the synthesis. The DLS technique presented that the average sizes of the nanoparticles were about 103 nm (CS MNP-S1), 86 nm (CS MNP-S2), 66 nm (CS MNP-S3) and 58 nm (CS MNP-S4). These results were in parallel with the results inferred by TEM. The TGA technique indicated that the principle chains of chitosan began to degrade at about 250°C and the final temperature of decomposition was $\sim 700^\circ\text{C}$. The average mass content of chitosan in CS MNP nanoparticles were around 23% (CS MNP-S1), 20% (CS MNP-S2), 17% (CS MNP-S3) and 15% (CS MNP-S4). The VSM technique showed that the M_s values were about 39 emu/g (CS MNP-S1), 33 emu/g (CS MNP-S2), 29 emu/g (CS MNP-S3) and 25 emu/g (CS MNP-S4). There is no M_r and H_c observed in the hysteresis curves of all CS MNP nanoparticles. The M_s values of CS MNP nanoparticles increased with the size of the magnetic core.

Chapter 3

Research methodology

3.1 Materials

- Sodium tripolyphosphate (TPP), Commercial grade, Union Chemical 1986.
- Chitosan (deacetylation >98%), Commercial grade, Bio21 Co., Ltd.
- Ammonium ferrous sulphate hexahydrate ((NH₄)₂SO₄FeSO₄·6H₂O), Analytical grade, Loba Chemie.
- Ferric chloride hexahydrate (FeCl₃·6H₂O), Analytical grade, Loba Chemie.
- Sodium hydroxide (NaOH), Analytical grade, Carlo Erba.
- Acetic acid (CH₃COOH), Analytical grade, Labscan Asia.
- Distilled water

3.2 Apparatus

- Differential scanning calorimeters (DSC), NETZSCH, DSC 204 F1
- Thermogravimetric analyzer (TGA), PERKIN ELMER, PYRIS 1 TGA
- X-ray diffractometer (XRD), Bruker, SRS 3400
- An in-house vibrating sample magnetometer (VSM), Kasetsart University
- Transmission electron microscope (TEM), FEI, TECNAI G² 20stwin
- Freeze dryer, Labogene, Coolsafe 110-4
- Glass bottle and lid for hydrothermal method
- Glassware
- Heating mantle
- Magnetic stirrer, IKA
- Oven

3.3 Studied parameters

Preparation of CHI/IO nanocomposites

- Precursor preparation method; i.e. adsorption and *in-situ* methods
- Initial concentration of TPP solution; i.e. 0.2, 0.3, 0.4, 0.5 and 0.6 %w/v
- Synthesis method; i.e. hydrothermal and refluxing methods
- Hydrothermal reaction temperature; i.e. 75, 100 and 125°C

3.4 Experimental procedure

3.4.1 Preparation of iron oxide nanoparticles (IO)

10 mL of 0.625 M ammonium ferrous sulphate hexahydrate ((NH₄)₂SO₄FeSO₄·6H₂O) solution was mixed with 10 mL of 1.25 M ferric chloride hexahydrate (FeCl₃·6H₂O) solution and mechanically stirred for 30 min. The as-prepared mixture was added into 50 mL of 1.5 M NaOH solution treated by hydrothermal method at 100°C for 90 min in pressurized glass vessel. The treated precipitate was filtered and washed with 50 mL of distilled water. Finally, the obtained precipitate was dried overnight in the hot air oven at 100°C. Fig. 3.1 shows the process for preparation of IO nanoparticles.

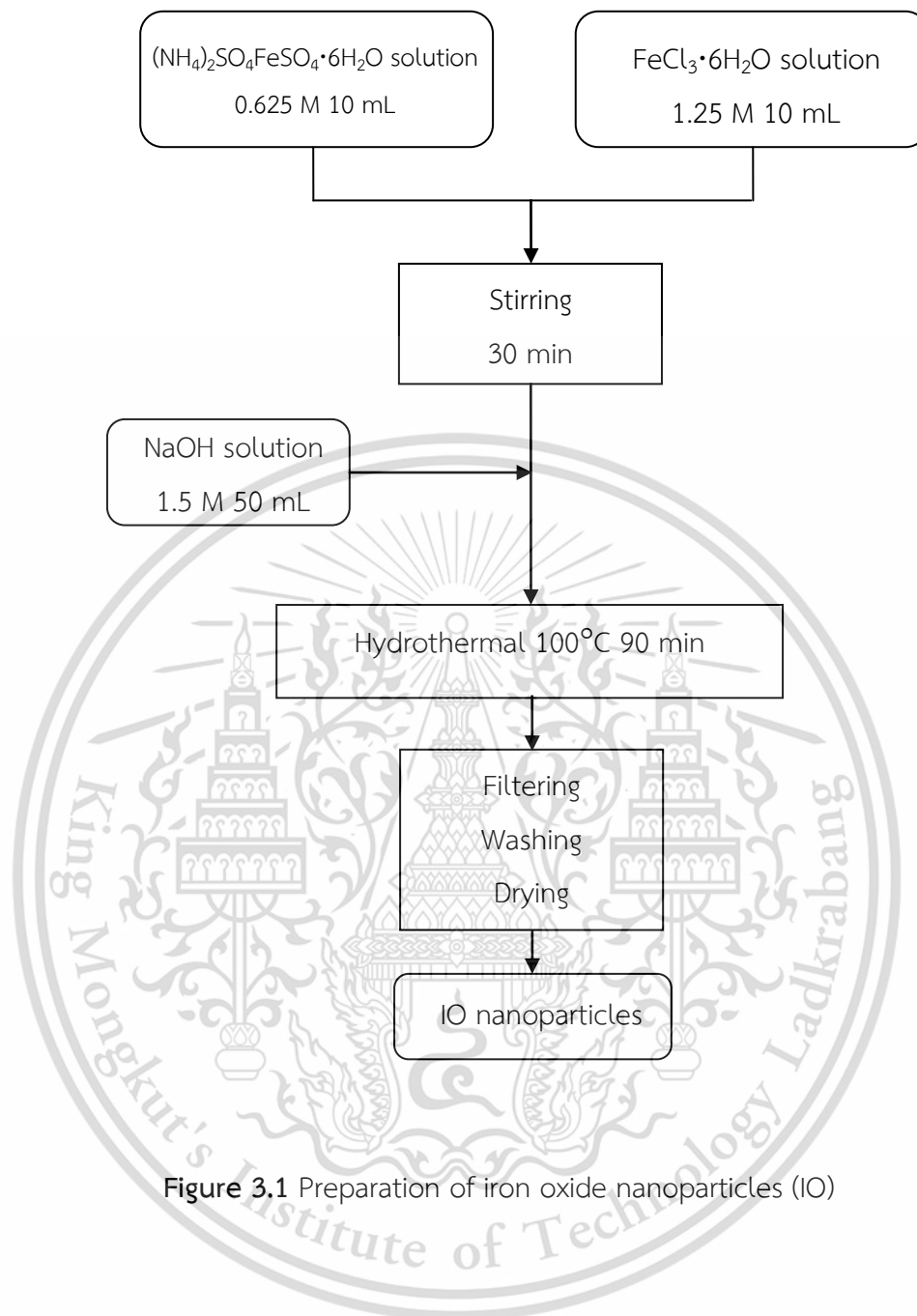


Figure 3.1 Preparation of iron oxide nanoparticles (IO)

3.4.2 Preparation of crosslinked chitosan precipitates (CC)

1.2 g of chitosan was dissolved in 20 mL of 2 %v/v acetic acid solution and mechanically stirred for 30 min. The obtained solution was dropped into 100 mL of sodium tripolyphosphate (TPP) solution and mechanically stirred for 30 min. The initial concentrations of TPP solution were varied, i.e. 0.3, 0.4, 0.5 and 0.6 %w/v. The crosslinked chitosan precipitates (CC) were filtered, washed with distilled water and dried using freeze dryer. Fig. 3.2 shows the process for preparation of CC precipitates.

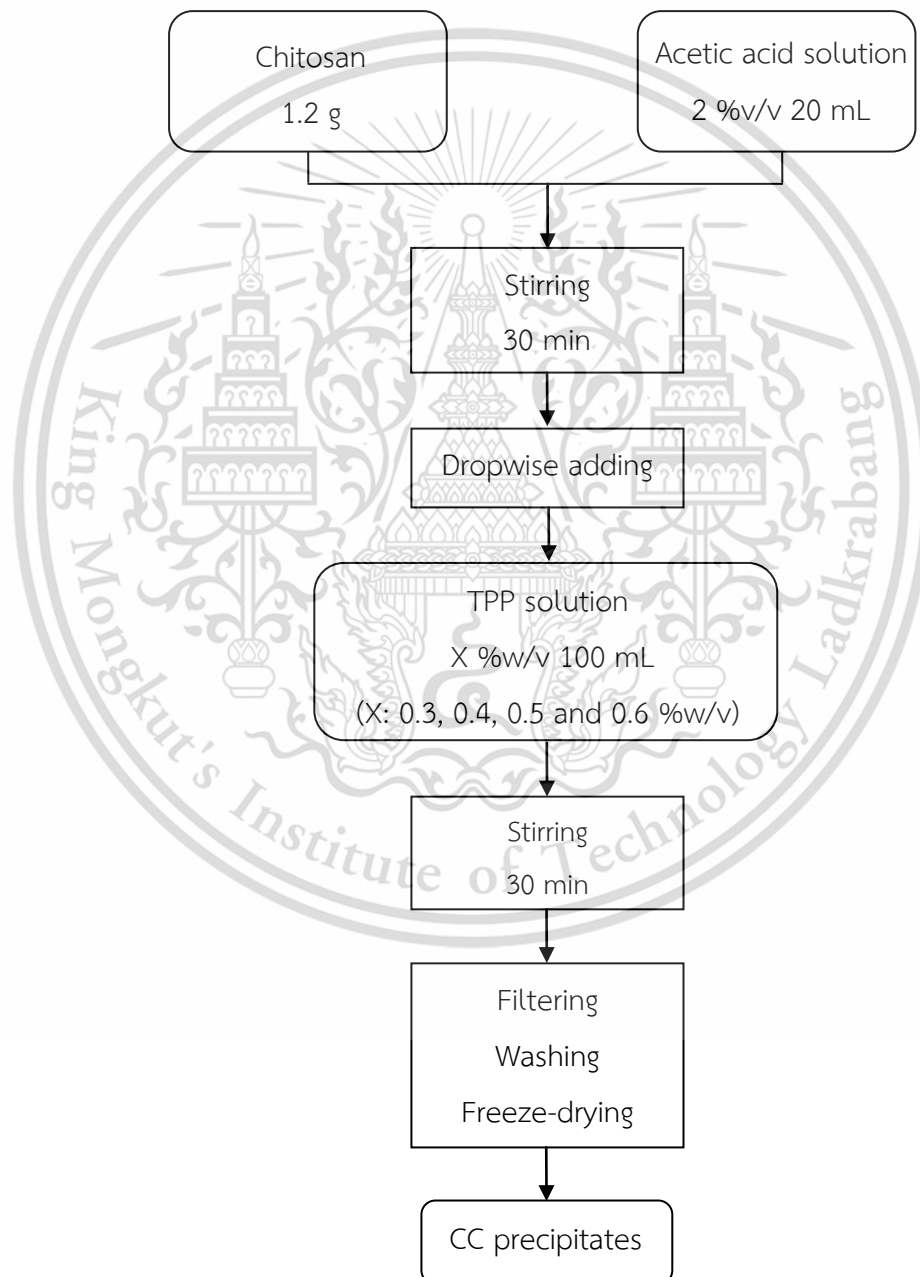


Figure 3.2 Preparation of crosslinked chitosan precipitates (CC)

This material is reserved for educational use only, not allowed for commercial use.

Forbidden to modify the content, and cite the document when use.

3.4.3 Preparation of chitosan/iron oxide nanocomposites (CS/IO) by *in-situ* method

20 mL of 0.625 M ammonium ferrous sulphate hexahydrate ((NH₄)₂SO₄FeSO₄·6H₂O) solution was mixed with 20 mL of 1.25 M ferric chloride hexahydrate (FeCl₃·6H₂O) solution. The mixture was mechanically stirred for 30 min. Meanwhile, 1.2 g of chitosan was dissolved in 20 mL of 2 %v/v acetic acid solution and mechanically stirred for 30 min. The mixture of iron solutions was mixed with the chitosan solution with stirring for 30 min. The mixture was dropwisely added into 100 mL of TPP solution, in which the initial concentrations of TPP solution were varied, i.e. 0.2, 0.3, 0.4, 0.5 and 0.6 %w/v. Then the as-prepared mixture was stirred for 30 min, resulting in the CHI/Fe²⁺Fe³⁺ precursor. The CHI/Fe²⁺Fe³⁺ precursor was filtered and added into 100 mL of 1.5 M NaOH solution. The obtained mixture was treated by hydrothermal method at 75, 100 and 125°C for 90 min or refluxing method for 90 min. The treated precipitates were filtered and washed with 100 mL of distilled water. Finally, the obtained precipitates were dried using freeze-dryer. Fig. 3.3 shows the procedure for preparation of CS/IO nanocomposites by *in-situ* method.

The preparation of CS/IO nanocomposites by *in-situ* method was performed using various conditions as follow:

- Initial concentration of TPP solution; i.e. 0.2, 0.3, 0.4, 0.5 and 0.6 %w/v
- Synthesis method; i.e. hydrothermal and refluxing methods
- Hydrothermal temperature; i.e. 75, 100 and 125°C

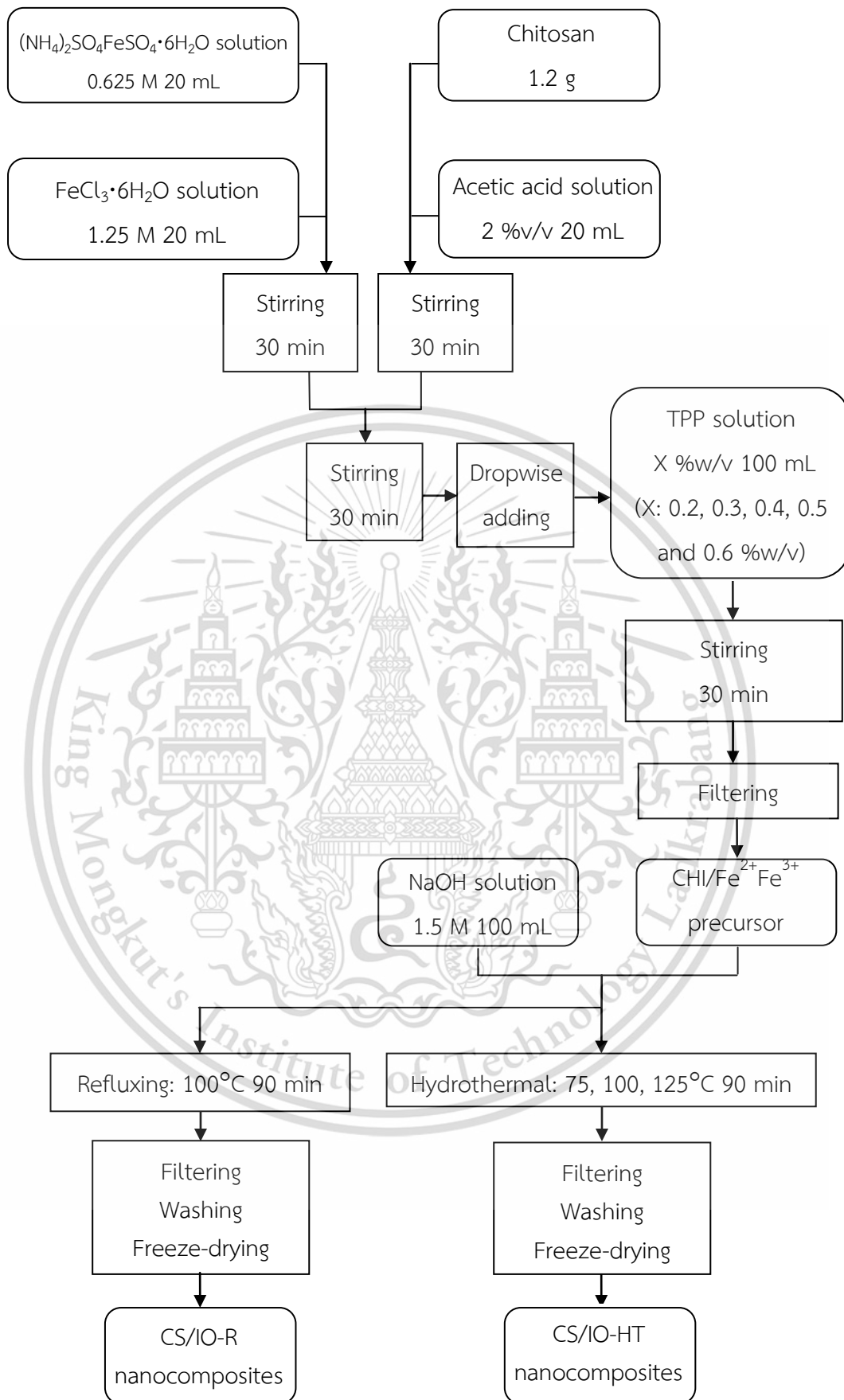


Figure 3.3 Preparation of CHI/IO nanocomposites by *in-situ* method, i.e. CS/IO-HT

This material is and CS/IO-R nanocomposites only, not allowed for commercial use.

Forbidden to modify the content, and cite the document when use.

3.4.4 Preparation of crosslinked chitosan/iron oxide nanocomposites (CC/IO) by adsorption method

20 mL of 0.625 M ammonium ferrous sulphate hexahydrate ($(\text{NH}_4)_2\text{SO}_4\text{FeSO}_4\cdot 6\text{H}_2\text{O}$) solution was mixed with 20 mL of 1.25 M ferric chloride hexahydrate ($\text{FeCl}_3\cdot 6\text{H}_2\text{O}$) solution and then the mixture was mechanically stirred for 30 min. The as-prepared CC precipitate was added into the mixture of iron solutions with mechanical stirring for 30 min in order to adsorb the iron ions into the CC structure, resulting in the $\text{CC}/\text{Fe}^{2+}\text{Fe}^{3+}$ precursor. The $\text{CC}/\text{Fe}^{2+}\text{Fe}^{3+}$ precursor was filtered and added into 100 mL of 1.5 M NaOH solution. Then the obtained mixture was treated by hydrothermal method at 100°C for 90 min or refluxing method for 90 min, producing the CC/IO nanocomposites. The resultant nanocomposites were filtered, washed with 100 mL of distilled water, and dried using freeze-dryer. Fig. 3.4 shows the process for preparation of CC/IO nanocomposites by adsorption method.

The preparation of CC/IO nanocomposites by adsorption method was performed using various conditions as follow:

- Initial concentration of TPP solution; i.e. 0.3, 0.4 and 0.5 %w/v
- Synthesis method; i.e. hydrothermal and refluxing methods

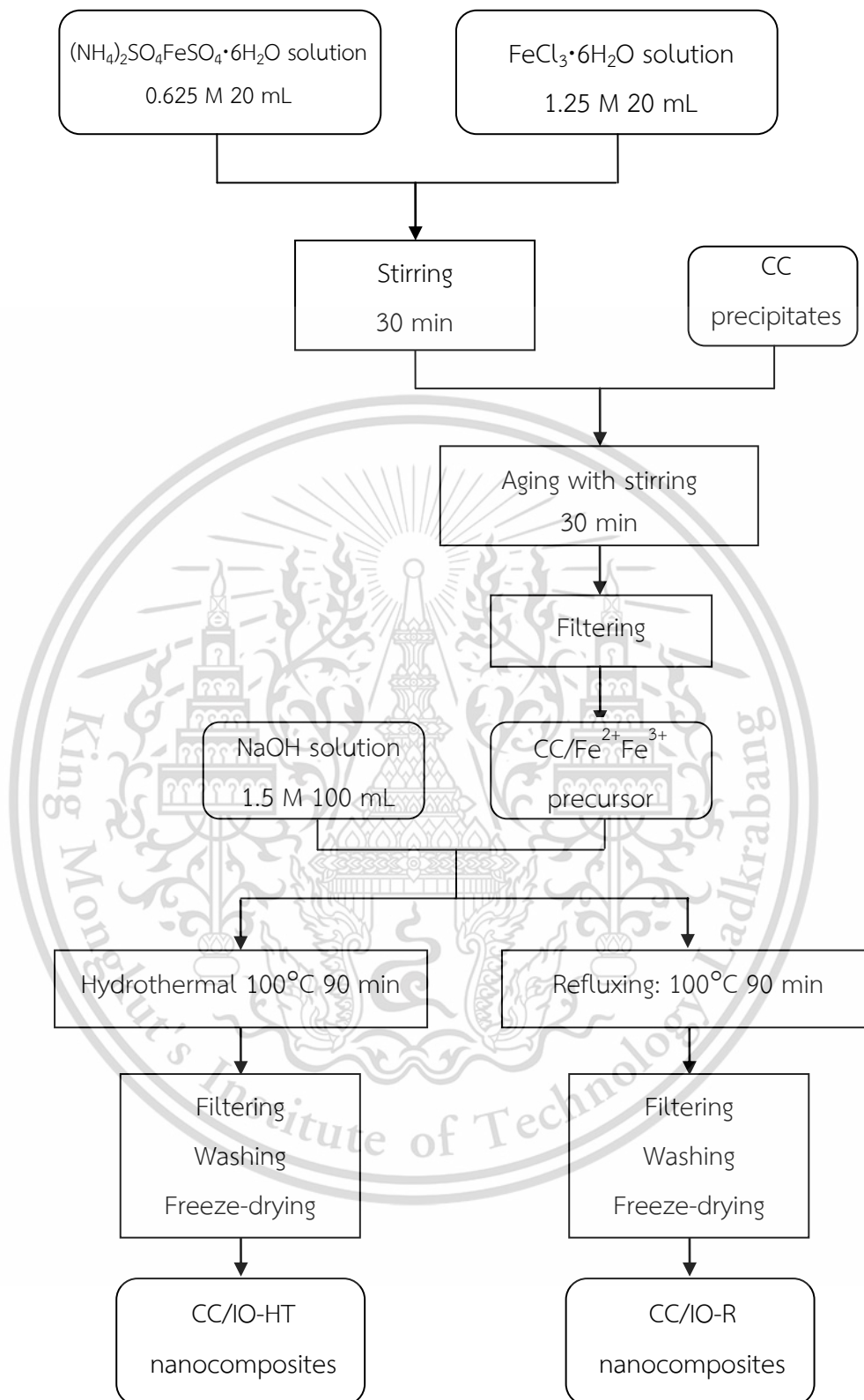


Figure 3.4 Preparation of CHI/IO nanocomposites by adsorption method, i.e. CC/IO-

HT and CC/IO-R nanocomposites

This material is reserved for educational use only, not allowed for commercial use.

Forbidden to modify the content, and cite the document when use.

Table 3.1 Experimental conditions and abbreviations of the samples

Sample	Chitosan:TPP		Synthesis conditions				
	g:g	%w/v	Synthesis method	Heating method	Temperature (°C)		
IO-HT100	-	-	-	Hydrothermal	100		
CC0.3	1:1.67	1:0.3	-	-			
CC0.4	1:2	1:0.4	-	-			
CC0.5	1:2.5	1:0.5	-	-			
CC0.6	1:3	1:0.6	-	-			
CS0.3/IO-HT75	1:1.67	1:0.3	<i>In-situ</i>	Hydrothermal	75		
CS0.3/IO-HT125	1:1.67	1:0.3			125		
CS0.2/IO-HT100	1:1	1:0.2			100		
CS0.3/IO-HT100	1:1.67	1:0.3					
CS0.4/IO-HT100	1:2	1:0.4					
CS0.5/IO-HT100	1:2.5	1:0.5					
CS0.6/IO-HT100	1:3	1:0.6					
CS0.2/IO-R	1:1	1:0.2			<i>In-situ</i>	Refluxing	100
CS0.3/IO-R	1:1.67	1:0.3					
CS0.4/IO-R	1:2	1:0.4					
CS0.5/IO-R	1:2.5	1:0.5					
CS0.6/IO-R	1:3	1:0.6					
CC0.3/IO-HT100	1:1.67	1:0.3	Adsorption	Hydrothermal	100		
CC0.4/IO-HT100	1:2	1:0.4					
CC0.5/IO-HT100	1:2.5	1:0.5					
CC0.3/IO-R	1:1.67	1:0.3	Adsorption	Refluxing	100		
CC0.4/IO-R	1:2	1:0.4					
CC0.5/IO-R	1:2.5	1:0.5					

This material is reserved for educational use only, not allowed for commercial use.

Forbidden to modify the content, and cite the document when use.

3.4.5 Characterization and testing of CHI/IO nanocomposites

- **X-ray diffractometer (XRD)**

The crystalline phase of synthesized IO nanoparticles and CHI/IO nanocomposites were analyzed by XRD technique by scanning 2θ from 20 to 70°, step size of 0.02°/step and step time of 1 sec/step.

- **Differential scanning calorimeter (DSC)**

The thermal properties of the as-prepared CHI/IO nanocomposites were analyzed by DSC technique using a heating rate of 10 °C/min in the temperature range of 25–400°C under nitrogen (N₂) atmosphere (flow rate of N₂ = 20 mL/min).

- **Thermogravimetric analysis (TGA)**

The thermal stability of the CHI/IO nanocomposites were analyzed by TGA technique using a heating rate of 10 °C/min in the temperature range of 50–800°C under air zero atmosphere and nitrogen (N₂) atmosphere (flow rate of N₂ = 20 mL/min).

- **Transmission electron microscopy (TEM)**

The morphologies of the synthesized IO nanoparticles and CHI/IO nanocomposites were analyzed by transmission electron microscopy (TEM, FEI, Tecnai G2 20 S-Twin, bright field image mode, 200 kV). The CHI/IO nanocomposites, dispersed in distilled water, were dropped onto a carbon coated Cu grid and then dried overnight at room temperature for TEM analysis. The average sizes of IO nanocrystals in the CS/IO nanocomposites were determined from the TEM images at 150000x magnification (60 particles) using ImageJ software. While the average sizes of IO nanocrystals in the CC/IO nanocomposites and their size distributions were determined from the TEM images at 150000x magnification (50 particles) using ImageJ software.

- **Vibrating sample magnetometer (VSM)**

An in-house developed vibrating sample magnetometer (VSM) calibrated with a 3 mm-diameter Ni sphere (Lakeshore 730908, USA) was used for determination the magnetic properties of the as-prepared IO nanoparticles in comparison with those of CHI/IO nanocomposites. The measurement was performed using the magnetic field (H) from -10,000 to 10,000 Oe at room temperature with time per point of 5 s/pt.

3.4.6 Cell viability assays

Cell viability of the as-prepared CHI/IO nanocomposites were tested using African green monkey fibroblast (Vero) cells by Dulbecco's Modified Eagle's Medium (DMEM) elution method or Primary screening. In the preparation of stock solution, 0.4 g of the sample was sterilized at 121°C for 15 min. Then the sample was mixed with 10 mL of DMEM and 5% Fetal Bovine Serum (FBS). The mixture was incubated at 37°C for 24 h, then the fermented substance was filtered and diluted to a concentration of 1,000 µg/mL. In the cell culture, 100 µL of the mixture of cells and cell culture media with the concentration of 5×10^4 cells/mL was dispensed into well. The as-prepared sample was incubated at 37°C for 24 h under 5% carbon dioxide (CO₂) atmosphere. Then, the cell culture media was sucked out and 100 µL of the as-prepared stock solution was added into well. The sample was incubated at 37°C for 24 h. Then, 10 µL of MTT solution with the concentration of 5 mg/mL was added into well. The sample was incubated at 37°C for 4 h under 5% CO₂ atmosphere. The MTT solution was sucked out and 150 µL of the mixture of 100% dimethyl sulfoxide (DMSO) and 10% sodium dodecyl sulfate (SDS) with the volume ratio of 9:1-DMSO:SDS was added into well. The sample was mechanically shaken for 5 min, then the optical density (OD) of sample was measured at a wavelength 570 nm using a microplate reader (Thermo Fisher Scientific, Varioskan). The percentage of cell viability (% Cell viability) was calculated as shown in Eq. 3.1 [57]:

$$\% \text{ Cell viability} = \frac{B}{A} \times 100 \quad (\text{Eq.3.1})$$

where A is the absorbance of the control well that has cells in the cell culture media, B is the absorbance of the sample's well that has cells in the stock solution, A and B must be removed the absorbance of the blank's well that has only 100% DMSO:10% SDS off before calculating.

Chapter 4

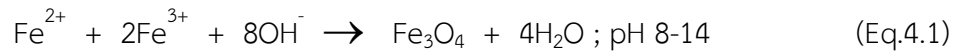
Main results and discussion

4.1 Synthesis of IO nanoparticles

Iron oxide exists in several phases, including hematite (α -Fe₂O₃), magnetite (Fe₃O₄), maghemite (γ -Fe₂O₃), goethite (α -FeOOH) and feroxyhite (δ' -FeOOH). However, some phases, i.e. magnetite and maghemite have the magnetic properties. Especially, the nano-sizes of magnetite and maghemite exhibit superparamagnetic properties which are useful for medical applications. In this synthesis, the Fe²⁺Fe³⁺-precursor was hydrothermally treated in NaOH solution at 100°C for 90 min in pressurized glass vessel. The pressurized system produced the magnetite and maghemite nanoparticles which had the superparamagnetic properties.

- **Crystal structure and morphology**

Fig. 4.1 shows the XRD patterns of IO-HT100 nanoparticles synthesized by hydrothermal method at reaction temperature of 100°C. It can be seen that the XRD peaks of IO-HT100 samples appeared at $2\theta = 30.2, 35.5, 43.4, 53.5, 57.2,$ and 62.7° corresponding to (220), (311), (400), (422), (511), and (440) planes, respectively. The XRD patterns were corresponded to the crystalline phases of magnetite (Fe₃O₄) in the JCPDS No.19-0629 and/or maghemite (γ -Fe₂O₃) in the JCPDS No.04-0755. Although the main crystalline peaks of magnetite and maghemite phases almost overlapped, the concurrent presence of magnetite and maghemite phases brought about the formation of asymmetrical shoulder of the diffraction peak at $2\theta \sim 35.5^\circ$. The formation of magnetite and maghemite phases occurred from the reaction between the stoichiometric proportion of Ferrous (Fe²⁺) and Ferric (Fe³⁺) ions with the hydroxide ions (OH⁻) of strong basic solution, producing the magnetite nanocrystals as described in Eq. 4.1. It was, however, the magnetite nanocrystals could be partially oxidized further in the presence of oxygen to maghemite nanocrystals as shown in Eq. 4.2 [58-59].



The average crystallite size of magnetite-maghemite nanocrystals (D_{XRD}) calculated from the (311) peak by using Scherrer equation of IO-HT100 was about 16.2 nm as shown in Table 4.1.

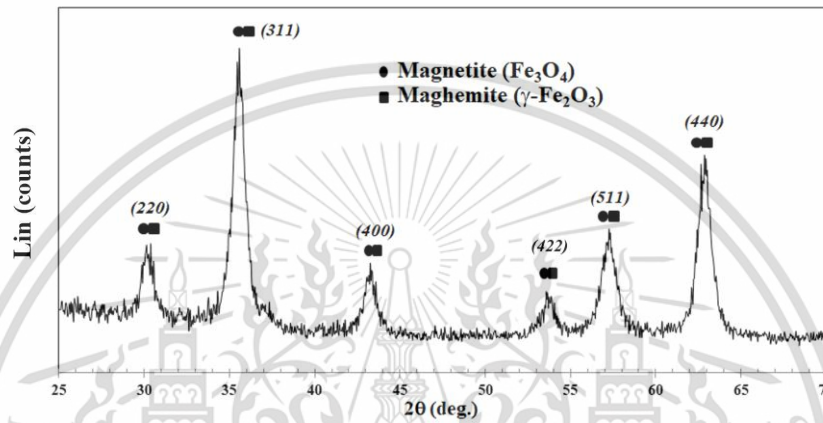


Figure 4.1 XRD pattern of IO-HT100 nanoparticles

Table 4.1 Parameters used for *in-situ* synthesis of CS/IO nanocomposites and their XRD and TEM data

Sample	Synthesis conditions			XRD		TEM			
	% TPP (%w/v)	Heating method	T (°C)	Phase	D _{XRD} (nm)	Shape of IO	Avg. size of IO (nm)		
IO-HT100	-	Hydrothermal	100	Fe ₃ O ₄ /γ-Fe ₂ O ₃	D ₍₃₁₁₎ 16.2	n/a	n/a		
CS0.3/IO-HT75	0.3	Hydrothermal	75	δ'-FeOOH	D ₍₀₀₂₎ 32.2	Rod-like	L 12.5–31.3 W 1.6–4.7		
				α-FeOOH	D ₍₁₁₀₎ 34.3				
CS0.2/IO-HT100	0.2	Hydrothermal	100	Fe ₃ O ₄ /γ-Fe ₂ O ₃	D ₍₃₁₁₎ 4.3	Irregular spherical	D 4.3		
CS0.3/IO-HT100	0.3			Fe ₃ O ₄ /γ-Fe ₂ O ₃	D ₍₃₁₁₎ 3.9	Irregular spherical	D 4.2		
CS0.4/IO-HT100	0.4			Fe ₃ O ₄ /γ-Fe ₂ O ₃	D ₍₃₁₁₎ 4.1	Irregular spherical	D 4.1		
CS0.5/IO-HT100	0.5			Fe ₃ O ₄ /γ-Fe ₂ O ₃	D ₍₃₁₁₎ 4.3	Irregular spherical	D 4.3		
CS0.6/IO-HT100	0.6			Fe ₃ O ₄ /γ-Fe ₂ O ₃	D ₍₃₁₁₎ 4.3	Irregular spherical	D 4.3		
CS0.3/IO-HT125	0.3			Fe ₃ O ₄ /γ-Fe ₂ O ₃	D ₍₃₁₁₎ 3.9	Irregular spherical	D 4.4		
CS0.2/IO-R	0.2			Reflux	100	Fe ₃ O ₄ /γ-Fe ₂ O ₃	D ₍₃₁₁₎ 3.7	Irregular spherical	D 3.8
CS0.3/IO-R	0.3					Fe ₃ O ₄ /γ-Fe ₂ O ₃	D ₍₃₁₁₎ 3.9	Irregular spherical	D 3.8
CS0.4/IO-R	0.4	Fe ₃ O ₄ /γ-Fe ₂ O ₃	D ₍₃₁₁₎ 3.3			Irregular spherical	D 3.5		
CS0.5/IO-R	0.5	Fe ₃ O ₄ /γ-Fe ₂ O ₃	D ₍₃₁₁₎ 3.2			Irregular spherical	D 3.5		
CS0.6/IO-R	0.6	Fe ₃ O ₄ /γ-Fe ₂ O ₃	D ₍₃₁₁₎ 2.8			Irregular spherical	D 3.1		

**T=Temperature, L=Length, W=Width, D=Diameter

4.2 *In-situ* synthesis of CS/IO nanocomposites

The superparamagnetic properties depend on the particle size of iron oxide nanoparticles. However, the small iron oxide nanoparticles promote the agglomeration due to their high surface energy and magnetic interactions leading to the decrease of superparamagnetic properties [28]. In the *in-situ* synthesis, the Fe²⁺ and Fe³⁺ ions trapped in the free volume space of crosslinked chitosan network. The iron oxide nanoparticles were obtained in the 3D network by low temperature heat treatment in NaOH solution. It was found that the crosslinked chitosan prevent the agglomeration of MNPs; therefore, the synthesized nanocomposites had the superparamagnetic properties due to the nano-size of iron oxide nanoparticles.

4.2.1 Effect of hydrothermal temperature

Iron oxide forms in several phases which depend on synthesis conditions such as temperature and pressure. In this synthesis, the chitosan/iron oxide precursor was treated in basic solution by hydrothermal method at 75, 100 and 125°C for 90 min because the different hydrothermal temperatures led to the various phases of iron oxide.

● Crystal structure and morphology

Fig. 4.2 shows the XRD patterns of CS/IO nanocomposites synthesized by hydrothermal from the chitosan/ Fe²⁺ Fe³⁺ precursors crosslinked by 0.3 %w/v TPP. It can be seen that the XRD pattern of CS0.3/IO-HT75 nanocomposite synthesized by hydrothermal method at reaction temperature of 75°C was composed of goethite (α -FeOOH) and feroxyhite (δ' -FeOOH) phases, in which their formation reactions were described in Eq. 4.3–4.5. This result indicated that the hydrothermal temperature of 75°C could induce the hydrolysis of Fe²⁺ Fe³⁺-precursor impregnated in the crosslinked chitosan, however, this reaction temperature was not high enough to transform the goethite and feroxyhite phases to magnetite and/or maghemite phases [58-59].



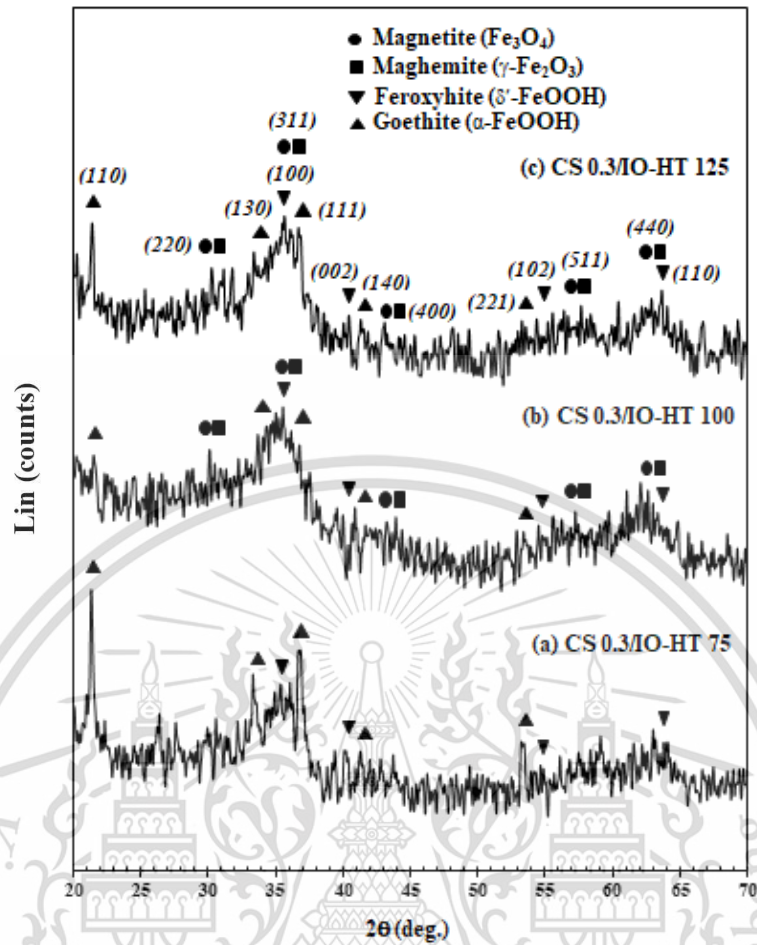


Figure 4.2 XRD patterns of (a) CS0.3/IO-HT75, (b) CS0.3/IO-HT100 and (c) CS 0.3/IO-HT125 nanocomposites

In Fig. 4.3(a), the TEM image of CS0.3/IO-HT75 nanocomposite was composed of the rod-like nanocrystals dispersed in the crosslinked chitosan matrix. These rod-like nanocrystals were corresponded to the orthorhombic crystal structure of goethite (ICSD No.00-029-0713) and hexagonal crystal structure of feroxyhite (ICSD No.00-013-0087) [59]. The average crystallite size of rod-like nanocrystals of feroxyhite calculated from the (002) peak and goethite calculated from the (110) peak were about 32.2 and 34.3 nm, respectively, as shown in Table 4.1. Similarly, the lengths and widths of feroxyhite-goethite nanocrystals obtained from TEM images were in the range of 12.5–31.3 nm and 1.6–4.7 nm, respectively. It can be seen that the average crystallite sizes of rod-like nanocrystals of feroxyhite and goethite were correlated to lengths of nanocrystals obtained from TEM image [60].

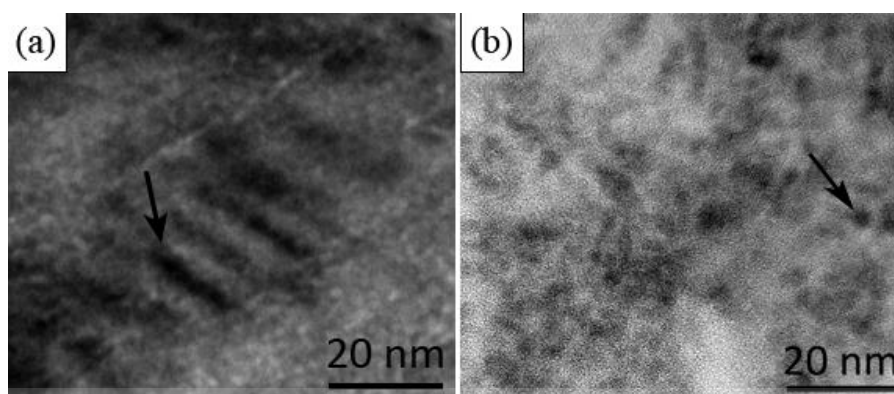


Figure 4.3 TEM images of (a) CS0.3/IO-HT75 and (b) CS0.3/IO-HT100 nanocomposites

In Fig. 4.2(b) and 4.2(c), the crystalline peaks observed in the XRD patterns of CS0.3/IO-HT100 and CS0.3/IO-HT125 nanocomposites synthesized by hydrothermal method at reaction temperature of 100 and 125°C, respectively, were assigned to magnetite (Fe_3O_4) and/or maghemite ($\gamma\text{-Fe}_2\text{O}_3$) phases as observed in the IO-HT100 nanoparticles. However, the crystalline peaks in the XRD patterns of all nanocomposites were obviously broadened, indicating the formation of very small magnetite-maghemite nanocrystals within chitosan matrix. These results were considered to be because the Fe^{2+} and Fe^{3+} ions impregnated in the crosslinked chitosan of chitosan/ Fe^{2+} / Fe^{3+} precursors could simultaneously react with hydroxide ions in the solution media creating the magnetite-maghemite phase when the reaction temperature was about 100°C or higher. It was, however, the growth of magnetite-maghemite crystals were restricted to nano-size due to the confinement of crosslinked chitosan network. In Fig. 4.3(b), the microstructure of magnetite-maghemite crystals in the CS0.3/IO-HT100 nanocomposite was observed as the irregular quasi-spherical nanocrystals formed in the crosslinked chitosan matrix, in which these nanocrystals were considered to be corresponded to the cubic inverse spinel and cubic tetragonal structures of magnetite and maghemite, respectively.

The average crystallite sizes of magnetite-maghemite nanocrystals formed in the CS0.3/IO-HT100 and CS0.3/IO-HT125 nanocomposites calculated from the (311) peak were quite similar, in which they were about 3.9 nm as summarized in Table 4.1. The average particle sizes of the CS0.3/IO-HT100 and CS0.3/IO-HT125 nanocomposites evaluated from the TEM images were about 4.2 and 4.4 nm,

respectively, in which they were in agreement with their average crystallite sizes calculated from the XRD data. It can be concluded from these results that the magnetite-maghemite nanoparticles might form as polycrystalline phases in the chitosan matrix. Besides, the increase of hydrothermal treatment temperature from 100 to 125°C had no obvious effect on the average crystallite sizes of the synthesized iron oxide nanocrystals. It was considered to be because the network structure of crosslinked chitosan matrix plays a dominant role in the constraint on growth of iron oxide nanocrystals.

These finding suggested that the various hydrothermal temperatures contributed to the different phases of iron oxide. The reaction temperature of 75°C could induce the goethite and feroxyhite phases. The increase of hydrothermal temperature from 100 to 125°C could transform to magnetite and/or maghemite with irregular spherical shape. However, the temperature increased in this range had no significantly effect on the average crystallite sizes of iron oxide nanocrystals due to the constraint on their growth by the crosslinked chitosan network.

Fig. 4.4 shows the schematic model represented the formation of CS/IO nanocomposites. When the mixture solution of Fe^{2+} , Fe^{3+} and protonated chitosan was added into the TPP crosslinking solution, the protonated amine groups ($-\text{NH}_3^+$) of chitosan reacted with the phosphate groups ($-\text{PO}_4^{3-}$) of TPP, resulting in the ionotropic gelation of chitosan as the network structure. The Fe^{2+} and Fe^{3+} ions were simultaneously swallowed in the crosslinked chitosan network, in which it was obtained as the chitosan/ $\text{Fe}^{2+}\text{Fe}^{3+}$ precursor as shown in step (I). In step (II), the Fe^{2+} and Fe^{3+} ions embedded in the chitosan/ $\text{Fe}^{2+}\text{Fe}^{3+}$ precursor were reacted with the hydroxyl groups ($-\text{OH}$) in the basic media during the hydrothermal and refluxing methods as expressed in Eq. 4.1, in which the magnetite nanocrystals were obtained in the crosslinked chitosan matrix forming as the CS/IO nanocomposites. The magnetite nanocrystals formed at the surface of nanocomposites might partially react with oxygen as expressed in Eq. 4.2, forming as the maghemite nanocrystals. The CS/IO nanocomposites were then composed of biphasic iron oxide.

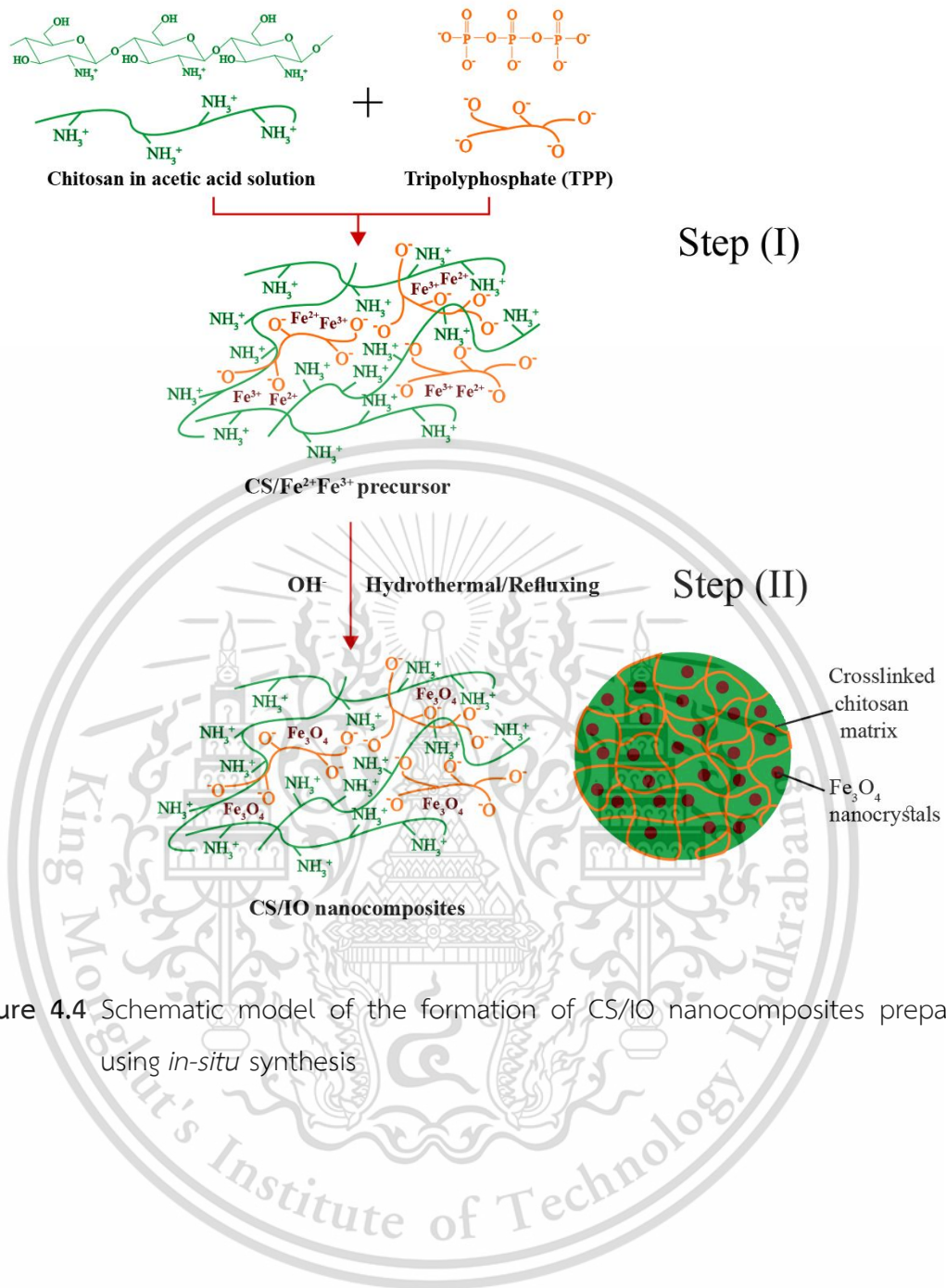


Figure 4.4 Schematic model of the formation of CS/IO nanocomposites prepared using *in-situ* synthesis

● Thermal properties

The TGA and DTG thermograms of CS0.3/IO-HT75, CS0.3/IO-HT100 and CS0.3/IO-HT125 nanocomposites were shown in Fig. 4.5. The decomposition temperatures (T_d) of crosslinked chitosan matrix in the nanocomposites were determined from the TGA and DTG profiles analyzed under N_2 atmosphere as shown in Fig. 4.5 (N_2), while the percentages of weight loss were determined from the TGA profiles analyzed under air zero atmosphere as shown in Fig. 4.5 (O_2). Similar trend of thermal behavior was observed in all nanocomposites, in which the major stage of decomposition of these nanocomposites occurred at the T_d in the range of 222.8–255.6°C with 14–20% weight loss as summarized in Table 4.2.

This thermal event was considered to be the cleavage of glucosidic linkages of crosslinked chitosan matrix via dehydration and deamination reactions [15]. The T_d value of CS0.3/IO-HT125 nanocomposite shifted to the lower value than those of the CS0.3/IO-HT75 and CS0.3/IO-HT100 nanocomposites. It was considered to be because the higher hydrothermal reaction temperature, the higher swelling capacity of crosslinked chitosan might be obtained, promoting the growth of magnetite-maghemite nanocrystals and weakening the crosslinked structure of chitosan network. Besides, the percentage of residuals in those nanocomposites were in the range of 70–75% weight, indicating the quantities of iron oxide nanocrystals formed in the nanocomposites and trace of phosphorus from the TPP crosslinker. Besides, the percentages of water and organic solvent in these nanocomposites were in the range of 10–11%.

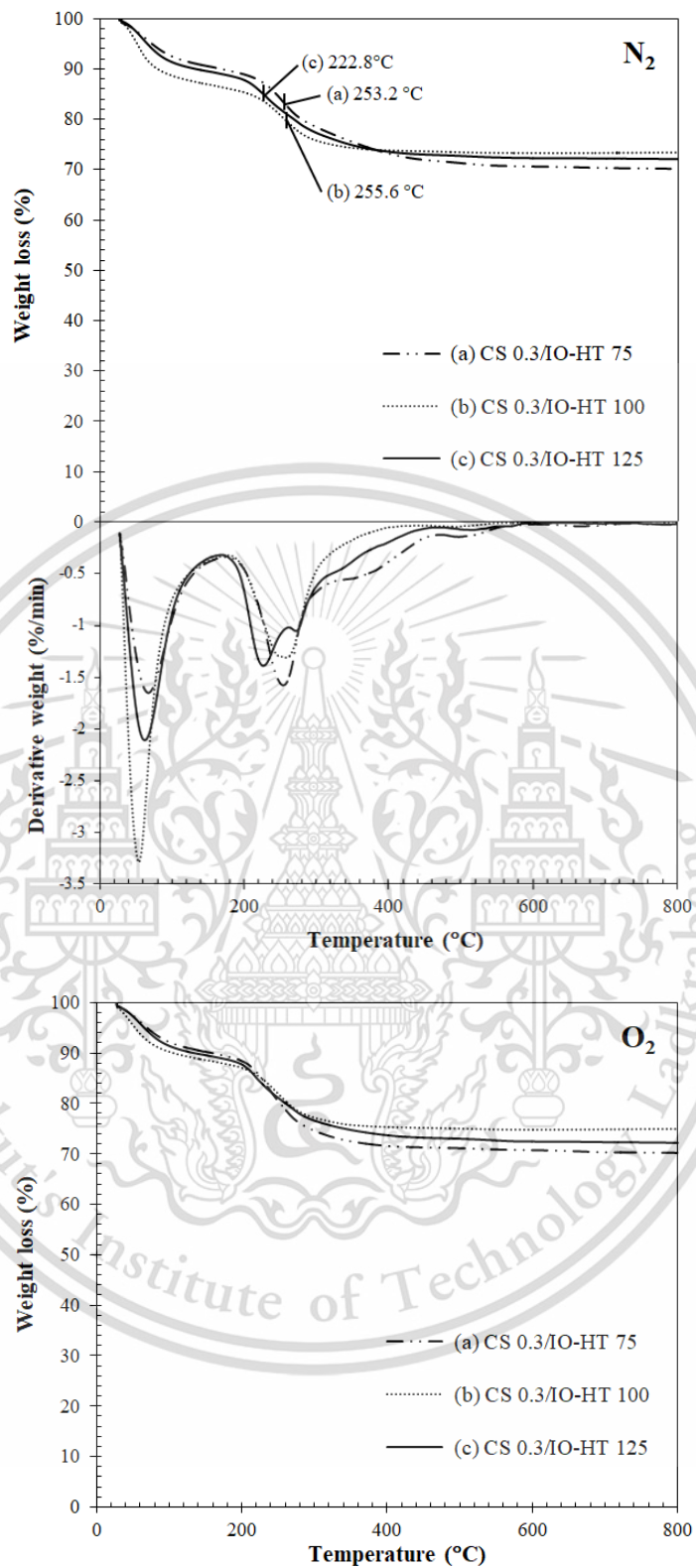


Figure 4.5 TGA and DTG thermograms of (a) CS0.3/IO-HT75, (b) CS0.3/IO-HT100 and (c) CS0.3/IO-HT125 nanocomposites under N₂ and air zero atmospheres

Table 4.2 TGA, DSC, VSM and cell viability of CS/IO nanocomposites synthesized by *in-situ* synthesis

Sample	TGA			DSC		VSM			Cell viability (%)
	T _d * (°C)	Weight loss at T _d (%)**	Residual (%)**	T _m (°C)	ΔH (J/g)	Mmax (emu/g)	Mr (emu/g)	H _c (Oe)	
IO-HT 100	-	-	-	-	-	53.3	1.0	7.8	68
CS 0.3/IO-HT 75	253.2	20	70	189.6	117.7	7.0	0	0	n/a
CS 0.2/IO-HT 100	261.5	20	71	190.5	136.2	9.6	0	0	90
CS 0.3/IO-HT 100	255.6	14	75	185.3	194.0	14.5	0	0	82
CS 0.4/IO-HT 100	241.6	16	74	184.4	164.5	13.6	0	0	95
CS 0.5/IO-HT 100	233.8	13	72	189.9	153.9	14.0	0	0	96
CS 0.6/IO-HT 100	250.0	19	71	174.3	202.9	14.3	0	0	93
CS 0.3/IO-HT 125	222.8	17	72	186.8	139.9	15.0	0	0	92
CS 0.2/IO-R	220.9	18	70	183.6	183.6	7.2	0	0	72
CS 0.3/IO-R	254.9	17	73	183.1	193.3	14.2	0	0	75
CS 0.4/IO-R	259.0	19	69	180.7	202.9	11.0	0	0	75
CS 0.5/IO-R	223.1	19	69	185.1	179.2	9.7	0	0	57
CS 0.6/IO-R	256.2	20	69	176.3	165.0	10.3	0	0	90

* T_d values of chitosan were determined from TGA profiles under N₂.

** Weight losses at T_d and residual were determined from the TGA profiles under air zero. The remaining fraction out of the weight loss at T_d and residual was considered to be the amount of water and organic solvent.

This material is reserved for educational use only, not allowed for commercial use.

Forbidden to modify the content, and cite the document when use.

Fig. 4.6 shows the DSC thermograms of CS0.3/IO-HT75, CS0.3/IO-HT100 and CS0.3/IO-HT125 nanocomposites. It was found that the endothermic peaks observed in all samples were in the range of 185.3–189.6°C, corresponding to the melting temperatures (T_m) of crosslinked chitosan [24]. The T_m values were slightly different on each samples, it might be because all samples were synthesized by using the same concentration of TPP crosslinking agent. It was, however, the values of enthalpy of fusion (ΔH) were significantly varied in the range of 117.7–194.0 J/g as summarized in Table 4.2.

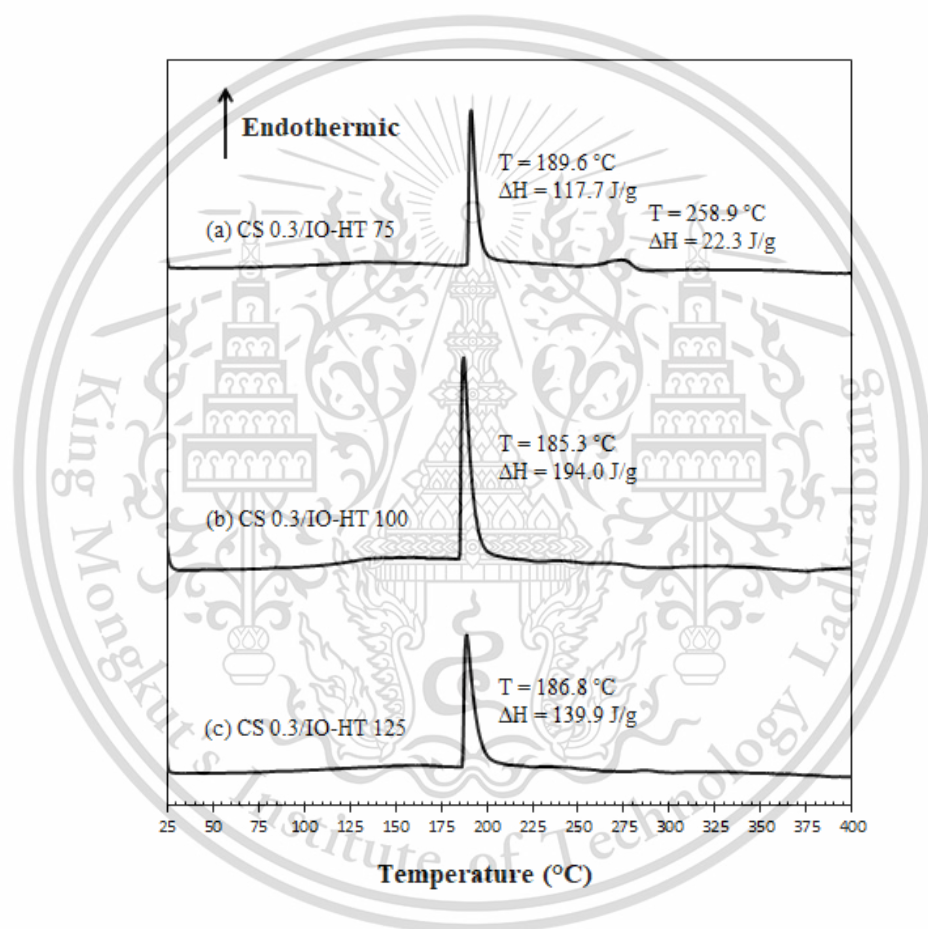


Figure 4.6 DSC thermograms of (a) CS0.3/IO-HT75, (b) CS0.3/IO-HT100 and (c) CS0.3/IO-HT125 nanocomposites

The ΔH value of CS0.3/IO-HT100 nanocomposite was higher than that of CS0.3/IO-HT75 nanocomposite. This result was considered to be the effect of different hydrothermal reaction temperature resulted in the formation of different crystalline phases of iron compounds in these nanocomposites as described

previously. The presence of irregular quasi-spherical magnetite-maghemite nanocrystals regularly distributed in the crosslinked chitosan and/or the interaction between O^{2-} of magnetite-maghemite and the free NH_3^+ of chitosan could enhance the thermal stability of CS0.3/IO-HT100 nanocomposite. In contrast, the ΔH value of CS0.3/IO-HT125 nanocomposite was significantly lower than that of CS0.3/IO-HT100 nanocomposite. These results insisted the weakening of crosslinked chitosan structure when the reaction temperature was increased to 125°C as discussed in the TGA results.

These results suggested that all nanocomposites had a similar thermal behavior trend. The major decomposition of crosslinked chitosan matrix in these nanocomposites occurred at the T_d in the range of 222.8–255.6°C with 14–20% weight. The residual, 70–75% weight, was considered to be the components of iron oxide nanocrystals and trace of phosphorus from the TPP crosslinker. Besides, the presence of irregular quasi-spherical magnetite-maghemite nanocrystals uniformly distributed in the crosslinked chitosan could enhance thermal stability in the CS0.3/IO-HT100 nanocomposite due to the interaction between O^{2-} of magnetite-maghemite and the free NH_3^+ of chitosan. However, the thermal stability decreased when the reaction temperature was increased to 125°C because of the weakening of crosslinked chitosan structure as shown in the lower T_d and ΔH value in the CS0.3/IO-HT125 nanocomposite.

● Magnetic properties

Fig. 4.7 shows the VSM curves of CS0.3/IO-HT75, CS0.3/IO-HT100 and CS0.3/IO-HT125 nanocomposites. It can be seen that the maximum magnetization (M_{max}) value of CS0.3/IO-HT75 nanocomposite was about 7 emu/g. This low M_{max} value was considered to be because of the existence of non-magnetic phases of goethite and ferroxhite. Therefore, its magnetic characteristic was considered to be weak antiferromagnetic.

The M_{max} values of CS0.3/IO-HT100 and CS0.3/IO-HT125 nanocomposites possessed the magnetite-maghemite phases were significantly higher than that of the CS0.3/IO-HT75 nanocomposite, i.e. 14.5 and 15 emu/g, respectively, with zero coercivity (H_c) and magnetic remanence (M_r), as shown in Table 4.2. These results

indicated that the M_{\max} values increased with the increase of size of iron oxide nanocrystals. Moreover, the obtained iron oxide nanocrystals had the single magnetic domain structure with the superparamagnetic behavior due to their particle sizes that were less than the superparamagnetic critical diameter of both magnetite and maghemite, which they were about 12 nm for magnetite and 20 nm for maghemite.

The hysteresis curves obtained from CS0.3/IO-HT100 and CS0.3/IO-HT125 nanocomposites revealed that their magnetic characteristics were superparamagnetic. However, the M_{\max} values of these nanocomposites were lower than IO-HT100 nanoparticles, in which it was 53.3 emu/g. It was considered that the large reduction of M_{\max} values occurred due to the significant decrease of the size of iron oxide nanoparticle [56, 61-65].

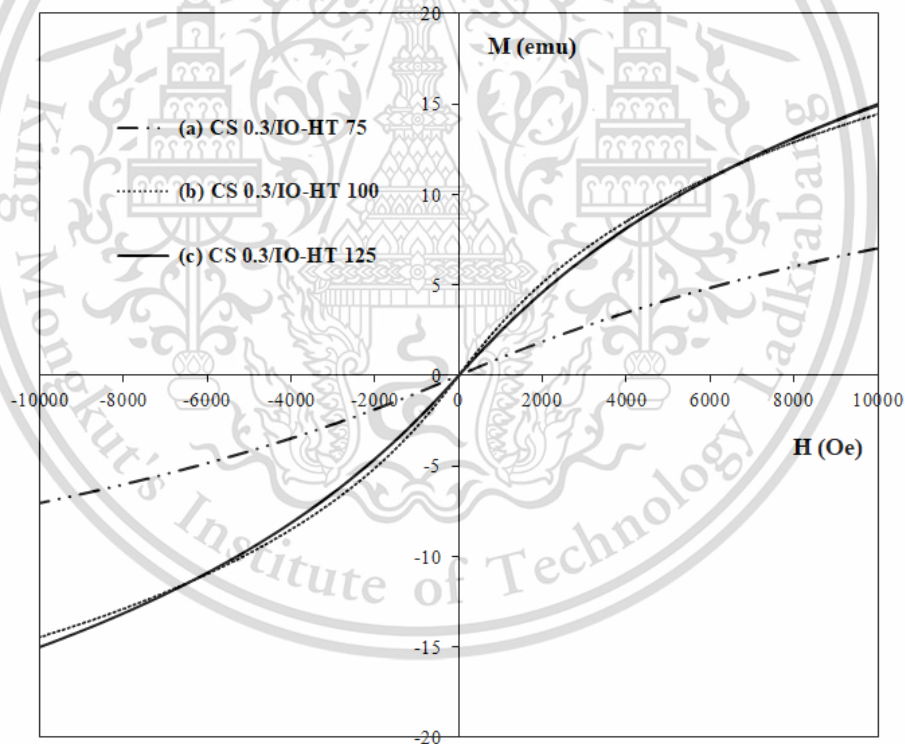


Figure 4.7 VSM curves of (a) CS0.3/IO-HT75, (b) CS0.3/IO-HT100 and (c) CS0.3/IO-HT125 nanocomposites

4.2.2 Effect of synthesis method and the initial concentration of TPP solution

The heat treatment methods for synthesis of chitosan/iron oxide nanocomposites, i.e. hydrothermal and refluxing, exhibited the different effects on crystal growth in the nanocomposites. The hydrothermal method was carried out under the pressurized system, in which it could promote the formation reaction of iron oxide nanocrystals; however, it could destroy the crosslinked chitosan structure. Besides, the initial concentration of TPP solution led to the various crosslinking densities in crosslinked chitosan templates. These results affected the properties of chitosan/iron oxide nanocomposites, especially their thermal stabilities.

- **Crystal structure and morphology**

Fig. 4.8 shows the XRD patterns of CS/IO nanocomposites hydrothermally synthesized from the chitosan/ $\text{Fe}^{2+}\text{Fe}^{3+}$ precursors crosslinked by different TPP concentrations, i.e. 0.2 %w/v (CS0.2/IO-HT100), 0.3 %w/v (CS0.3/IO-HT100), 0.4 %w/v (CS0.4/IO-HT100), 0.5 %w/v (CS0.5/IO-HT100) and 0.6 %w/v (CS0.6/IO-HT100). Fig. 4.9 shows the XRD patterns of CS/IO nanocomposites synthesized by refluxing method from the chitosan/ $\text{Fe}^{2+}\text{Fe}^{3+}$ precursors crosslinked by the similar TPP concentrations, i.e. 0.2 %w/v (CS0.2/IO-R), 0.3 %w/v (CS0.3/IO-R), 0.4 %w/v (CS0.4/IO-R), 0.5 %w/v (CS0.5/IO-R) and 0.6 %w/v (CS0.6/IO-R).

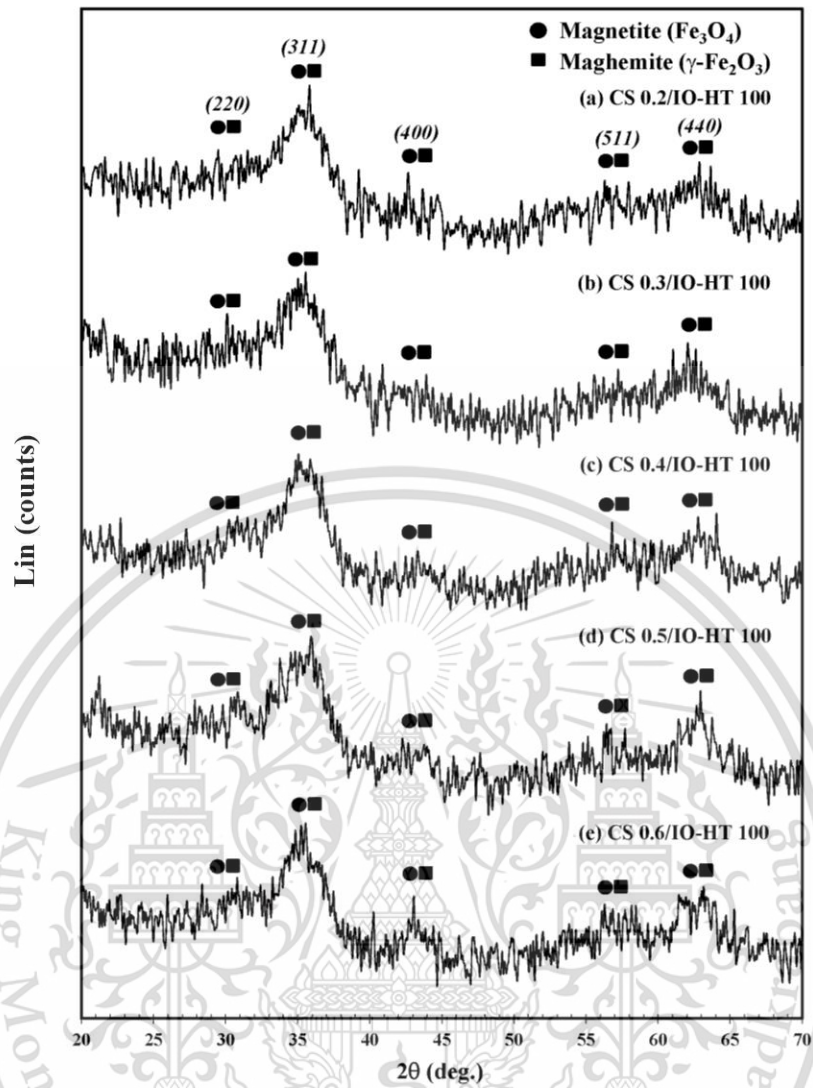


Figure 4.8 XRD patterns of (a) CS0.2/IO-HT100, (b) CS0.3/IO-HT100, (c) CS0.4/IO-HT100, (d) CS0.5/IO-HT100 and (e) CS0.6/IO-HT100 nanocomposites

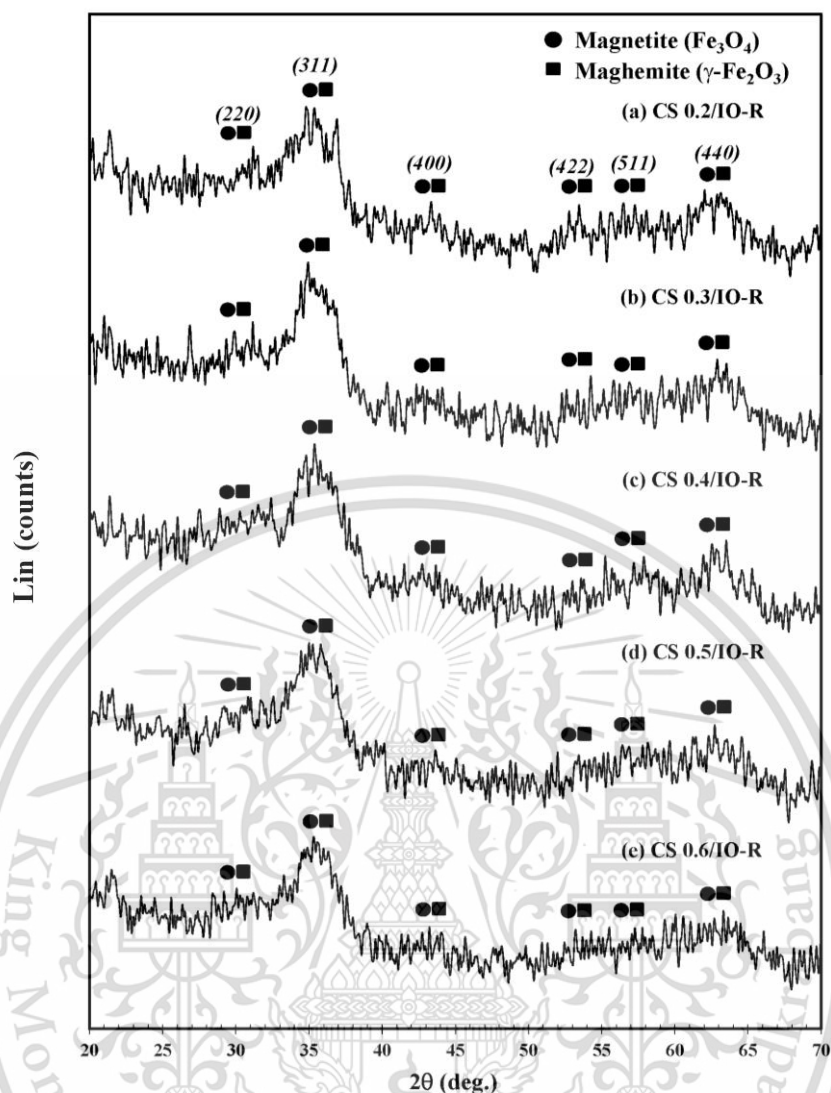


Figure 4.9 XRD patterns of (a) CS0.2/IO-R, (b) CS0.3/IO-R, (c) CS0.4/IO-R, (d) CS0.5/IO-R and (e) CS0.6/IO-R nanocomposites

The XRD patterns revealed that the magnetite and maghemite in these nanocomposites were main crystalline phases of iron oxide corresponded to the JCPDS No.19-0629 and JCPDS No.04-0755, respectively. The crystalline peaks were noticeably broadened due to the formation of very small magnetite-maghemite nanocrystals in crosslinked chitosan matrix. The average crystallite sizes of magnetite-maghemite nanocrystals of CS/IO nanocomposites synthesized by hydrothermal and refluxing methods, in which they were calculated from the (311) peak, were in the range of 3.9–4.3 nm and 2.8–3.9 nm, respectively, as shown in Table 4.1. It can be seen that the TPP concentration used in the *in-situ* preparation

This material is reserved for educational use only, not allowed for commercial use.

had no significant effect on the crystalline phases of iron oxide nanocrystals obtained in the nanocomposites; however, it showed the effect on the average crystallite size of iron oxide nanocrystals. Fig. 4.10 shows the relationship between the average crystallite sizes of iron oxide (IO) nanocrystals in the CS/IO nanocomposites calculated from the (311) peak and the varied TPP concentrations used in the synthesis. The average crystallite sizes of iron oxide nanocrystals in CS/IO-HT and CS/IO-R samples represented the sizes of iron oxide in the nanocomposites synthesized using hydrothermal and refluxing methods, respectively. The average crystallite sizes of CS/IO-R samples tended to decrease with the increase of TPP concentrations, in which it was considered to be the effect of TPP concentration on the crosslinking density of chitosan matrix. Besides, the average crystallite sizes of magnetite-maghemite nanocrystals of CS/IO-HT samples were bigger than those of CS/IO-R samples. These results were because the pressurized system of hydrothermal method could promote the nucleation and growth of iron oxide nanocrystals to be greater than those in the refluxing method.

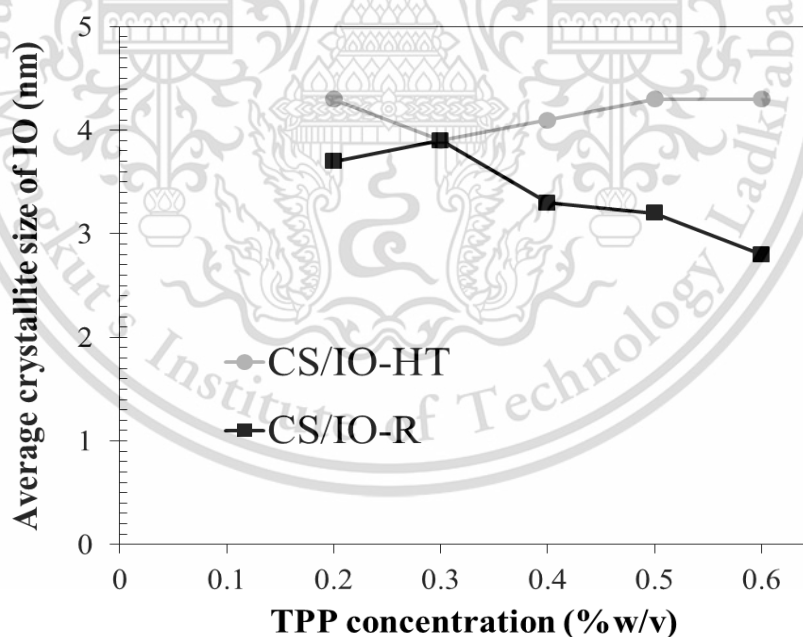


Figure 4.10 Relationship between the average crystallite sizes of iron oxide (IO) nanocrystals in CS/IO nanocomposites synthesized using hydrothermal method (CS/IO-HT) and refluxing method (CS/IO-R) and TPP concentrations used in the synthesis

Fig. 4.11 shows the TEM images of CS0.2/IO-HT100, CS0.3/IO-HT100, CS0.4/IO-HT100, CS0.5/IO-HT100 and CS0.6/IO-HT100 nanocomposites while Fig. 4.12 shows the TEM images of CS0.2/IO-R, CS0.3/IO-R, CS0.4/IO-R, CS0.5/IO-R and CS0.6/IO-R nanocomposites. All nanocomposites were composed of the irregular quasi-spherical nanocrystals dispersed in the crosslinked chitosan matrix. These nanocrystals were considered to be corresponded to the cubic inverse spinel and cubic tetragonal structures of magnetite and maghemite, respectively.

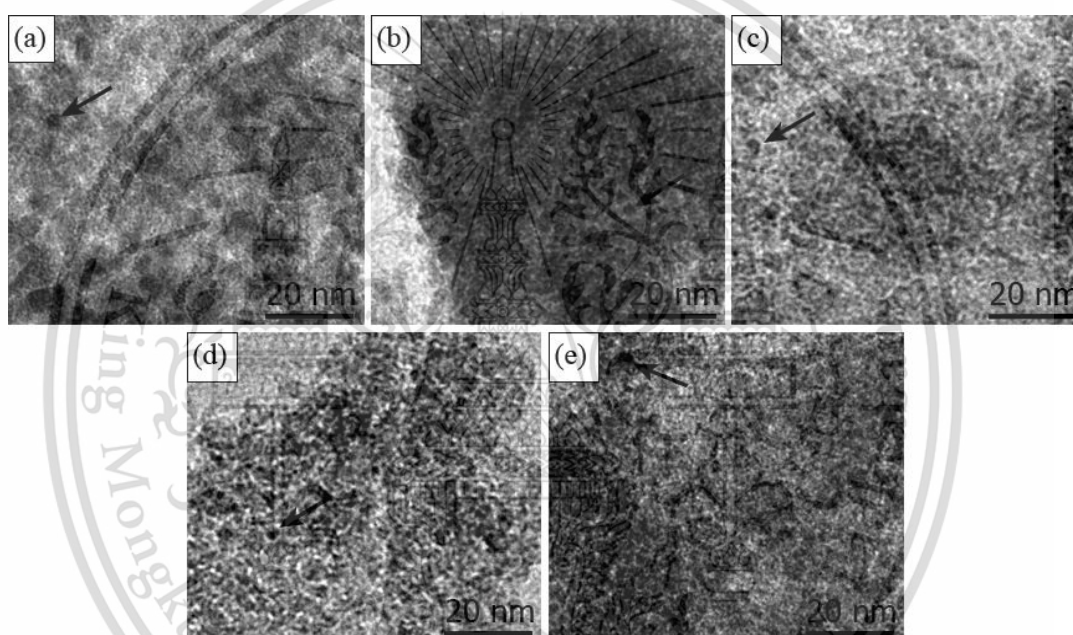


Figure 4.11 TEM images of (a) CS0.2/IO-HT100, (b) CS0.3/IO-HT100, (c) CS0.4/IO-HT100, (d) CS0.5/IO-HT100 and (e) CS0.6/IO-HT100 nanocomposites

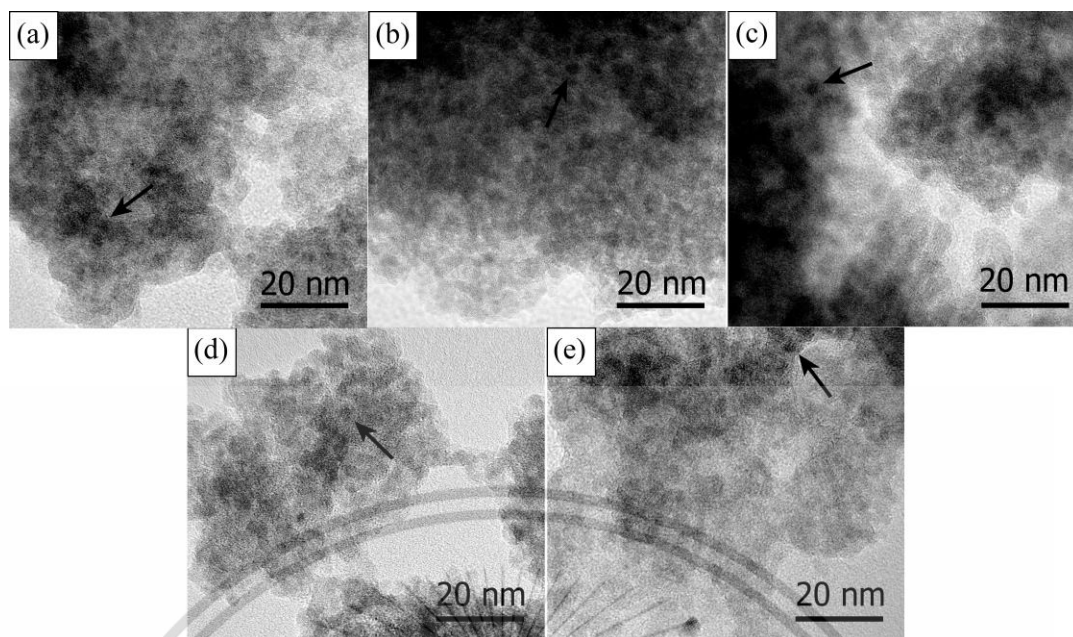


Figure 4.12 TEM images of (a) CS0.2/IO-R, (b) CS0.3/IO-R, (c) CS0.4/IO-R, (d) CS0.5/IO-R and (e) CS0.6/IO-R nanocomposites

The average particle sizes of magnetite-maghemite nanocrystals of CS/IO nanocomposites synthesized by hydrothermal method were quite similar in all nanocomposites, in which they were in the range of 4.1–4.3 nm while those of CS/IO nanocomposites synthesized by refluxing method were different, in which they were in the range of 3.1–3.8 nm as summarized in Table 4.1. It was considered to be because the pressurized system of hydrothermal method brought about the distortion of crosslinked chitosan network; therefore, it cannot be obviously seen the effect of TPP concentration on the size of magnetite-maghemite nanocrystals. Besides, it can be seen the average particle sizes of magnetite-maghemite nanocrystals of CS/IO nanocomposites synthesized by hydrothermal method were bigger than those of CS/IO nanocomposites synthesized by refluxing method. Fig 4.13 shows the relationship between the average particle sizes of iron oxide nanocrystals obtained from TEM images of CS/IO nanocomposites synthesized using hydrothermal method (CS/IO-HT) and refluxing method (CS/IO-R) and TPP concentrations. The average particle sizes of CS/IO-R samples tended to decrease with the increase of TPP concentration because of the effect of crosslinking density of chitosan matrix. Besides, the average crystallite sizes of iron oxide of CS/IO-HT

samples were bigger than those of CS/IO-R samples. These results were in agreement with the XRD results, in which it was because the pressurized system of hydrothermal method could promote the nucleation and growth of iron oxide nanocrystals. In contrast, it cannot be obviously seen the effect of TPP concentration on the shape of magnetite-maghemite nanocrystals. Those of all nanocomposites were in agreement with their average crystallite sizes from the XRD data. Besides, the SAED pattern of the CS0.6/IO-HT100 sample as the ring pattern as shown in Fig. 4.14. Thus, it can be concluded that the magnetite-maghemite might form as polycrystals in the chitosan matrix.

These results indicated that the heat treatment conditions and the initial TPP concentrations used in the *in-situ* preparation had no significant effect on the crystalline phases and shapes of iron oxide nanocrystals. All nanocomposites were composed of irregular spherical magnetite-maghemite nanocrystals dispersed in the crosslinked chitosan matrix. However, the pressurized system of hydrothermal method brought about greater nucleation and growth of iron oxide nanocrystals than the refluxing method. Besides, the average crystallite size decreased as TPP concentration increased because the TPP concentration affected the crosslinking density of chitosan matrix.

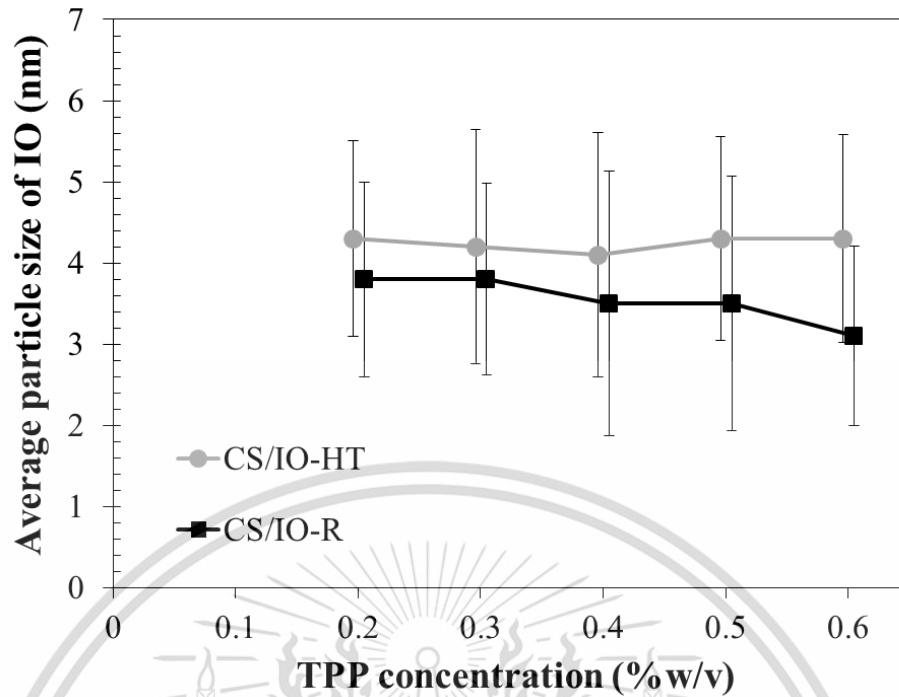


Figure 4.13 Relationship between the average particle sizes of iron oxide (IO) nanocrystals in CS/IO nanocomposites synthesized using hydrothermal method (CS/IO-HT) and refluxing method (CS/IO-R) and TPP concentrations used in the synthesis

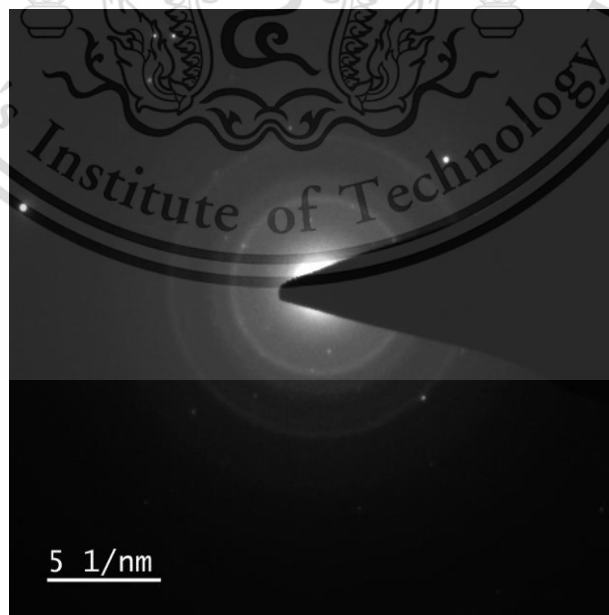


Figure 4.14 Electron diffraction of CS_{0.6}/IO-HT₁₀₀

This material is reserved for educational use only, not allowed for commercial use.

Forbidden to modify the content, and cite the document when use.

● Thermal properties

TGA and DTG thermograms of CS0.2/IO-HT100, CS0.3/IO-HT100, CS0.4/IO-HT100, CS0.5/IO-HT100 and CS0.6/IO-HT100 nanocomposites analyzed under N₂ and air zero atmosphere were shown in Fig. 4.15(N₂) and 4.15(O₂), respectively. While TGA and DTG thermograms of CS0.2/IO-R, CS0.3/IO-R, CS0.4/IO-R, CS0.5/IO-R and CS0.6/IO-R nanocomposites analyzed under N₂ and air zero atmosphere were shown in Fig. 4.16(N₂) and 4.16(O₂), respectively. It can be seen from the summarized data in Table 4.2 that all nanocomposites exhibited the similar trend of thermal behaviors. The T_d values of CS/IO nanocomposites synthesized by hydrothermal and refluxing method, in which they were in the range of 233.8–261.5°C and 220.9–259.0°C, respectively. Fig. 4.17 shows the relationship between the decomposition temperatures of chitosan (T_d) in CS/IO nanocomposites synthesized using hydrothermal method (CS/IO-HT) and refluxing method (CS/IO-R) and TPP concentrations. The T_d values of CS/IO-HT samples tended to decrease with the increase of TPP concentration. However, The T_d values of CS/IO-R samples were fluctuated because the higher TPP concentration promoted the greater difference in crosslinking density of chitosan in the CS/IO-R samples.

The percentages of weight loss of chitosan matrix were in the range of 13–20%; therefore, the percentages of iron oxide were in the range of 69–75%. These results suggested that the *in-situ* preparation of chitosan/ Fe²⁺Fe³⁺ precursor using different TPP concentrations resulted in the similar content of Fe²⁺Fe³⁺ ions swallowed into the crosslinked chitosan network; therefore, the compositions of resultant nanocomposites were quite similar. This result did not show any significant data about the effect of synthesis method on the thermal behavior of resultant nanocomposites.

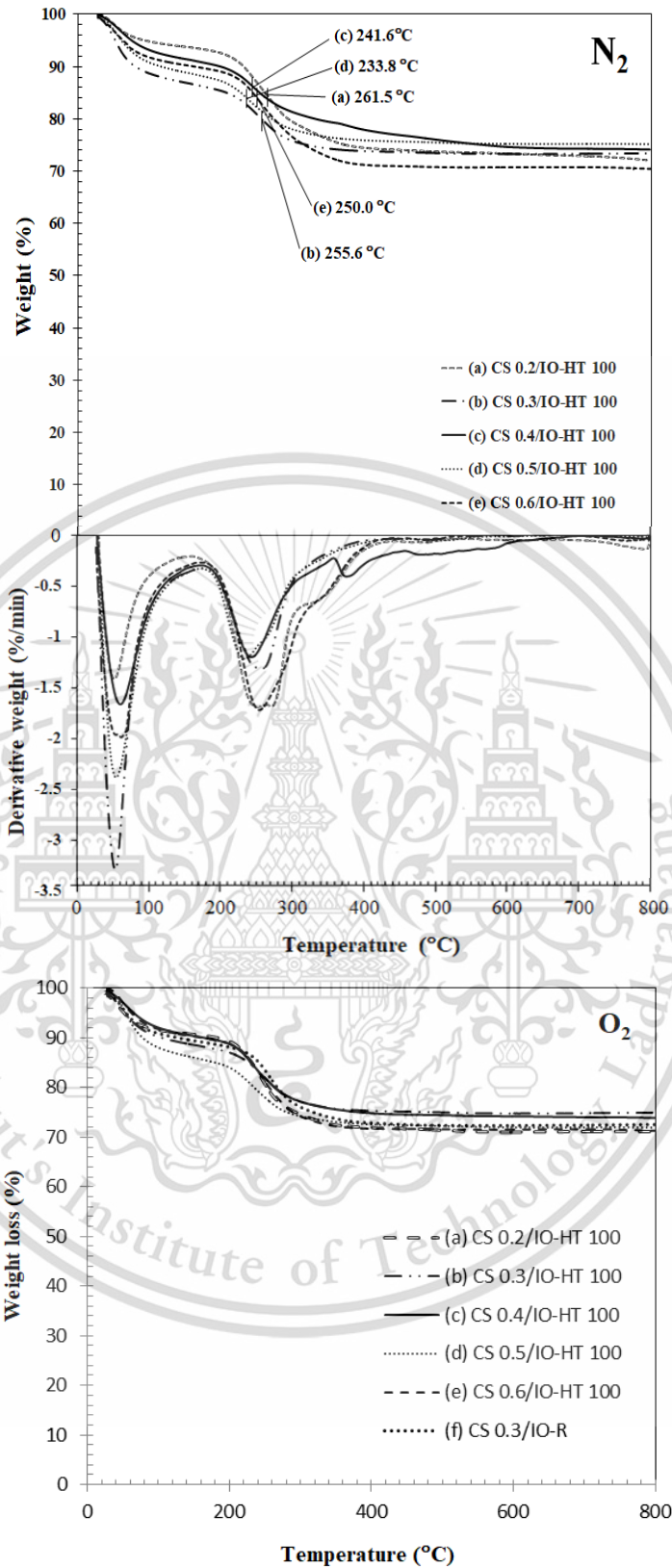


Figure 4.15 TGA and DTG thermograms of (a) CS0.2/IO-HT100, (b) CS0.3/IO-HT100, (c) CS0.4/IO-HT100, (d) CS0.5/IO-HT100 and (e) CS0.6/IO-HT100 nanocomposites under N₂ and air zero atmospheres

This material is reserved for educational use only, not allowed for commercial use.

Forbidden to modify the content, and cite the document when use.

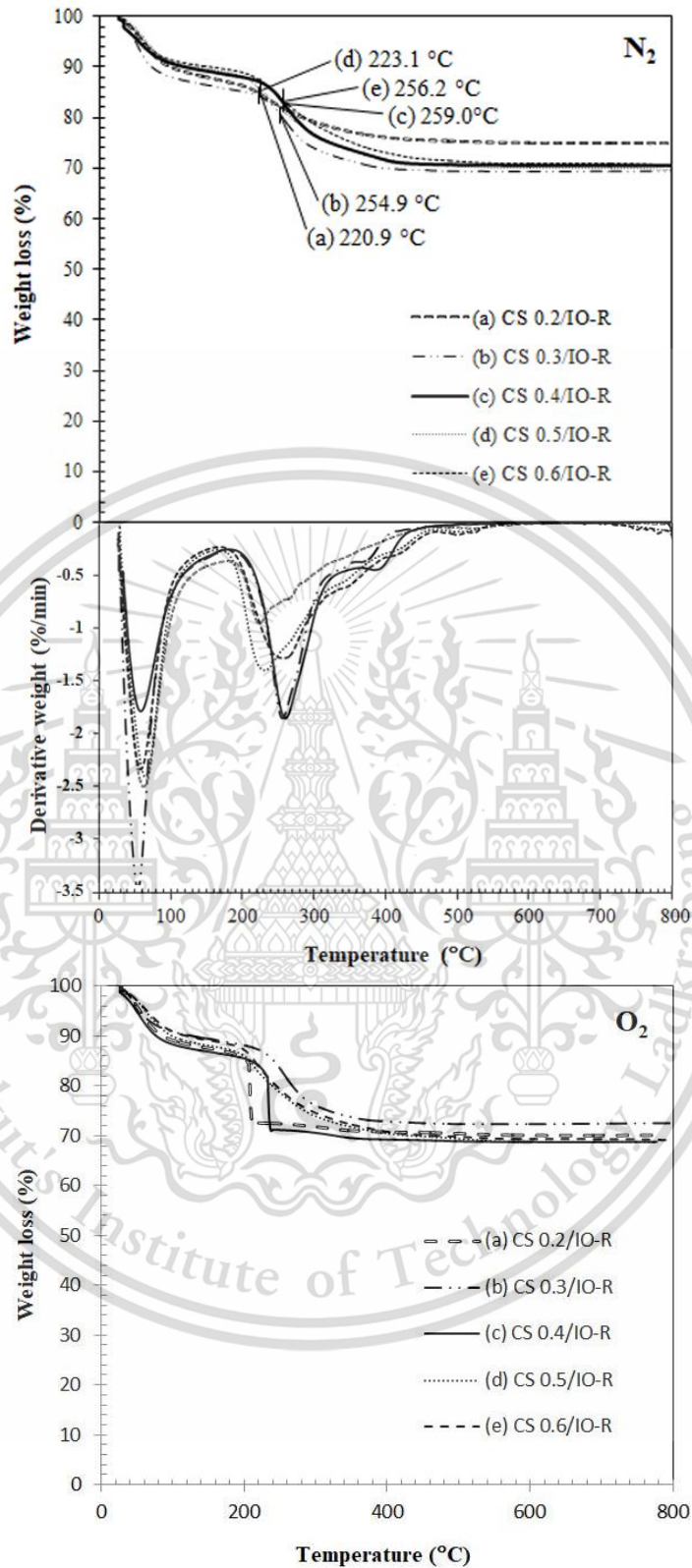


Figure 4.16 TGA and DTG thermograms of (a) CS0.2/IO-R, (b) CS0.3/IO-R, (c) CS0.4/IO-R, (d) CS0.5/IO-R and (e) CS0.6/IO-R nanocomposites under N₂ and air zero atmosphere

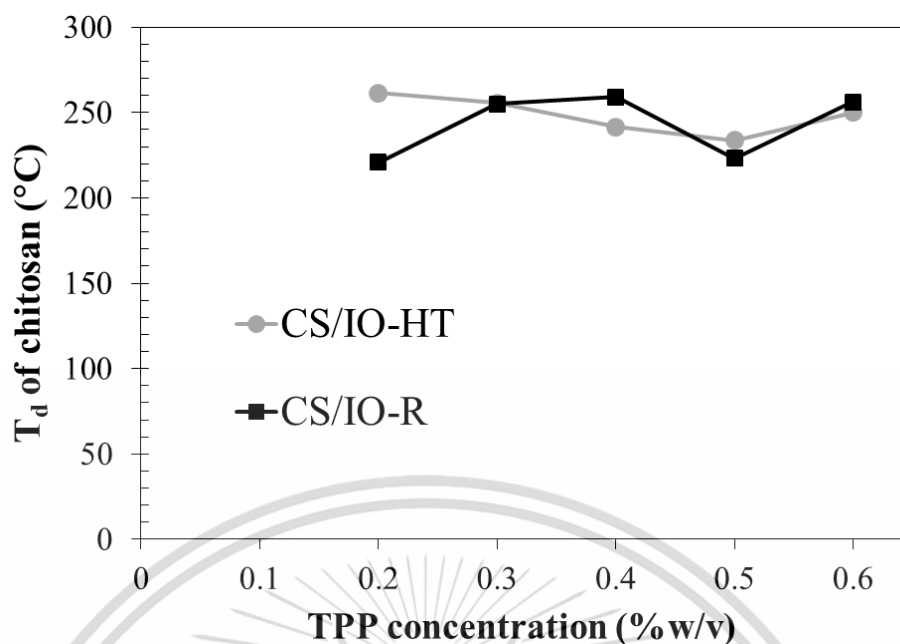


Figure 4.17 Relationship between the decomposition temperatures of chitosan (T_d) in CS/IO nanocomposites synthesized using hydrothermal method (CS/IO-HT) and refluxing method (CS/IO-R) and TPP concentrations used in the synthesis

Fig. 4.18 shows the DSC profiles under N_2 atmosphere of CS0.2/IO-HT100, CS0.3/IO-HT100, CS0.4/IO-HT100, CS0.5/IO-HT100 and CS0.6/IO-HT100 nanocomposites. It can be seen that the T_m values of crosslinked chitosan matrix in these nanocomposites were in the range of 184.4–190.5°C as summarized in Table 4.2, in which they slightly changed when the TPP concentrations were increased from 0.2 to 0.5 %w/v. However, the CS 0.2/IO-HT100 nanocomposite showed the lowest ΔH value, that is 136.2 J/g.

The ΔH value significantly increased to 194.0 J/g when the TPP concentration was increased from 0.2 to 0.3 %w/v in the CS0.3/IO-HT100 nanocomposite, attributing to the increase of degree of crosslinking. It was, however, the ΔH values decreased when the TPP concentration was increased from 0.3 to 0.4 and 0.5 %w/v, and then the ΔH values again increased when the TPP concentration was increased to 0.6 %w/v. The fluctuation of ΔH values was considered to be owing to the increase pH of *in-situ* preparation by increasing the TPP concentration.

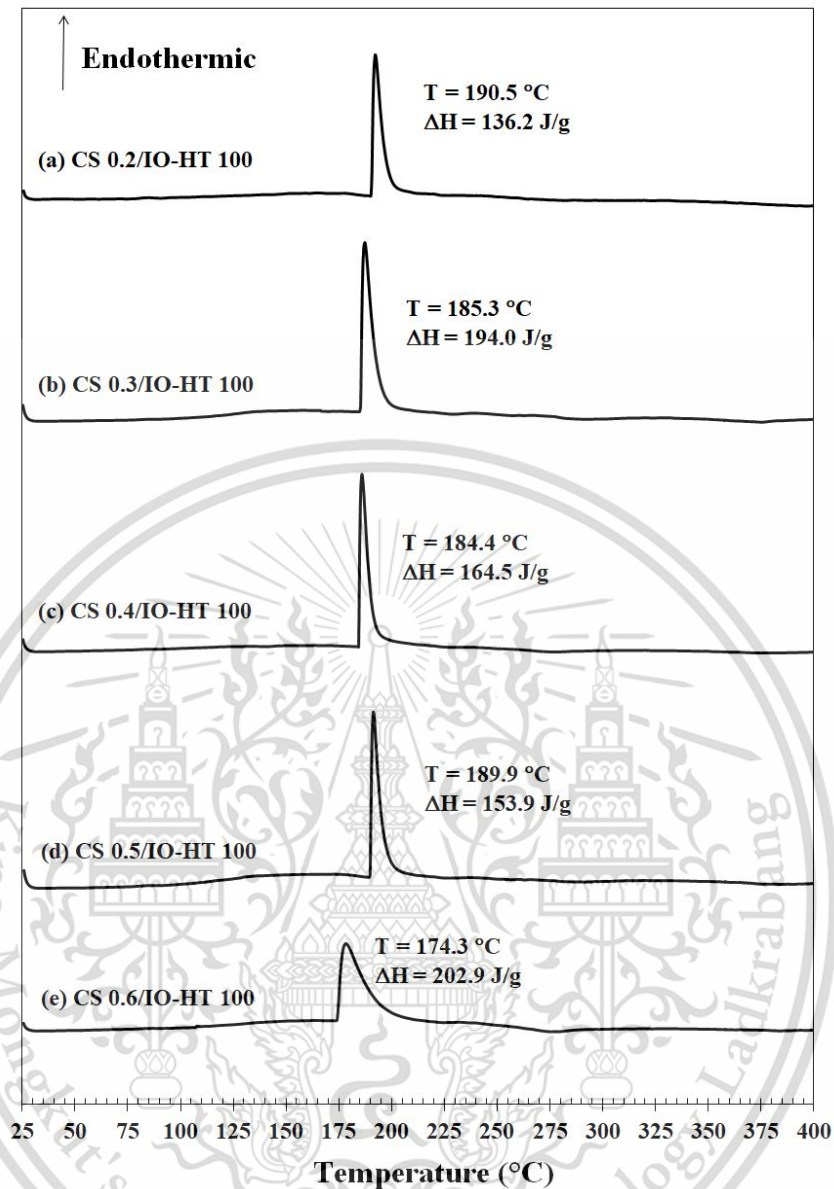


Figure 4.18 DSC thermograms of (a) CS0.2/IO-HT100, (b) CS0.3/IO-HT100, (c) CS0.4/IO-HT100, (d) CS0.5/IO-HT100 and (e) CS0.6/IO-HT100 nanocomposites

The TPP crosslinker normally dissociated into hydroxide and phosphoric ions at high pH values, in which they can rapidly interact with the $-\text{NH}_3^+$ groups of chitosan, resulting in the formation of crosslinked chitosan particles. The higher TPP concentration, the faster crosslinking and then the higher difference of crosslinking density between the outer surface and the inner bulk of nanocomposite particles were obtained, leading to the non-uniform crosslinked network. The formation of

non-uniform crosslinked chitosan network could evidentially observe as the broad DSC peak and the shift of T_m value to 174.3°C corresponded to the T_m of crosslinked chitosan with the absence of iron oxide nanocrystals were obtained in the CS 0.6/IO-HT100 nanocomposite as shown in Fig. 4.18(e) [37, 66].

Fig. 4.19 shows the DSC profiles under N_2 atmosphere of (a) CS0.2/IO-R, (b) CS0.3/IO-R, (c) CS0.4/IO-R, (d) CS0.5/IO-R and (e) CS0.6/IO-R nanocomposites. The T_m values in these nanocomposites were in the range of $180.7\text{--}185.1^\circ\text{C}$ as summarized in Table 4.2. The thermal properties of nanocomposites of refluxing method were slightly lower than those of hydrothermal method. The ΔH values significantly increased to 202.9 J/g when the TPP concentration was increased from 0.2 to 0.4 %w/v in the CS0.4/IO-R nanocomposite due to the increase of degree of crosslinking. However, the ΔH values decreased when the TPP concentration was increased from 0.4 to 0.6 %w/v. Moreover, the T_m value of the CS0.6/IO-R nanocomposite decreased to 176.3°C . These results insisted the formation of non-uniform crosslinked chitosan network. The higher TPP concentration, the faster crosslinking occurred, resulting in the greater difference in crosslinking density of chitosan in the CS0.6/IO-R nanocomposite.

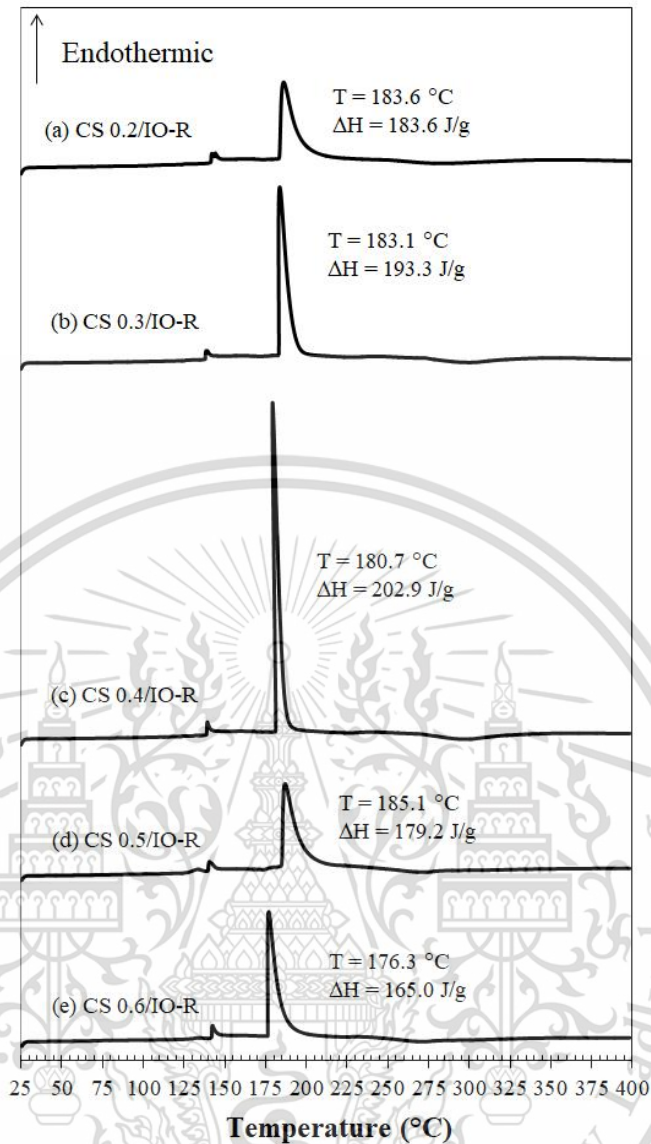


Figure 4.19 DSC thermograms of (a) CS0.2/IO-R, (b) CS0.3/IO-R, (c) CS0.4/IO-R, (d) CS0.5/IO-R and (e) CS0.6/IO-R nanocomposites

These results showed that the fluctuation of T_d and ΔH values in the CS/IO nanocomposites synthesized using hydrothermal and refluxing methods was considered to be because the higher TPP concentration promoted the higher difference of crosslinking density. The non-uniform crosslinked network formed in the nanocomposites. Besides, the thermal properties of hydrothermal nanocomposites were superior to those of refluxing nanocomposites because of the slightly larger proportion of iron oxide nanocrystals in the hydrothermal CS/IO nanocomposites.

This material is reserved for educational use only, not allowed for commercial use.

- Magnetic properties

Fig. 4.20 shows the VSM curves of CS0.2/IO-HT100, CS0.3/IO-HT100, CS0.4/IO-HT100, CS0.5/IO-HT100 and CS0.6/IO-HT100 nanocomposites, while Fig. 4.21 shows the VSM curves of CS0.2/IO-R, CS0.3/IO-R, CS0.4/IO-R, CS0.5/IO-R and CS0.6/IO-R nanocomposites. It can be seen that the hysteresis curves of these nanocomposites revealed their superparamagnetic behavior with zero coercivity and magnetic remanence, in which their magnetic properties were summarized in Table 4.2.

The CS0.2/IO-HT100 and CS0.2/IO-R nanocomposites possessed the low M_{max} values of about 9.6 and 7.2 emu/g, respectively, in which it was because the deficiency of TPP resulted in the presence of free $-NH_3^+$ groups of chitosan. The free $-NH_3^+$ group could interact with iron oxide nuclei, resulting in the inhibition of formation and growth of some iron oxide nuclei [56].

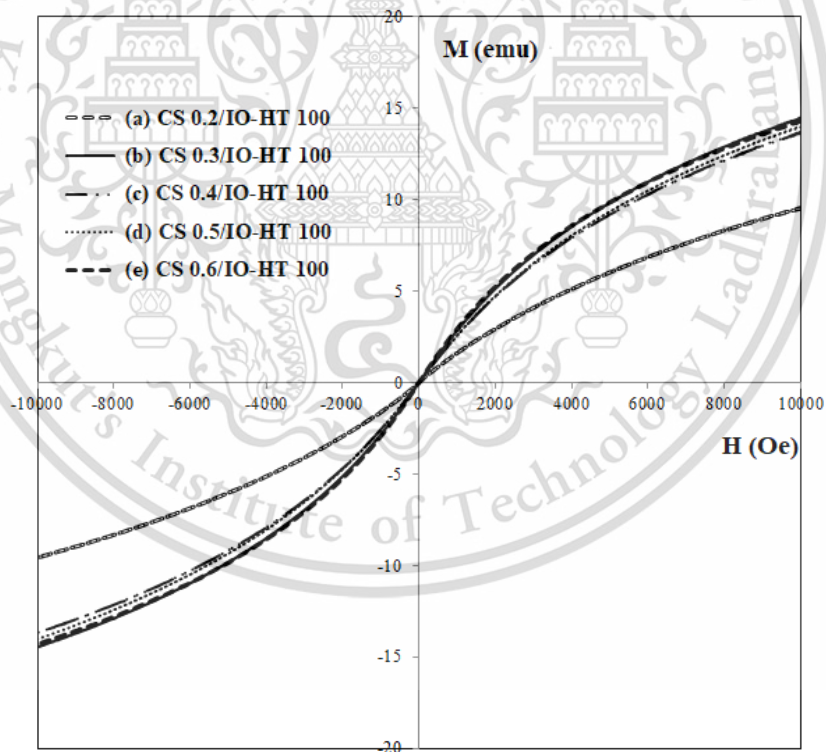


Figure 4.20 VSM curves of (a) CS0.2/IO-HT100, (b) CS0.3/IO-HT100, (c) CS0.4/IO-HT100, (d) CS0.5/IO-HT100 and (e) CS0.6/IO-HT100 nanocomposites

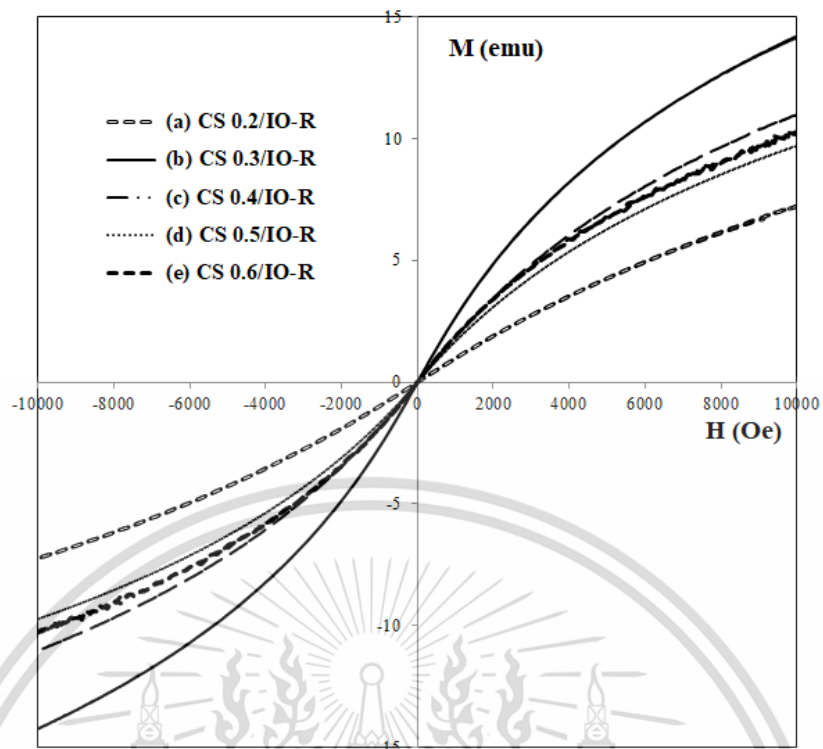


Figure 4.21. VSM curves of (a) CS0.2/IO-R, (b) CS0.3/IO-R, (c) CS0.4/IO-R, (d) CS0.5/IO-R and (e) CS0.6/IO-R nanocomposites

The M_{\max} values significantly increased about 14 emu/g in the CS0.3/IO-HT100, CS0.4/IO-HT100, CS0.5/IO-HT100, CS0.6/IO-HT100 and CS0.3/IO-R nanocomposites; however, they decrease to the range of 10–11 emu/g in the CS0.4/IO-R, CS0.5/IO-R and CS0.6/IO-R nanocomposites. Fig. 4.22 shows the relationship between the average particle sizes of iron oxide nanocrystals in CS/IO nanocomposites synthesized using hydrothermal and refluxing method and the highest M_{\max} value of each size. The M_{\max} values of CS/IO nanocomposites tended to increase with the increase of particle size of iron oxide nanocrystals. Moreover, the obtained magnetite-maghemite nanoparticles of CS/IO nanocomposites had the single magnetic domain structure with the superparamagnetic properties because their particle size was below the superparamagnetic critical diameter of both magnetite (12 nm) and maghemite (20 nm).

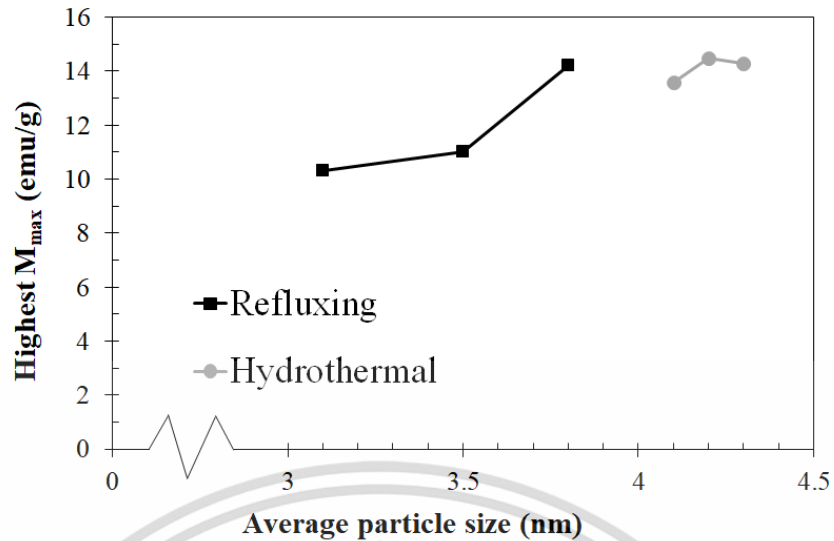


Figure 4.22 Relationship between the average particle sizes of iron oxide (IO) nanocrystals in CS/IO nanocomposites synthesized using hydrothermal and refluxing method and the highest maximum magnetization (M_{max}) of each size

In the *in-situ* synthesis, the very small particle size of magnetite-maghemite nanocrystals in all CS/IO nanocomposites were caused by the constraining effect of the crosslinked chitosan network on the growth of the nanocrystals. The magnetite-maghemite nanocrystals in all CS/IO nanocomposites possessed the irregular spherical shape with the particle size of 3.1–4.4 nm. Besides, the magnetite-maghemite nanocrystals decreased in crystallite size with an increase of the crosslinking density in the CC templates: the CS/IO nanocomposites crosslinked by 0.3 %w/v TPP resulted in magnetite-maghemite nanocrystals with the smallest average crystallite size, 3.9 nm. The high proportions of iron oxide in all CS/IO nanocomposites were in the range of 69–75%, while the proportions of chitosan matrix were in the range of 13–20%. The CS0.3/IO-HT100 nanocomposites synthesized using 0.3 %w/v TPP concentration and treated by hydrothermal method at 100°C had an average particle size of 3.9 nm and M_{max} value of 14.5 emu/g with the highest degree of crosslinking. The resultant nanocomposites have the potential to be further developed for hyperthermia application.

4.3 Adsorption synthesis of CC/IO nanocomposites

In the adsorption preparation of the chitosan/iron oxide nanocomposites, the chitosan solution was mixed with TPP solution, resulting in the crosslinked chitosan (CC) template. Then the CC template was soaked in the mixture of iron solutions with stirring. The crosslinked chitosan swelled and adsorbed Fe^{2+} and Fe^{3+} ions in the 3D network of CC template. The $\text{Fe}^{2+}/\text{Fe}^{3+}$ ions reacted with hydroxide ions in the free volume of the crosslinked chitosan template as shown in Fig 4.23.

The nucleation and growth of iron oxide nanoparticles embedded in crosslinked chitosan templates were considered to minimize oxidation and increase dispersion, hence improving the superparamagnetic characteristics of the resultant nanocomposites. Moreover, the constrained swelling of crosslinked chitosan could limit the amount of adsorbed iron ions, resulting in a high proportion of chitosan matrix in the nanocomposites. For hyperthermia applications, a large proportion of the chitosan matrix could be loaded or functionalized by medicinal substances for cancer treatment. As a result, the nanocomposites could be used as hybrid materials with specificity to the target organ.

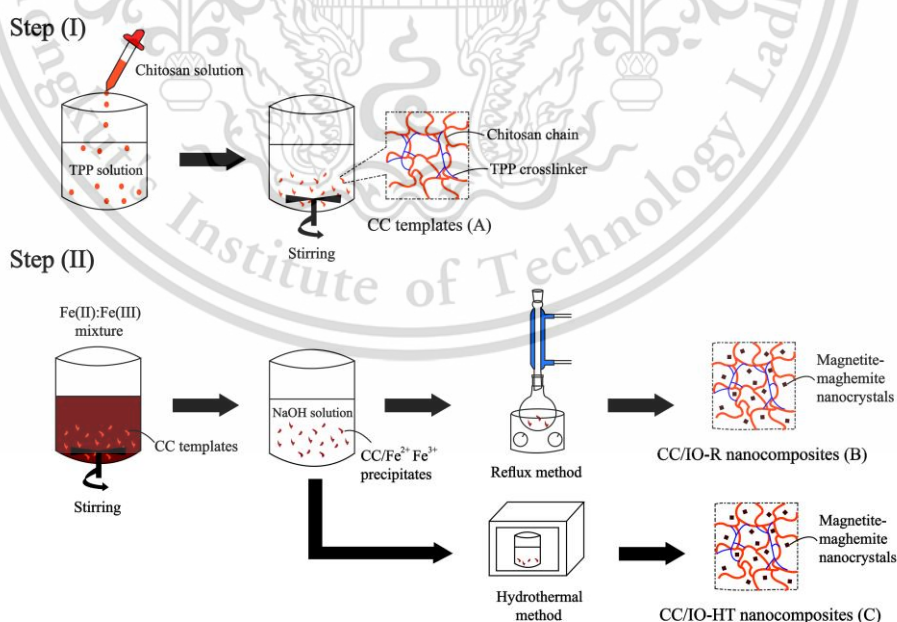


Figure 4.23 The adsorption preparation of the chitosan/iron oxide nanocomposites

4.3.1 Effect of TPP concentration on CHI templates

The effect of TPP concentrations on crosslinked structures of CC templates were analyzed from DSC thermograms. Fig. 4.24 shows the DSC thermograms of CC0.3, CC0.4, CC0.5 and CC0.6 templates obtained by using TPP concentrations of 0.3, 0.4, 0.5 and 0.6 %w/v, respectively. The melting temperatures (T_m) of the CC templates were in the range of 158.3–178.5°C, corresponded to the crosslinked chitosan.

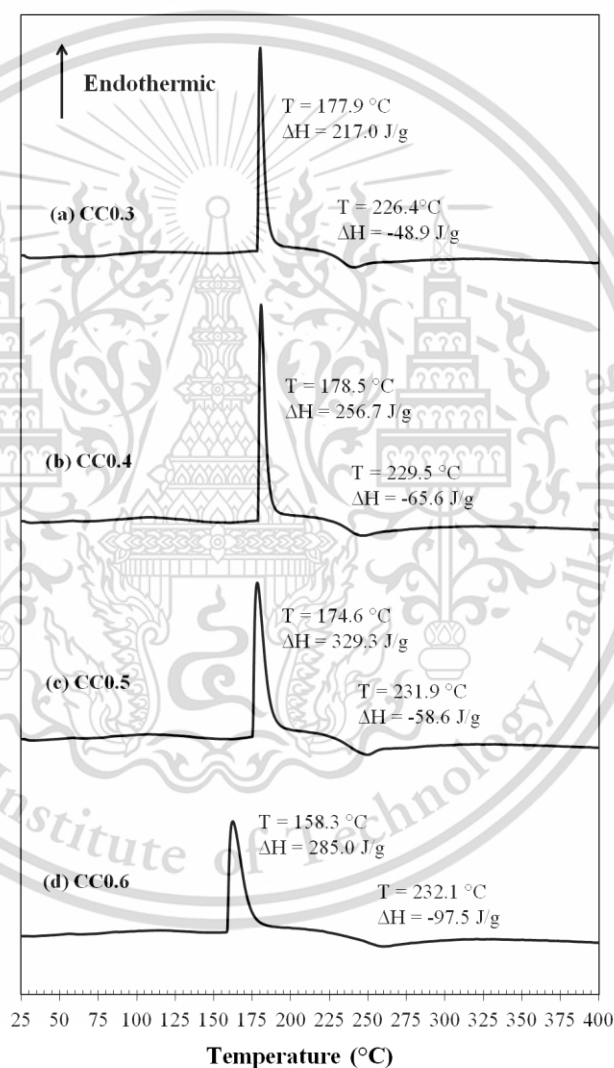


Figure 4.24 DSC thermograms of (a) CC0.3, (b) CC0.4, (c) CC0.5 and (d) CC0.6 templates

The melting enthalpy (ΔH_m) values of the CC templates were considered to be related to the crosslinking density of chitosan. It can be seen that the T_m values of CC0.3, CC0.4 and CC0.5 templates were almost similar, however, their ΔH_m values significantly increased with the increasing of TPP concentration used in the preparation of CC templates from 0.3 to 0.5 %w/v. The higher TPP concentration induced the higher dissociation of phosphoric and hydroxide ions, therefore, these ions speedily interacted with the $-\text{NH}_3^+$ groups of chitosan for crosslinking, resulting in the higher crosslinking densities. In the opposite direction, the T_m and ΔH_m values of CC0.6 template drastically decreased when the TPP concentration was increased to 0.6 %w/v. This result was considered to be because the rapid crosslinking immediately occurred when the droplets of chitosan solution were added to very high TPP concentration, resulting in the difference of crosslinking density between the outer surface and inner bulk of chitosan. Therefore, the CC0.6 template formed as non-uniform crosslinked chitosan, in which it can be evidentially shown as the broad endothermic peak around 158°C.

In addition, all samples showed the exothermic change at the temperature ranging from 226.4 to 232.1°C, in which it was related to the decomposition of free amine units in chitosan [66]. It was, therefore, the decomposition enthalpy (ΔH_d) was corresponded to the number of free amine groups of chitosan. These ΔH_d values were fluctuated by increasing the TPP concentrations. The ΔH_d value of CC0.6 templates was higher than those of CC0.3, CC0.4 and CC0.5 templates. It was considered to be because the higher quantity of free amine groups of chitosan and lower crosslinking density were obtained in the CC0.6 template. These results insisted that the usage of high TPP concentration created a gradient crosslinking between the outer surface and inner bulk of chitosan, resulting in the non-uniform crosslinked density and high quantity of free amine groups of CC templates as obviously observed in the CC0.6 sample [37]. It was, therefore, the CC templates prepared by using TPP concentrations of 0.3, 0.4 and 0.5 %w/v would be further used as the precursors for the preparation of CC/IO nanocomposites.

4.3.2 Effect of synthesis method and the initial concentration of TPP solution on CC/IO nanocomposites

In the adsorption method for preparation of the CC/IO nanocomposites, the constrained swelling of crosslinked chitosan could limit the particle sizes and amount of magnetite-maghemite nanocrystals in the nanocomposites. Higher TPP concentration could promote higher crosslinking density and non-uniform crosslinked structure, leading to varying particle sizes of iron oxide nanocrystals in the CC/IO nanocomposites. The different particle sizes of iron oxide nanocrystals influenced the interfacial interaction between the nanocrystals and CC templates, resulting in varying thermal stability. Besides, the pressurized hydrothermal reaction system could induce the turbulent movement of materials within the system. The iron oxide precursors might partially migrate from the CC template during the nucleation and growth of the nanocrystals and then hydrothermally reacted in the solution media. This phenomenon could promote the different particle sizes of iron oxide nanocrystals, resulting in the fluctuation of thermal stability of the nanocomposites.

- **Crystal structure and morphology**

Fig. 4.25 shows the XRD patterns of CC0.3/IO-HT100, CC0.4/IO-HT100 and CC0.5/IO-HT100 nanocomposites, while Fig. 4.26 shows the XRD patterns of CC0.3/IO-R, CC0.4/IO-R and CC0.5/IO-R nanocomposites. The main characteristic peaks of all CC/IO nanocomposites synthesized using reflux and hydrothermal methods were corresponded to the overlapping peaks of crystalline phases of magnetite (Fe_3O_4) (JCPDS No.19-0629) and maghemite ($\gamma\text{-Fe}_2\text{O}_3$) (JCPDS No.04-0755). The asymmetrical shoulder observed around $2\theta \sim 35.5^\circ$ was considered to be due to the concomitant presence of the magnetite and maghemite phases in the CC/IO nanocomposites. The formation of magnetite occurred from the reaction of $\text{Fe}^{2+}/\text{Fe}^{3+}$ ions and the hydroxide ions (OH^-) of strong basic solution, producing the magnetite nanocrystals. However, the magnetite phase might be oxidized further to maghemite resulting in the biphasic iron oxide nanocrystals. The crystallite sizes (D_{XRD}) of magnetite-maghemite nanocrystals in the CC/IO nanocomposites were calculated from the (311) peak ($2\theta = 35.6^\circ$) using the Scherrer equation with $K = 0.9$. It was found that the $D_{(311)}$ values were in the range of 11–14 nm as summarized in Table 4.3.

This material is reserved for educational use only, not allowed for commercial use.

The magnetite-maghemite nanocrystals grew and embedded in the restricted free volume among the crosslinked structure of CC templates, leading to the finite particle sizes of magnetite-maghemite nanocrystals. It was, therefore, the CC templates positively impacted on the growth of magnetite-maghemite nanocrystals with the small particle sizes and the narrow size distribution [67].

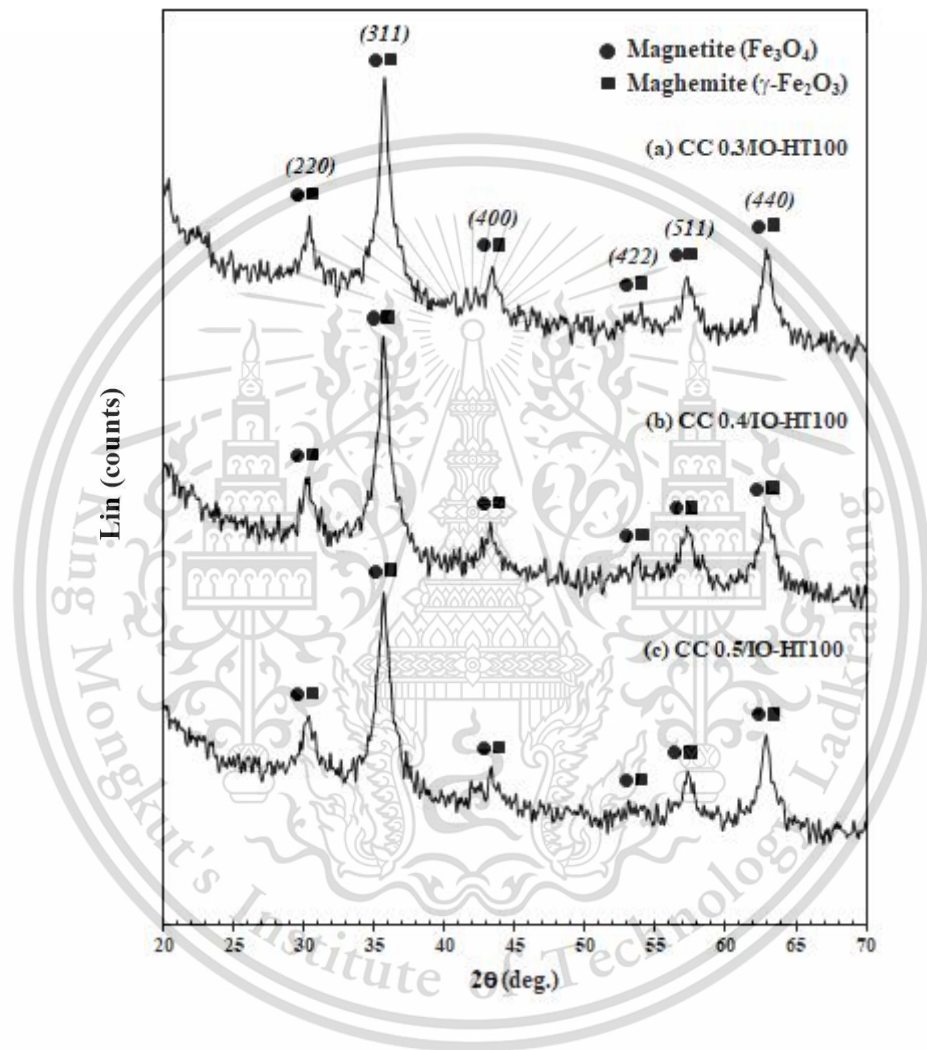


Figure 4.25 XRD patterns of (a) CC0.3/IO-HT100, (b) CC0.4/IO-HT100, (c) CC0.5/IO-HT100 and (d) CC0.6/IO-HT100 nanocomposites

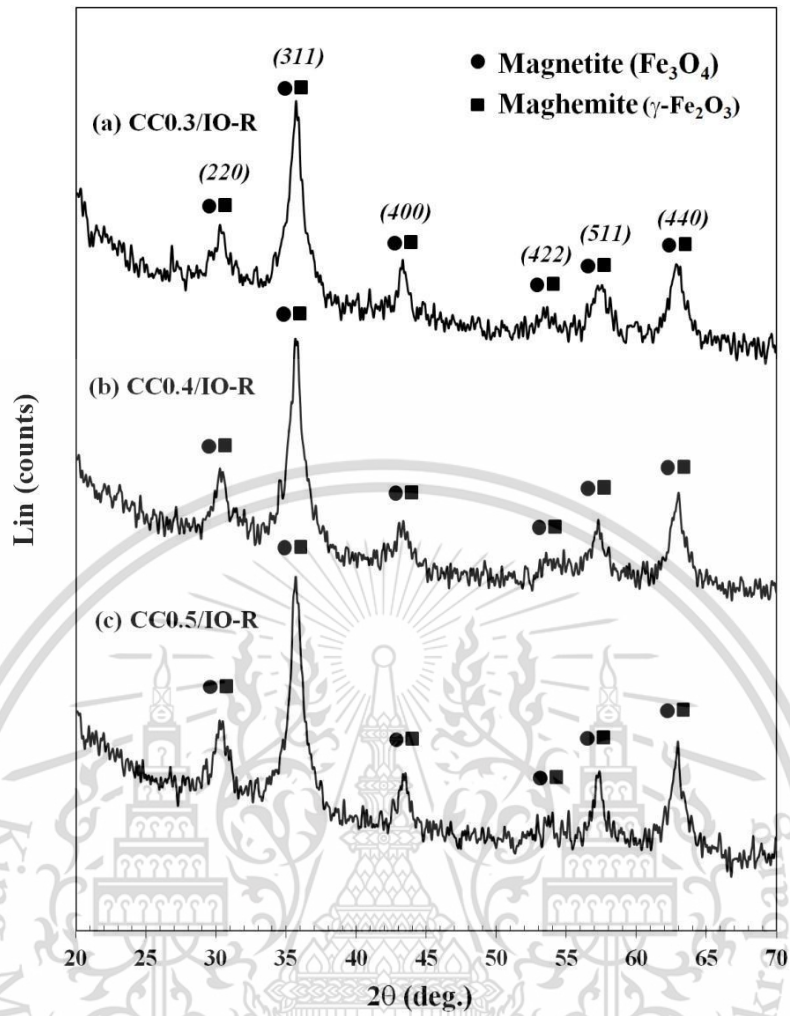


Figure 4.26 XRD patterns of (a) CC0.3/IO-R, (b) CC0.4/IO-R, (c) CC0.5/IO-R and (d) CC0.6/IO-R nanocomposites

Table 4.3 Parameters used for adsorption synthesis of CC/IO nanocomposites and their XRD and TEM data

Sample	Synthesis conditions			XRD		TEM	
	% TPP (%w/v)	Heating method	T* (°C)	Phase	D ₍₃₁₁₎ ** (nm)	Shape of IO	Avg. size of IO*** (nm)
CC0.3/IO-HT100	0.3	Hydrothermal	100	Fe ₃ O ₄ / γ-Fe ₂ O ₃	14.0	Quadrilateral	D 10.9
CC0.4/IO-HT100	0.4	Hydrothermal	100	Fe ₃ O ₄ / γ-Fe ₂ O ₃	11.7	Quadrilateral	D 10.7
CC0.5/IO-HT100	0.5	Hydrothermal	100	Fe ₃ O ₄ / γ-Fe ₂ O ₃	11.3	Quadrilateral	D 13.1
CC0.3/IO-R	0.3	Reflux	100	Fe ₃ O ₄ / γ-Fe ₂ O ₃	12.4	Quadrilateral	D 10.3
CC0.4/IO-R	0.4	Reflux	100	Fe ₃ O ₄ / γ-Fe ₂ O ₃	11.2	Quadrilateral	D 13.5
CC0.5/IO-R	0.5	Reflux	100	Fe ₃ O ₄ / γ-Fe ₂ O ₃	14.1	Quadrilateral	D 12.5

*T was the temperature of heating method.

**D₍₃₁₁₎ was calculated by Scherrer equation.

***IO nanocrystals size was analyzed by ImageJ software.

The TEM images and particle size distributions of CC0.3/IO-HT100, CC0.4/IO-HT100 and CC0.5/IO-HT100 nanocomposites are shown in Fig. 4.27, while those of CC0.3/IO-R, CC0.4/IO-R and CC0.5/IO-R nanocomposites are shown in Fig. 4.28. The microstructures of all nanocomposites were observed as the quadrilateral nanocrystals of magnetite-maghemite embedded in the CC templates. These nanocrystals were associated with the cubic inverse spinel structure of magnetite and the cubic tetragonal structure of maghemite, inferred from the XRD patterns. Some researches [68-69] reported that the magnetite nanoparticles treated by refluxing method had the outstanding cubic morphology with a board size in the range of 9–80 nm. Besides, maghemite nanoparticles treated by hydrothermal method had the quadrilateral shape with an average size of 11 nm. However, the IO nanoparticles in this study were corresponded to the quadrilateral nanocrystals of magnetite-maghemite embedded in the CC templates synthesized using adsorption synthesis.

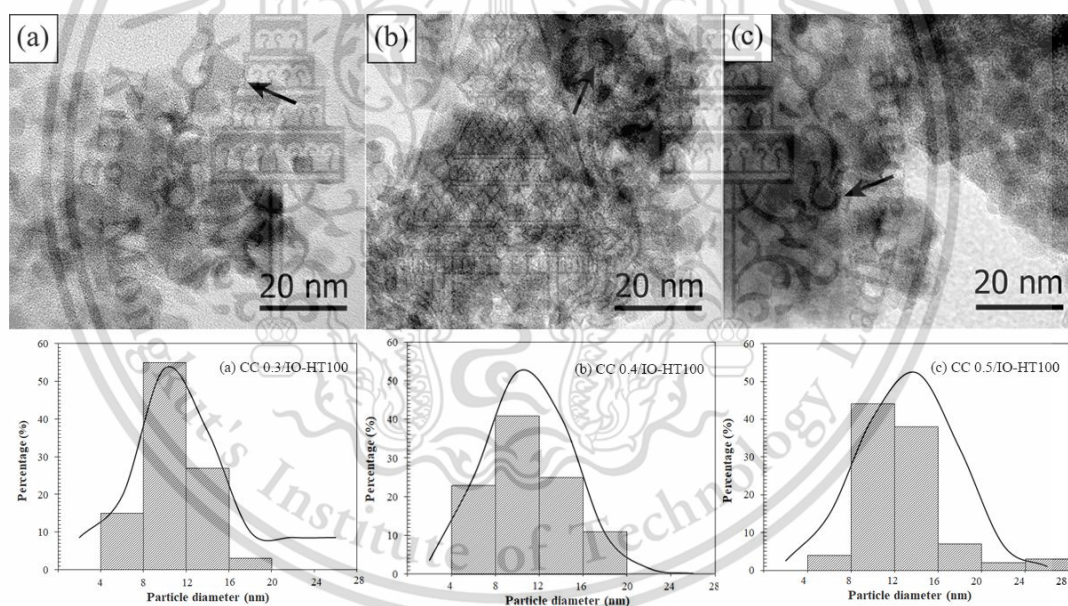


Figure 4.27 TEM patterns and particle size distribution (PSD) of (a) CC0.3/IO-HT100, (b) CC0.4/IO-HT100 and (c) CC0.5/IO-HT100 nanocomposites

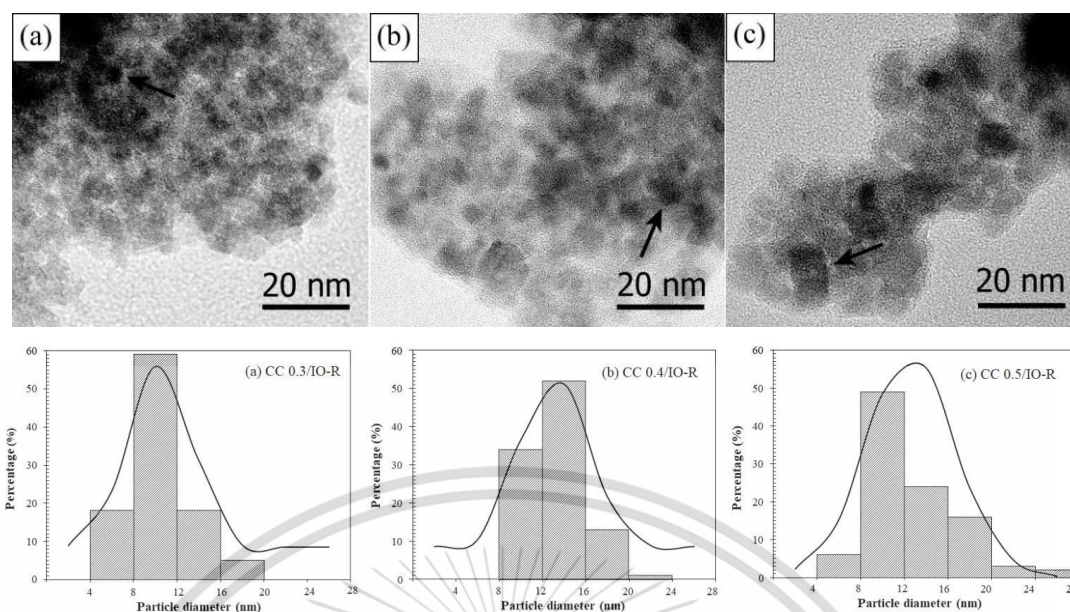


Figure 4.28 TEM patterns and particle size distribution (PSD) of (a) CC0.3/IO-R, (b) CC0.4/IO-R and (c) CC0.5/IO-R nanocomposites

The average sizes of magnetite-maghemite nanocrystals measured from the TEM images were in the range of 10–14 nm as shown in Table 4.3, in which they were in agreement with their average crystallite sizes from XRD data. The magnetite-maghemite nanocrystals in the particle size distribution of the CC0.3/IO-HT100, CC0.4/IO-HT100 and CC0.5/IO-HT100 nanocomposites showed the primary size in the range of 4–16, 4–20 and 8–16 nm, respectively. Meanwhile, the magnetite-maghemite nanocrystals in the CC0.3/IO-R, CC0.4/IO-R and CC0.5/IO-R nanocomposites were found to be primarily in the range of 8–12, 8–16 and 8–20 nm, respectively. Besides, the size distributions of magnetite-maghemite nanocrystals synthesized by hydrothermal and refluxing methods became wider when the TPP concentration was increased. These findings were attributed to the fact that higher TPP concentrations promoted faster crosslinking, which resulted in greater difference in crosslinking density between the outer surface and the inner bulk of nanocomposite particles, leading to the non-uniform crosslinked network.

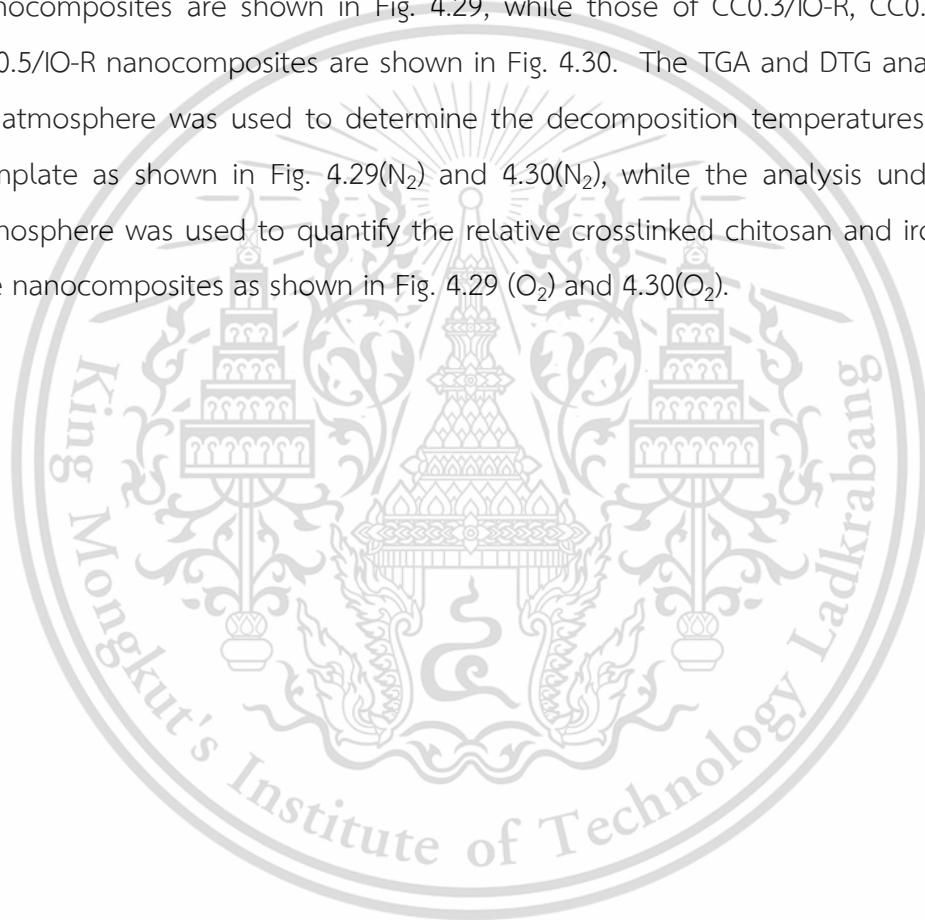
These findings indicated that the synthesis conditions used, as well as the initial TPP concentration used in the adsorption method, had no obvious effect on the crystalline phases and shapes of iron oxide nanocrystals. The quadrilateral magnetite-maghemite nanocrystals of all CC/IO nanocomposites grew and embedded

This material is reserved for educational use only, not allowed for commercial use.

in the restricted free volume of the CC templates, leading to the finite particle sizes of the nanocrystals. This effect led to the positive impact on the growth of magnetite-maghemite nanocrystals with small particle sizes and narrow size distributions. However, their size distributions were wider when the TPP concentration increased due to the presence of non-uniform crosslinked structure.

- **Thermal properties**

TGA and DTG curves of CC0.3/IO-HT100, CC0.4/IO-HT100 and CC0.5/IO-HT100 nanocomposites are shown in Fig. 4.29, while those of CC0.3/IO-R, CC0.4/IO-R and CC0.5/IO-R nanocomposites are shown in Fig. 4.30. The TGA and DTG analysis under N_2 atmosphere was used to determine the decomposition temperatures (T_d) of CC template as shown in Fig. 4.29(N_2) and 4.30(N_2), while the analysis under air zero atmosphere was used to quantify the relative crosslinked chitosan and iron oxide in the nanocomposites as shown in Fig. 4.29 (O_2) and 4.30(O_2).



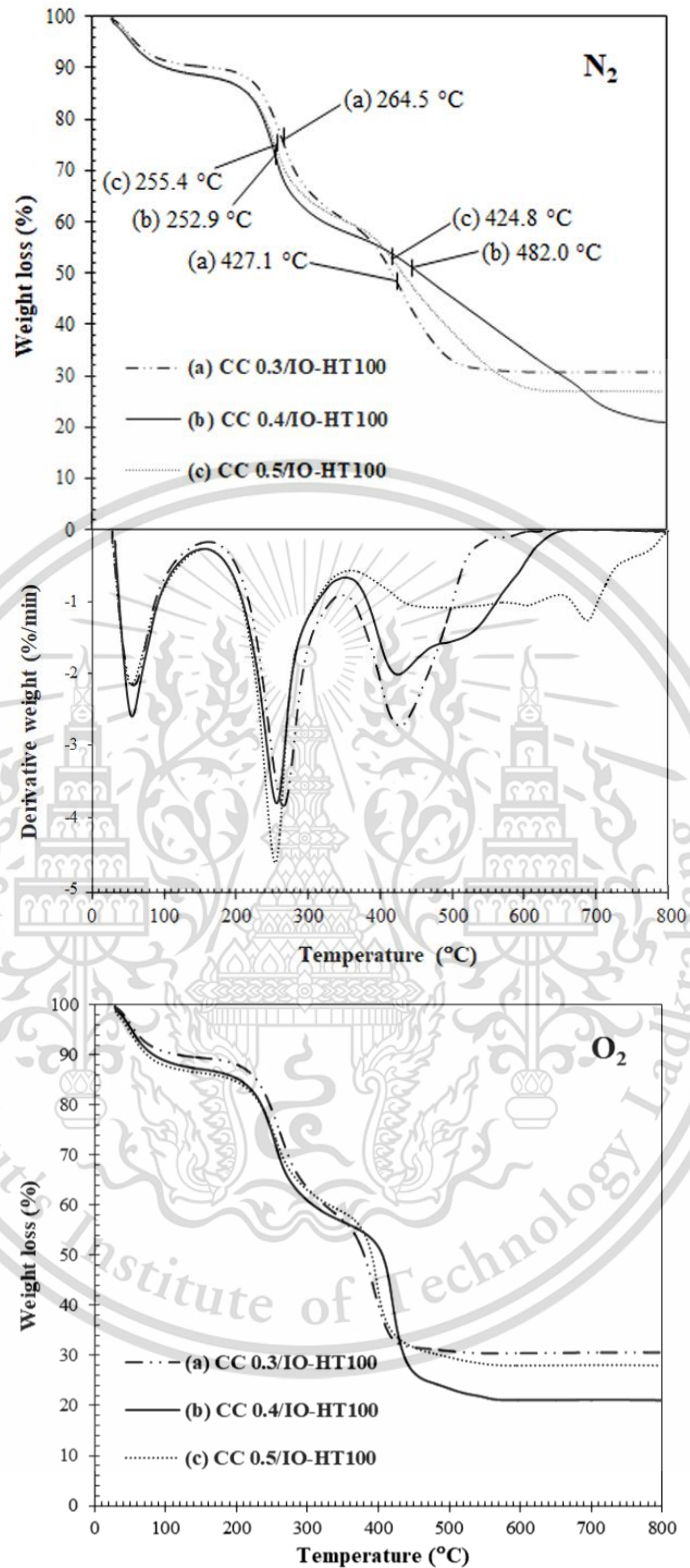


Figure 4.29 TGA and DTG thermograms of (a) CC0.3/IO-HT100, (b) CC0.4/IO-HT100 and (c) CC0.5/IO-HT100 nanocomposites under N₂ and air zero atmosphere

This material is reserved for educational use only, not allowed for commercial use.

Forbidden to modify the content, and cite the document when use.

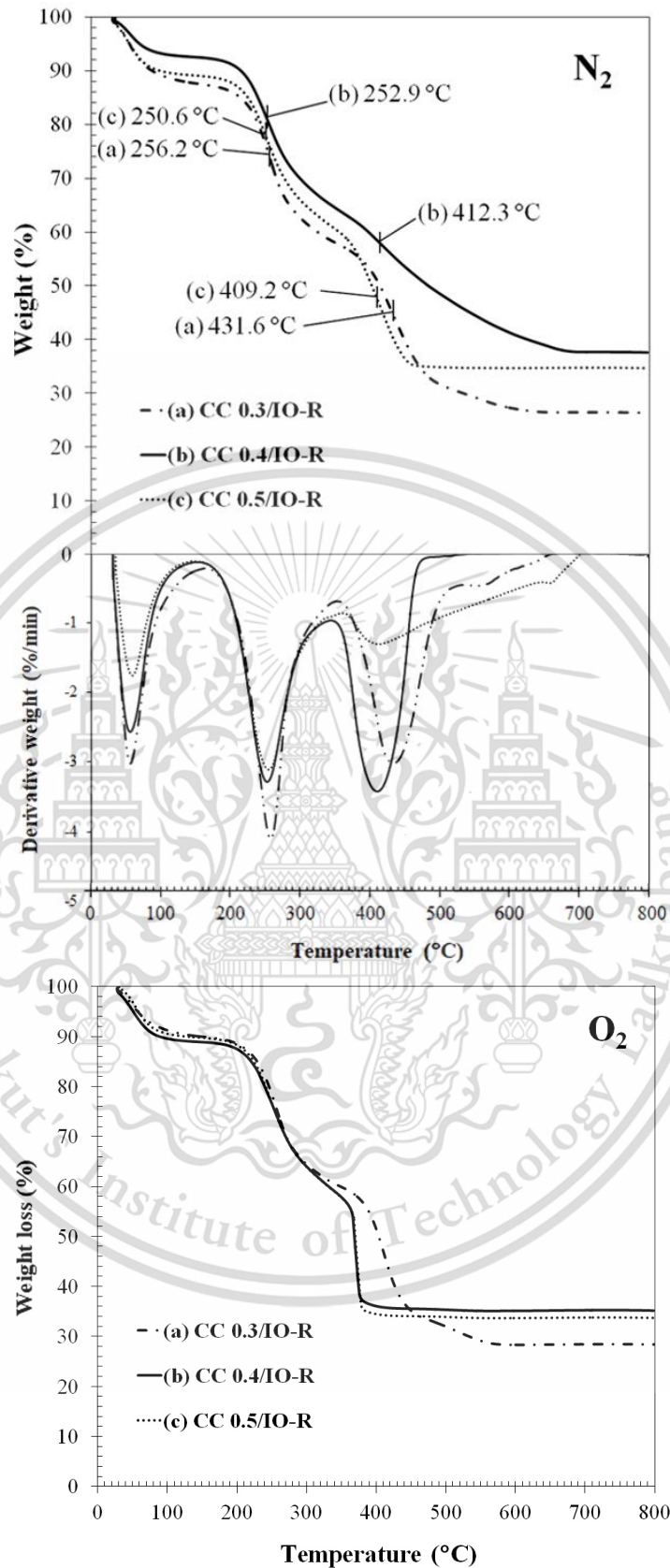


Figure 4.30 TGA and DTG thermograms of (a) CC0.3/IO-R, (b) CC0.4/IO-R and (c) CC0.5/IO-R nanocomposites under N_2 and air zero atmosphere

This material is reserved for educational use only, not allowed for commercial use.

Forbidden to modify the content, and cite the document when use.

The CC/IO nanocomposites synthesized by hydrothermal method showed similar thermal events as shown in Fig. 4.29(N₂). There are two major stages of degradations at T_{d1} and T_{d2} related to the degradation of CC templates. The T_{d1} value of the first degradation stage in all nanocomposites corresponded to the breaking of glucoside linkage [15] was observed in the range of 252.9–264.5°C – see Table 4.4. Fig. 4.31 shows the changes of the 1st decomposition temperature (T_{d1}) and the 2nd decomposition temperature (T_{d2}) of CC templates in CC/IO nanocomposites with the varying TPP concentrations used in the hydrothermal synthesis. The T_{d1} value tended to significantly decrease when the TPP concentrations were increased from 0.3 to 0.4 and 0.5 %w/v. These results were considered to be because the higher TPP concentration led to the higher crosslinking between chitosan chains and TPP crosslinker and then the hydrogen bonding of chitosan chains decreased. The decreasing of hydrogen bonding brought about the lower degradation temperature.

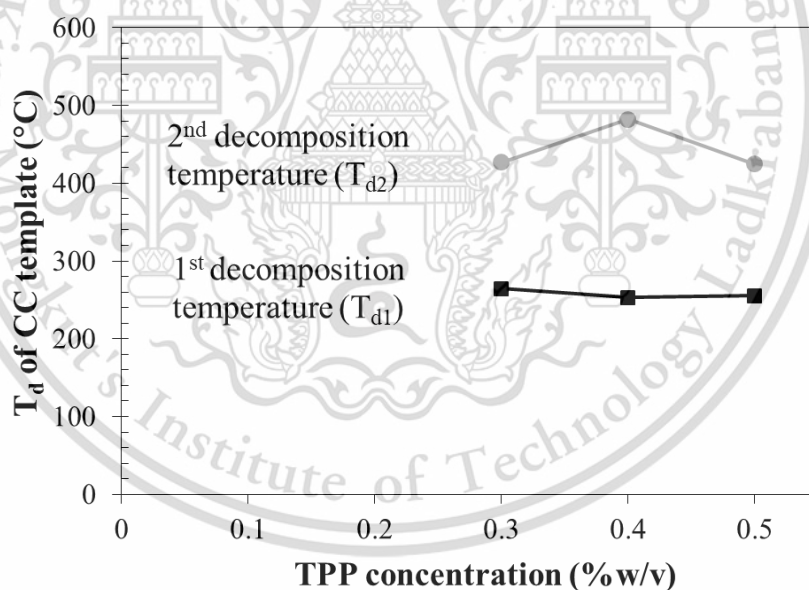


Figure 4.31 Changes of the 1st decomposition temperature (T_{d1}) and the 2nd decomposition temperature (T_{d2}) of CC templates in CC/IO nanocomposites with the varying TPP concentrations used in the hydrothermal synthesis

The second degradation stage was observed at the T_{d2} value of 424.8–482.0°C. This degradation temperature was considered to be caused by the degradation of the CC templates, which interacted with the magnetite-maghemite nanocrystals. Fig. 4.31 shows the T_{d2} value significantly increased to 482.0°C when the TPP concentration was increased from 0.3 to 0.4 %w/v in the CC0.4/IO-HT100 nanocomposite, attributing to the increase of small particle sizes of magnetite-maghemite nanocrystals inferred by the particle size distribution. It was, however, the T_{d2} value decreased when the TPP concentration was increased from 0.4 to 0.5 %w/v. The fluctuation of T_{d2} values was thought to be due to higher TPP concentration causing a non-uniform crosslinked structure, resulting in the different particle sizes of obtained magnetite-maghemite nanocrystals. The interfacial interaction between the magnetite-maghemite nanocrystals and CC templates increased when the proportion of small particle sizes of magnetite-maghemite nanocrystals increased, corresponding to the particle size distribution.

The thermal behavior of CC/IO nanocomposites synthesized by reflux method, as shown in Fig. 4.30(N₂), similarly occurred as those of CC/IO nanocomposites synthesized by hydrothermal method. The T_{d1} values of the CC/IO nanocomposites synthesized by refluxing method were in the range of 250.6–256.2°C. Fig. 4.32 shows the changes of the 1st decomposition temperature (T_{d1}) and the 2nd decomposition temperature (T_{d2}) of CC templates in CC/IO nanocomposites with the varying TPP concentrations used in the refluxing synthesis. The T_{d1} values slightly decreased when the TPP concentration was increased from 0.3 to 0.5 %w/v, attributing to the decrease of the hydrogen bonding of chitosan chains. Meanwhile, the T_{d2} values tended to significantly decrease with increasing TPP concentrations, reducing from 431.6°C to 409.2°C. These results demonstrated that increased TPP concentration resulted in a non-uniform crosslinked network. The large particle size of formed magnetite-maghemite nanocrystals reduced the interfacial interaction between the nanocrystals and CC templates.

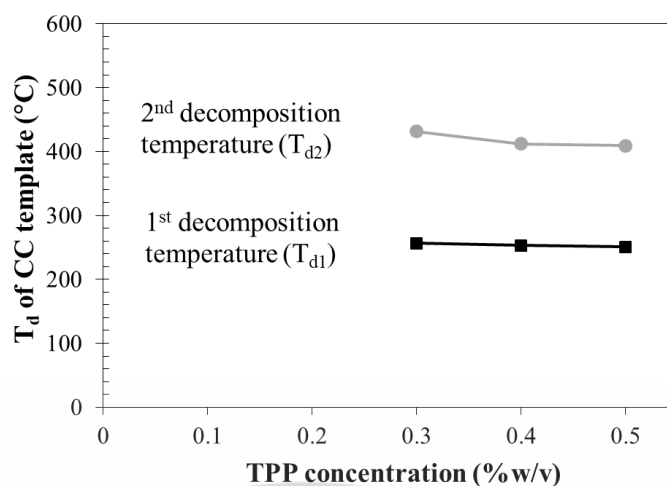


Figure 4.32 Changes of the 1st decomposition temperature (T_{d1}) and the 2nd decomposition temperature (T_{d2}) of CC templates in CC/IO nanocomposites with the varying TPP concentrations used in the refluxing synthesis

The fractions of CC templates and iron oxide in the CC/IO nanocomposites were determined using weight losses and remaining in the TGA thermograms under air zero atmosphere as shown in Fig. 4.29(O_2) and 4.30(O_2). All nanocomposites were composed of water and organic solvent, evaporating at around 53.0–55.1°C with the weight loss in the range of 10–15%. The large proportion calculated from the sum of weight losses at T_{d1} and T_{d2} was attributed to the chitosan quantity, in which the large proportions in all nanocomposites were in the range of 53–67%. While residuals ranged from 21 to 35% – see Table 4.4., representing the relative amount of iron oxide nanocrystals and a trace of phosphorus from the TPP crosslinker.

The CC0.4/IO-HT100 nanocomposites had the highest chitosan proportion around 67% and the lowest iron oxide and TPP proportions around 21%. These proportions in the CC0.4/IO-HT100 nanocomposites were significantly different from the other nanocomposites. This phenomenon was seen due to the turbulent movement of materials in the system caused by the pressurized hydrothermal reaction system. Therefore, the iron oxide precursors might partially migrate from the CC0.4 template and hydrothermally reacted in the solution media. Besides, the more proportion of small iron oxide nanocrystals in the CC0.4/IO-HT100 nanocomposites might contribute the migration of iron oxide nanocrystals in the reaction.

Table 4.4 TGA, DSC, VSM and cell viability of CC/IO nanocomposites synthesized by adsorption synthesis

Sample	TGA					DSC				VSM			Cell viability (%)
	T _{d1} of CC* (°C)	Weight loss at T _{d1} ** (%)	T _{d2} of CC* (°C)	Weight loss at T _{d2} ** (%)	Residual (%)	T _m (°C)	ΔH _m (J/g)	T _d (°C)	ΔH _d (J/g)	M _{max} (emu/g)	M _r (emu/g)	H _c (Oe)	
CC0.3/IO-HT100	264.5	31	427.1	28	31	185.0	94.7	245.7	-80.7	13.1	0.1	2.7	83
CC0.4/IO-HT100	252.9	31	482.0	36	21	185.4	104.1	258.0	-118.3	12.7	0.4	11.6	89
CC0.5/IO-HT100	255.4	26	424.8	32	28	185.5	119.9	254.6	-104.3	13.9	0.4	11.8	90
CC0.3/IO-R	256.2	30	431.6	27	28	184.0	133.3	251.2	-129.5	8.6	0	0	82
CC0.4/IO-R	252.9	28	412.3	25	35	183.1	111.6	249.8	-100.2	15.2	0	0	81
CC0.5/IO-R	250.6	29	409.2	27	34	187.7	67.5	249.4	-95.9	14.8	0	0	80

* T_d values of chitosan were determined from TGA profiles under N₂.

** Weight losses at T_d and residuals were determined from the TGA profiles under air zero. The remaining proportion out of the weight loss at T_d and residuals was considered to be the amount of water and organic solvent.

The DSC thermograms of CC0.3/IO-HT100, CC0.4/IO-HT100 and CC0.5/IO-HT100 nanocomposites are shown in Fig. 4.33. The melting points (T_m) of CC templates in these nanocomposites were about 185°C as summarized in Table 4.4. These T_m values were higher than the T_m of the as-prepared CC templates shown in section 4.3.1, insisting the occurrence of interfacial interaction between magnetite-maghemite nanocrystals and CC templates. The ΔH_m values of the nanocomposites increased with the increasing of TPP concentration. Furthermore, a large exothermic change was observed in all nanocomposites at temperatures ranging from 245.7 to 258.0°C, which occurred at a higher temperature than the precursor CC templates and were corresponded to T_{d1} values from the TGA data. The CC0.4/IO-HT100 sample had the highest ΔH_d value of 118.3 J/g because the smaller sizes of magnetite-maghemite nanocrystals promoted the higher interfacial interaction between magnetite-maghemite nanocrystals and CC templates.

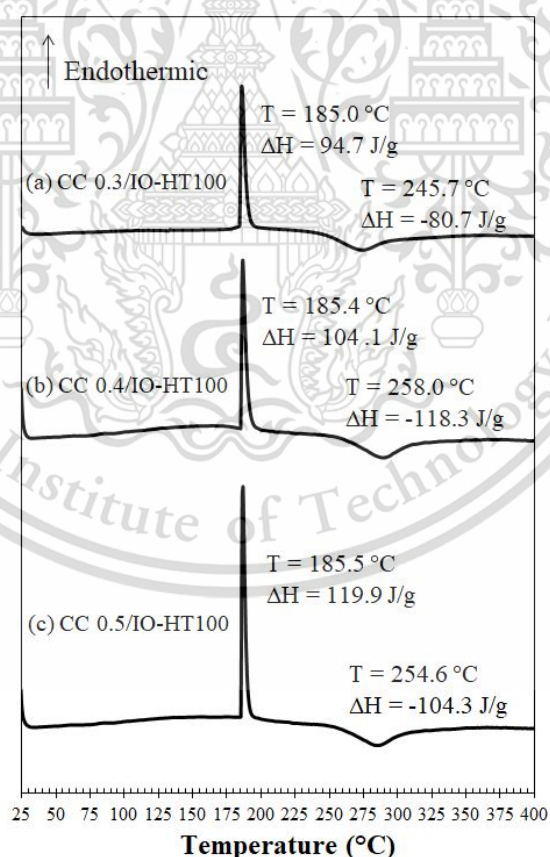


Figure 4.33 DSC thermograms of (a) CC0.3/IO-HT100, (b) CC0.4/IO-HT100 and (c) CC0.6/IO-HT100 nanocomposites

The DSC thermograms of CC0.3/IO-R, CC0.4/IO-R and CC0.5/IO-R nanocomposites are shown in Fig. 4.34. The T_m values of CC templates in these nanocomposites were in the range of 183.1–187.7°C as summarized in Table 4.4. These T_m values were similar to the T_m of the nanocomposites synthesized by hydrothermal method due to the presence of interfacial interaction between iron oxide nanocrystals and CC templates in both systems. The CC0.3/IO-R had a higher ΔH_m value than the CC0.4/IO-R and CC0.5/IO-R nanocomposite, in which they were attributed to the effect of interfacial interaction of nanocrystals and CC template. As previously mentioned, the CC0.3/IO-R nanocomposite had smaller magnetite-maghemite nanocrystals, which tended to provide a greater interfacial interaction with the CC0.3 template, resulting in a higher ΔH_m value than the others. The large exothermic peaks in all nanocomposites ranged from 249.4 to 251.2°C. The ΔH_d value decreased with the increasing of TPP concentration. The lone pair electrons of free amine groups could interact with the Fe^{2+} Fe^{3+} precursors and then react with the basic solution, forming as the magnetite-maghemite nanocrystals. As a result, nanocomposites containing small magnetite-maghemite nanocrystals would have higher ΔH_d values than those containing large nanocrystals.

These results insisted that higher TPP concentration promoted non-uniform crosslinked structure, forming the larger particle size of magnetite-maghemite nanocrystals in the CC/IO nanocomposites. This affected on the decrease of the interfacial interaction between the magnetite-maghemite nanocrystals and CC templates, resulting in the reduction of thermal stability in the nanocomposites. Furthermore, the thermal properties of CC/IO nanocomposites synthesized by hydrothermal method varied with the increasing of TPP concentration, corresponding to the variation of magnetite-maghemite nanocrystal primary size. These results were attributed to the turbulent movement of materials in the system caused by the pressurized hydrothermal reaction system. The iron oxide precursors might partially migrate from the CC template during the nucleation and growth of magnetite-maghemite nanocrystals and then hydrothermally reacted in the solution media. In contrast, the primary sizes of CC/IO nanocomposites synthesized by refluxing method were obviously wider as TPP concentration increased, indicating a decrease of thermal stability of the nanocomposites.

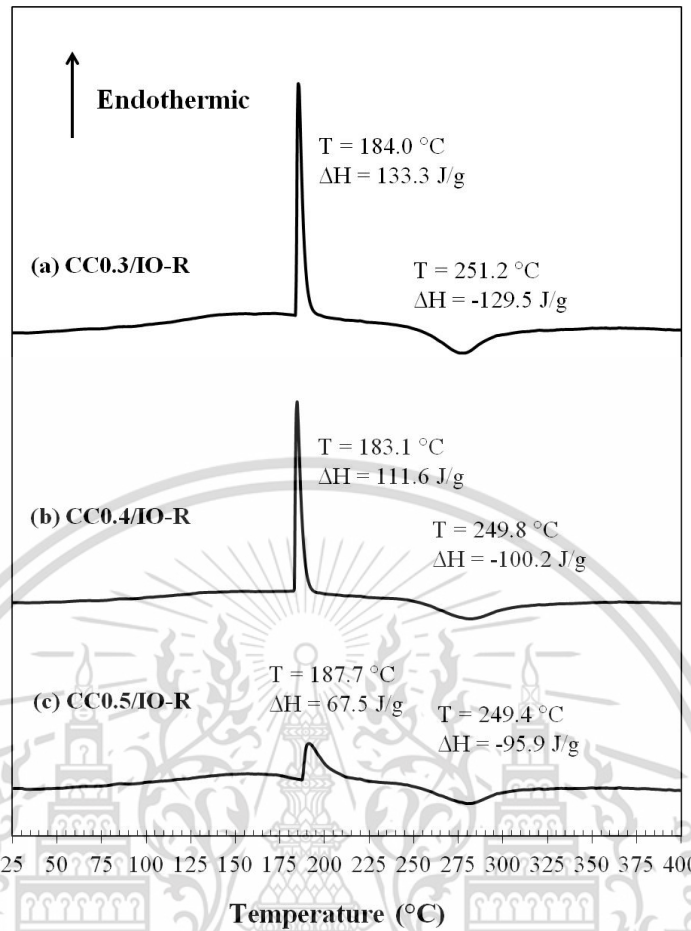


Figure 4.34 DSC thermograms of (a) CC0.3/IO-R, (b) CC0.4/IO-R and (c) CC0.5/IO-R nanocomposites

- **Magnetic properties**

The magnetic properties of CC/IO nanocomposites were measured as a function of the magnetic field at room temperature. The magnetization curves of CC0.3/IO-HT100, CC0.4/IO-HT100 and CC0.5/IO-HT100 nanocomposites are shown in Fig. 4.35 and summarized in Table 4.4. The hysteresis loops in all nanocomposites showed the superparamagnetic behavior. The maximum magnetization (M_{max}) values in all nanocomposites were in the range of 12.7–13.9 emu/g. The little change of M_{max} values can be explained by the size of magnetite-maghemite nanocrystals as discussed in the particle size distribution. However, the particle sizes of the synthesized magnetite-maghemite nanocrystals in all nanocomposites were less than the superparamagnetic critical diameter of both magnetite (12 nm) and maghemite (20 nm); therefore, they were considered to be single magnetic domain structures.

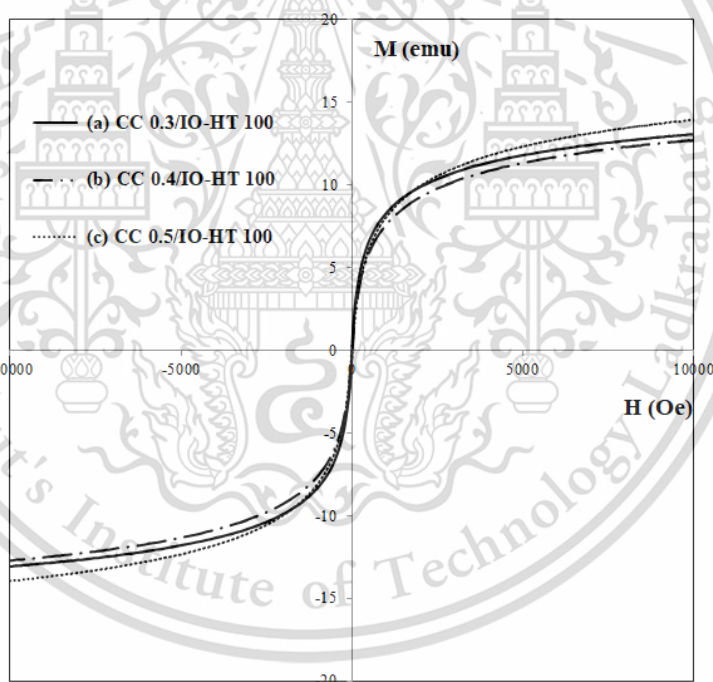


Figure 4.35 VSM curves of (a) CC0.3/IO-HT100, (b) CC0.4/IO-HT100 and (c) CC0.5/IO-HT100 nanocomposites

Meanwhile, the magnetization curves of CC0.3/IO-R, CC0.4/IO-R and CC0.5/IO-R nanocomposites are shown in Fig. 4.36. The absence of hysteresis loops was found in all nanocomposites because their coercivity (H_c) and magnetic

This material is reserved for educational use only, not allowed for commercial use.

remanence values (M_r) were close to zero, attributed to superparamagnetism. The CC0.3/IO-R nanocomposite showed the lowest value of maximum magnetization (M_{max}) of ~ 8.6 emu/g. The M_{max} values significantly increased to ~ 15 emu/g in the CC0.4/IO-R and CC0.5/IO-R nanocomposites. The lowest M_{max} value in the CC0.3/IO-R nanocomposite can be explained by the smallest size of magnetite-maghemite nanocrystals with the narrowest particle size distribution. The CC/IO nanocomposites are promising candidates for targeted delivery for alternative medical treatments due to their superparamagnetic behavior.

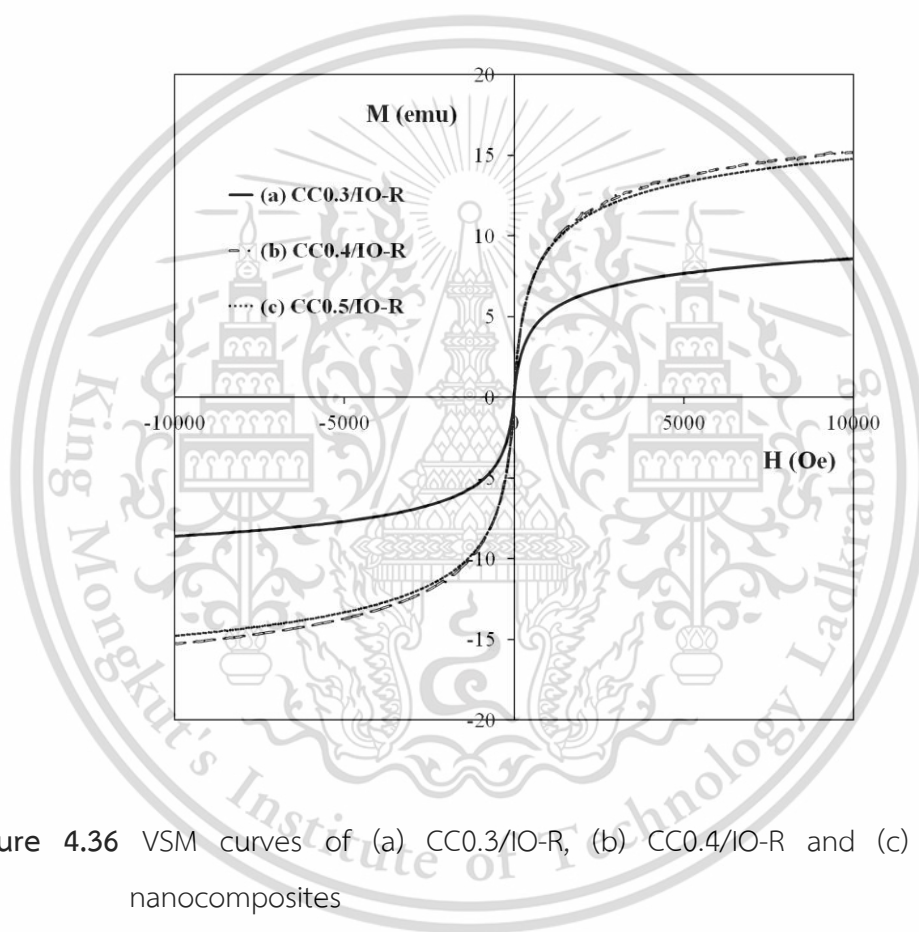


Figure 4.36 VSM curves of (a) CC0.3/IO-R, (b) CC0.4/IO-R and (c) CC0.5/IO-R nanocomposites

The crosslinked chitosan swelled and adsorbed Fe^{2+} and Fe^{3+} ions in the CC template during the adsorption synthesis. The Fe^{2+}/Fe^{3+} ions reacted with hydroxide ions, resulting in the nucleation and growth of magnetite-maghemite nanocrystals. The quadrilateral magnetite-maghemite nanocrystals in all CC/IO nanocomposites grew and embedded in the restricted free volume of CC templates, leading to the finite particle sizes, which their average particle sizes were in the range of 10.3–13.5

nm with the narrow size distribution. However, their size distributions widened as TPP concentration was increased because the higher TPP concentration, the greater difference in crosslinking density between the outer surface and the inner bulk of the nanocomposite, leading to the non-uniform crosslinked network as shown in Fig. 4.37. The difference of crosslinking density could evidently observe as the chitosan droplets when the chitosan solution was dropped into the TPP concentration of 0.6 %w/v. Furthermore, the restriction of $\text{Fe}^{2+}/\text{Fe}^{3+}$ ions by the free volume of crosslinked chitosan could improve the high proportion of chitosan matrix in the nanocomposites and the dispersion of iron oxide nanoparticles, leading to the improvement of superparamagnetic properties in the CC/IO nanocomposites. The CC0.4/IO-R nanocomposites synthesized using 0.4 %w/v TPP concentration and heat treated by refluxing method had an average particle size of 13.5 nm and the highest M_{max} value of 15.2 emu/g with zero coercivity and magnetic remanence. The CC/IO nanocomposites could enhance the superparamagnetic properties, therefore, they have the potential to be further developed for hyperthermia applications. Moreover, a large proportion of the chitosan matrix could be loaded or functionalized by medicinal substances for cancer treatment as hybrid materials with specificity to the target organs.

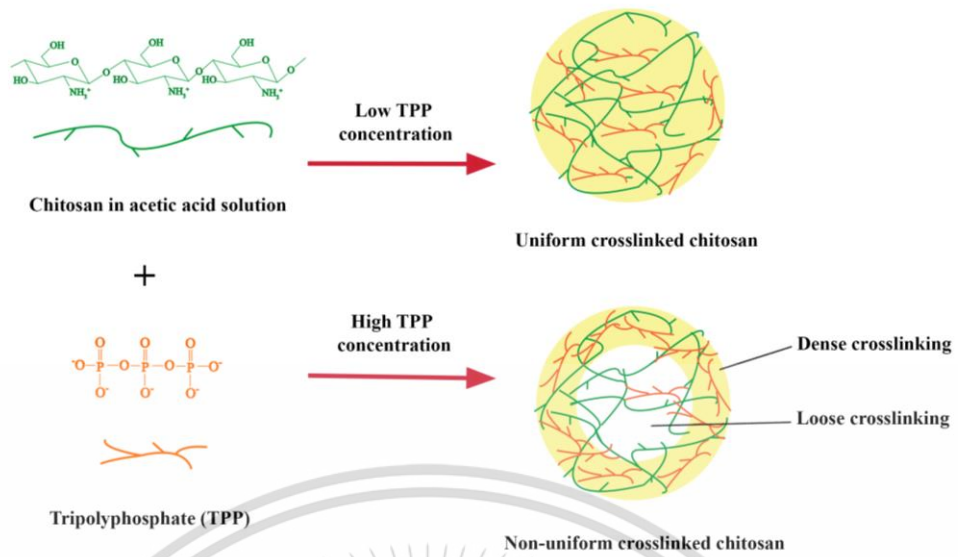


Figure 4.37 Schematic diagrams of the crosslinking chitosan networks in the CHI/IO nanocomposites obtained by using different TPP concentrations

4.4 Comparison of *in-situ* and adsorption syntheses

The synthesized CHI/IO nanocomposites obtained by *in-situ* and adsorption methods consisted of iron oxide nanoparticles embedded in CC matrix. The crosslinked chitosan network could prevent the agglomeration of formed magnetic nanoparticles, therefore, the resultant nanocomposites from both methods had the superparamagnetic properties due to the nano-size of iron oxide nanoparticles. However, the particle sizes and shapes of CHI/IO nanocomposites from both methods were significantly different, affecting on their superparamagnetic characteristics and thermal stabilities.

The CS0.3/IO-HT100 nanocomposite synthesized by the *in-situ* method was compared with the CC0.4/IO-R nanocomposites synthesized by the adsorption method because they were representatives with high M_{max} values and thermal stabilities. Although the iron oxide nanocrystals in both nanocomposites were magnetite and maghemite phases as shown in the XRD patterns (Fig. 4.38), the crystallize size of magnetite-maghemite nanocrystals in CC0.4/IO-R nanocomposite (11.2 nm) was approximately three times larger than the nanocrystals of CS0.3/IO-HT100 nanocomposite (3.9 nm), resulting in the sharper XRD pattern peaks of CC0.4/IO-R nanocomposite.

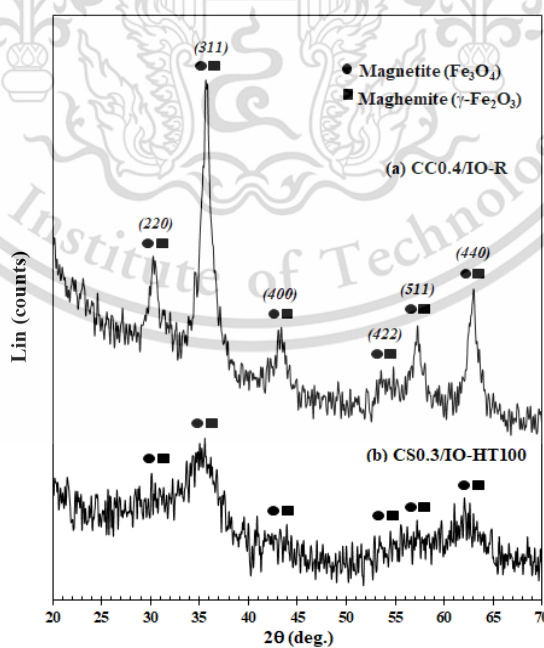


Figure 4.38 XRD patterns of (a) CC0.4/IO-R and (b) CS0.3/IO-HT100 nanocomposites

The magnetite-maghemite nanocrystals in the CC0.4/IO-R nanocomposite had a quadrilateral shape with primary sizes ranging from 8 to 20 nm as shown in Fig. 4.39(a) and 4.39(b). Meanwhile, the primary size of magnetite-maghemite nanocrystals with an irregular spherical shape in CS0.3/IO-HT100 nanocomposite was 2–8 nm as shown in Fig. 4.39(c) and 4.39(d). It can be seen that the particle size distribution of CC0.4/IO-R nanocomposite was obviously wider than another one. Although the magnetite-maghemite nanocrystals in the CC0.4/IO-R nanocomposite had a larger particle size than the CS0.3/IO-HT100 nanocomposite, their quantity was less. The M_{\max} values of both nanocomposites were similar, which they were about 15 emu/g as shown in Fig 4.40. This was thought to be because the M_{\max} value of the iron oxide nanocrystals in the nanocomposites increases with particle size and quantity. However, the hysteresis curve of CC0.4/IO-R nanocomposite had a more obvious S-shape than that of CS0.3/IO-HT100 nanocomposite. This result demonstrated the obvious superparamagnetic property of CC0.4/IO-R nanocomposite with rapid magnetization and demagnetization.

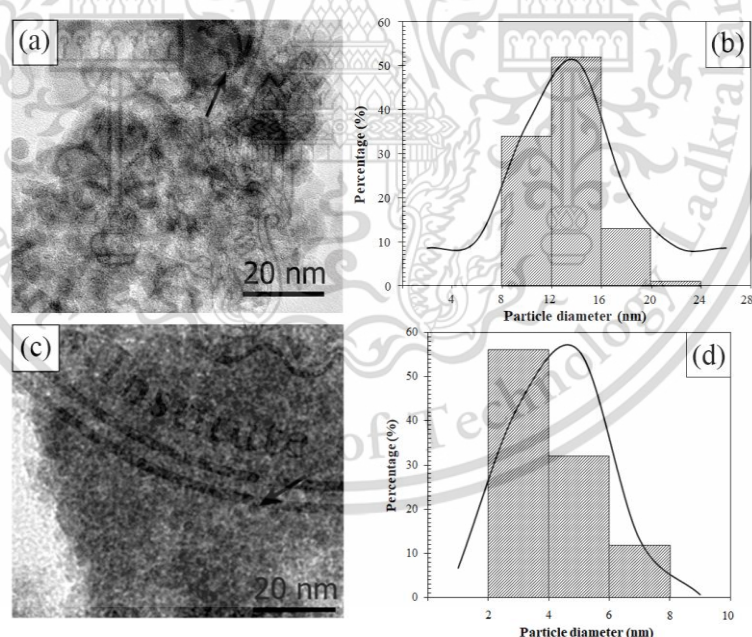


Figure 4.39 TEM images and particles size distributions of (a, b) CC0.4/IO-R and (c, d) CS0.3/IO-HT100 nanocomposites

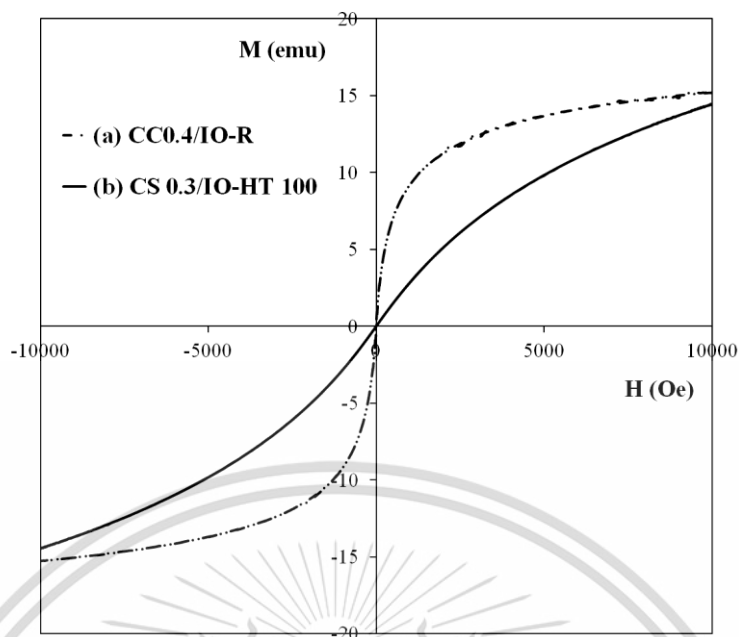


Figure 4.40 VSM curves of (a) CC0.4/IO-R and (b) CS0.3/IO-HT100 nanocomposites

Moreover, the CC0.4/IO-R nanocomposite had higher thermal stability than the other because it degraded in two major stages at 252.9°C and 412.3°C as shown in Fig. 4.41(N₂) related to the degradations of CC templates and CC templates which had the interfacial interaction with the embedded magnetite-maghemite nanocrystals, respectively. Meanwhile, the CS0.3/IO-HT100 nanocomposite showed only one stage of degradation at T_d values of 255.6°C. Besides, the content of degraded chitosan in CC0.4/IO-R nanocomposite was approximately 67%, in which it is about five times higher than that of 14% of CS0.3/IO-HT100 nanocomposite as shown in Fig. 4.41(O₂). The crosslinked chitosan network in the CC0.4/IO-R nanocomposite could limit the adsorption of Fe²⁺/Fe³⁺ ions through the constrained swelling, resulting in the high proportion of chitosan. The high proportion of chitosan matrix could be applied for loading some medicinal substances for cancer treatment; therefore, the CC0.4/IO-R nanocomposites have the potential to be hybrid materials for hyperthermia and drug-loading applications, as they had the specificity of target organs.

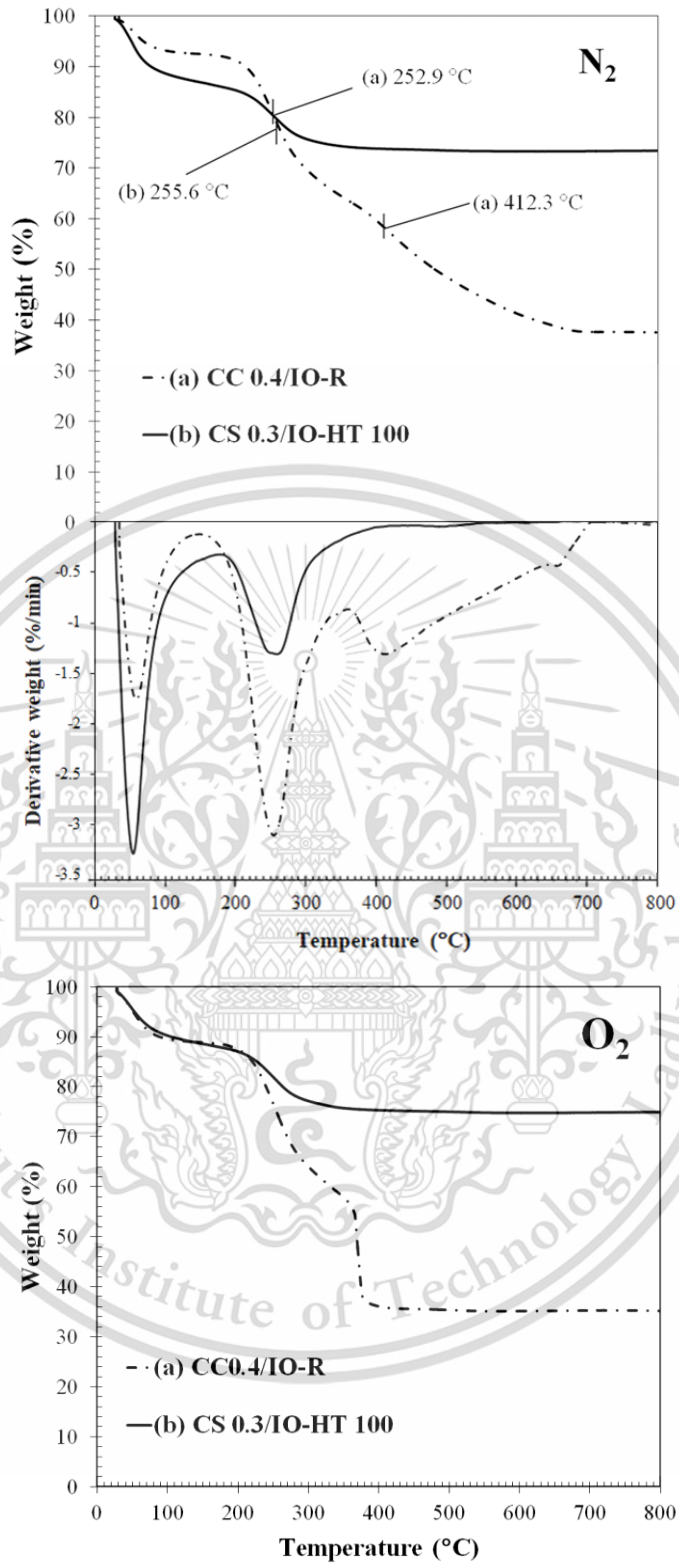
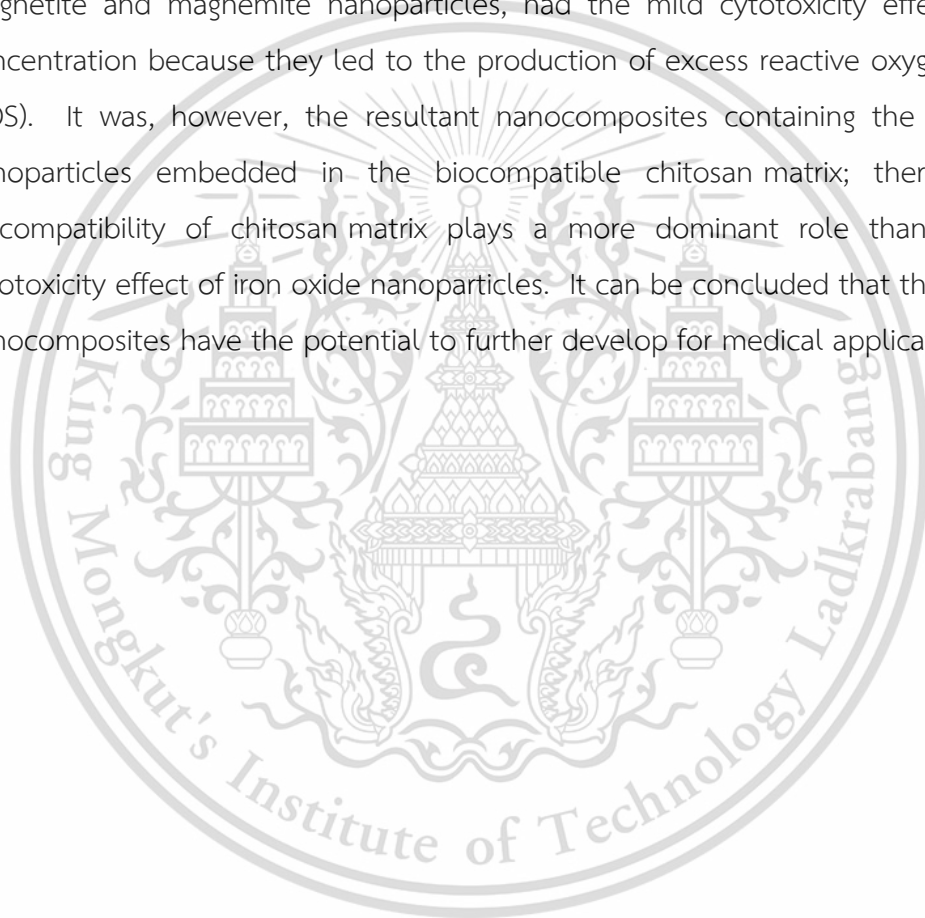


Figure 4.41 TGA thermograms of (a) CC0.4/IO-R and (b) CS0.3/IO-HT100 nanocomposites under N₂ and air zero atmosphere

4.5 Cell viability assays of CHI/IO nanocomposites

To assess the toxic behavior of the CC/IO nanocomposites to mammalian continuous cells, a preliminary study on the viability of African green monkey fibroblast (Vero) cells was performed. As shown in Table 4.2 and 4.4, most of all nanocomposites have cell viability in the range of 70–96%, indicating that they have high cell viability. All nanocomposites exhibit no toxic behavior. These findings supported the safety of CC/IO nanocomposites in mammalian continuous cells. Some researches [56, 70-71] reported that the iron oxide nanoparticles, such as magnetite and maghemite nanoparticles, had the mild cytotoxicity effect at high concentration because they led to the production of excess reactive oxygen species (ROS). It was, however, the resultant nanocomposites containing the iron oxide nanoparticles embedded in the biocompatible chitosan matrix; therefore, the biocompatibility of chitosan matrix plays a more dominant role than the mild cytotoxicity effect of iron oxide nanoparticles. It can be concluded that the resultant nanocomposites have the potential to further develop for medical applications.



Chapter 5

Conclusions and Suggestions

5.1 Conclusions

The chitosan/iron oxide nanocomposites (CHI/IO) were synthesized at low temperatures using an aqueous soft solution system. The tripolyphosphate crosslinked chitosan was used to control the particle size of iron oxide at the nano-level and prevent their agglomeration in order to maintain the superparamagnetic properties. The iron precursor ions were trapped in the crosslinked chitosan network and then heat treated in NaOH solution, leading to the formation of iron oxide nanoparticles embedded in crosslinked chitosan matrix. The magnetite-maghemite nanocrystals obtained in the resultant CHI/IO nanocomposites were mammal safe. The proposed synthesis systems were facile, low temperature hydrothermal and refluxing approaches that are soft solution eco-friendly and easy to scale up. The CHI/IO nanocomposites would demonstrate the synergistic effect of iron oxide nanocrystals and crosslinked chitosan matrix. The advantages of superparamagnetic nanoparticles were specificity to target organ and demagnetism after medical treatments. Therefore, they were considered to be the potential candidates for the hyperthermia applications.

5.1.1 *In-situ* synthesis

The CHI/IO nanocomposites were synthesized by using soft solution *in-situ* synthesis, i.e. hydrothermal and refluxing methods. These methods produced polycrystals of quasi-spherical shape having magnetite–maghemite crystalline phases distributed in a crosslinked chitosan matrix. The magnetite–maghemite nanocrystals in the nanocomposites synthesized by hydrothermal method ranged in size from 3.9–4.3 nm, while those of refluxing method were in the range of 2.8–3.9 nm. The pressurized hydrothermal system promoted the growth of iron oxide nanocrystals, leading to slightly larger crystallites, compared to the refluxing system. The magnetite–maghemite nanocrystals decreased in size with an increase of the crosslinking density in the chitosan matrix. The polycrystals of magnetite–maghemite

nanoparticles were caused by the constraining effect of the chitosan network on the growth of the nanocrystals. The resultant CHI/IO nanocomposites showed superparamagnetic behavior with low coercivity and magnetic remanence. Since the magnetite–maghemite particles formed in the CHI/IO nanocomposites had a single magnetic domain structure because they were smaller than the superparamagnetic critical radius. The CS0.3/IO-HT100 nanocomposite synthesized by the hydrothermal method at 100°C had an average 4.2 nm particle size and $M_{\max} = 14.5$ emu/g with the highest degree of crosslinking. Similarly, the M_{\max} value of CS0.3/IO-R nanocomposite synthesized by the refluxing method had 14.2 emu/g with an average particle size of 3.8 nm. The resultant CHI/IO nanocomposites were not toxic to healthy Vero cells; therefore, they have the potential to be further developed for medical applications.

5.1.2 Adsorption synthesis

The chitosan templates were crosslinked with 0.3, 0.4 and 0.5 %w/v of TPP crosslinker were utilized as the host materials for the nucleation and growth of iron oxide nanocrystals in hydrothermal and refluxing systems, resulting in the CC/IO nanocomposites. In the resultant nanocomposites, the hydrothermal and refluxing forms of iron oxide nanocrystals were detected as quadrilateral shaped magnetite–maghemite nanocrystals embedded in the CC matrix. The increase of TPP concentrations resulted in the increase of non-uniform crosslinked CC templates with higher free volume, leading to the formation of larger magnetite–maghemite nanocrystals in the CC/IO nanocomposites. The average crystallite sizes of magnetite–maghemite nanocrystals in the CC/IO nanocomposites were in the range of 10–14 nm, in which they were three times larger than those of CHI/IO nanocomposites prepared by *in-situ* synthesis, corresponding to the sharper XRD pattern. Furthermore, magnetite–maghemite nanocrystals hydrothermally grown in the CC/IO nanocomposites had a smaller crystallite size but a wider size distribution than those obtained by refluxing. The resultant CC/IO nanocomposites exhibited superparamagnetic behavior with M_{\max} values in the range of 8.6–15.2 emu/g. The hysteresis curve of the CC/IO nanocomposites was more obvious S-shape than CHI/IO nanocomposites from *in-situ* synthesis due to the larger size of iron oxide nanoparticle, resulting in the rapidly magnetize and demagnetize. Besides, all

nanocomposites demonstrated high cell viability, ranging from 80 to 89%, indicating that they were safe for mammals. The chitosan contents of CC/IO nanocomposites were in the range of 53–67%, in which they were about five times more than those of CHI/IO nanocomposites from *in-situ* synthesis. The high chitosan content in CC/IO nanocomposites could improve biocompatibility. Furthermore, the chitosan matrix could be modified for alternative medical treatments such as drug delivery, bioseparation, cell labeling, and hyperthermia. Because of their hybrid functions, the synthesized CC/IO nanocomposites are a promising candidate for improving the optimization of medical therapies.

5.1.3 Comparison of *in-situ* and adsorption syntheses

The CS0.3/IO-HT100 nanocomposite synthesized by the *in-situ* method was compared to the CC0.4/IO-R nanocomposites synthesized by the adsorption method because they were representatives with the highest M_{\max} values and thermal stabilities among all resultant nanocomposites. The iron oxide nanocrystals in both nanocomposites were composed of magnetite and maghemite phases. However, the nanocrystal shapes in both nanocomposites were different, in which the CC0.4/IO-R and CS0.3/IO-HT100 nanocomposites had a quadrilateral and irregular spherical shapes, respectively. The crystallize size of magnetite-maghemite nanocrystals in CC0.4/IO-R nanocomposite (11.2 nm) was approximately three times larger than the nanocrystals of CS0.3/IO-HT100 nanocomposite (3.9 nm). Although the magnetite-maghemite nanocrystals in the CC0.4/IO-R nanocomposite had a larger particle size than those in the CS0.3/IO-HT100 nanocomposite, their quantity was less. The M_{\max} values of both nanocomposites were similar (15 emu/g) because the M_{\max} value of the iron oxide nanocrystals in the nanocomposites increased with their particle size and quantity. However, the hysteresis curve of CC0.4/IO-R nanocomposite had a more obvious S-shape than that of CS0.3/IO-HT100 nanocomposite. This result demonstrated the obvious superparamagnetic property of CC0.4/IO-R nanocomposite, with rapid magnetization and demagnetization. Besides, the CC0.4/IO-R nanocomposite had higher thermal stability and proportion of chitosan matrix than the CS0.3/IO-HT100 nanocomposite. The content of degraded chitosan in the CC0.4/IO-R nanocomposite (67%) was about five times

higher than the CS0.3/IO-HT100 nanocomposite (14%). The high proportion of chitosan matrix in the CC0.4/IO-R nanocomposite could be applied for loading some medicinal substances for cancer treatment; therefore, the CC0.4/IO-R nanocomposites have the potential to be hybrid materials for hyperthermia and drug-loading applications.

5.2 Suggestions

- These synthesis methods should be further studied for the various pH values in chitosan-TPP crosslinking because TPP can dissociate into the various forms of TPP ions, i.e. $\text{P}_3\text{O}_{10}^{5-}$, $\text{HP}_3\text{O}_{10}^{4-}$, $\text{H}_2\text{P}_3\text{O}_{10}^{3-}$, $\text{H}_3\text{P}_3\text{O}_{10}^{2-}$, $\text{H}_4\text{P}_3\text{O}_{10}^{-}$, depending on the pH values. The effect of these various forms of TPP ions on the crosslinking density of chitosan and the particle size of iron oxide nanocrystals in CHI/IO nanocomposites will be investigated.

- The ferrofluids based on synthesized CHI/IO nanocomposites should be further studied for hyperthermia treatment with the magnetic field amplitudes and ferrofluid concentrations being varied for the highest heating efficiency.

References

- [1] Ministry of Public Health. 2015. **Thai People Who Die from Cancer** [online]. Available : http://pr.moph.go.th/iprg/include/admin_hotnew/show_hotnew.php?idHot_new=70684.
- [2] Padma, V.V. 2015. "An Overview of Targeted Cancer Therapy." *Biomedicine*. 5(4) : 19.
- [3] Datta, N.R. Ordóñez, S.G. Gaipl, U.S. Paulides, M.M. Crezee, H. Gellermann, D.M. Puric, E. and Bodis, S. 2015. "Local Hyperthermia Combined with Radiotherapy and/or Chemotherapy: Recent Advances and Promises for the Future." *Cancer Treatment Reviews*. 41(9) : 742-753.
- [4] Hayashi, K. Maeda, K. Moriya, M. Sakamoto, W. and Yogo, T. 2012. "In Situ Synthesis of Cobalt Ferrite Nanoparticle/Polymer Hybrid from a Mixed Fe-Co Methacrylate for Magnetic Hyperthermia." *Journal of Magnetism and Magnetic Materials* 324(19) : 3158-3164.
- [5] Amiri, S. and Shokrollahi, H. 2013. "The Role of Cobalt Ferrite Magnetic Nanoparticles in Medical Science." *Materials Science and Engineering C* 33(1) : 1-8.
- [6] Simonsen, L.O. Harbak, H. and Bennekou, P. 2012. "Cobalt Metabolism and Toxicology—A Brief Update." *Science of the Total Environment* 432 : 210-215.
- [7] Lahiri, B.B. Muthukumar, T. and Philip, J. 2016. "Magnetic Hyperthermia in Phosphate Coated Iron Oxide Nanofluids." *Journal of Magnetism and Magnetic Materials* 407 : 101-113.
- [8] Gupta, A.K. and Gupta, M. 2005. "Synthesis and Surface Engineering of Iron Oxide Nanoparticles for Biomedical Applications." *Biomaterials* 26(18) : 3995-4021.
- [9] Araújo-Neto, R.P. Silva-Freitas, E.L. Carvalho, J.F. Pontes, T.R.F. Silva, K.L. Damasceno, I.H.M. Egito, E.S.T. Dantas, A.L. Morales, M.A. Carriço, A.S. 2014. "Monodisperse Sodium Oleate Coated Magnetite High Susceptibility Nanoparticles for Hyperthermia Applications." *Journal of Magnetism and Magnetic Materials* 364 : 72-79.

- [10] Nikitin, A. Khramtsov, M. Garanina., A. Mogilnikov, P. Sviridenkova, N. Shchetinin, I. Savchenko, A., Abakumov, M. and Majouga, A. 2019. "Synthesis of Iron Oxide Nanorods for Enhanced Magnetic Hyperthermia." *Journal of Magnetism and Magnetic Materials* 469 : 443-449.
- [11] Nemati, Z. Salili, S.M. Alonso, J. Ataie, A. Das, R. Phan, M.H. and Srikanth, H. 2017. "Superparamagnetic Iron Oxide Nanodiscs for Hyperthermia Therapy: Does Size Matter?" *Journal of Alloys and Compounds* 714 : 709-714.
- [12] Saeedi, M. Vahidi, O. and Bonakdar, S. 2017. "Synthesis and Characterization of Glycyrrhizic Acid Coated Iron Oxide Nanoparticles for Hyperthermia Applications." *Materials Science and Engineering C* 77 : 1060-1067.
- [13] Easo, S.L. and Mohanan, P.V. 2013. "Dextran Stabilized Iron Oxide Nanoparticles: Synthesis, Characterization and *In Vitro* Studies." *Carbohydrate Polymers* 92 (1) : 726-732.
- [14] Thomas, R.G. Moon, M.J. Lee, H. Sasikala, A.R.K. Kim, C.S. Park, I.K. and Jeong, Y.Y. 2015. "Hyaluronic Acid Conjugated Superparamagnetic Iron Oxide Nanoparticle for Cancer Diagnosis and Hyperthermia Therapy." *Carbohydrate Polymers* 131 : 439-446.
- [15] Gomathi, T. Prasad, P.S. Sudha, P.N. and Anil, S. 2017. "Size Optimization and *In Vitro* Biocompatibility Studies of Chitosan Nanoparticles." *International Journal of Biological Macromolecules* 104(B) : 1794-1806.
- [16] Qu, J. Liu, G. WANG, Y. and Hong, R. 2016. "Preparation of Fe₃O₄-Chitosan Nanoparticles Used for Hyperthermia." *Advanced Powder Technology* 21(4) : 461-467.
- [17] Soares, P.I.P. Machado, D. Laia, C. Pereira, L.C.J. Coutinho, J.T. Ferreira, I.M.M. Novo, C.M.M. and Borges, J.P. 2016. "Thermal and Magnetic Properties of Chitosan-Iron Oxide Nanoparticles." *Carbohydrate Polymers* 149 : 382-390.
- [18] Mora, V.Z. Gutiérrez, M.F. Gómez, A.G. Sanz, B. Román, J.S. Goya, G.F. Hernández, R. and Mijangos, C. 2017. "Chitosan Nanoparticles for Combined Drug Delivery and Magnetic Hyperthermia: From Preparation to *In Vitro* Studies." *Carbohydrate Polymers* 157 : 361-370.
- [19] Hemalatha, T. Prabu, P. Gunadharini, D.N. and Gowthaman, M.K. 2018. "Fabrication and Characterization of Dual Acting Oleyl Chitosan

Functionalised Iron Oxide/Gold Hybrid Nanoparticles for MRI and CT Imaging.” *International Journal of Biological Macromolecules* 112 : 250-257.

- [20] Castelló , J. Gallardo, M. Busquets, M.A. and Estelrich, J. 2015. “Chitosan (or Alginate)-Coated Iron Oxide Nanoparticles: A Comparative Study.” *Colloids and Surfaces A: Physicochemical and Engineering Aspects* 468 : 151-158.
- [21] Cornell, R.M. and Schwertmann, U. 2003. **The Iron Oxides : Structure, Properties, Reactions, Occurrences and Uses.** 2nd Edition. Weinheim : WILEY-VCH.
- [22] Baumgartner, J. Morin, G. Menguy, N. Gonzalez, T.P. Widdrat, M. Cosmidis, J. and Faivre, D. 2013. “Magnetotactic Bacteria form Magnetite from a Phosphate-Rich Ferric Hydroxide via Nanometric Ferric (Oxyhydr)oxide Intermediates.” *PNAS* 110(37) : 14883-14888.
- [23] Teja, A.S. and Koh, P.Y. 2009. “Synthesis, Properties, and Applications of Magnetic Iron Oxide Nanoparticles.” *Progress in Crystal Growth and Characterization of Materials* 55(1-2) : 22-45.
- [24] Fhaitakham, S. Plienklin, T. and Vaewbundit, S. 2014. “Synthesis of Magnetite-Chitosan Nanocomposites.” A Special Project of the Degree of Bachelor, King Mongkut’s Institute of Technology Ladkrabang.
- [25] Salazar-Alvarez, G. 2004. “Synthesis, Characterisation and Applications of Iron Oxide Nanoparticles.” Ph.D. Dissertation. KTH Royal Institute of Technology.
- [26] Rahdar, A. Taboada, P. Aliahmad, M. Hajinezhad, M.R. and Sadeghfar, F. 2018. “Iron Oxide Nanoparticles: Synthesis, Physical Characterization, and Intraperitoneal Biochemical Studies in *Rattus Norvegicus*.” *Journal of Molecular Structure* 1173 : 240-245.
- [27] Tiefenauer, L.X. 2007. “Magnetic Nanoparticles as Contrast Agents for Medical Diagnosis” 29(1)-29(16). in Vo-Dinh, T. **Nanotechnology in Biology and Medicine : Methods, Devices, and Applications.** Boca Raton : CRC Press.
- [28] Karimi, Z. Karami, L. and Shokrollahi, H. 2013. “Nano-Magnetic Particles Used in Biomedicine: Core and Coating Materials.” *Materials Science and Engineering C* 38 : 2465-2475.

- [29] Huitle, C.A.M. Jara, C.C. Lopez, M.C. and Quiroz, M.A. 2009. "Chitosan-Modified Glassy Carbon Electrodes: Electrochemical Behaviour as a Function of the Preparation Method and pH." *Canadian Journal of Analytical Sciences and Spectroscopy* 54(2) : 53-62.
- [30] Karimi, Z. Karimi, L. and Shokrollahi, H. 2013. "Nano-Magnetic Particles Used in Biomedicine: Core and Coating Materials." *Materials Science and Engineering C* 33 : 2465-2475.
- [31] Aranaz, I. Mengibar, M. Harris, R. Paños, I. Miralles, B. Acosta, N. Galed, G. and Heras, A. 2009. "Functional Characterization of Chitin and Chitosan." *Current Chemical Biology* 3(2) : 203-230.
- [32] Salazar, M.J.C. and Negrón, A.C.V. 2017. "Release of Anthocyanins from Chitosan Films Cross-linked with Sodium Tripolyphosphate." *Revista de la Sociedad Química del Perú* 83(1) : 115-125.
- [33] Bugnicourt, L. and Ladavière, C. 2016. "Interests of Chitosan Nanoparticles Ionically Cross-linked with Tripolyphosphate for Biomedical Applications." *Progress in Polymer Science* 60 : 1-17.
- [34] Pati, F. Adhikari, B. and Dhara, S. 2011. "Development of Chitosan-Tripolyphosphate Fibers through pH Dependent Ionotropic Gelation." *Carbohydrate Research* 346 : 2582-2588.
- [35] Rázga, F. Vnuková, D. Némethová, V. Mazancová, P. and Lacík, I. 2016. "Preparation of Chitosan-TPP Sub-Micron Particles: Critical Evaluation and Derived Recommendations." *Carbohydrate Polymers* 151 : 488-499.
- [36] Pant, A. and Negi, J.S. 2018. "Novel Controlled Ionic Gelation Strategy for Chitosan Nanoparticles Preparation Using TPP- β -CD Inclusion Complex." *European Journal of Pharmaceutical Sciences* 112 : 180-185.
- [37] Gierszewska, M. and Czubenko, J.O. 2016. "Chitosan-Based Membranes with Different Ionic Crosslinking Density for Pharmaceutical and Industrial Applications." *Carbohydrate Polymers* 153 : 501-511.
- [38] Yoshimura, M. 2006. "Soft Solution Processing: Concept and Realization of Direct Fabrication of Shaped Ceramics (Nano-Crystals, Whiskers, Films, and/or Patterns) in Solutions without Post-Firing." *Journal of Materials Science* 41 : 1299-1306.
- [39] Yoshimura, M. Han, K.S. and Suchanek, W. "Soft Solution Processing : Low-Energy
- This material is reserved for educational use only, not allowed for commercial use.

Direct Fabrication of Advanced Inorganic Materials.” *Bulletin of the Korean Chemical Society* 20(8) : 875-878.

- [40] Robertz, B. Boschini, F. Cloots, R. and Rulmont, A. 2001. “Importance of Soft Solution Processing for Advanced BaZrO₃ Materials.” *International Journal of Inorganic Materials* 3(8) : 1185-1187.
- [41] Laurent, S. Forge, D. Port, M. Roch, A. Robic, C. Elst, L.V. and Muller, R.N. 2008. “Magnetic Iron Oxide Nanoparticles: Synthesis, Stabilization, Vectorization, Physicochemical Characterizations, and Biological Applications.” *Chemical Reviews* 108(6) : 2064-2110.
- [42] Aditha, S.K. Kurdekar, A.D. Chunduri, L.A.A. Patnaik, S. and Kamiseti, V. 2016. “Aqueous Based Reflux Method for Green Synthesis of Nanostructures: Application in CZTS Synthesis.” *MethodsX* 3 : 35-42.
- [43] Mody, V.V. Singh, A. and Wesley, B. 2013. “Basics of Magnetic Nanoparticles for their Application in the Field of Magnetic Fluid Hyperthermia.” *European Journal of Nanomedicine* 5(1) : 11-21.
- [44] Abraham, J.P. 2012. “Nanoparticle Heat Transfer and Fluid Flow.” in Minkowycz, W.J. and Sparrow, E.M. **Advances in Numerical Heat Transfer**. Volume 4. 1st Edition. Boca Raton : CRC Press.
- [45] Wallyn, J. Anton, N. and Vandamme, T.F. 2019. “Synthesis Principles and Properties of Magnetite Nanoparticles for In-vivo Imaging Applications—a Review.” *Pharmaceutics* 601(11) : 11110601.
- [46] Beik, J. Abed, Z. Ghoreishi, F.S. Nami, S.H., Mehrzadi, S., Zadeh, A.S. and Kamrava, S.K. 2016. “Nanotechnology in Hyperthermia Cancer Therapy: From Fundamental Principles to Advanced Applications.” *Journal of Controlled Release* 235 : 205-221.
- [47] Ristic, M. Krehula, S. Reissner, M. Jean, M. Hannoyer, B. and Music, S. 2017. “Synthesis and Properties of Precipitated Cobalt Ferrite Nanoparticles.” *Journal of Molecular Structure* 1140 : 32-38.
- [48] Amirabadizadeh, A. Salighe, Z. Sarhaddi, R. and Lotfollahi, Z. 2017. “Synthesis of Ferrofluids Based on Cobalt Ferrite Nanoparticles: Influence of Reaction Time on Structural, Morphological and Magnetic Properties.” *Journal of Magnetism and Magnetic Materials* 434 : 78-85.
- [49] Cabuil, V. Dupuis, V. Talbot, D. and Neveu, S. 2011. “Ionic Magnetic Fluid Based

This material is reserved for educational use only, not allowed for commercial use.

on Cobalt Ferrite Nanoparticles: Influence of Hydrothermal Treatment on the Nanoparticle Size.” *Journal of Magnetism and Magnetic Materials* 323 : 1238-1241.

[50] Briceño, S. Suarez, J. and Gonzalez, G. 2017. “Solvothelmal Synthesis of Cobalt Ferrite Hollow Spheres with Chitosan.” *Materials Science and Engineering C* 78 : 842-846.

[51] de Lima, L.J. Brito, E.L. da Silva, R.B. Franco Jr, A. da Costa, J.A.P. de Vasconcelos, C.L. and Soares, J.M. 2017. “Magnetic Behavior in $\text{CoFe}_2\text{-CoFe}_2\text{O}_4$ Nanocomposites Obtained from Colloidal Synthesis Using Chitosan and Borohydride Reduction.” *Journal of Magnetism and Magnetic Materials* 444 : 378-382.

[52] Fazio, E. Santoro, M. Lentini, G. Franco, D. Guglielmino, S.P.P. and Neri, F. 2016. “Iron Oxide Nanoparticles Prepared by Laser Ablation: Synthesis, Structural Properties and Antimicrobial Activity.” *Colloids and Surfaces A: Physicochemical and Engineering Aspects* 490 : 98-103.

[53] Das, H. Sakamoto, N. Aono, H. Shinozaki, K. Suzuki, H. and Wakiya, N. 2015. “Investigations of Superparamagnetism in Magnesium Ferrite Nano-Sphere Synthesized by Ultrasonic Spray Pyrolysis Technique for Hyperthermia Application.” *Journal of Magnetism and Magnetic Materials* 392 : 91-100.

[54] Harraz, F.A. 2008. “Polyethylene Glycol-Assisted Hydrothermal Growth of Magnetite Nanowires : Synthesis and Magnetic Properties.” *Physica E* 40 : 3131-3136.

[55] Tran, H.V. Tran L.D. and Nguyen, T.N. 2010. “Preparation of Chitosan/Magnetite Composite Beads and their Application for Removal of Pb(II) and Ni(II) from Aqueous Solution.” *Materials Science and Engineering C* 30 : 304-310.

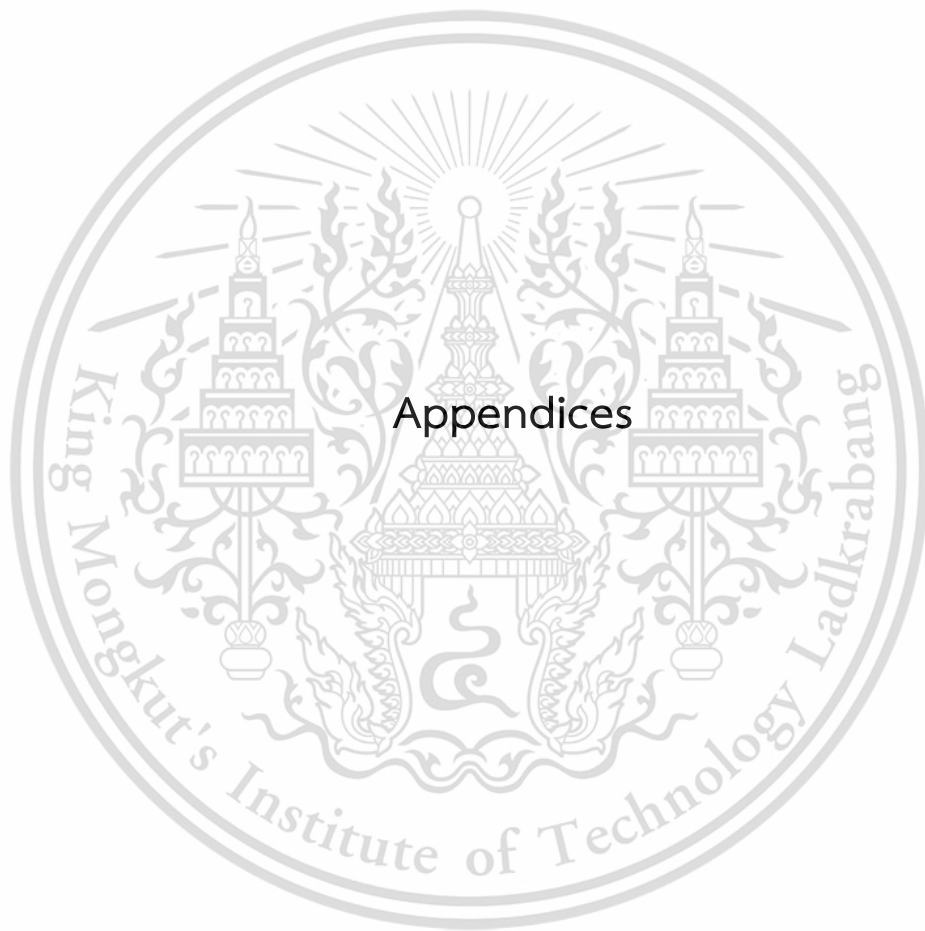
[56] Unsoy, G. Yalcin, S. Khodadust, R. Gunduz, G. and Gunduz, U. 2012. “Synthesis Optimization and Characterization of Chitosan-Coated Iron Oxide Nanoparticles Produced for Biomedical Applications.” *Journal of Nanoparticle Research* 14 : 964.

[57] Srisawat, T. Chumkaew, P. Heed-Chim, W. Sukpondma, Y. and Kanokwiroon, K. 2013. “Phytochemical Screening and Cytotoxicity of Crude Extracts of *Vatica Diospyroides* Symington Type LS.” *Tropical Journal of*

Pharmaceutical Research 12(1) : 71-76.

- [58] Miyazaki, T. Iwanaga, A. Shirozaki, Y. and Kawashita, M. 2019. "In situ Synthesis of Magnetic Iron Oxide Nanoparticles in Chitosan Hydrogels as a Reaction Field Effect of Cross-linking Density." *Colloids and Surfaces B: Biointerfaces* 179 : 334-339.
- [59] Ramimoghadam, D. Bagheri, S. and Hamid, S.B.A. 2014. "Progress in Electrochemical Synthesis of Magnetic Iron Oxide Nanoparticles." *Journal of Magnetism and magnetic materials* 368 : 207-229.
- [60] Nishida, N. Amagasa, S. Kobayashi, Y. and Yamada Y. 2016. "Synthesis of Superparamagnetic δ -FeOOH Nanoparticles by a Chemical Method." *Applied Surface Science* 387 : 996-1001.
- [61] Akbarzadeh, A. Samiei, M. and Davaran, S. 2012. "Magnetic Nanoparticles: Preparation, Physical Properties, and Applications in Biomedicine." *Nanoscale Research Letters* 7(1) : 144.
- [62] Bezdorozhev, O. Kolodiazhnyi, T. and Vasylykiv, O. 2017. "Precipitation Synthesis and Magnetic Properties of Self-Assembled Magnetite-Chitosan Nanostructures." *Journal of Magnetism and magnetic materials* 428 : 406-411.
- [63] Li, Q. Kartikowati, C.W. Horie, S. Ogi, T. Iwaki, T. and Okuyama, K. 2017. "Correlation Between Particle Size-Domain Structure and Magnetic Properties of Highly Crystalline Fe₃O₄ Nanoparticles." *Scientific Report* 7 : 9894.
- [64] Karade, V.C. Parit, S.B. Dawkar, V.V. Devan, R.S. Choudhary, R.J. Kedge, V.V. Pawar, N.V. Kim, J.H. and Chougale, A.D. 2019. "A Green Approach for the Synthesis of α -Fe₂O₃ Nanoparticles from *Gardenia Resinifera* Plant and its *In Vitro* Hyperthermia Application." *Heliyon* 5(7) : e02044.
- [65] Lanier, O.L. Korotych, O.I. Monsalve, A.G. Wable, D. Savliwala, S. and Grooms, N.W.F. 2019. "Evaluation of Magnetic Nanoparticles for Magnetic Fluid Hyperthermia." *International Journal of Hyperthermia* 36(1) : 686-700.
- [66] Bhumkar, D.R. and Pokharkar, V.B. 2006. "Studies on Effect of pH on Cross-linking of Chitosan with Sodium Tripolyphosphate: A Technical Note." *AAPS PharmSciTech* 7(2) : E138.

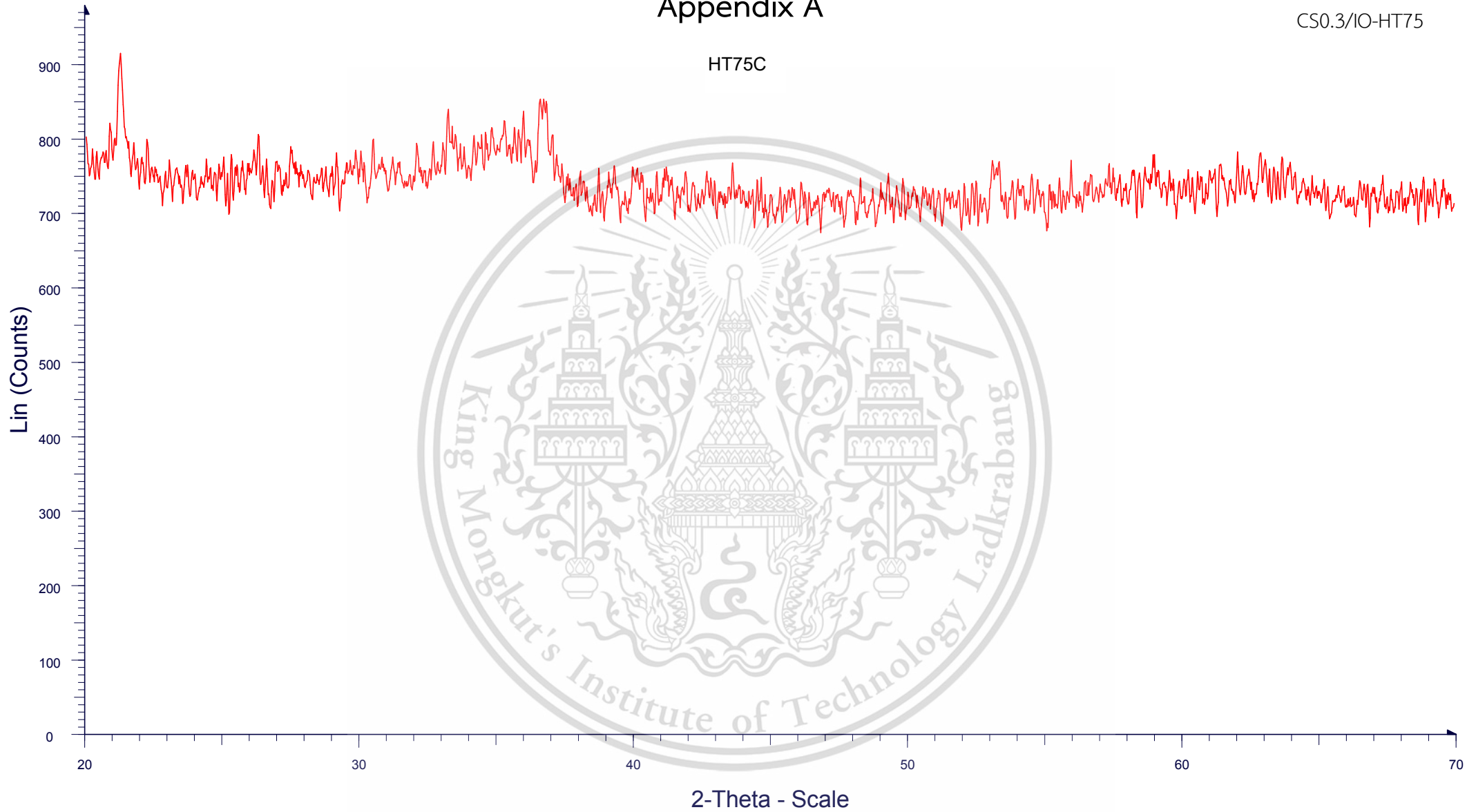
- [67] Freire, T.M. Dutra, L.M.U. Queiroz, D.C. Ricardo, N.M.P.S. Barreto, K. Denardin, J.C. Wurm, F.R. Sousa, C.P. Correia, A.N. de Lima-Neto, P. and Fachine, P.B.A. 2016. "Fast Ultrasound Assisted Synthesis of Chitosan-Based Magnetite Nanocomposites as a Modified Electrode Sensor." *Carbohydrate Polymers* 151 : 760-769.
- [68] Cruces, J.M. Roca, A.G. Ortega, A.L. Fantechi, E. del-Pozo-Bueno, D. Estradé, S. Peiró, F. Sepúlveda, B. Pineider, F. Sangregorio, C. and Nogues, J. 2019. "Precise Size Control of the Growth of Fe₃O₄ Nanocubes over a Wide Size Range Using a Rationally Designed One-Pot Synthesis." *ACS Nano* 13(7) : 7716-7728.
- [69] Rožič, B. Jagodič, M. Gyergyek, S. Drofenik, M. Kralj, S. Lahajnar, G. Jagličić, Z. and Kutnjak, Z. 2011. "Orientational Order-Magnetization Coupling in Mixtures of Magnetic Nanoparticles and the Ferroelectric Liquid Crystal." *Ferroelectrics* 410 : 37-41.
- [70] Valdiglesias, V. Kiliç, G. Costa, C. Bertólez, N.F. Pásaro, E., Teixeira, J.P. and Laffon, B. 2015. "Effects of Iron Oxide Nanoparticles: Cytotoxicity, Genotoxicity, Developmental Toxicity and Neurotoxicity." *Environmental and Molecular Mutagenesis* 56(2) : 125-148.
- [71] Zavisova, V. Koneracka, M. Kovac, J. Kubovcikova, M. Antal, I. Kopcansky, P. Bednarikova, M. and Muckova, M. 2015. "The Cytotoxicity of Iron Oxide Nanoparticles with Different Modifications Evaluated *In Vitro*." *Journal of Magnetism and magnetic materials* 380 : 85-89.



Appendix A

CS0.3/IO-HT75

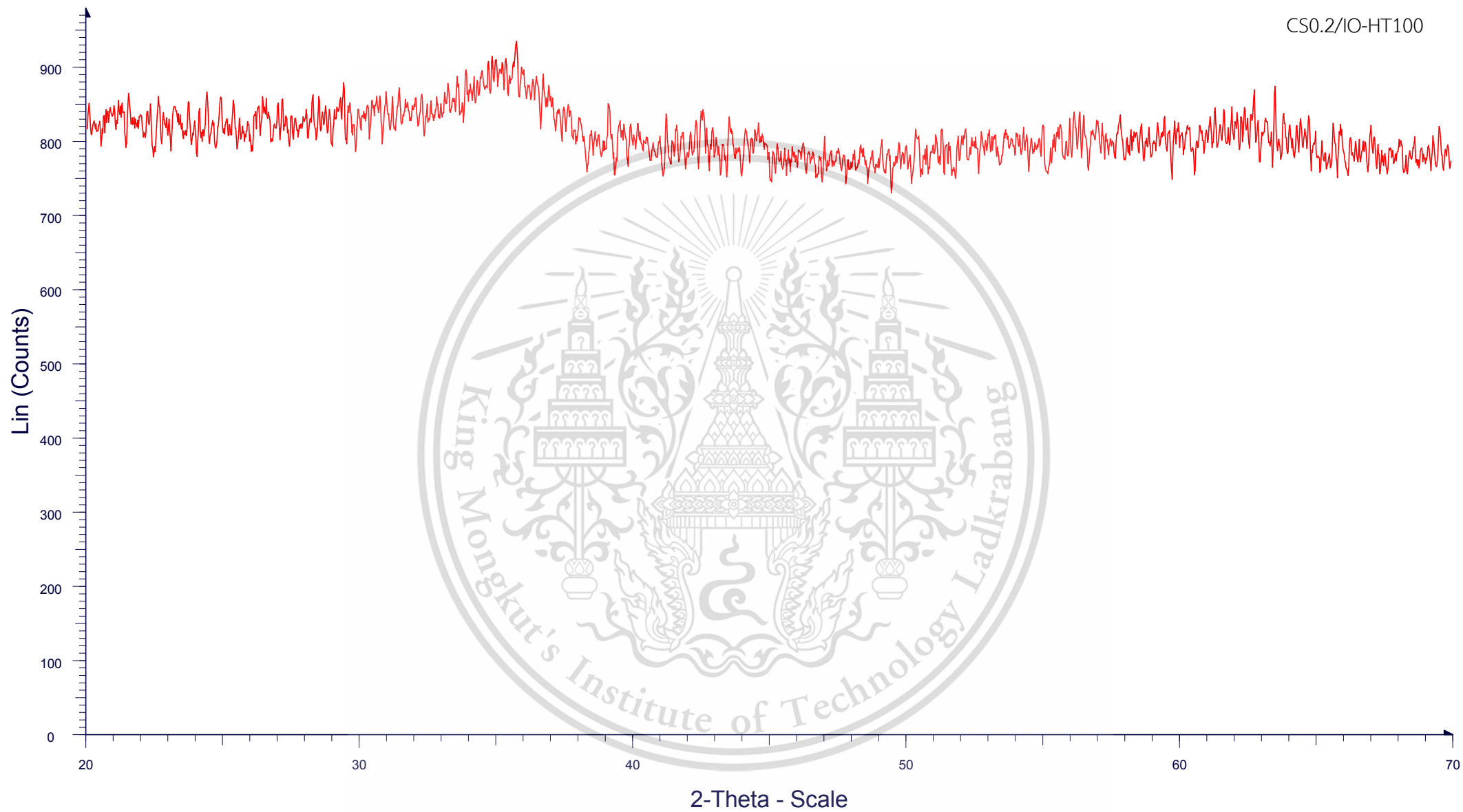
HT75C



File: 602802-0719_07.raw - Type: 2Th/Th locked - Start: 20.0000 ° - End: 70.0008 ° - Step: 0.0229 ° - Step time: 192.4 s - Temp.: 25 °C (Room)
Operations: Smooth 0.080 | Import

HT1

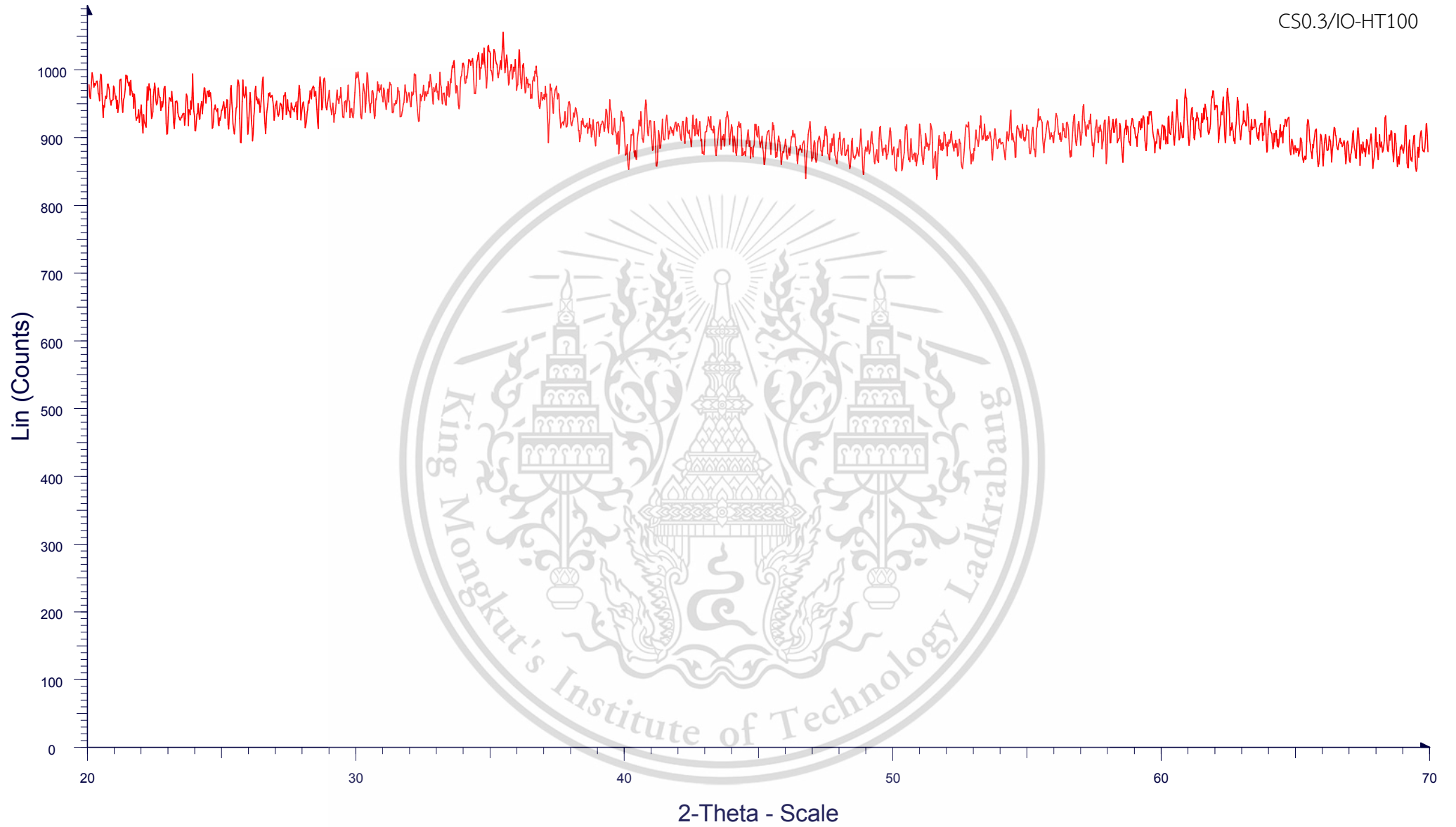
CS0.2/IO-HT100



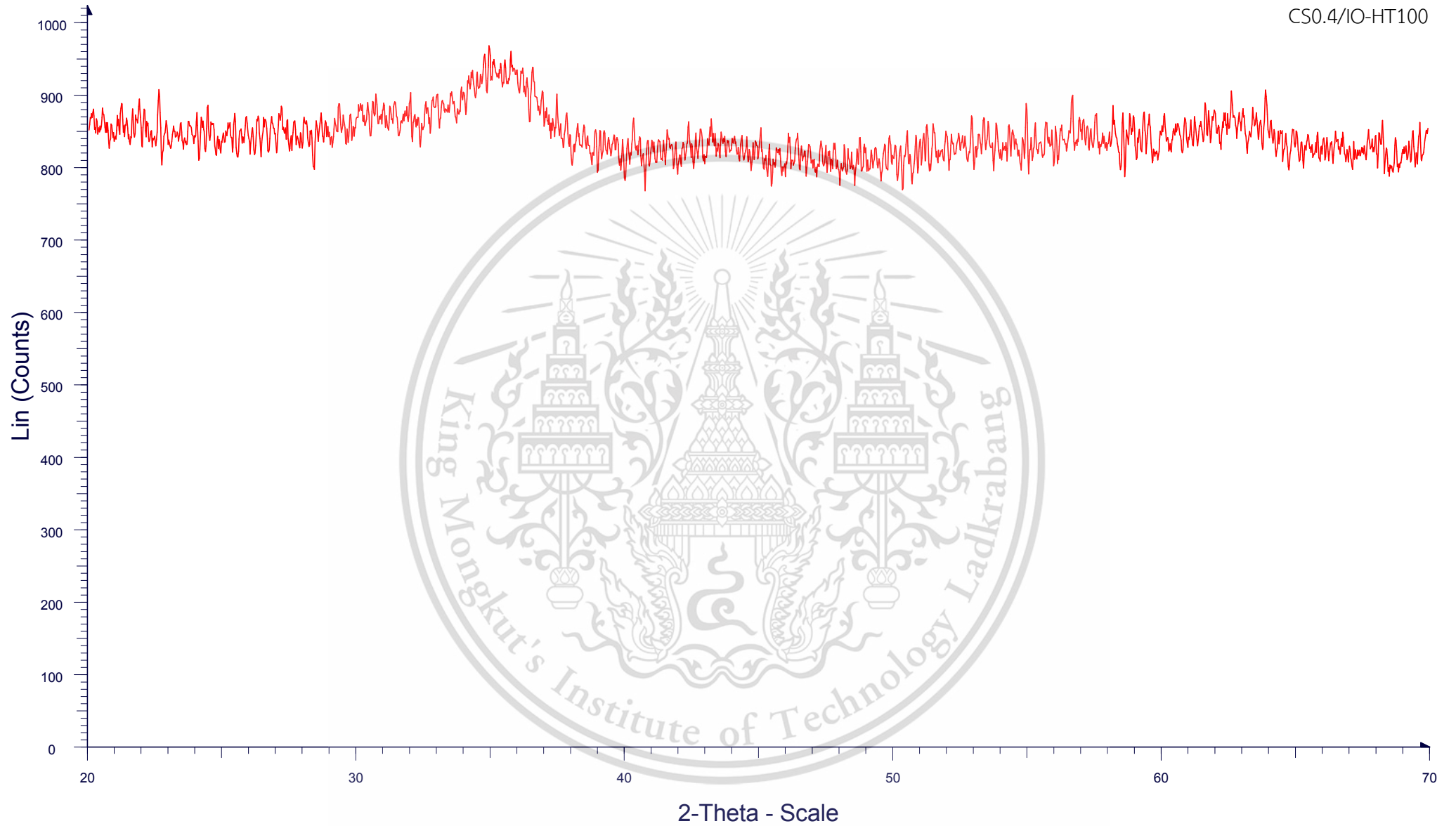
File: 602802-0719_06.raw - Type: 2Th/Th locked - Start: 20.0000 ° - End: 70.0008 ° - Step: 0.0229 ° - Step time: 192.4 s - Temp.: 25 °C (Room)
Operations: Smooth 0.080 | Import

HT 90 min

CS0.3/IO-HT100



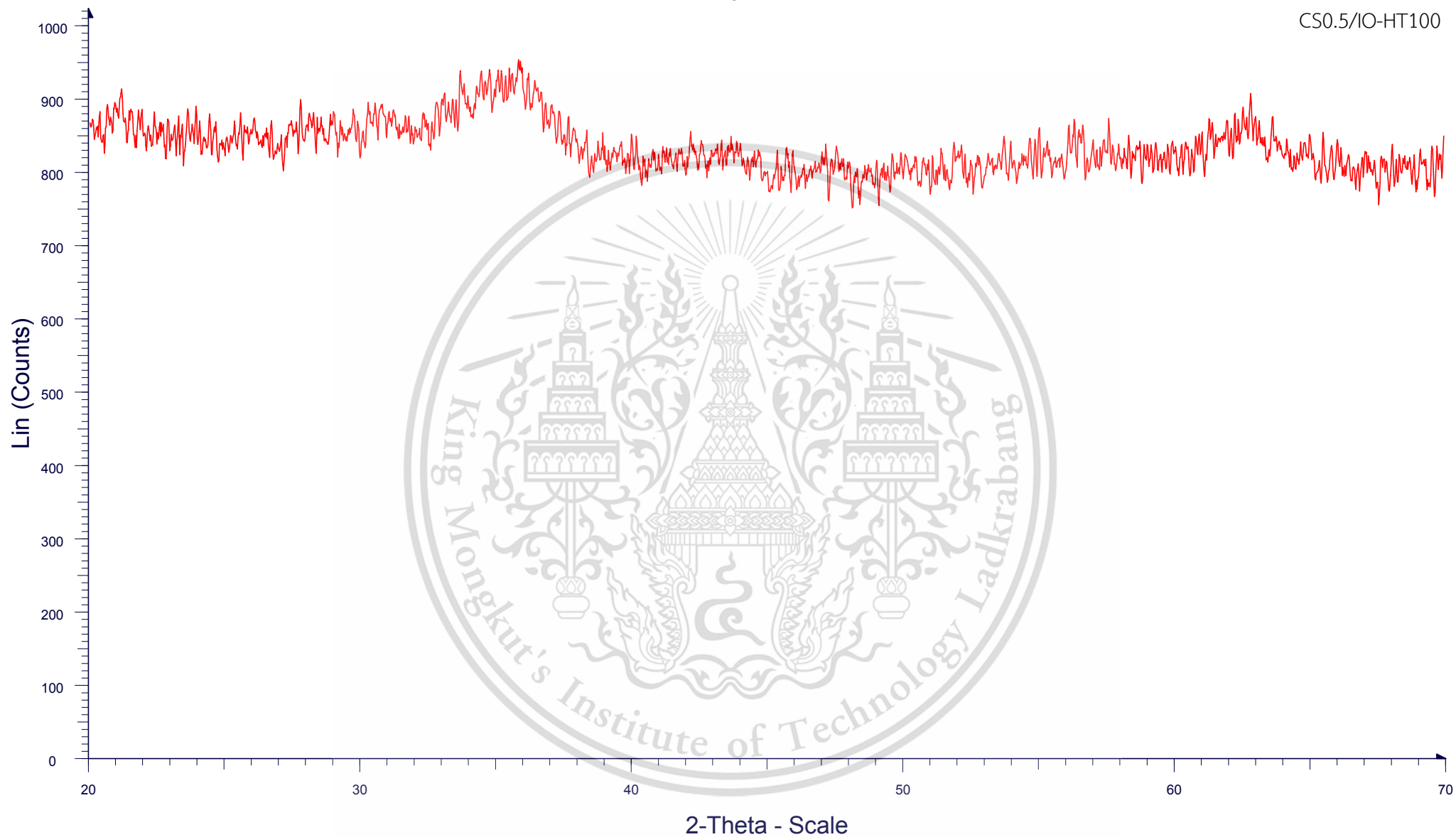
File: 590507-1251_05.raw - Type: 2Th/Th locked - Start: 20.0000 ° - End: 70.0008 ° - Step: 0.0229 ° - Step time: 192.4 s - Temp.: 25 °C (Room)
Operations: Smooth 0.080 | Import



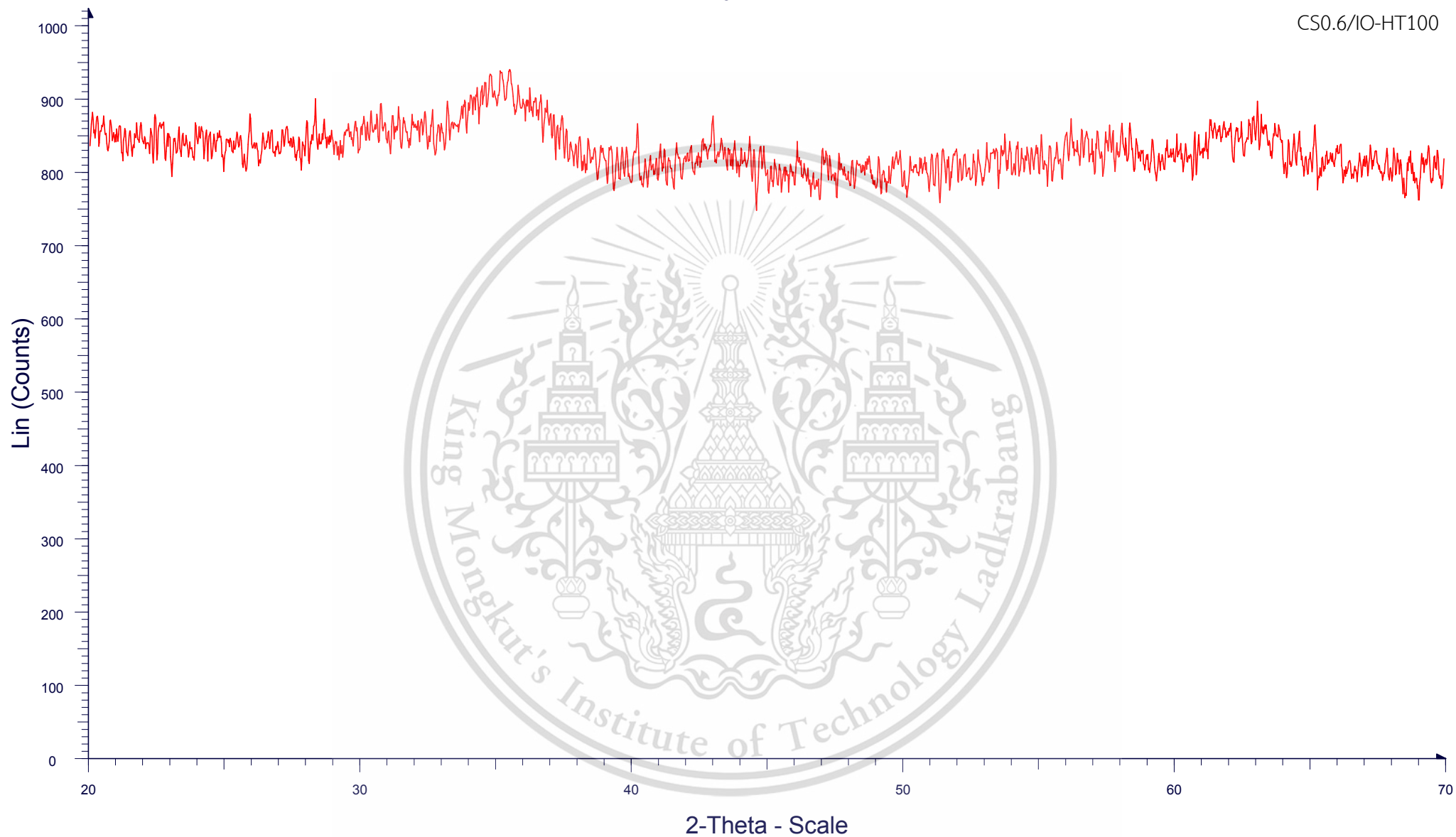
File: 590709-0375_02.raw - Type: 2Th/Th locked - Start: 20.0000 ° - End: 70.0008 ° - Step: 0.0229 ° - Step time: 192.4 s - Temp.: 25 °C (Room)
Operations: Smooth 0.080 | Import

2.5

CS0.5/IO-HT100



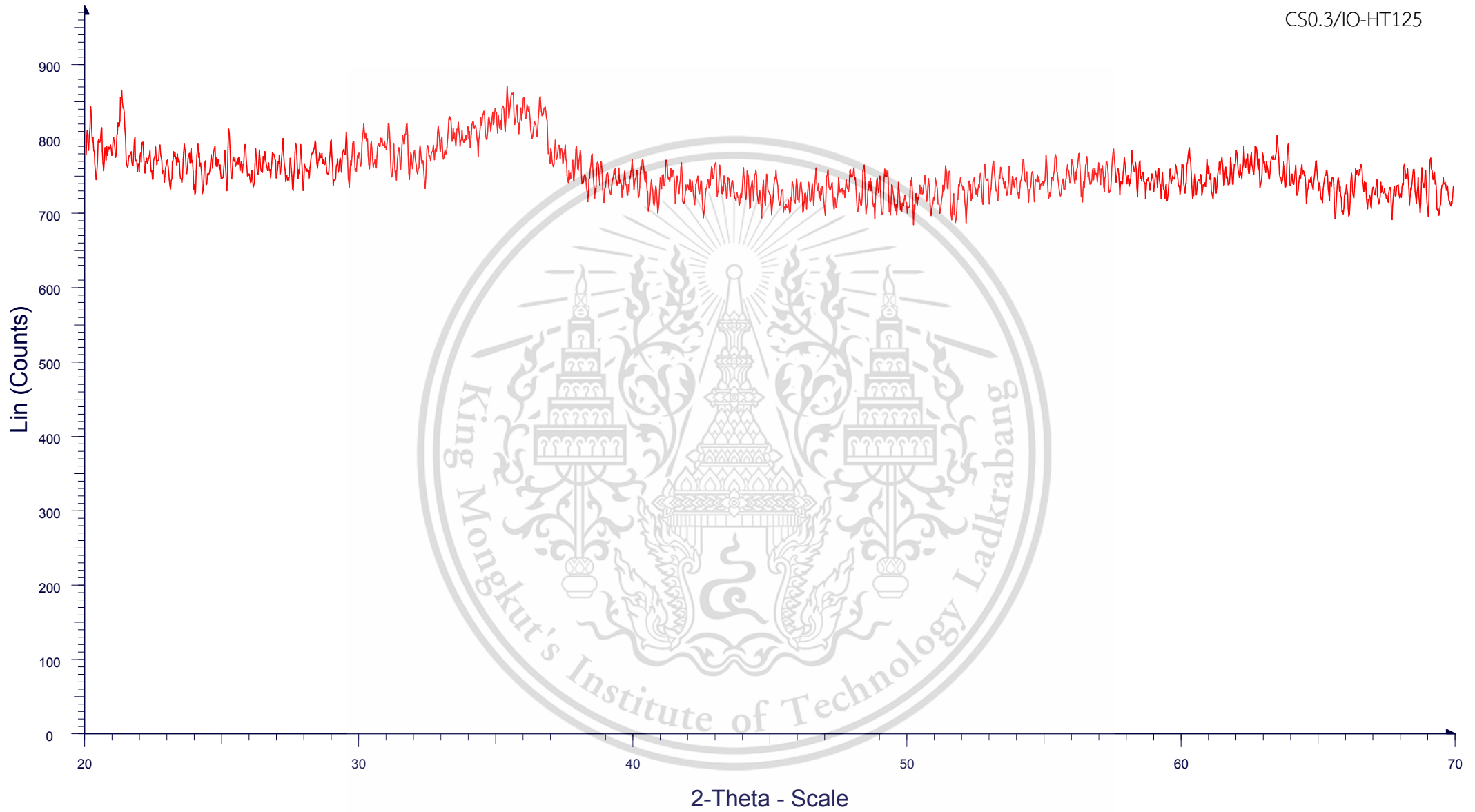
File: 590709-0375_03.raw - Type: 2Th/Th locked - Start: 20.0000 ° - End: 70.0008 ° - Step: 0.0229 ° - Step time: 192.4 s - Temp.: 25 °C (Room)
Operations: Smooth 0.080 | Import



File: 590709-0375_04.raw - Type: 2Th/Th locked - Start: 20.0000 ° - End: 70.0008 ° - Step: 0.0229 ° - Step time: 192.4 s - Temp.: 25 °C (Room)
Operations: Smooth 0.080 | Import

HT125C

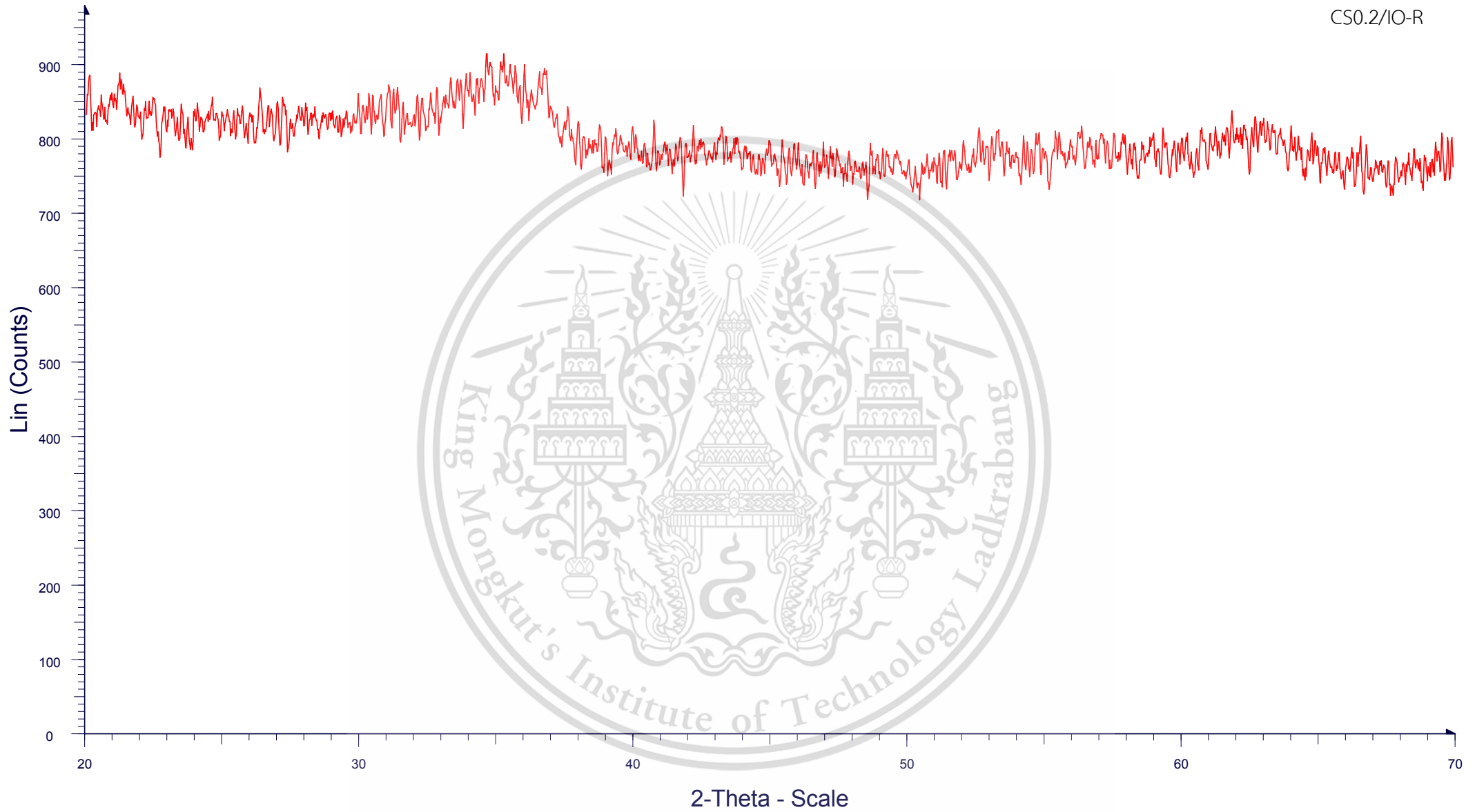
CS0.3/IO-HT125



File: 602802-0719_08.raw - Type: 2Th/Th locked - Start: 20.0000 ° - End: 70.0008 ° - Step: 0.0229 ° - Step time: 192.4 s - Temp.: 25 °C (Room)
Operations: Smooth 0.080 | Import

R1

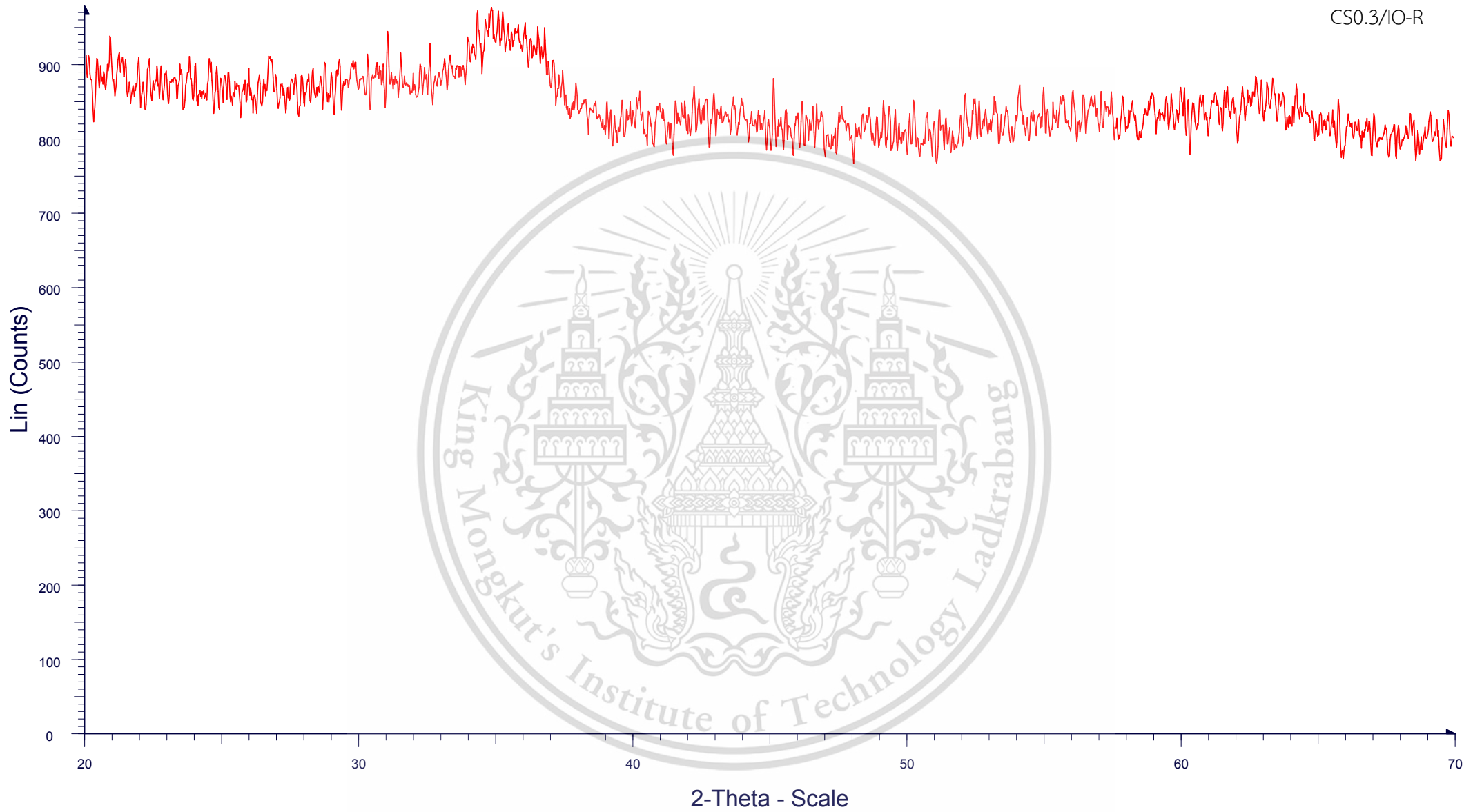
CS0.2/IO-R



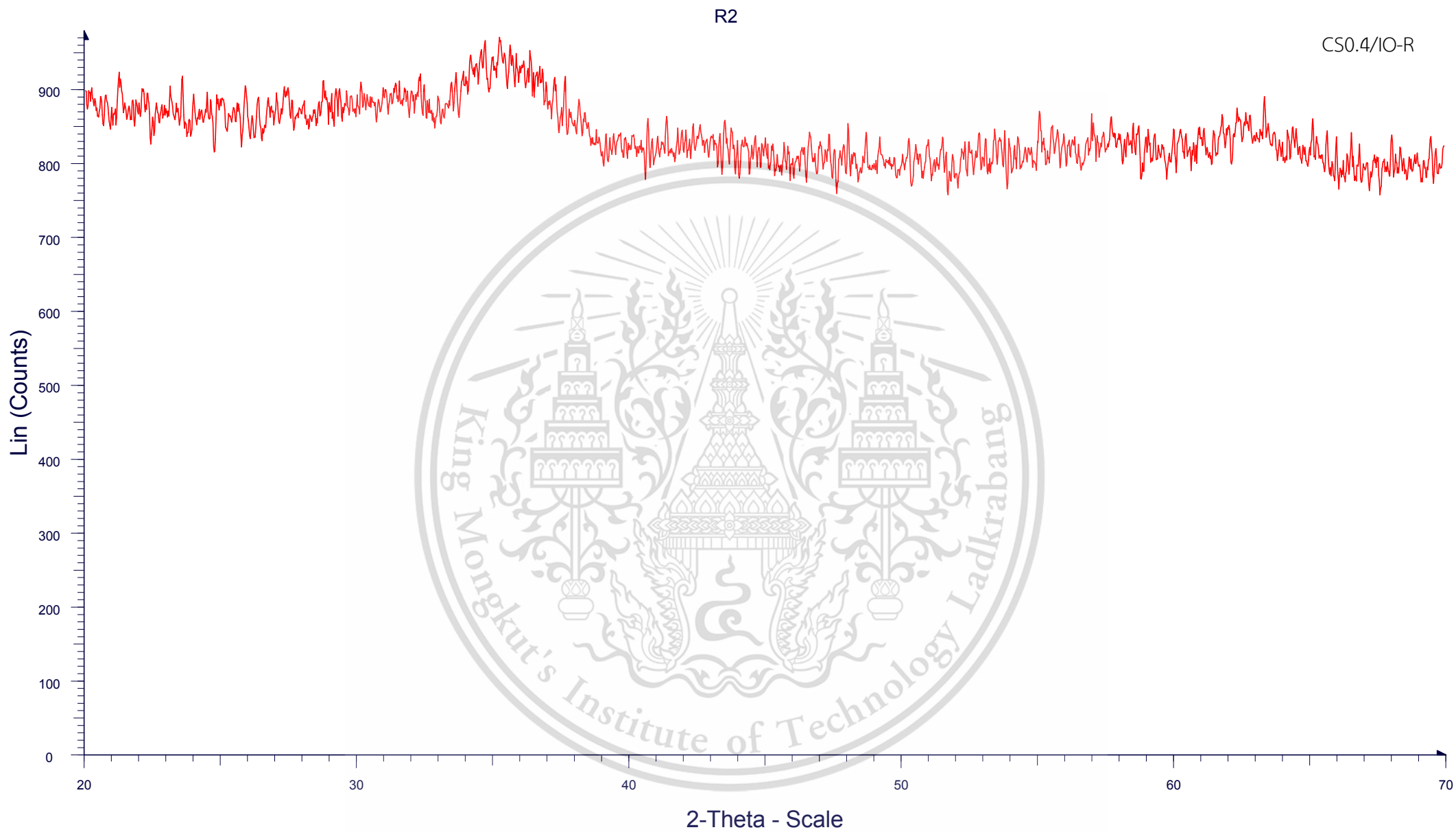
File: 602802-0719_01.raw - Type: 2Th/Th locked - Start: 20.0000 ° - End: 70.0008 ° - Step: 0.0229 ° - Step time: 192.4 s - Temp.: 25 °C (Room)
Operations: Smooth 0.080 | Import

R1.67

CS0.3/IO-R



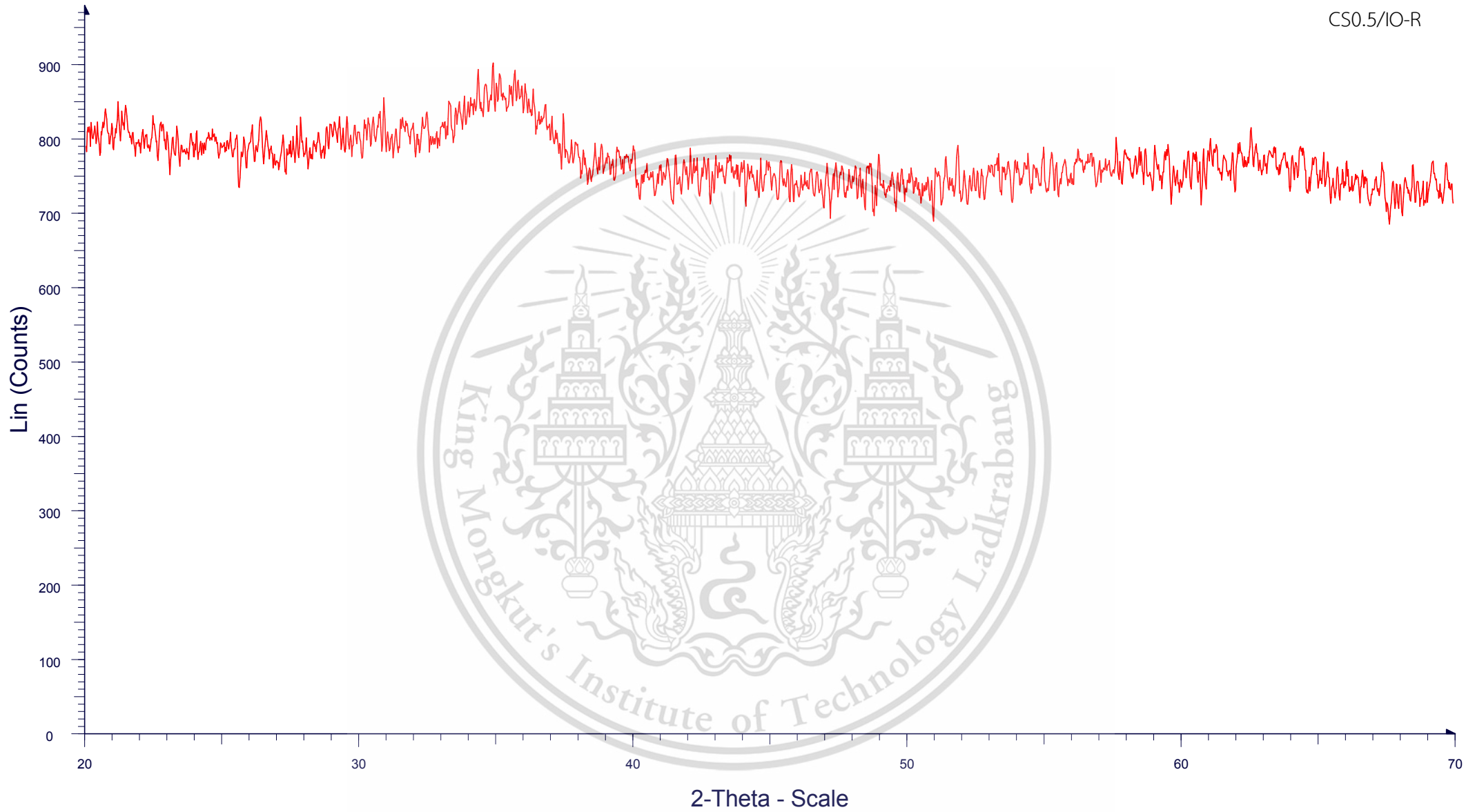
File: 602802-0719_02.raw - Type: 2Th/Th locked - Start: 20.0000 ° - End: 70.0008 ° - Step: 0.0229 ° - Step time: 192.4 s - Temp.: 25 °C (Room)
Operations: Smooth 0.080 | Import



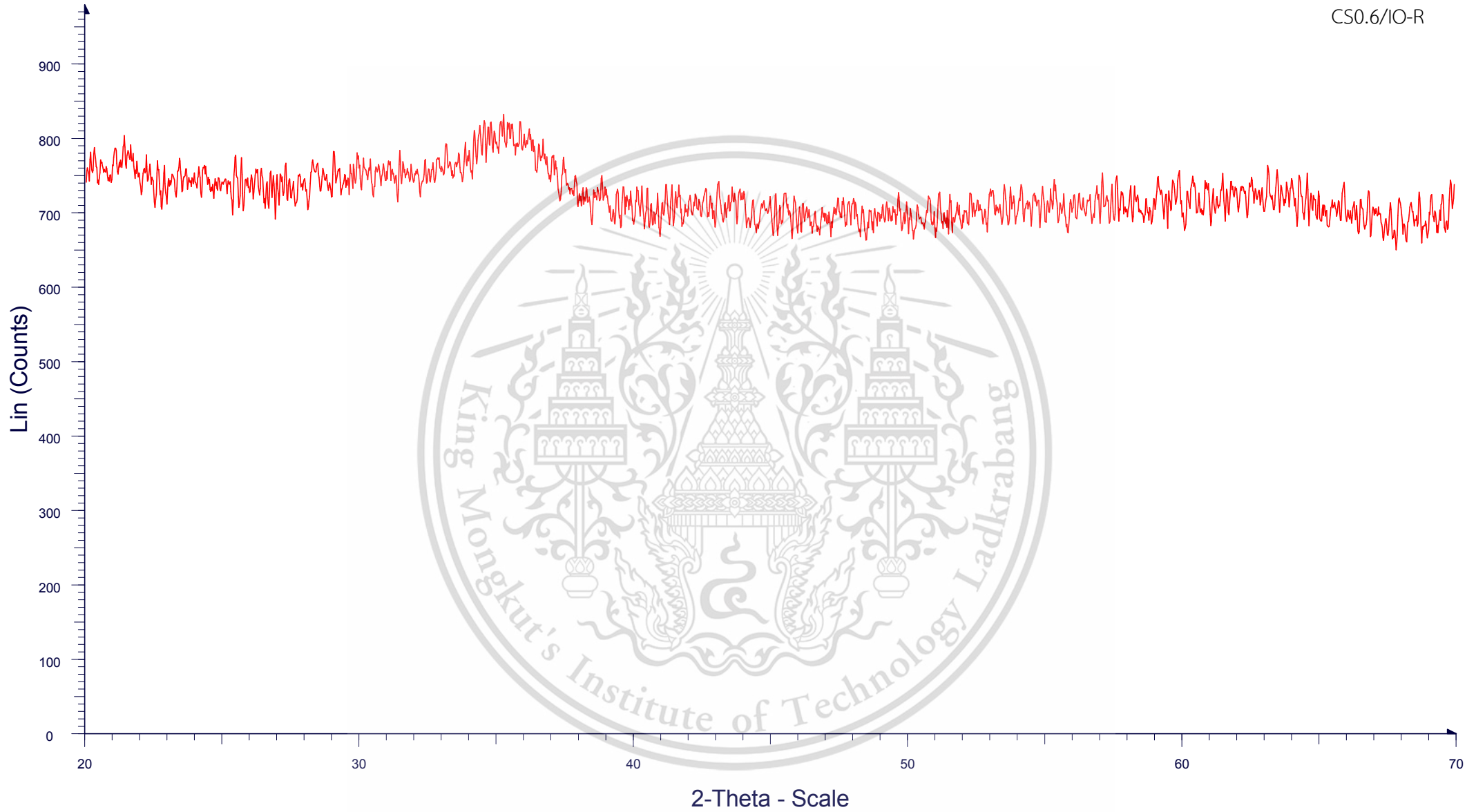
File: 602802-0719_03.raw - Type: 2Th/Th locked - Start: 20.0000 ° - End: 70.0008 ° - Step: 0.0229 ° - Step time: 192.4 s - Temp.: 25 °C (Room)
Operations: Smooth 0.080 | Import

R2.5

CS0.5/IO-R



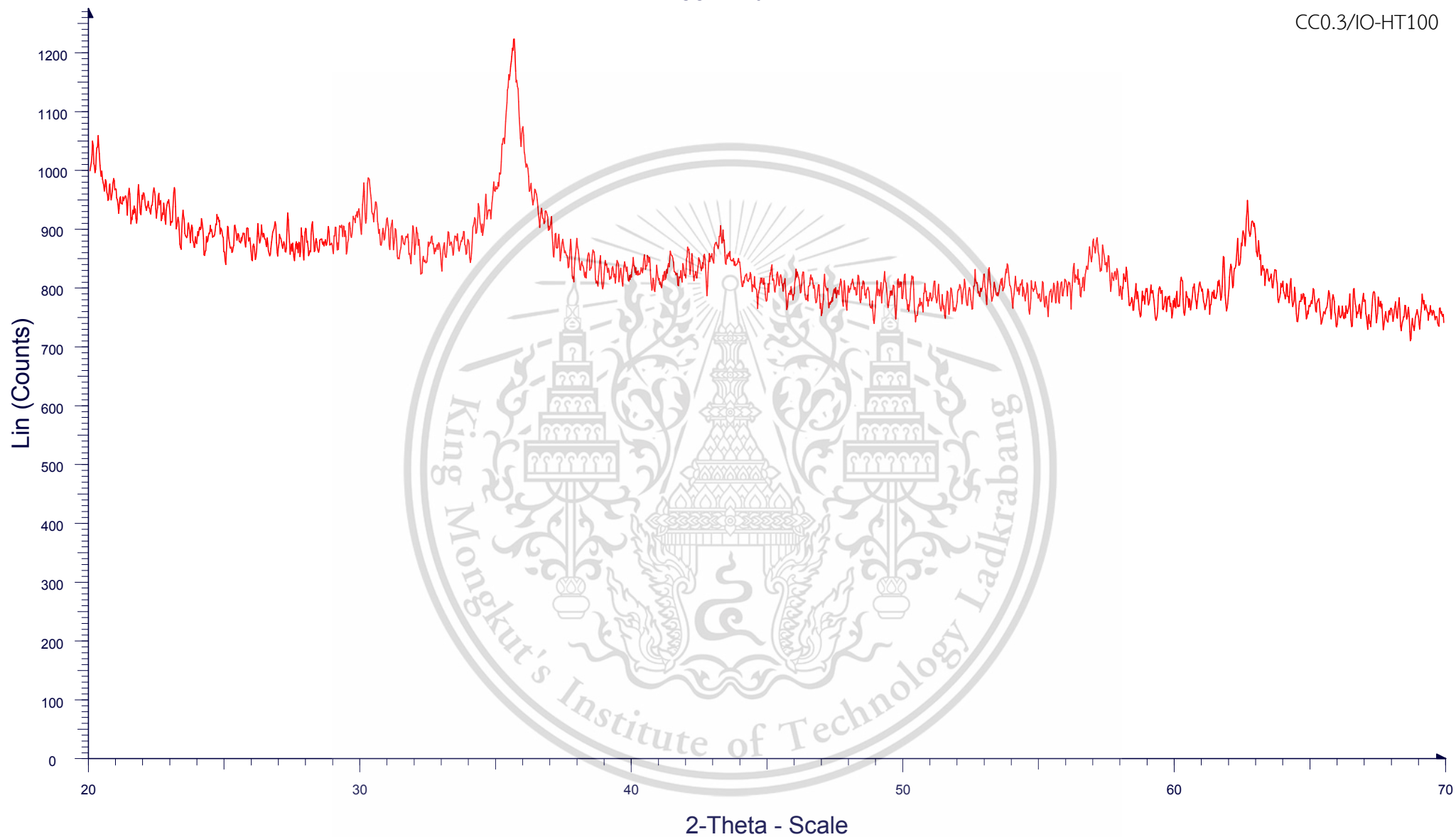
File: 602802-0719_04.raw - Type: 2Th/Th locked - Start: 20.0000 ° - End: 70.0008 ° - Step: 0.0229 ° - Step time: 192.4 s - Temp.: 25 °C (Room)
Operations: Smooth 0.080 | Import



File: 602802-0719_05.raw - Type: 2Th/Th locked - Start: 20.0000 ° - End: 70.0008 ° - Step: 0.0229 ° - Step time: 192.4 s - Temp.: 25 °C (Room)
Operations: Smooth 0.080 | Import

CCHT 1.67

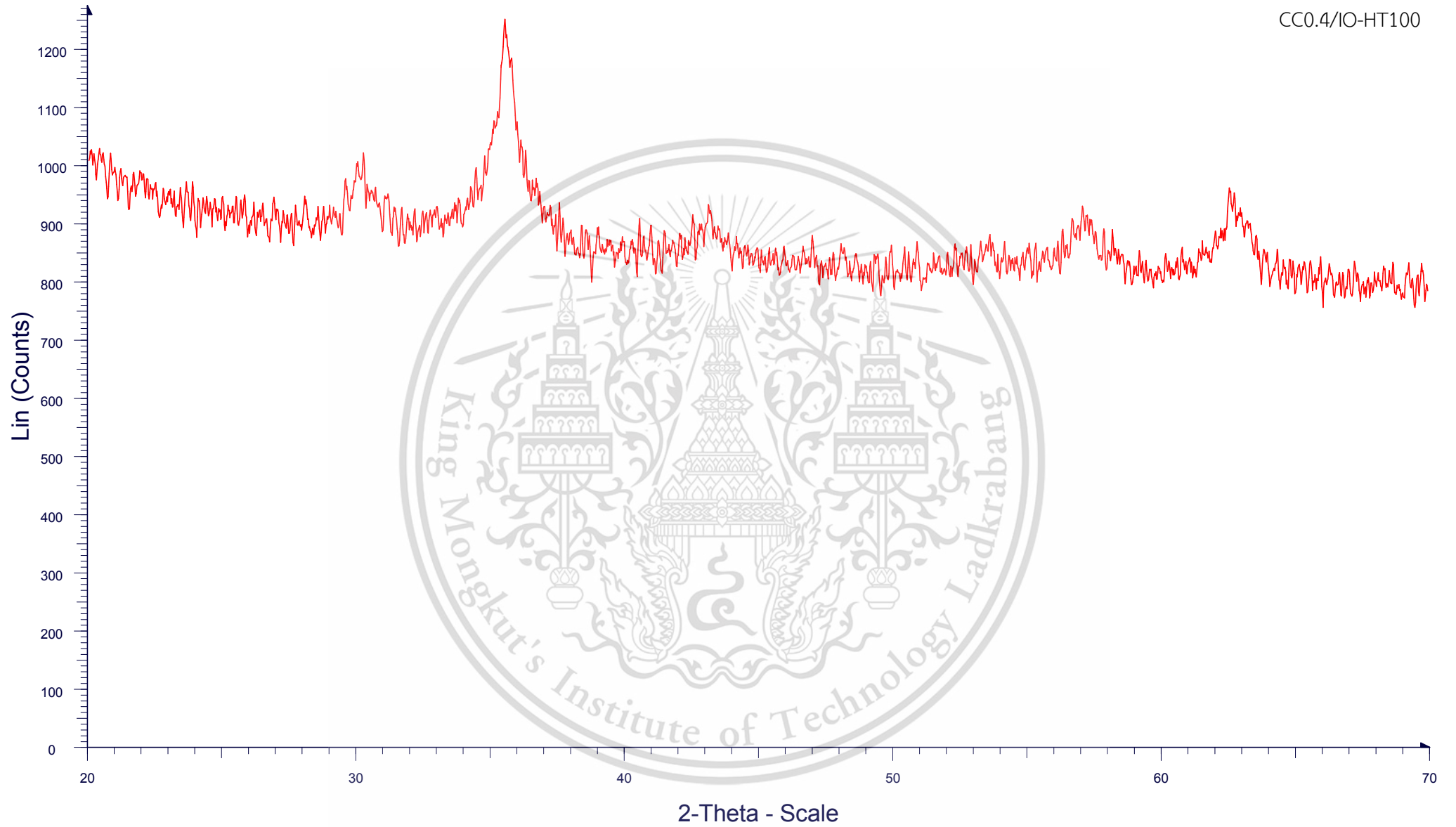
CC0.3/IO-HT100



File: 590709-0375_09.raw - Type: 2Th/Th locked - Start: 20.0000 ° - End: 70.0008 ° - Step: 0.0229 ° - Step time: 192.4 s - Temp.: 25 °C (Room)
Operations: Smooth 0.080 | Import

CCHT 2

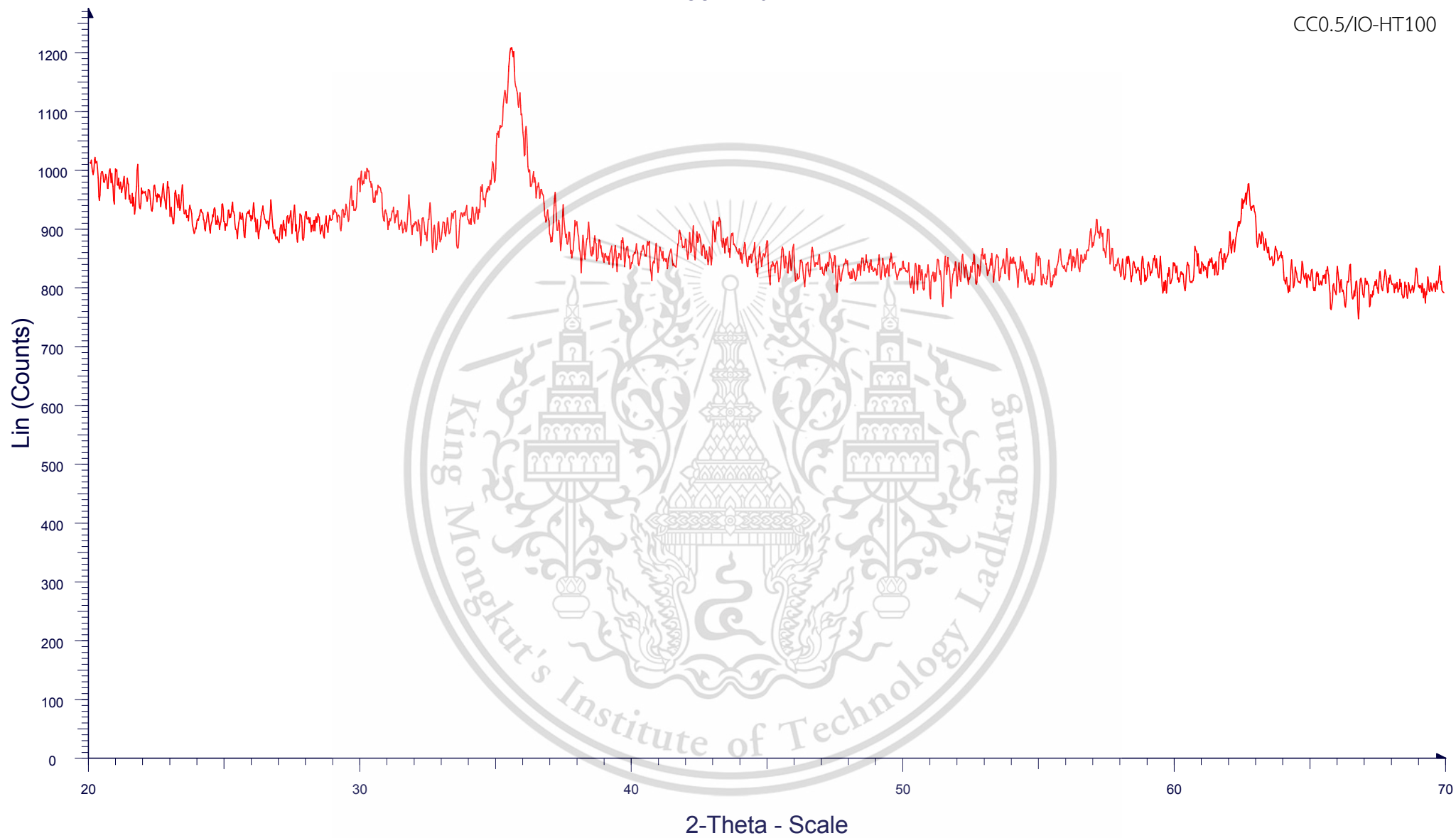
CC0.4/IO-HT100



File: 590709-0375_10.raw - Type: 2Th/Th locked - Start: 20.0000 ° - End: 70.0008 ° - Step: 0.0229 ° - Step time: 192.4 s - Temp.: 25 °C (Room)
Operations: Smooth 0.080 | Import

CCHT 2.5

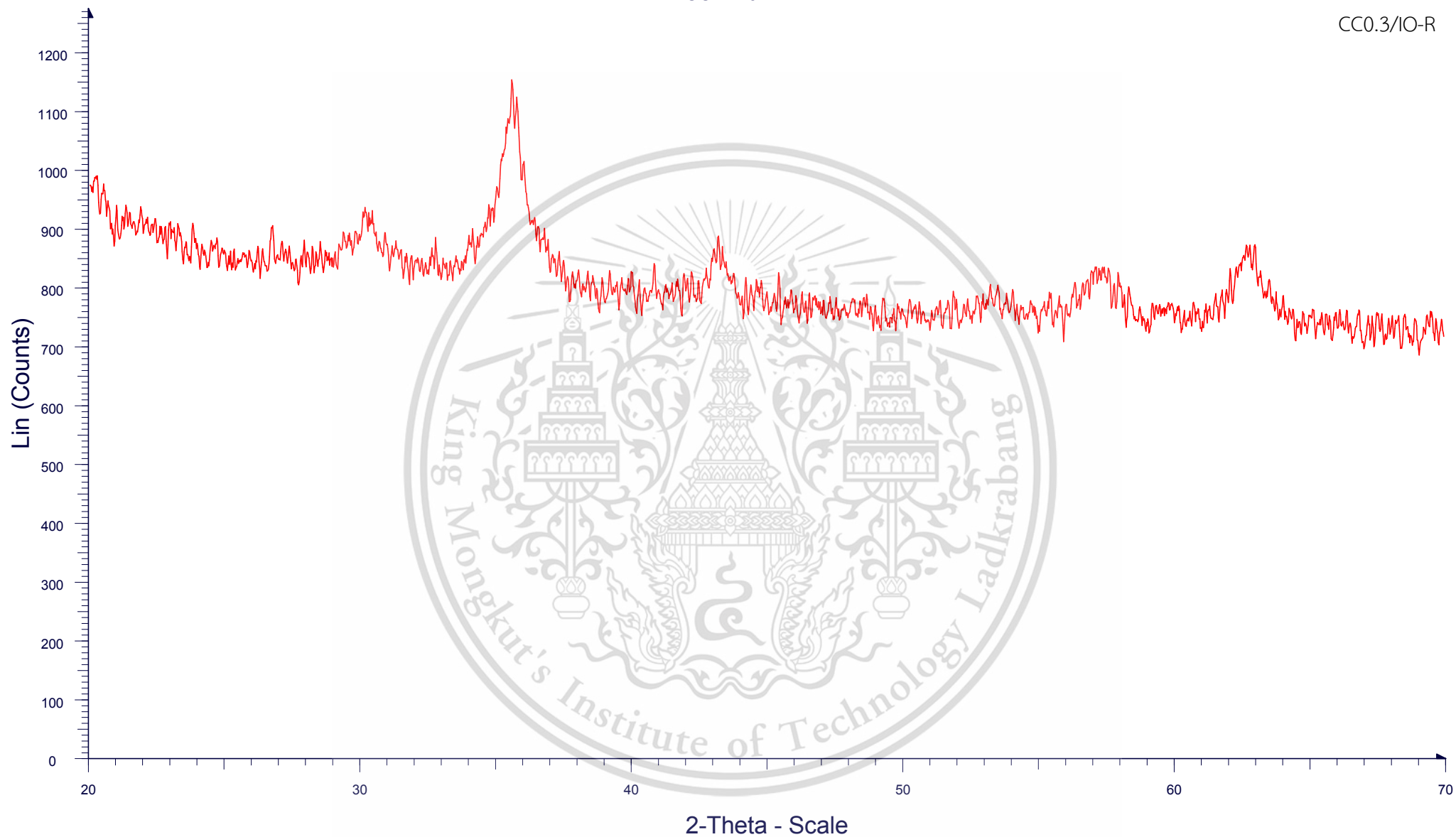
CC0.5/IO-HT100



File: 590709-0375_11.raw - Type: 2Th/Th locked - Start: 20.0000 ° - End: 70.0008 ° - Step: 0.0229 ° - Step time: 192.4 s - Temp.: 25 °C (Room)
Operations: Smooth 0.080 | Import

CCR 1.67

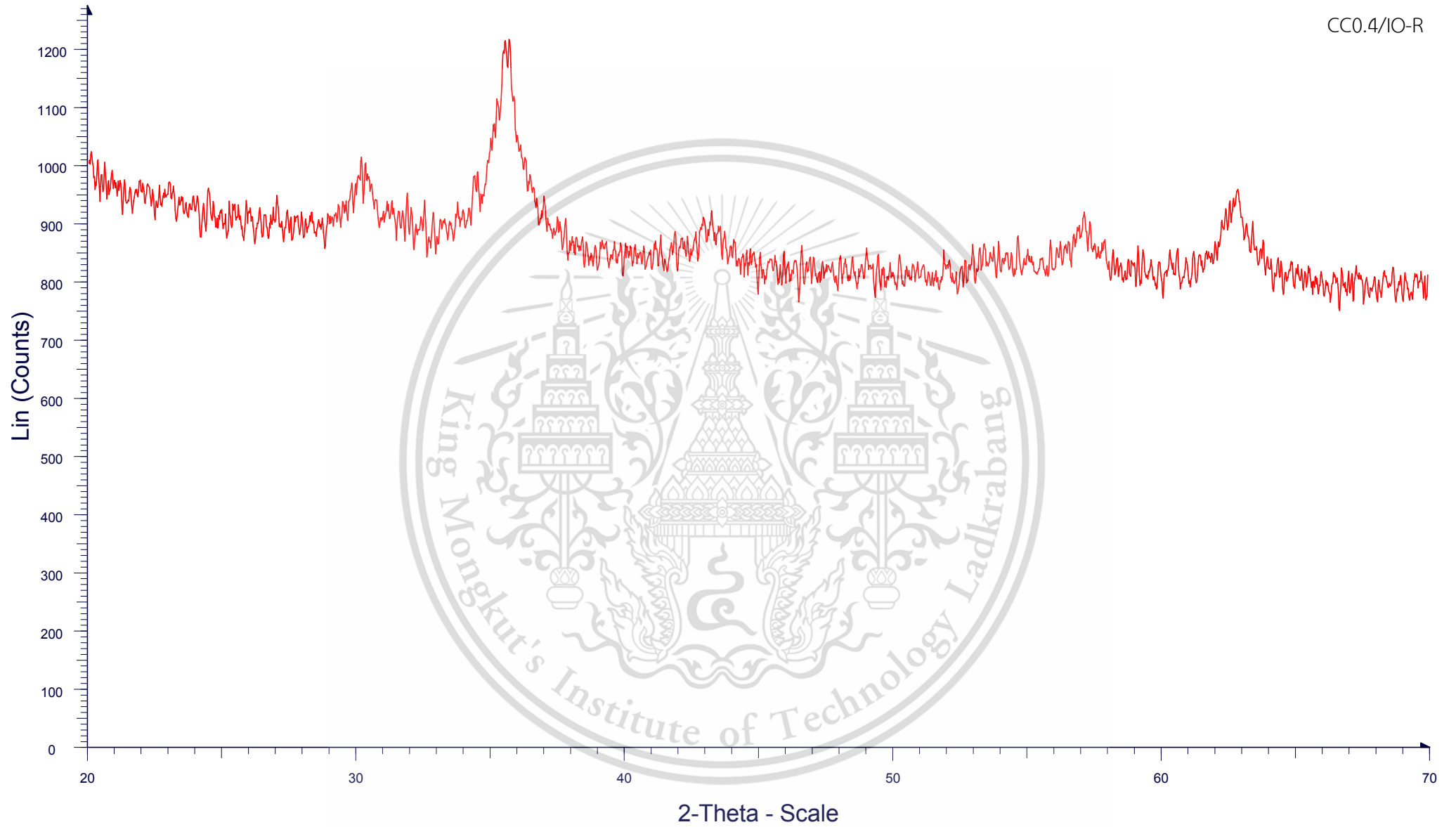
CC0.3/IO-R



File: 590709-0375_05.raw - Type: 2Th/Th locked - Start: 20.0000 ° - End: 70.0008 ° - Step: 0.0229 ° - Step time: 192.4 s - Temp.: 25 °C (Room)
Operations: Smooth 0.080 | Import

CCR 2

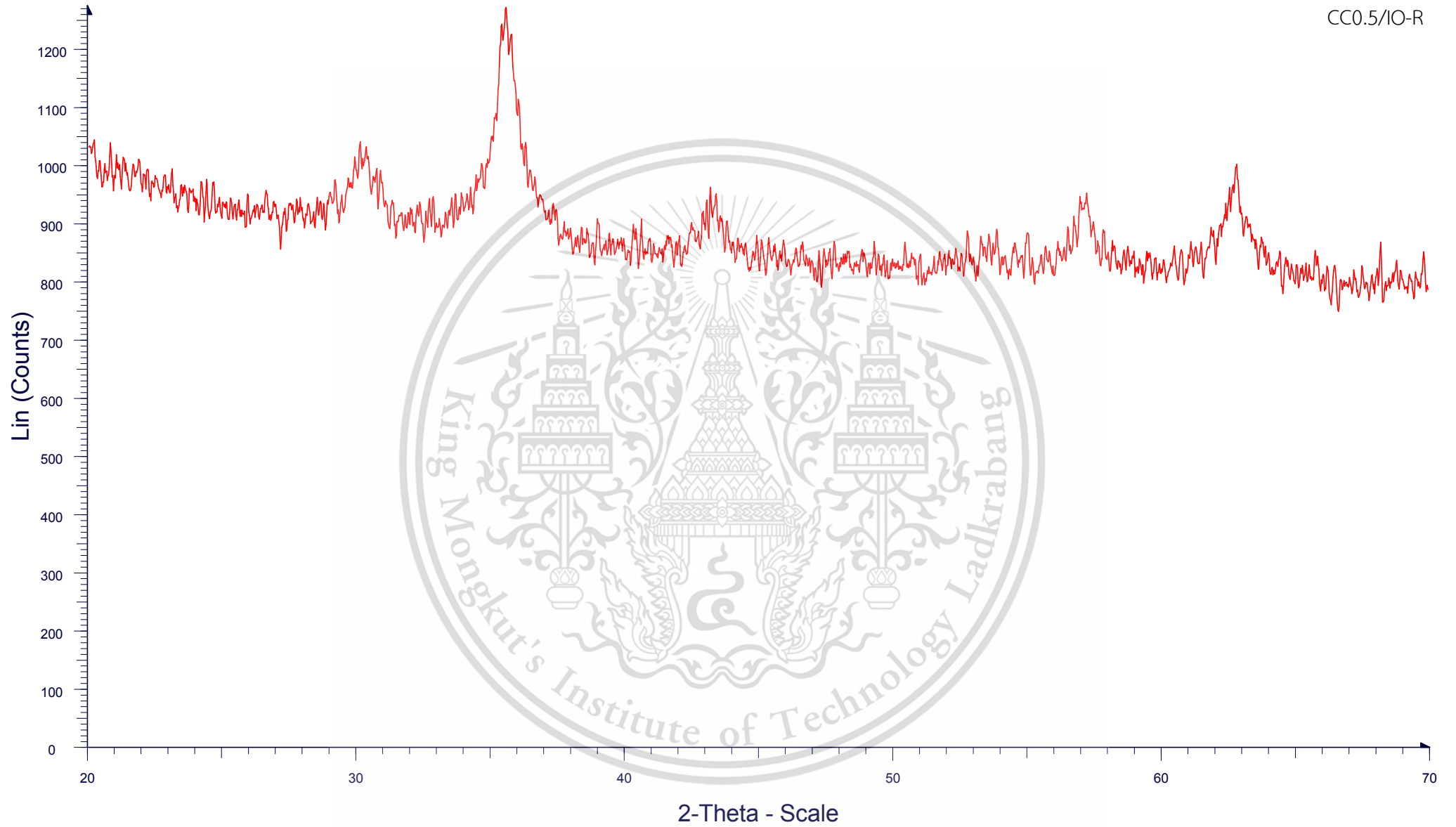
CC0.4/IO-R



File: 590709-0375_06.raw - Type: 2Th/Th locked - Start: 20.0000 ° - End: 70.0008 ° - Step: 0.0229 ° - Step time: 192.4 s - Temp.: 25 °C (Room)
Operations: Smooth 0.080 | Import

CCR 2.5

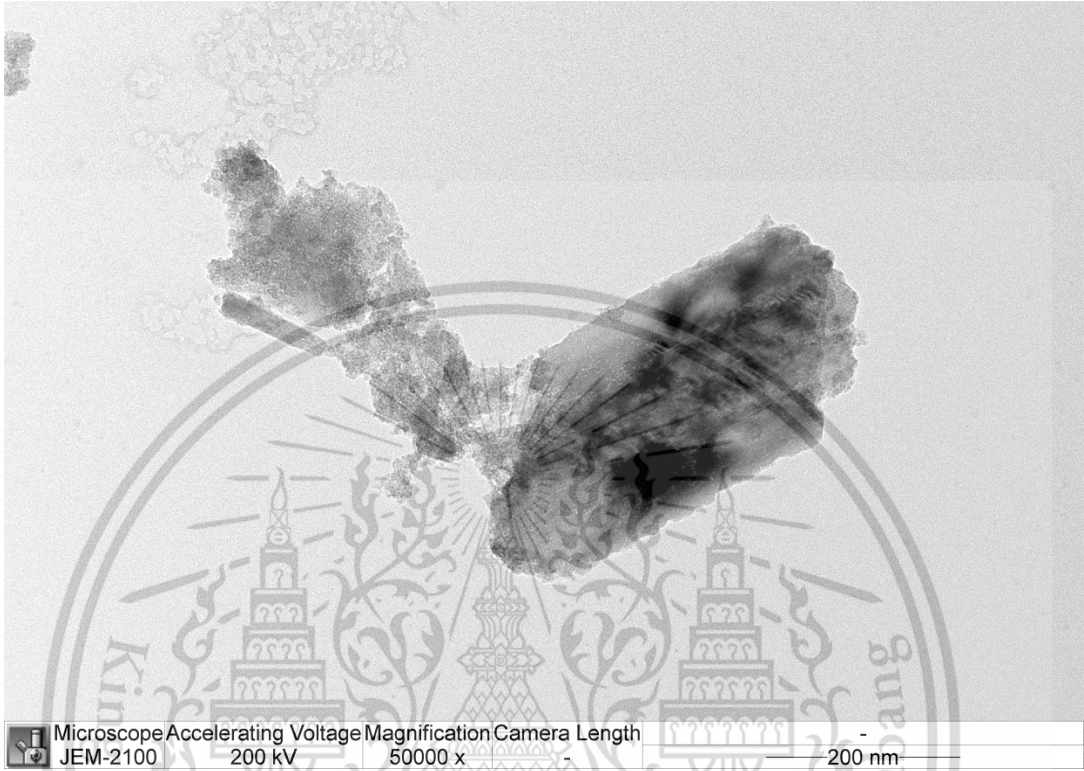
CC0.5/IO-R



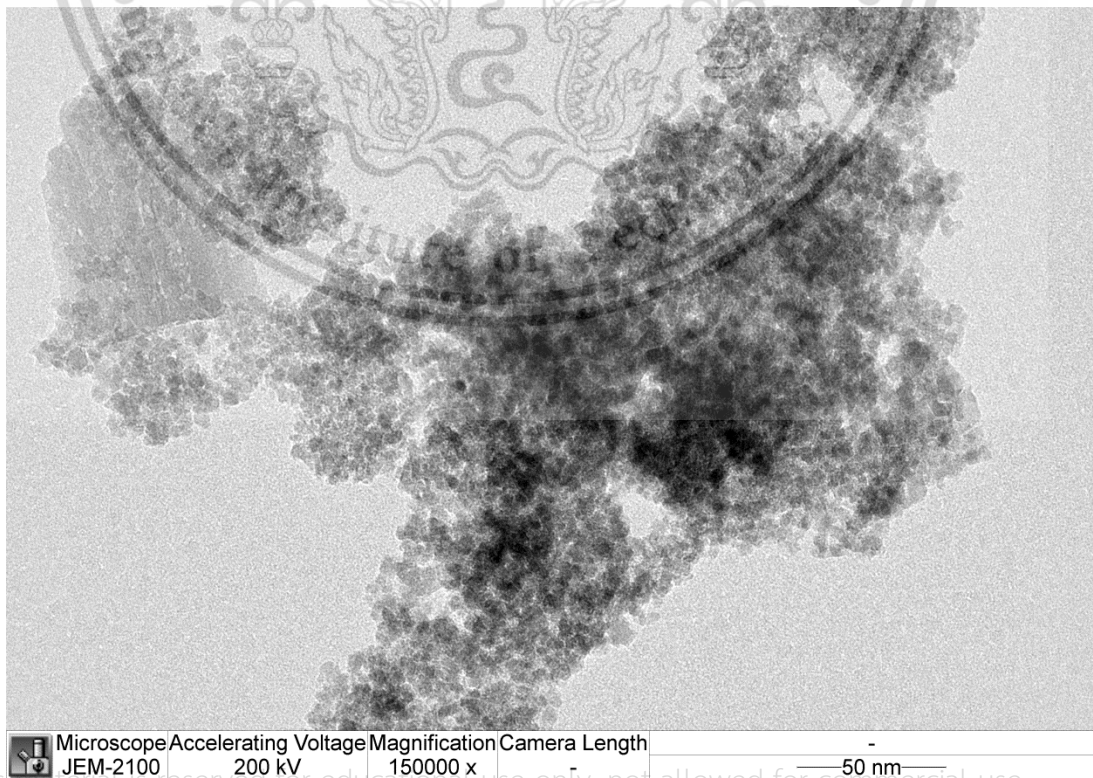
File: 590709-0375_07.raw - Type: 2Th/Th locked - Start: 20.0000 ° - End: 70.0008 ° - Step: 0.0229 ° - Step time: 192.4 s - Temp.: 25 °C (Room)
Operations: Smooth 0.080 | Import

Appendix B

CS0.3/IO-HT75

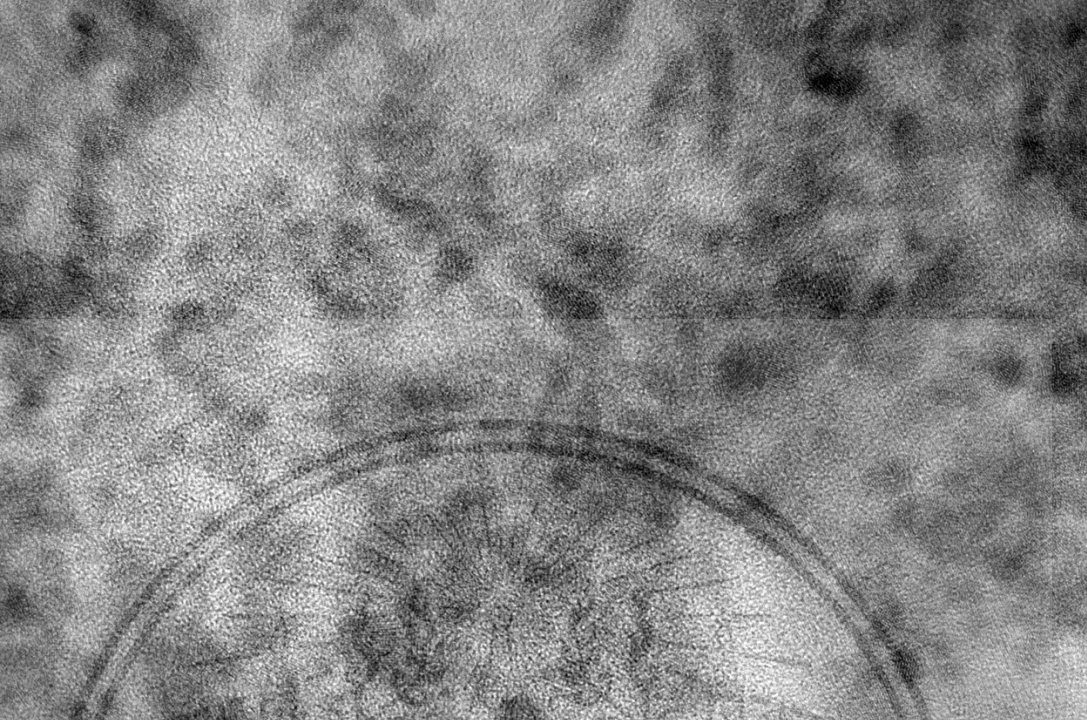


CS0.2/IOHT100



This material is reserved for educational use only, not allowed for commercial use.

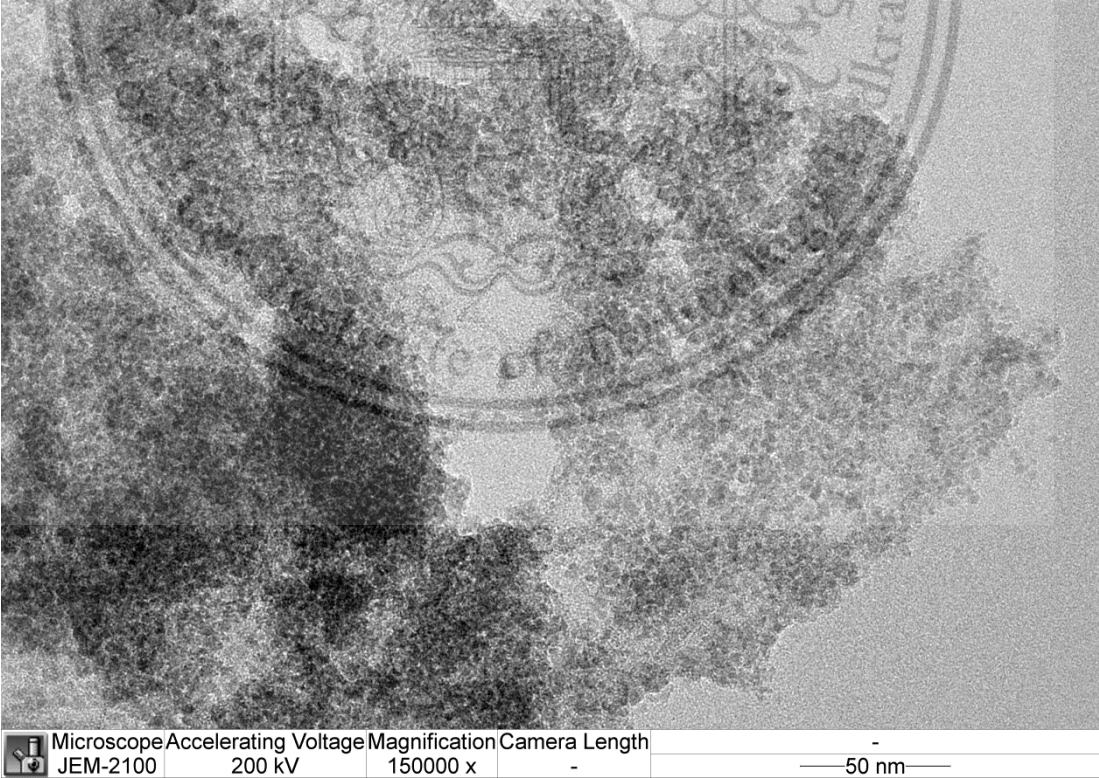
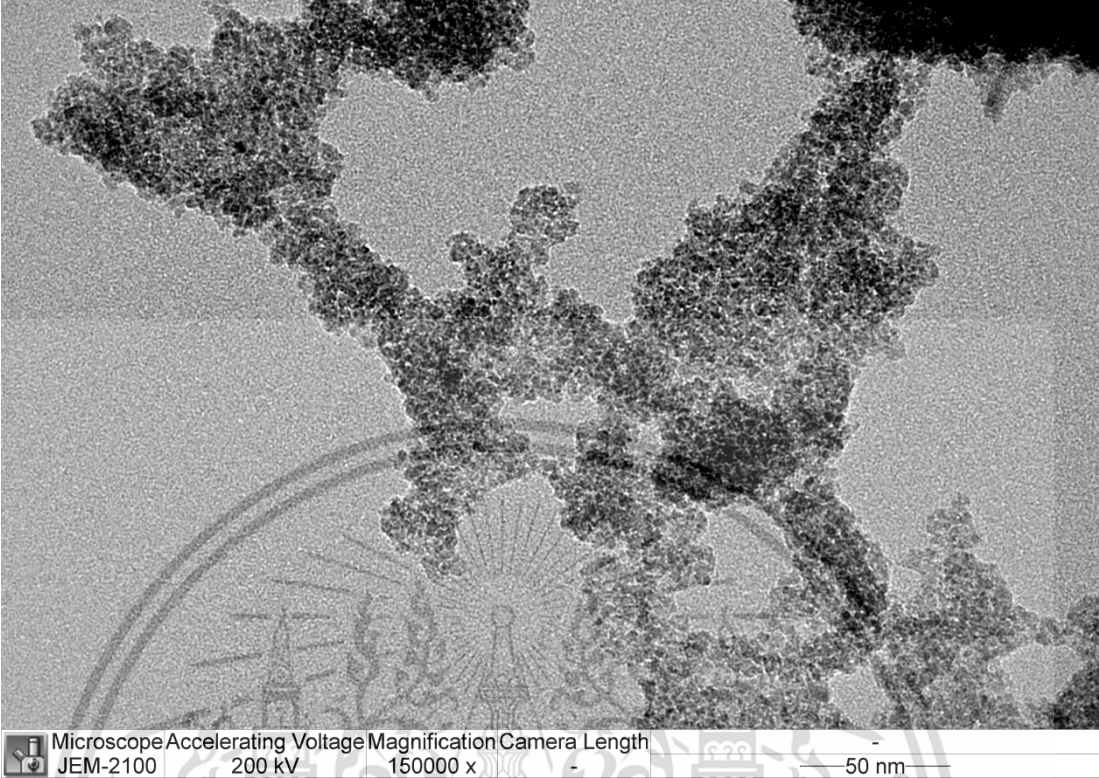
Forbidden to modify the content, and cite the document when use.

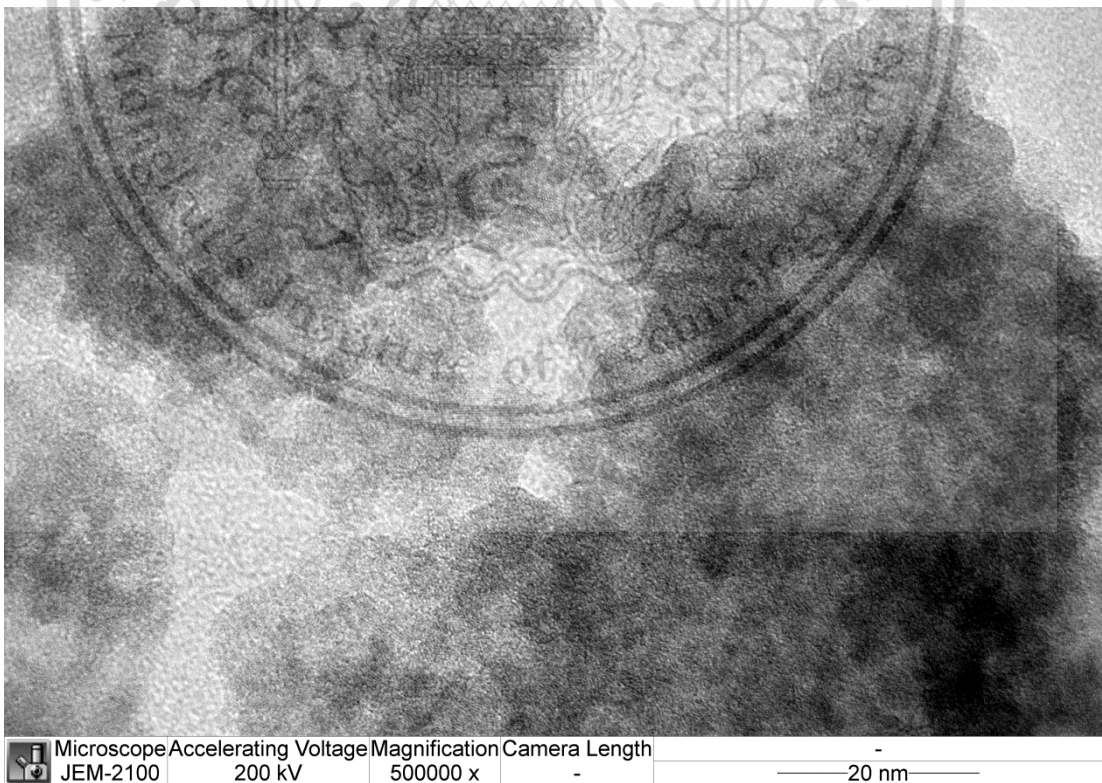
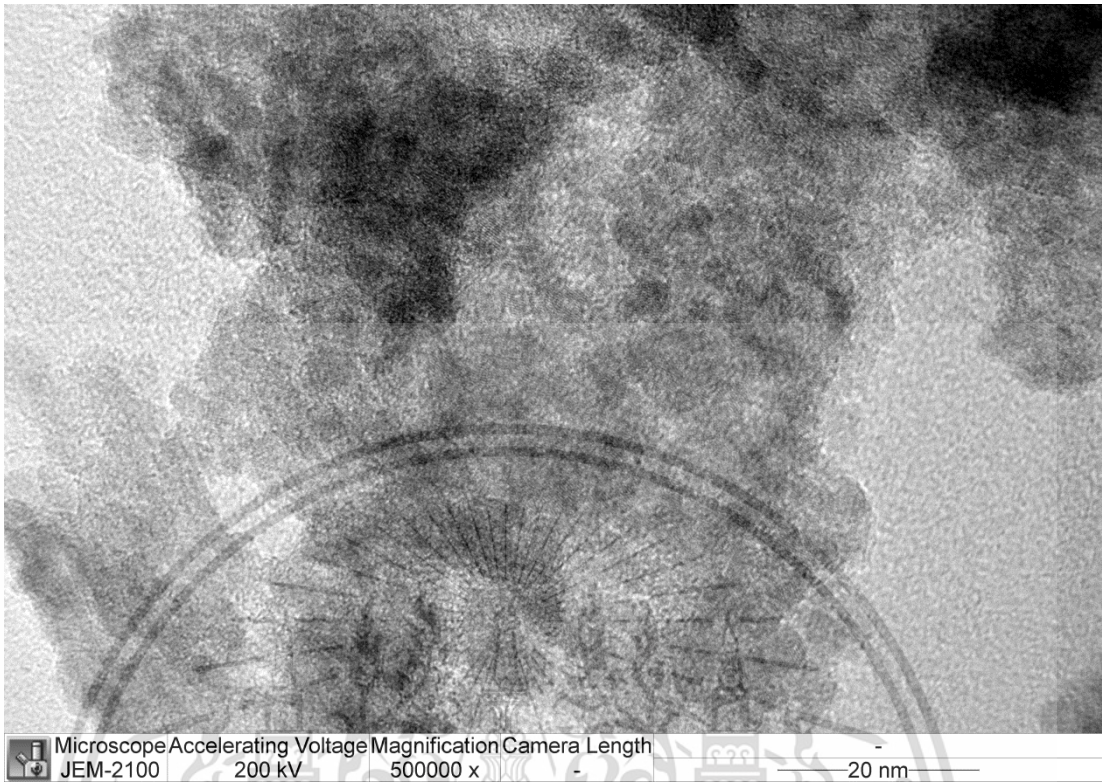


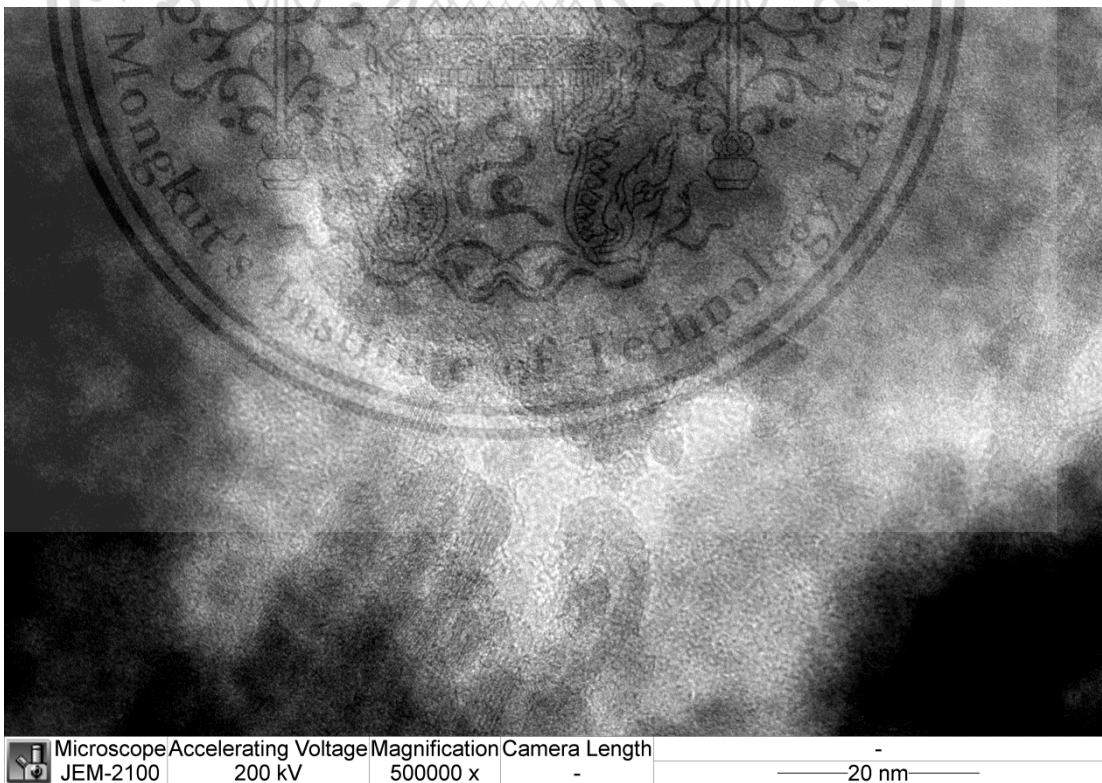
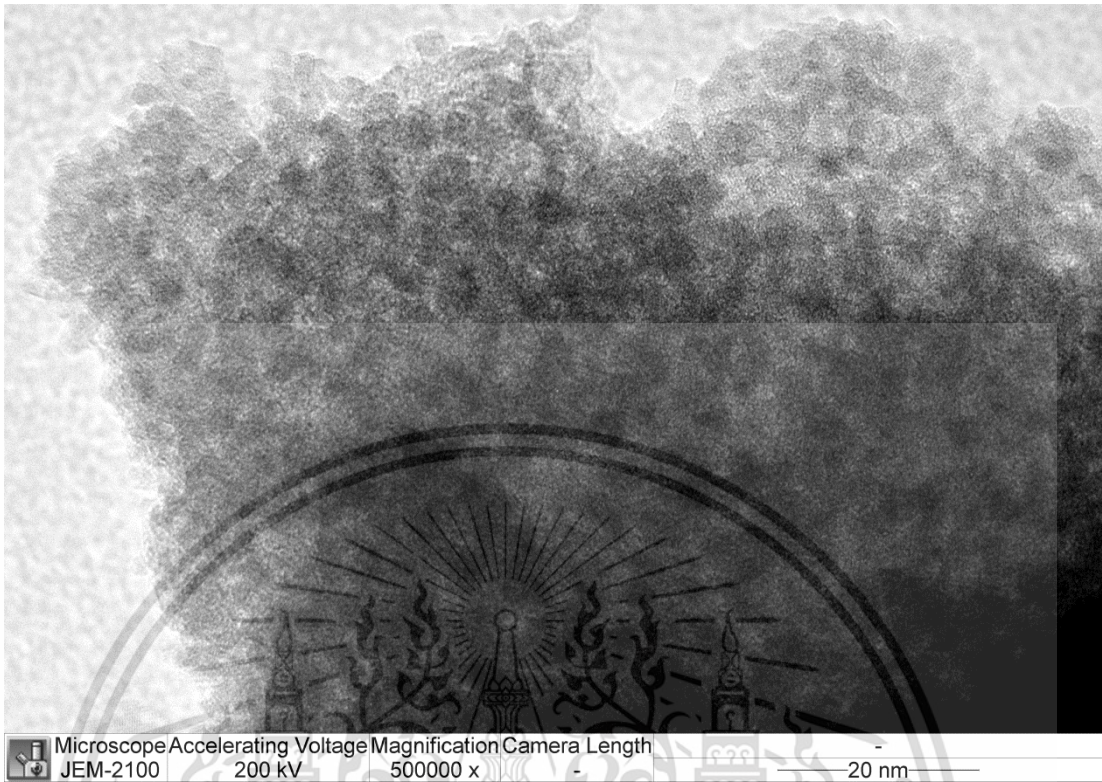
Microscope	Accelerating Voltage	Magnification	Camera Length	
JEM-2100	200 kV	500000 x	-	20 nm

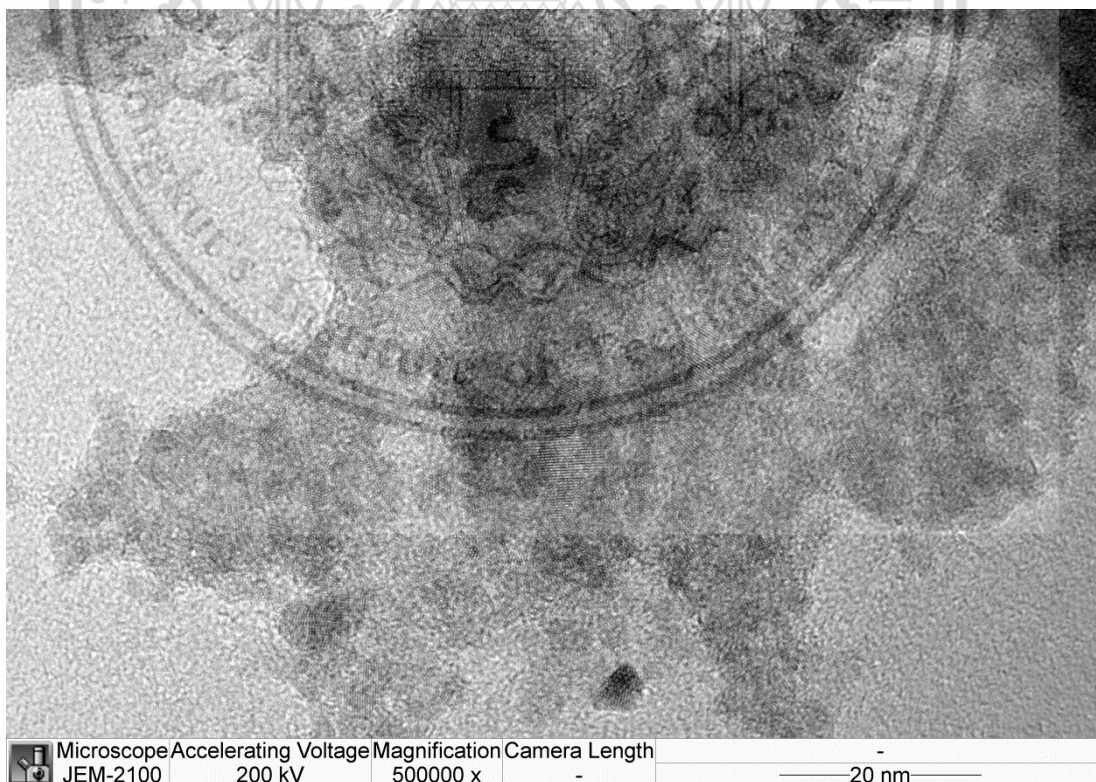
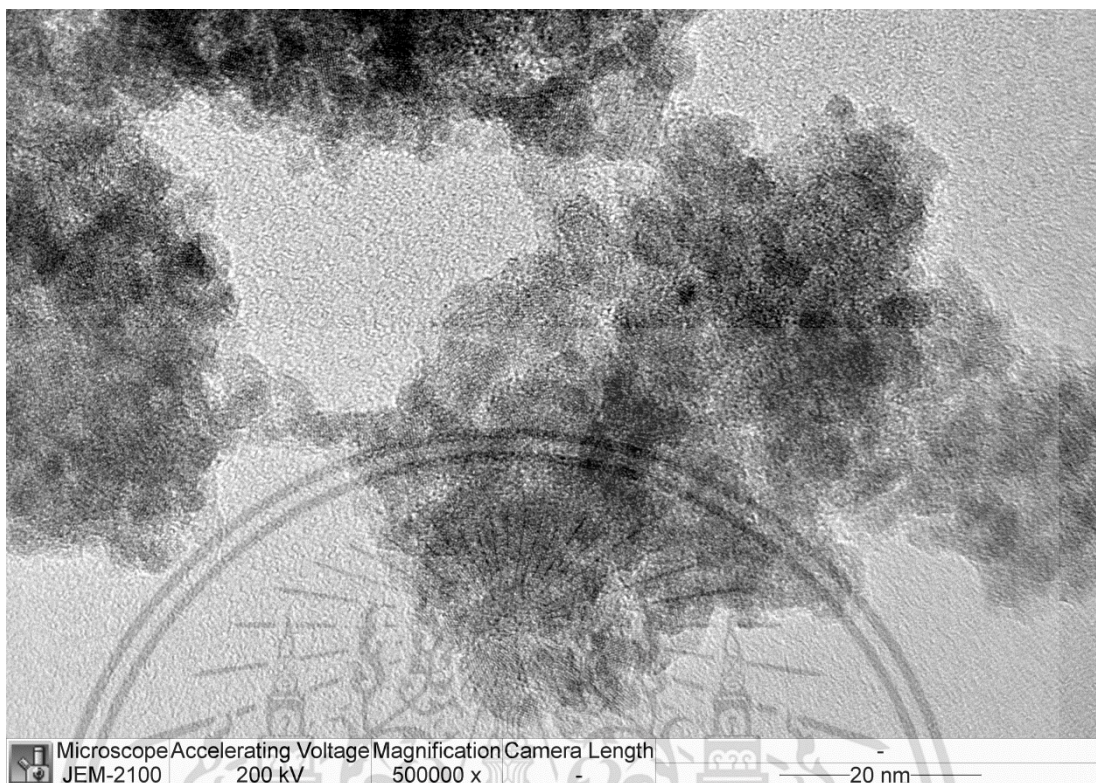


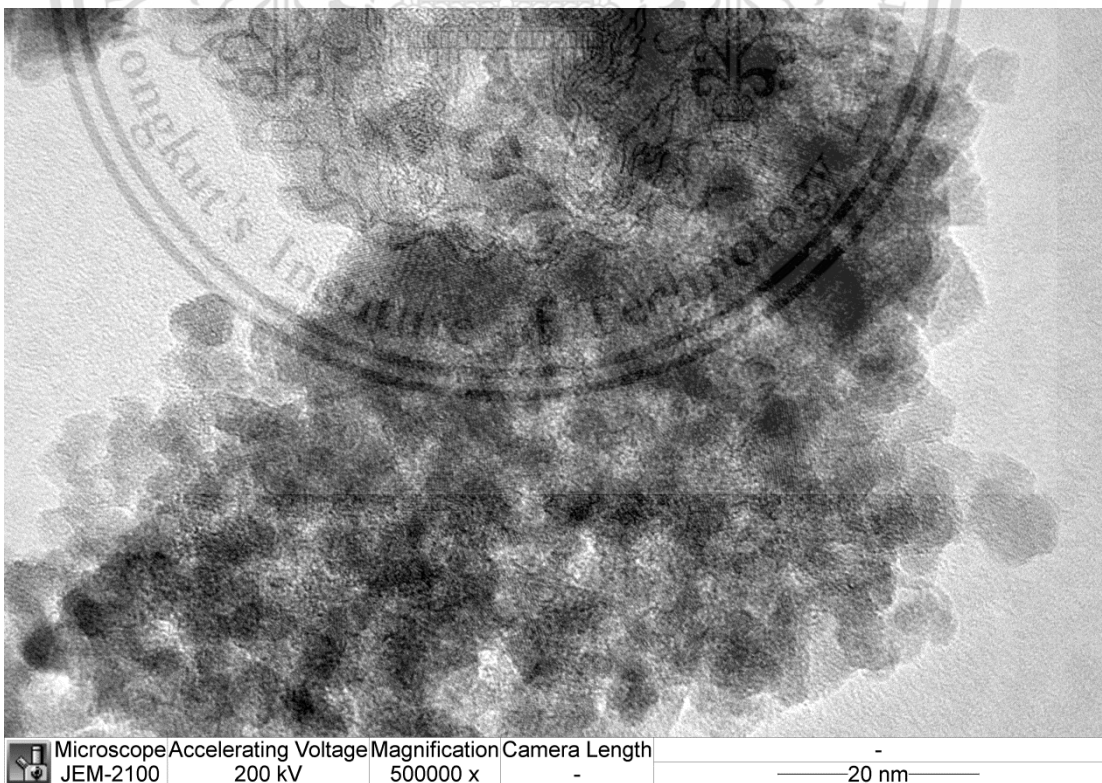
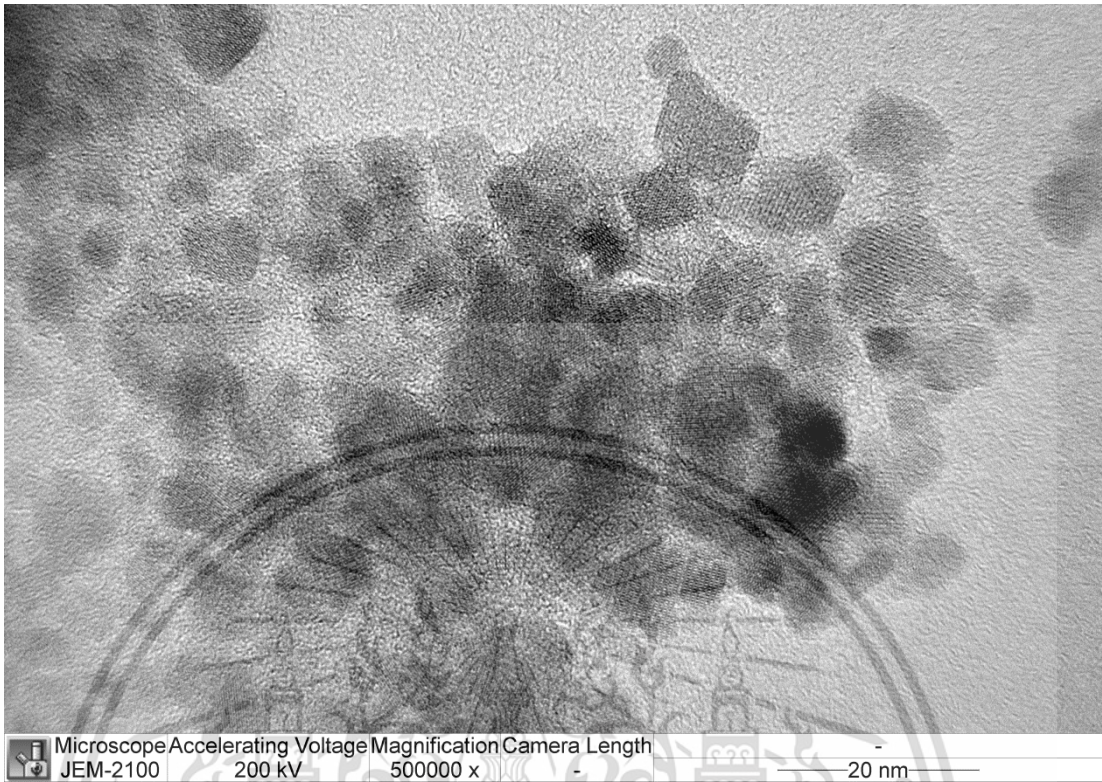
Microscope	Accelerating Voltage	Magnification	Camera Length	
JEM-2100	200 kV	150000 x	-	50 nm

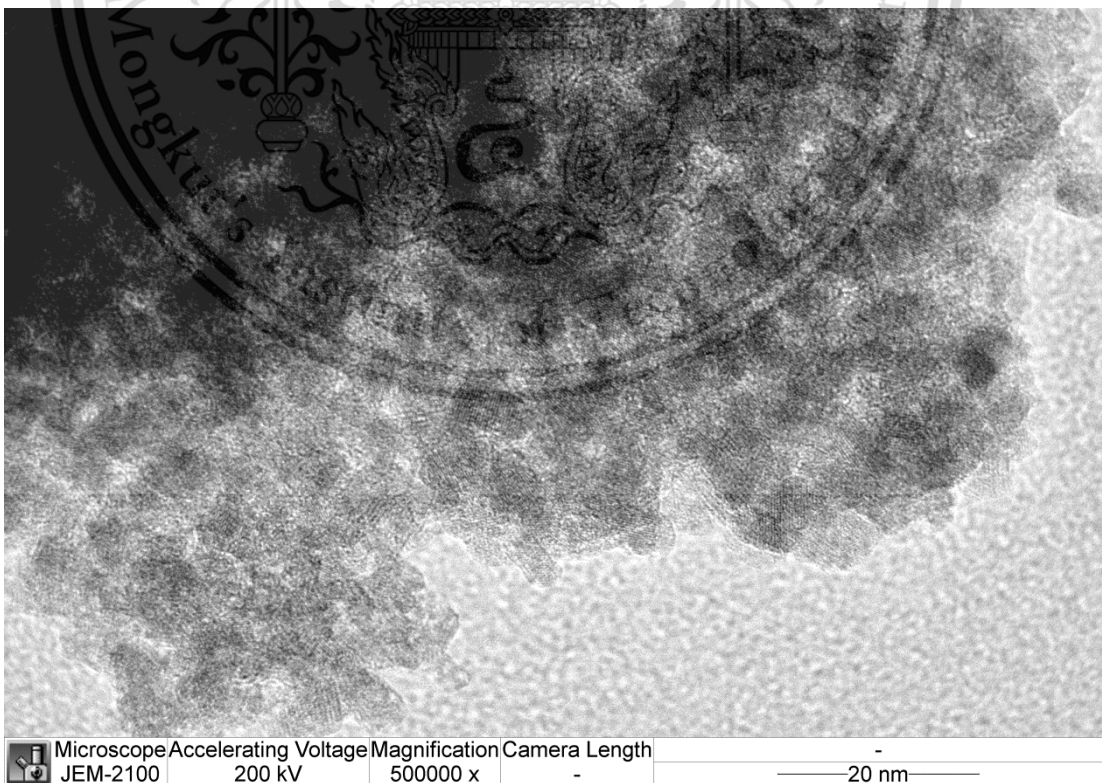
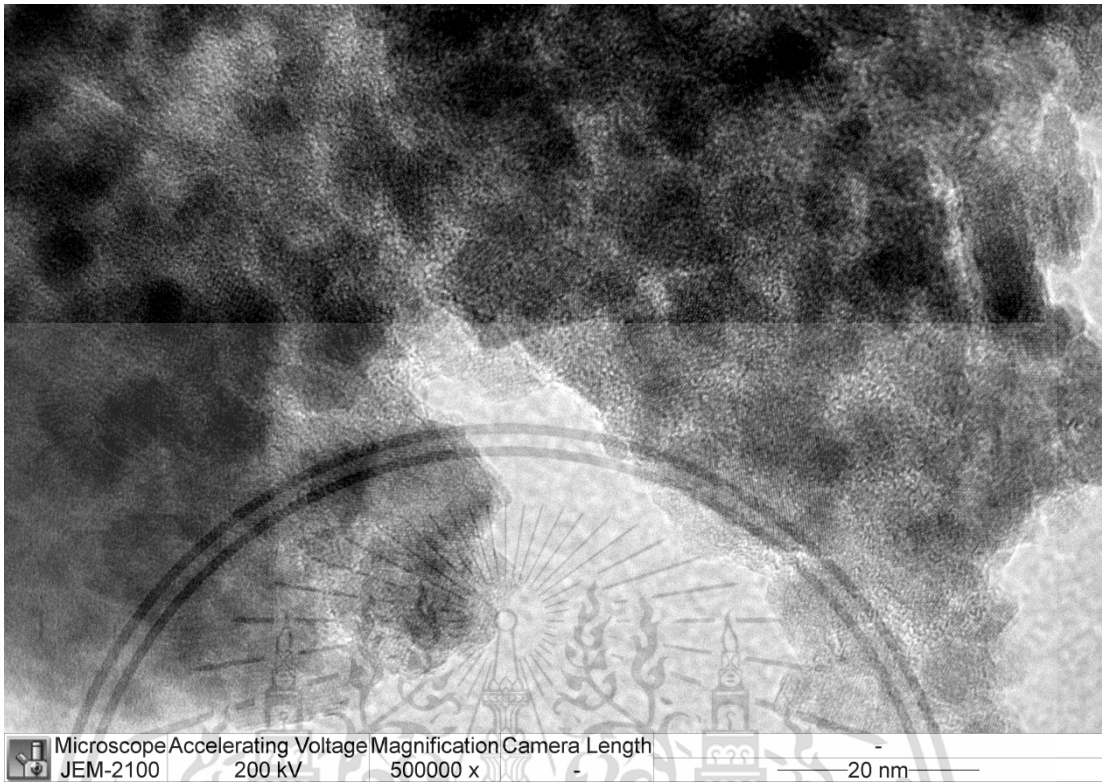


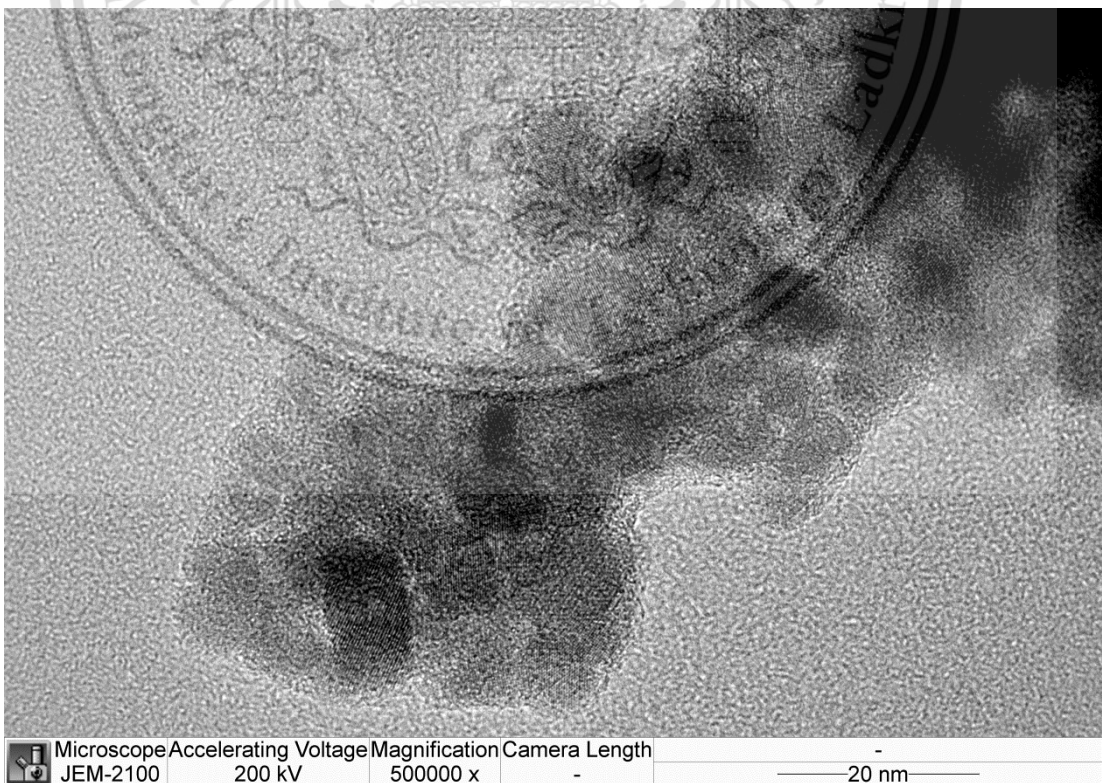
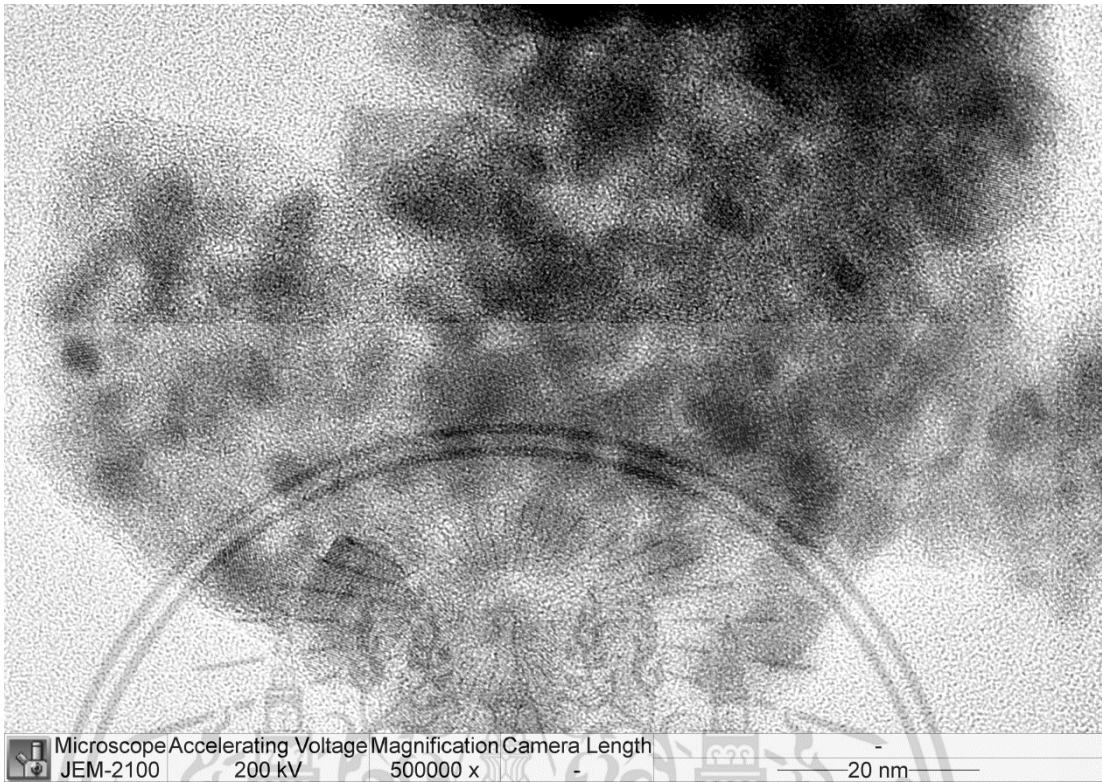


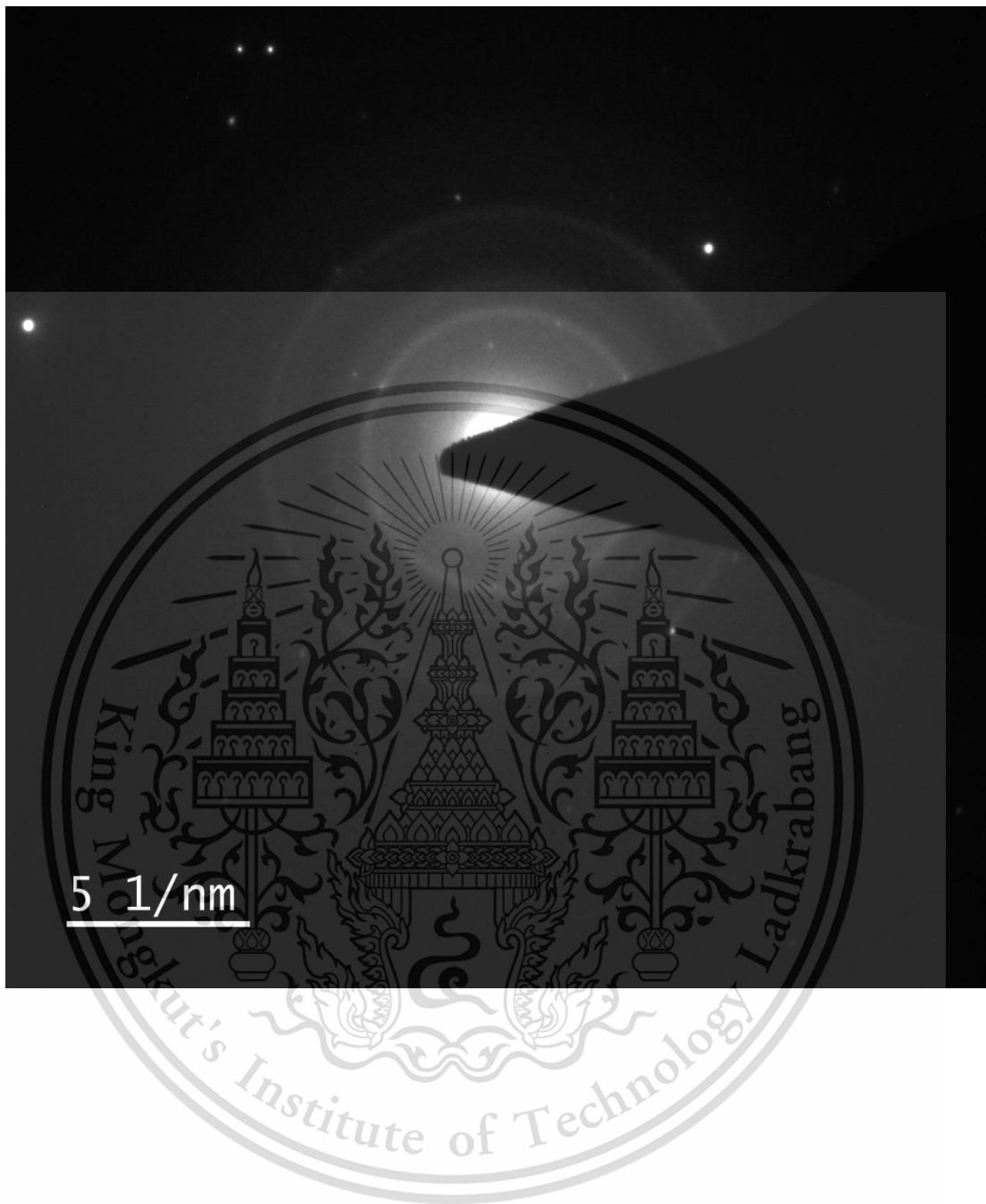








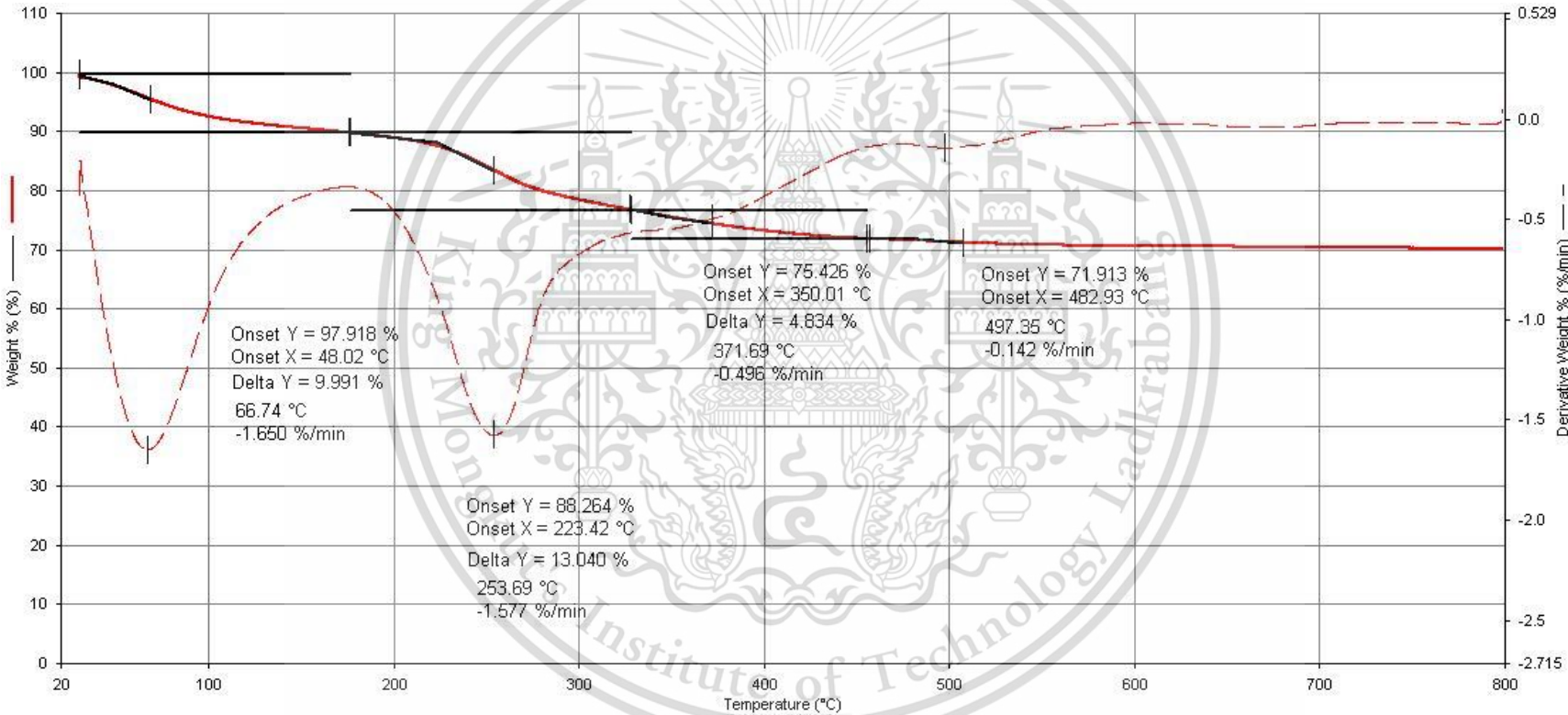


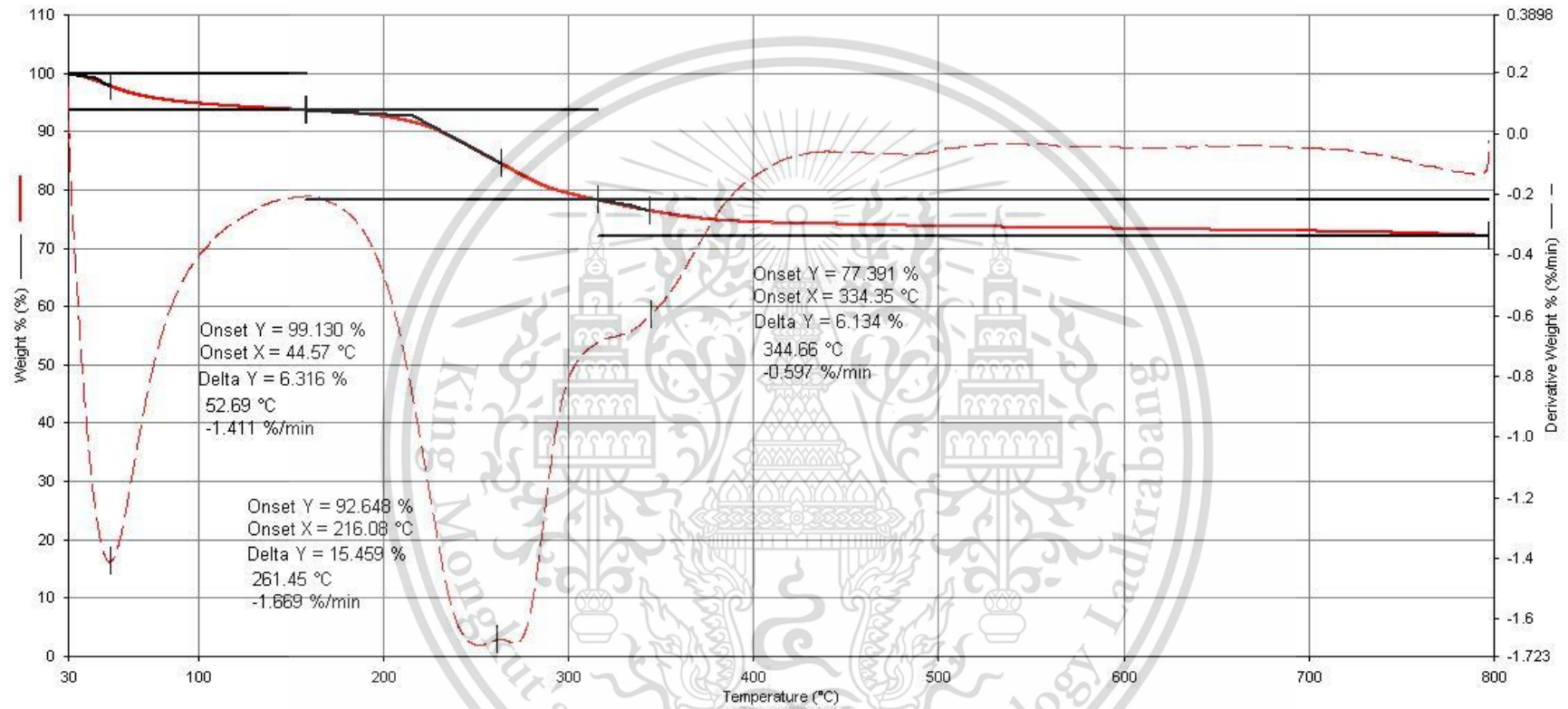


Appendix C

(TGA in N₂)

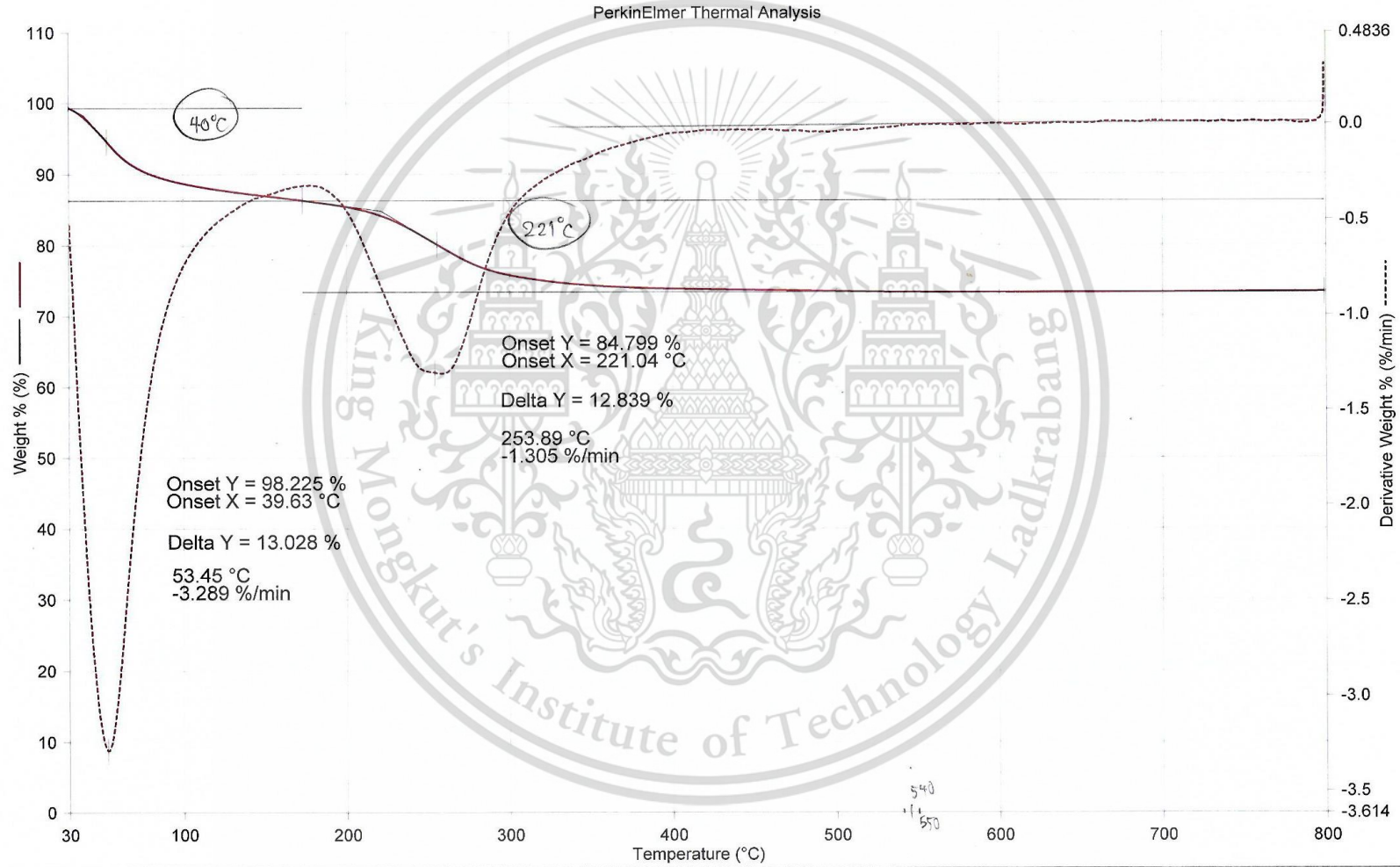
CS0.3/IO-HT75



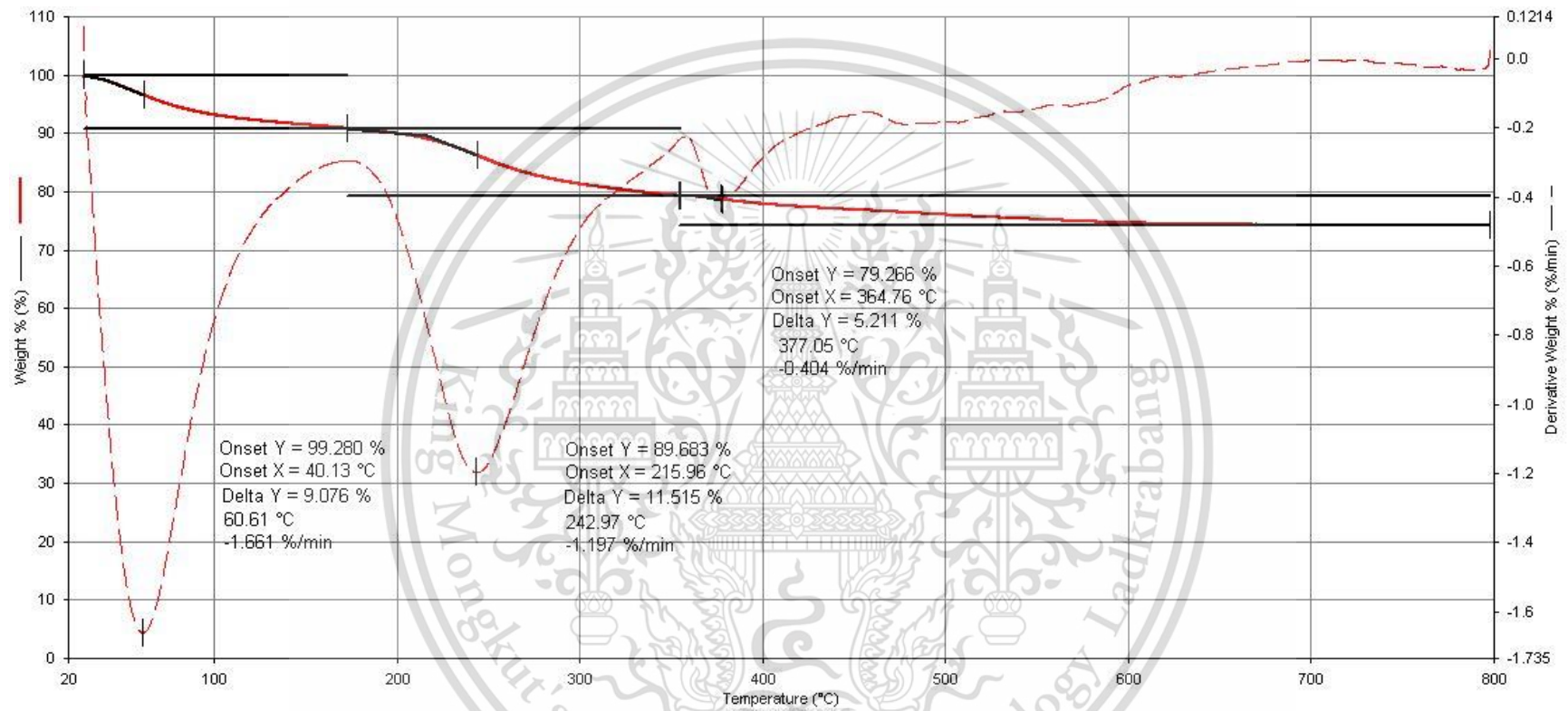


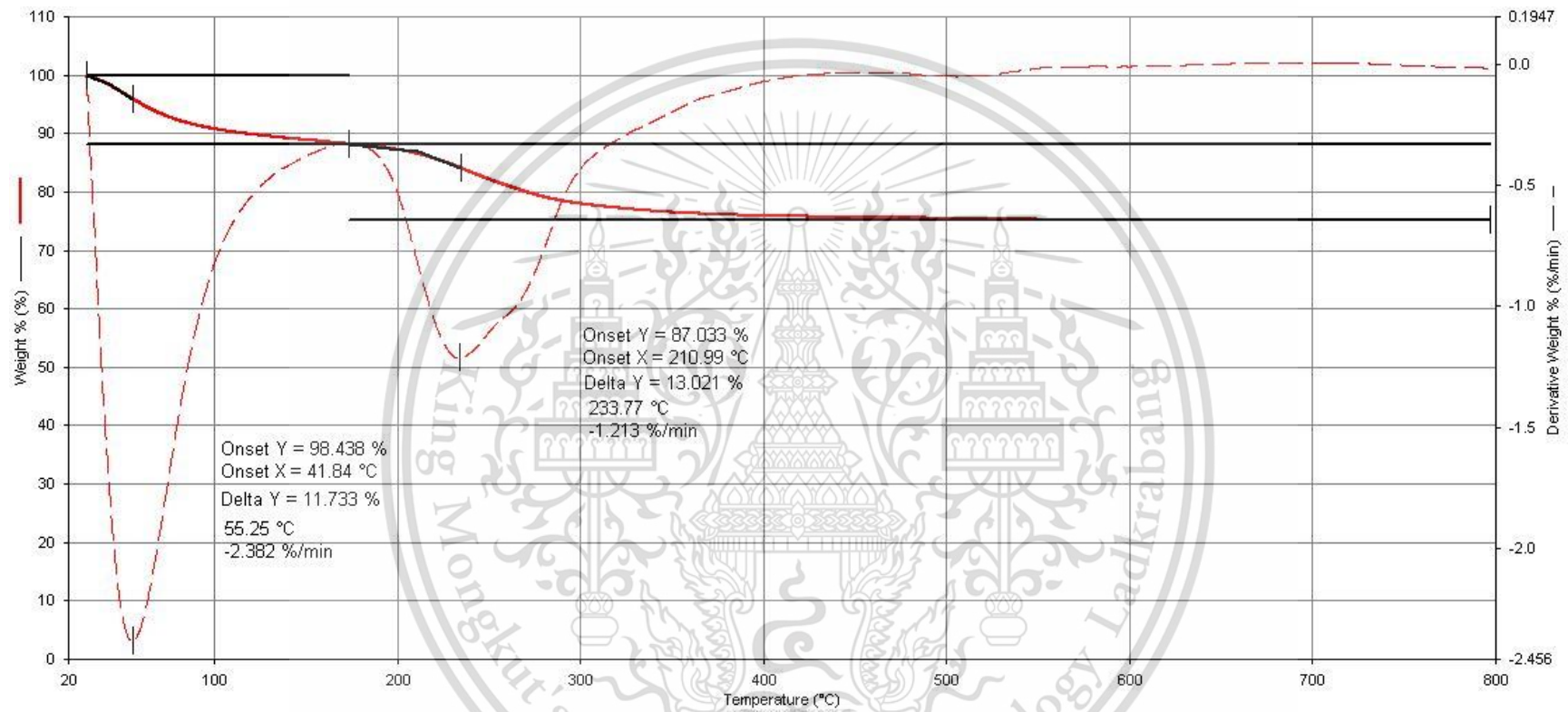
Filename: C:\Program F...\ITG60_064_01_HT 1.67_N2.th1d
Operator ID:
Sample ID: HT 1.67_N2
Sample Weight: 5.092 mg
Comment:

CS0.3/IO-HT100



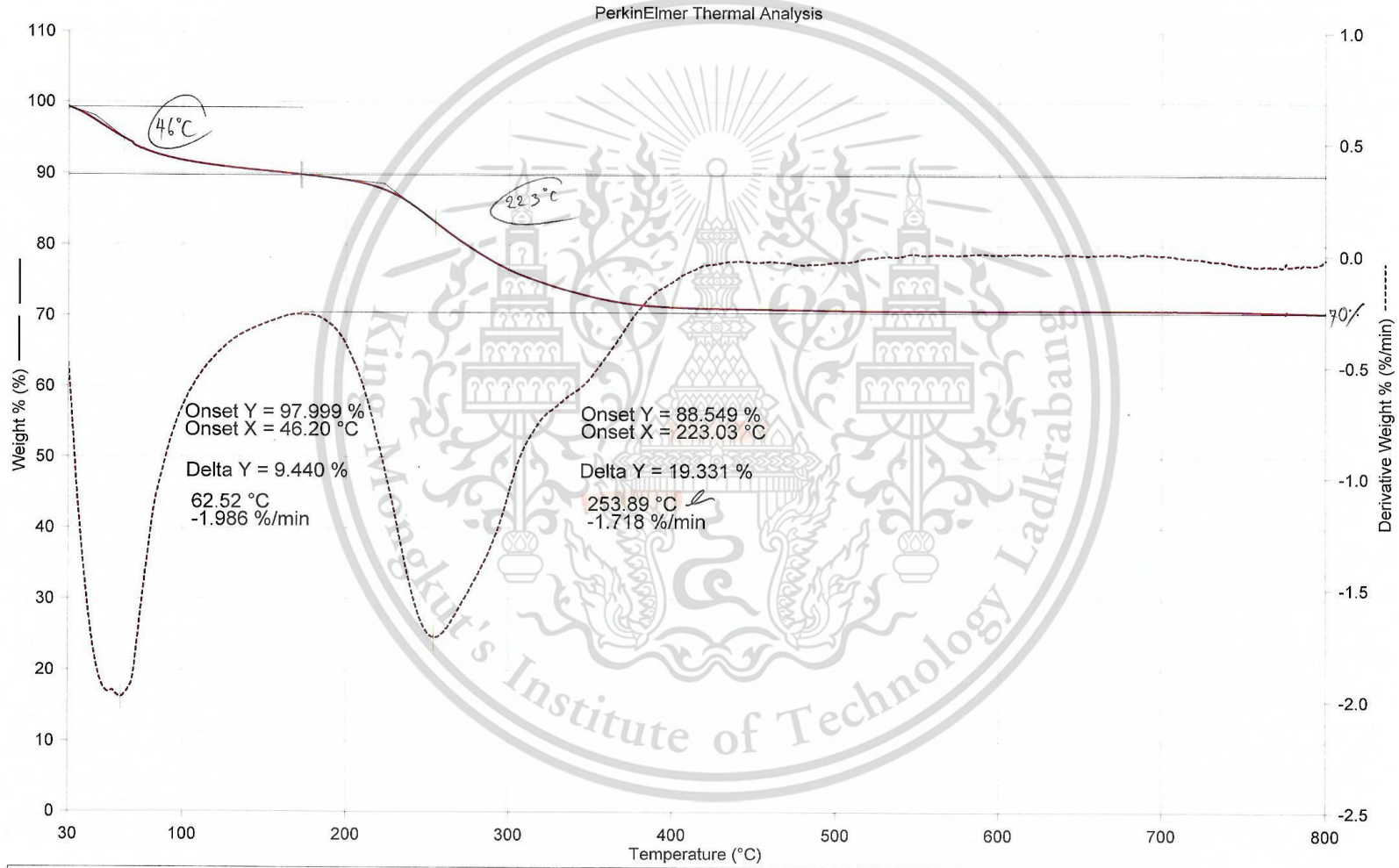
1) Heat from 50.00°C to 800.00°C at 10.00°C/min



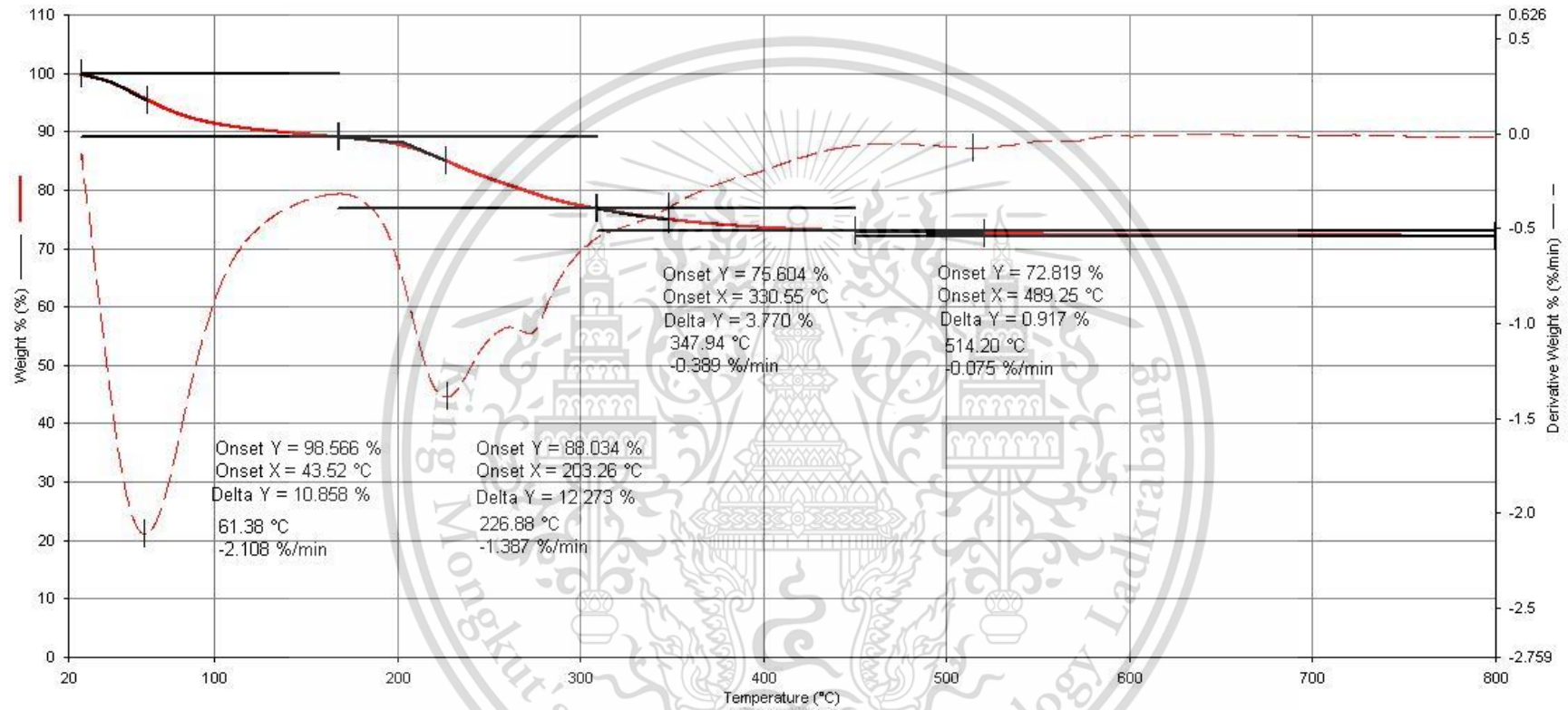


Filename: C:\Program Files\...\TG60_016_02_3_N2.th1d
Operator ID:
Sample ID: *N1 3 N2*
Sample Weight: 3.272 mg
Comment:

CS0.6/IO-HT100

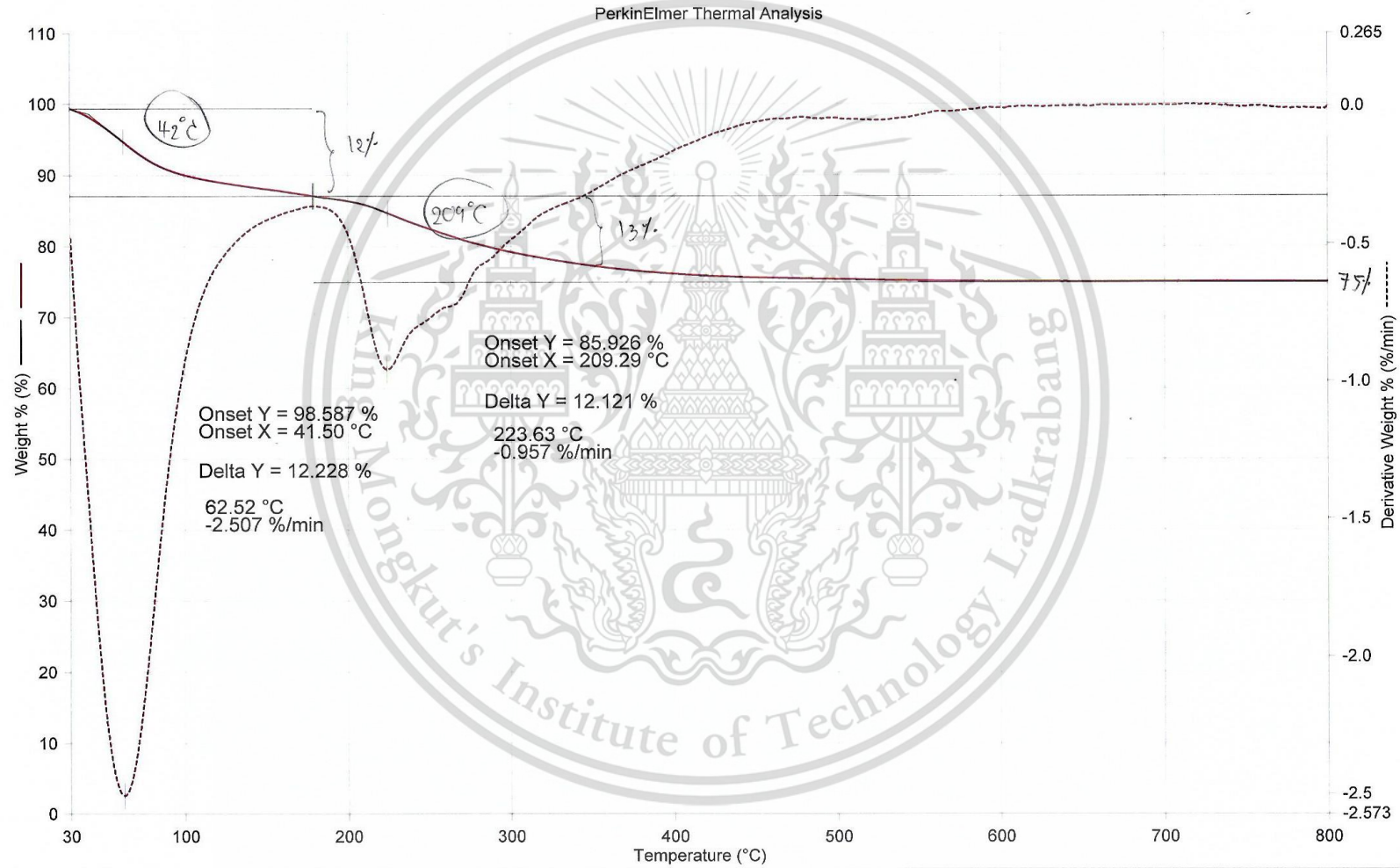


1) Heat from 35.00°C to 800.00°C at 10.00°C/min



Filename: C:\Program Files\Pyr...\TG60_065_01_R1.th1d
 Operator ID:
 Sample ID: R1 N₂
 Sample Weight: 8.743 mg
 Comment:

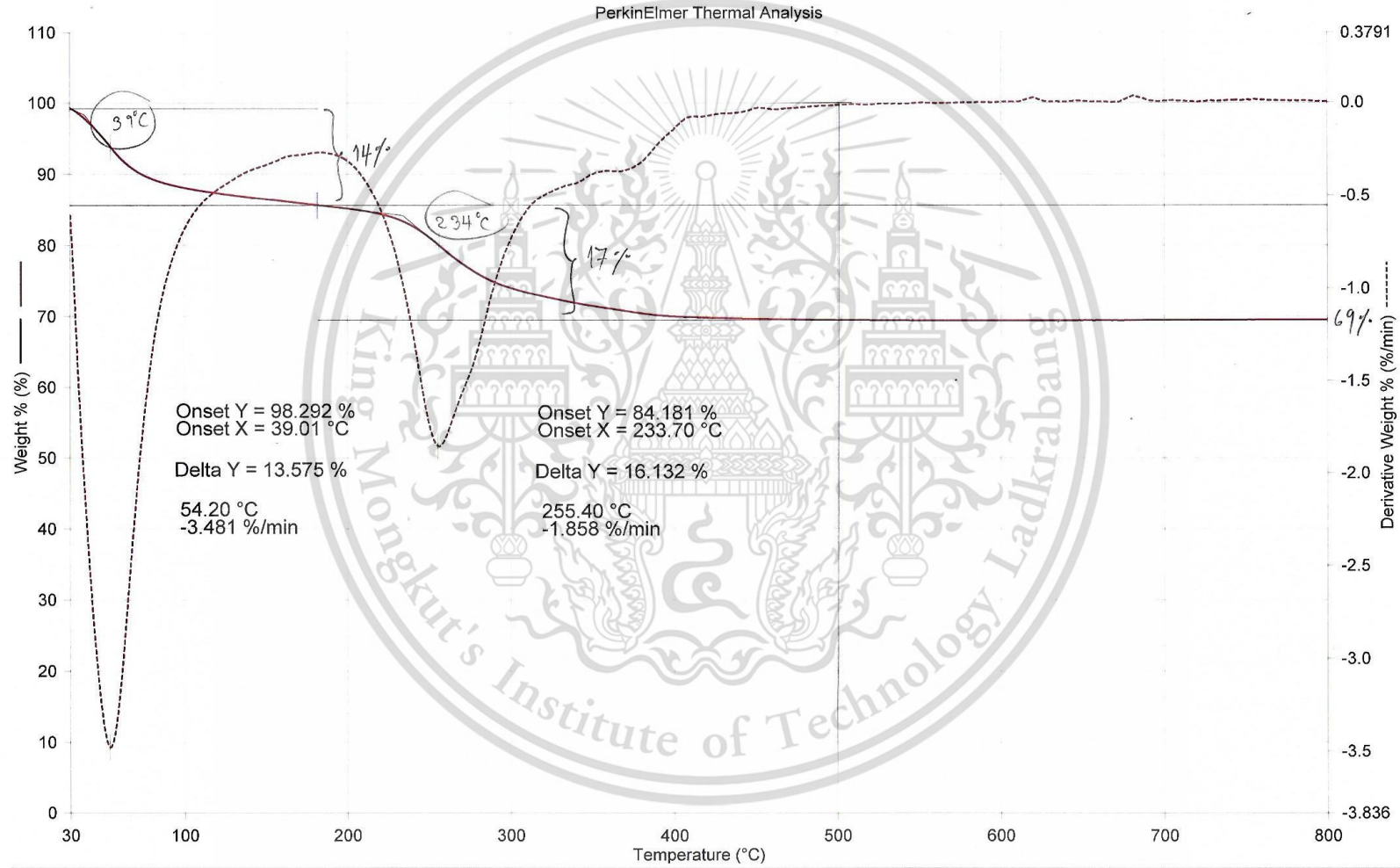
CS0.2/IO-R



1) Heat from 50.00°C to 800.00°C at 10.00°C/min

Filename: C:\Program Fi...\TG60_064_04_R 1.67_N2.th1d
 Operator ID:
 Sample ID: R 1.67_N2
 Sample Weight: 4.918 mg
 Comment:

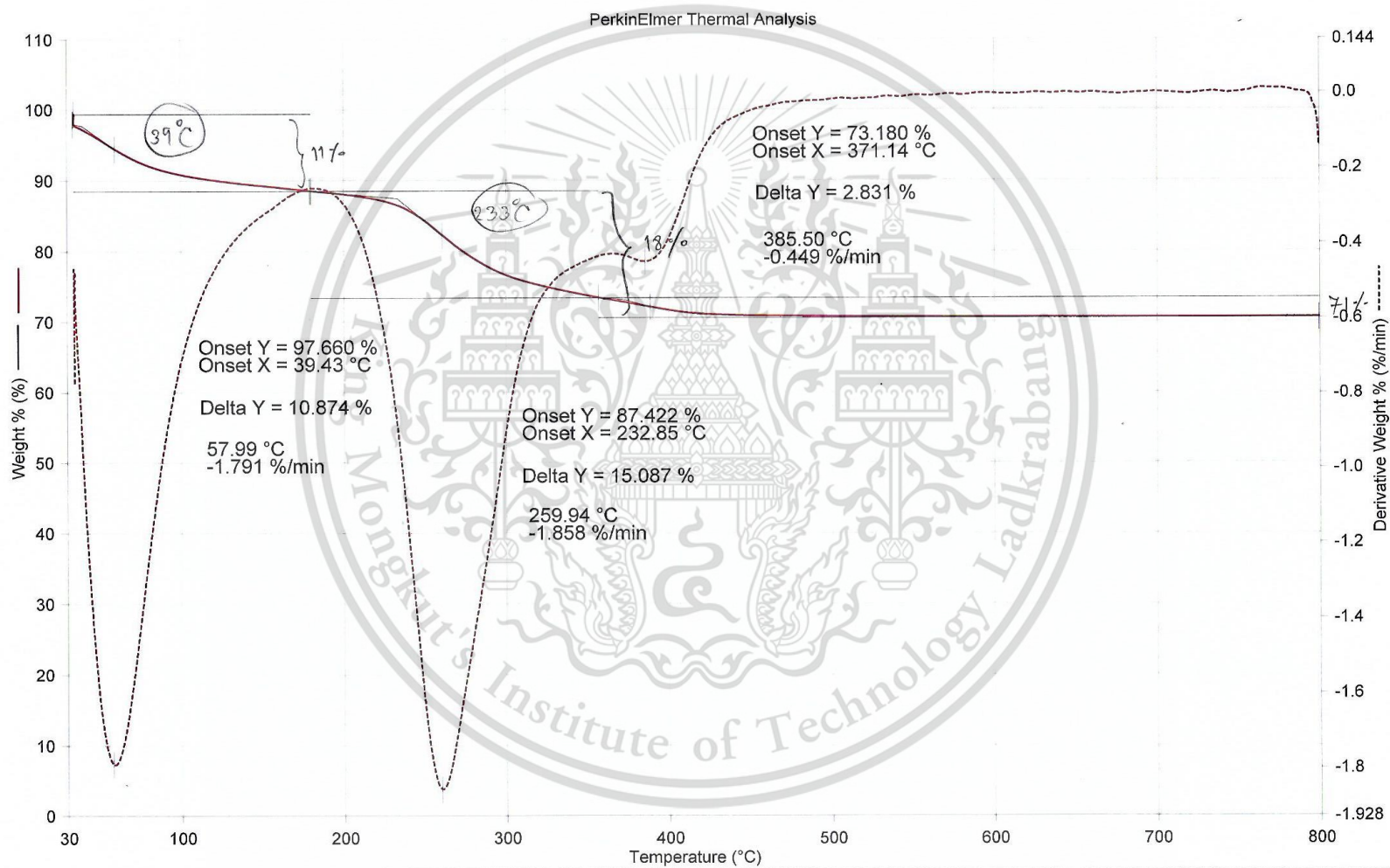
CS0.3/IO-R



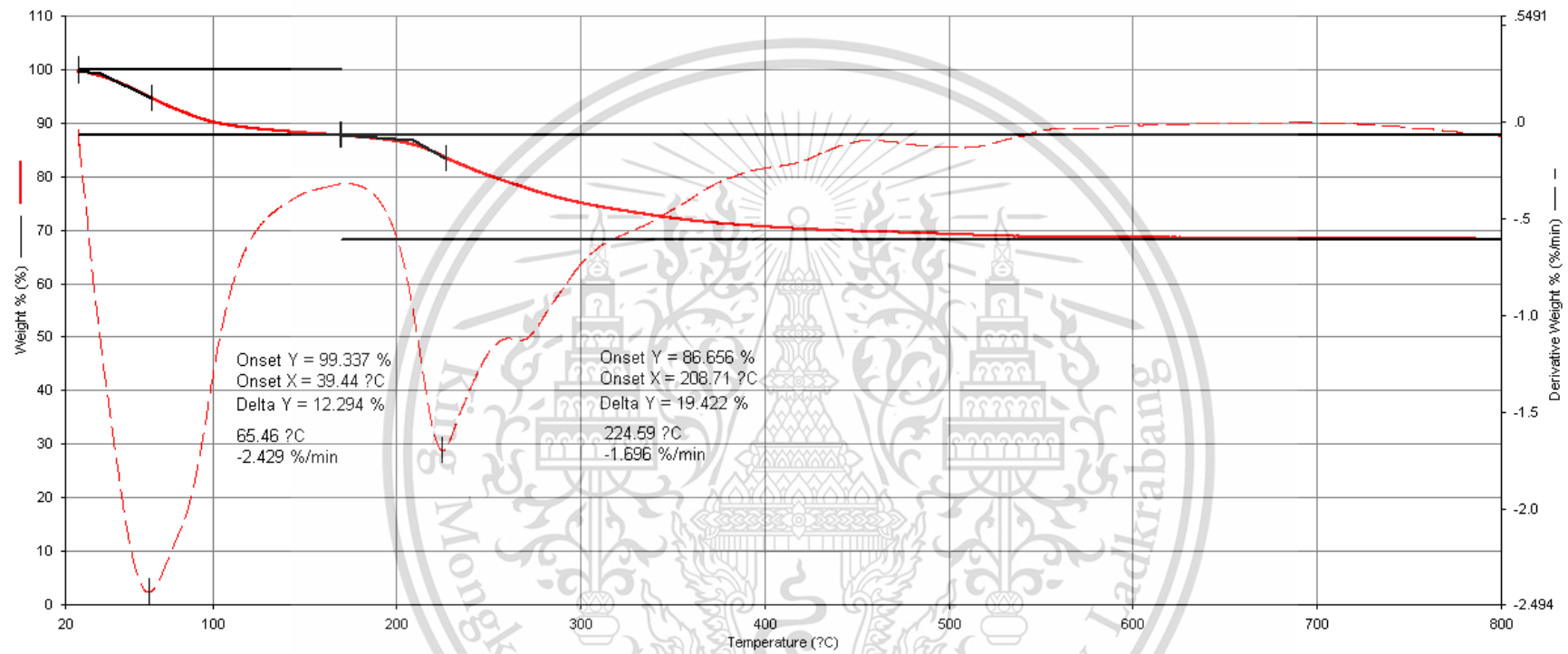
1) Heat from 50.00°C to 800.00°C at 10.00°C/min

Filename: C:\Program Files\Pyr...\TG60_065_02_R2.th1d
 Operator ID:
 Sample ID: R2 N₂
 Sample Weight: 8.229 mg
 Comment:

CS0.4/IO-R

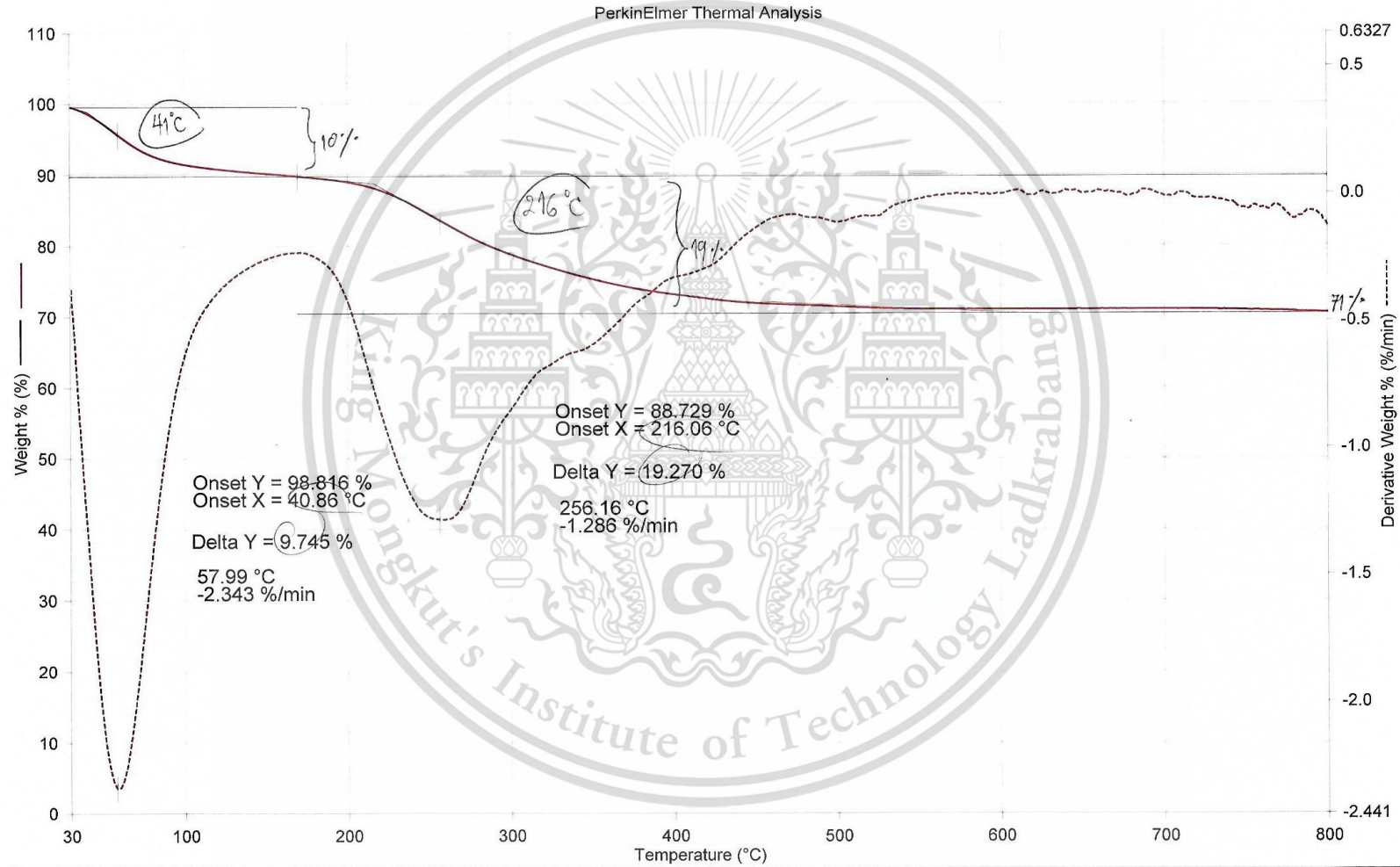


1) Heat from 50.00°C to 800.00°C at 10.00°C/min



Filename: C:\Program Files...\TG60_064_05_R_3_N2.th1d
Operator ID:
Sample ID: R_3_N2
Sample Weight: 4.709 mg
Comment:

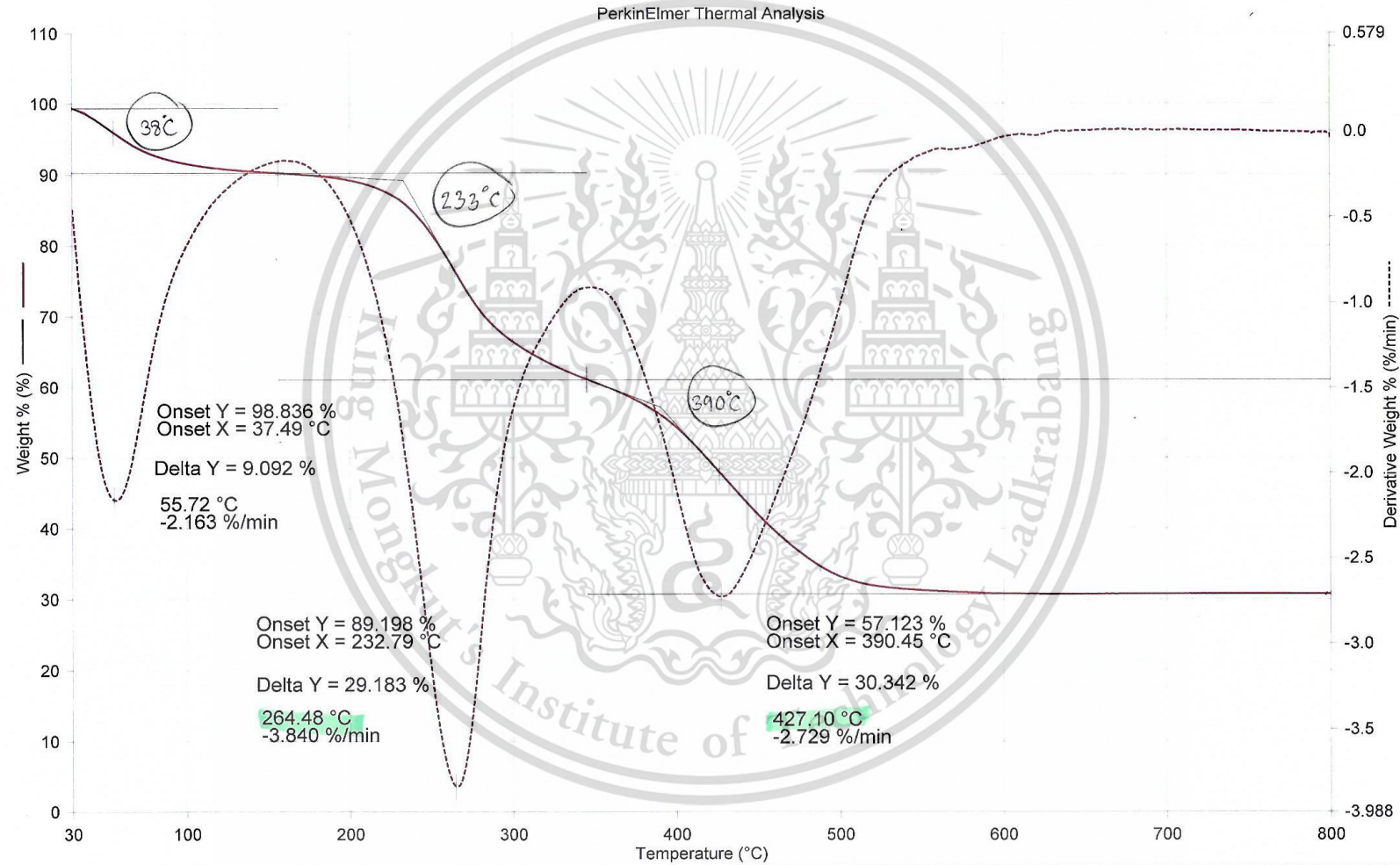
CS0.6/IO-R



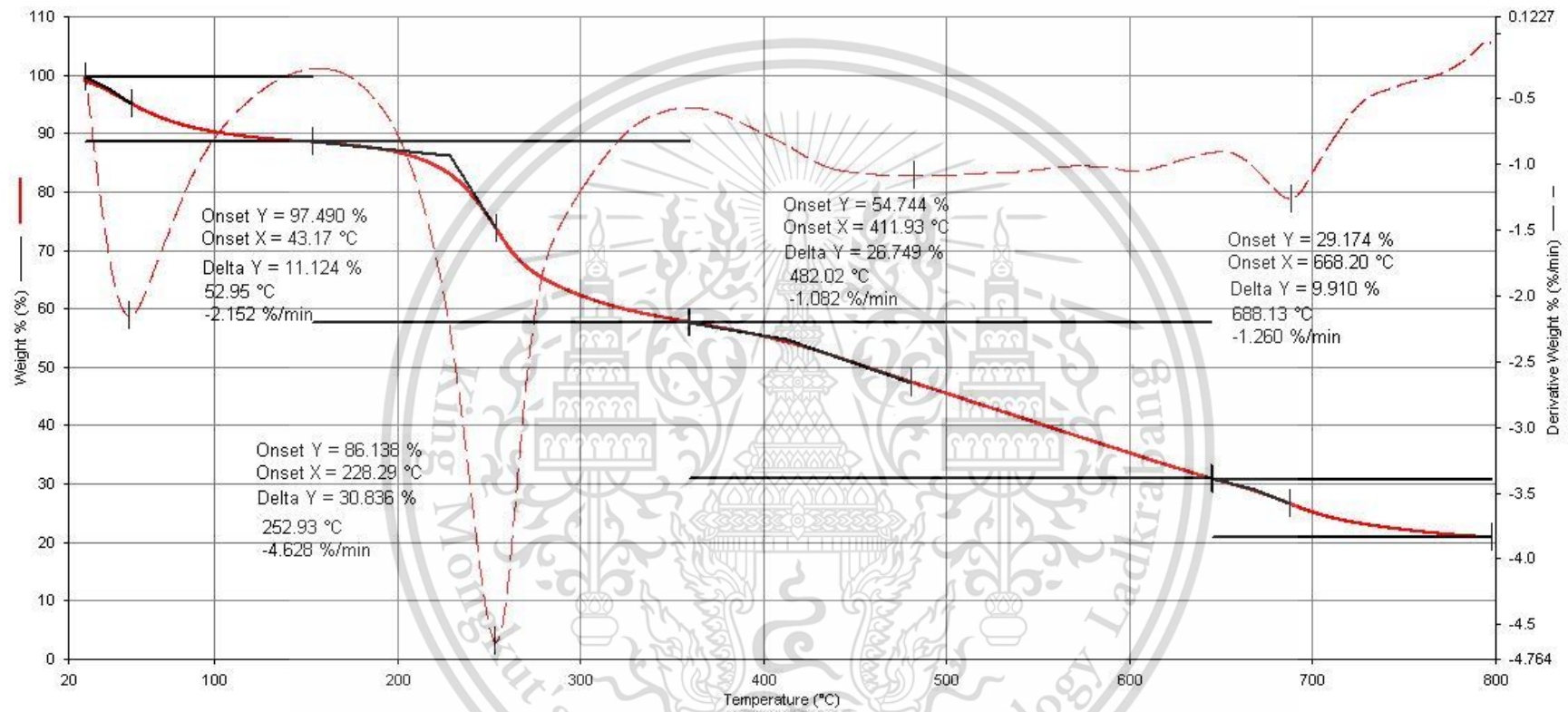
1) Heat from 50.00°C to 800.00°C at 10.00°C/min

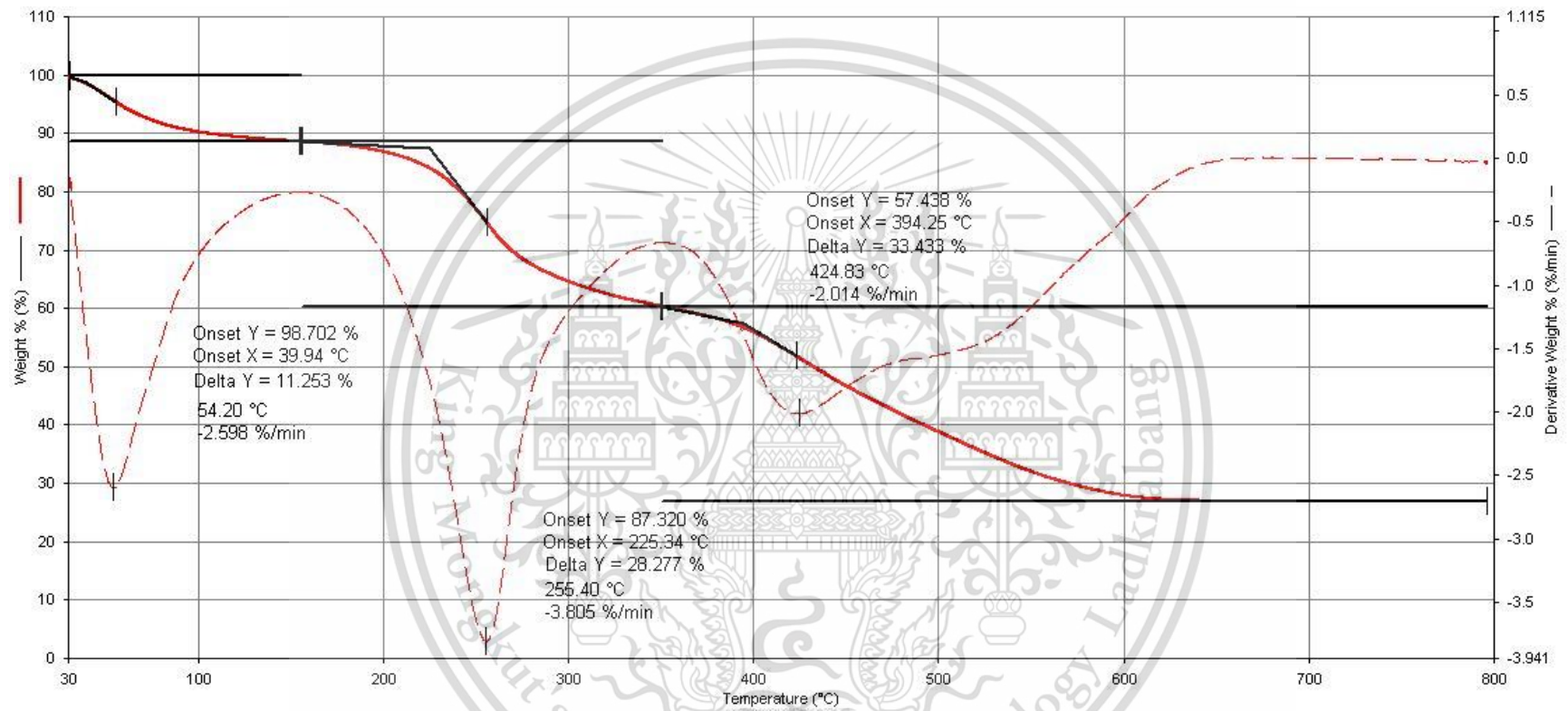
Filename: C:\Program...TG60_064_02_CCHT 1.67_N2.th1d
Operator ID:
Sample ID: CCHT 1.67_N2
Sample Weight: 5.077 mg
Comment:

CC0.3/IO-HT100



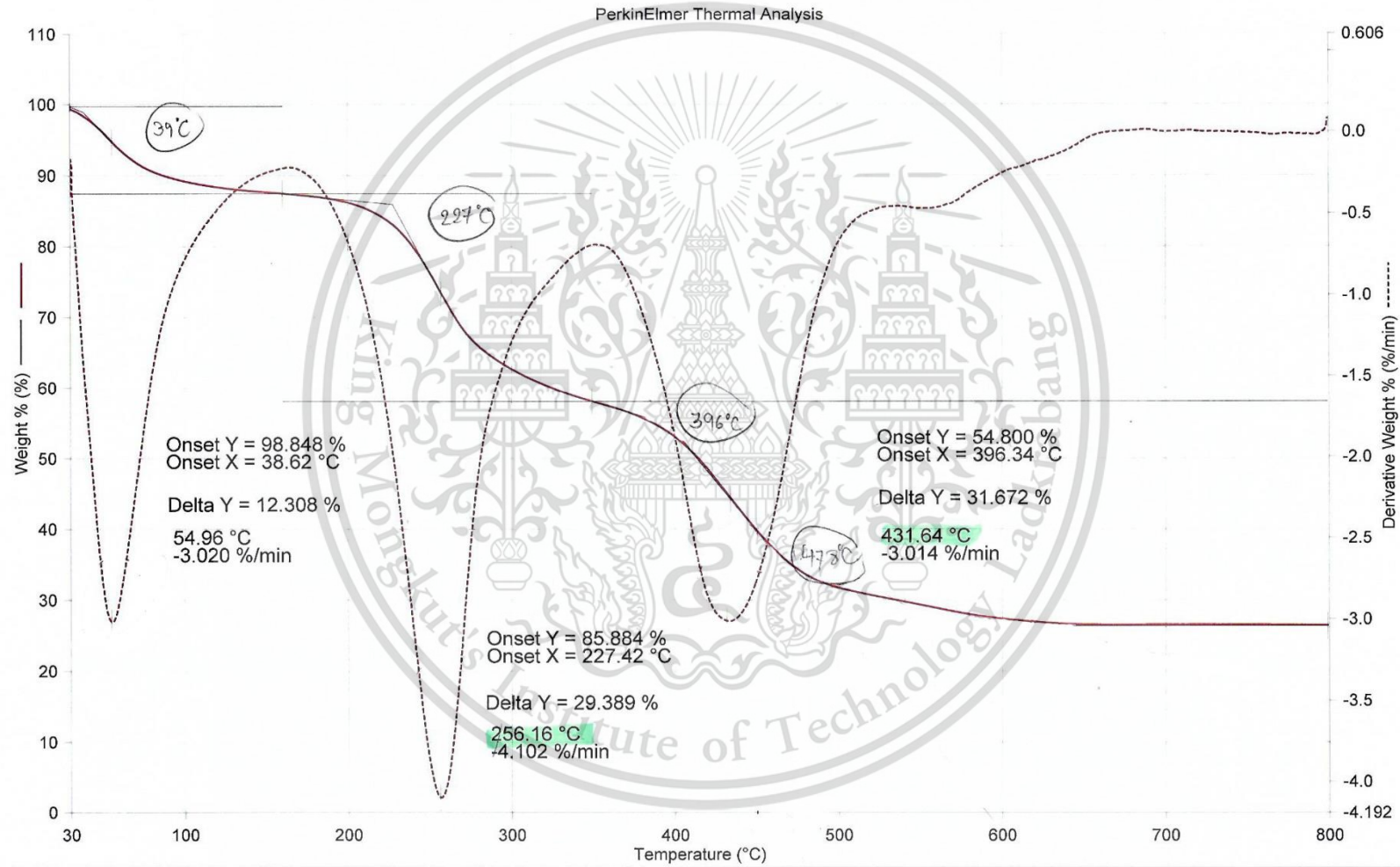
1) Heat from 50.00°C to 800.00°C at 10.00°C/min

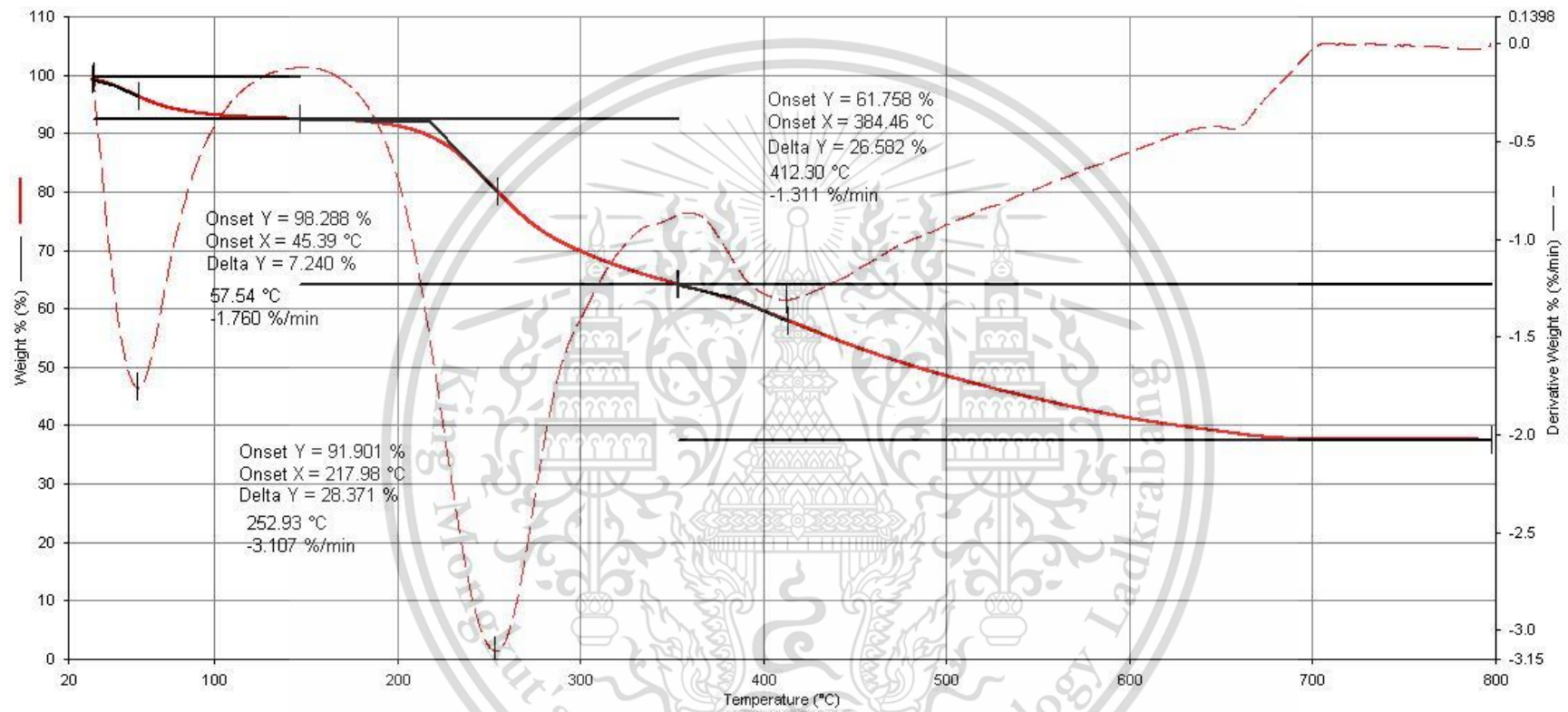


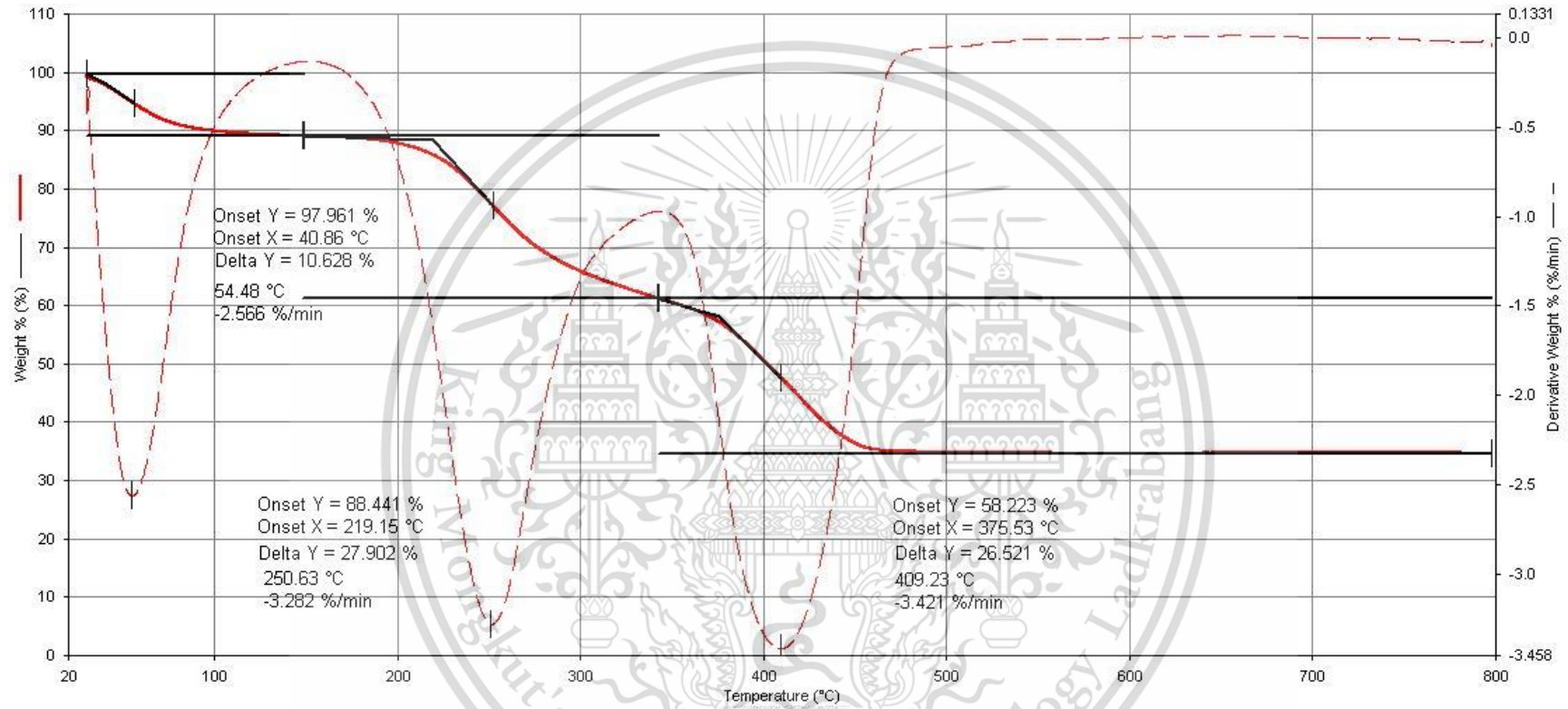


Filename: C:\Program ...TG60_064_03_CCR 1.67_N2.th1d
 Operator ID:
 Sample ID: CCR 1.67_N2
 Sample Weight: 4.823 mg
 Comment:

CC0.3/IO-R



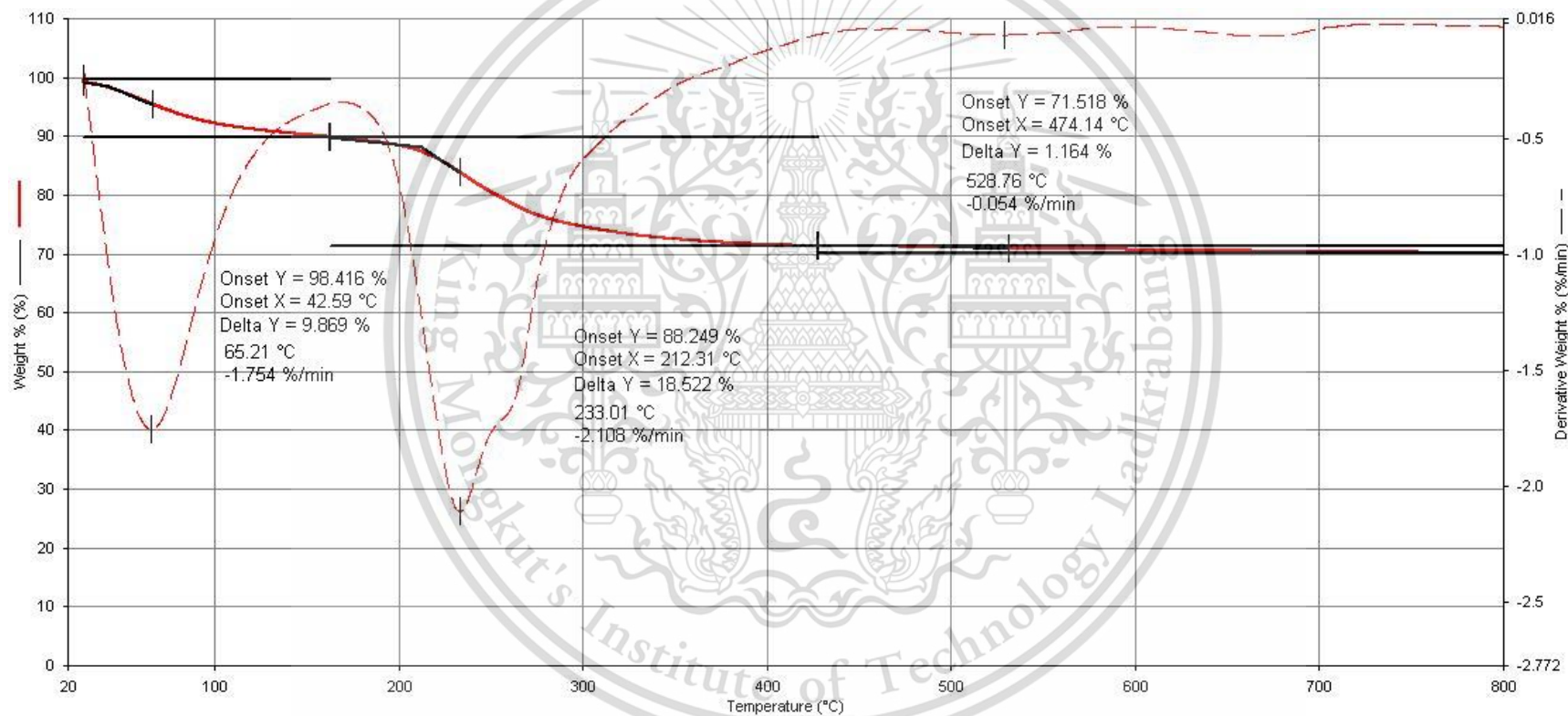


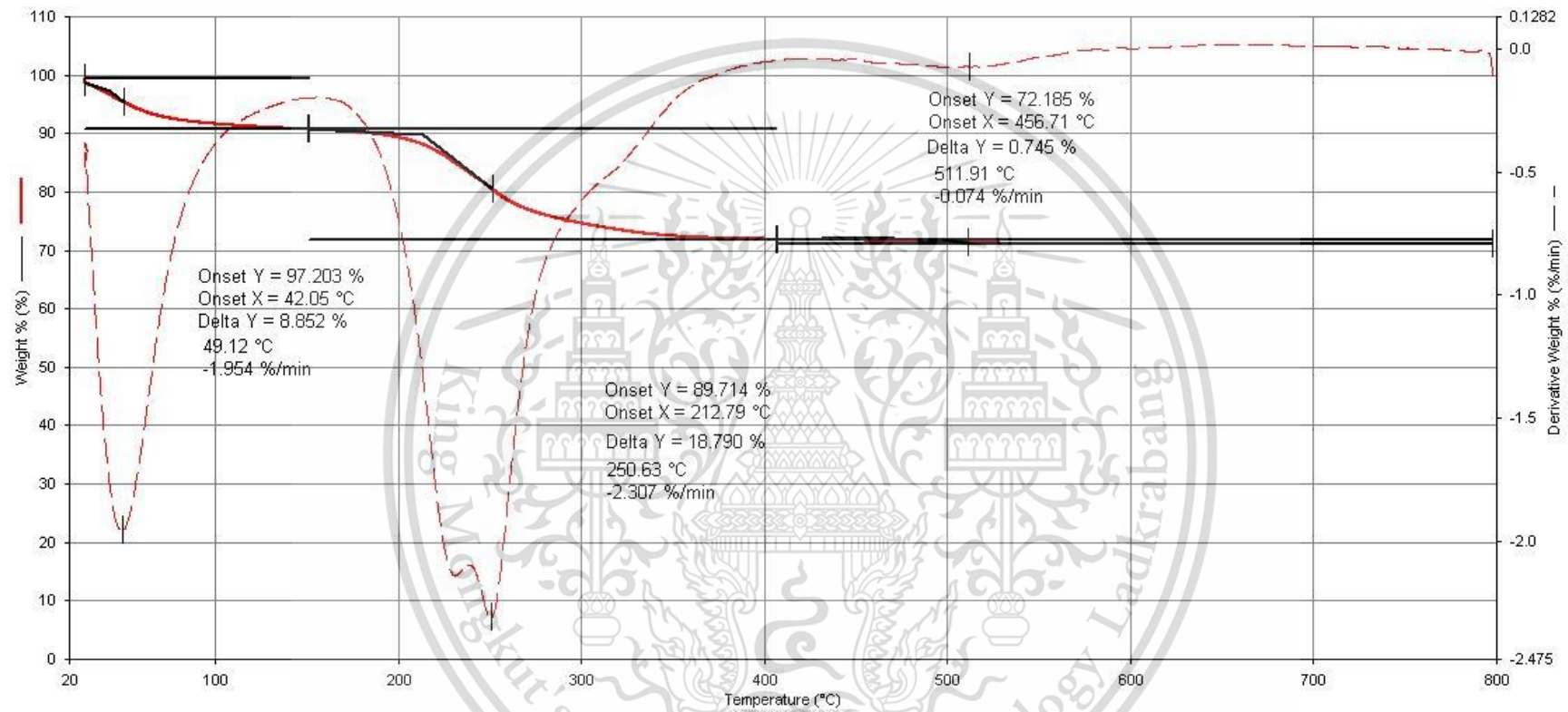


Appendix D

(TGA in O₂)

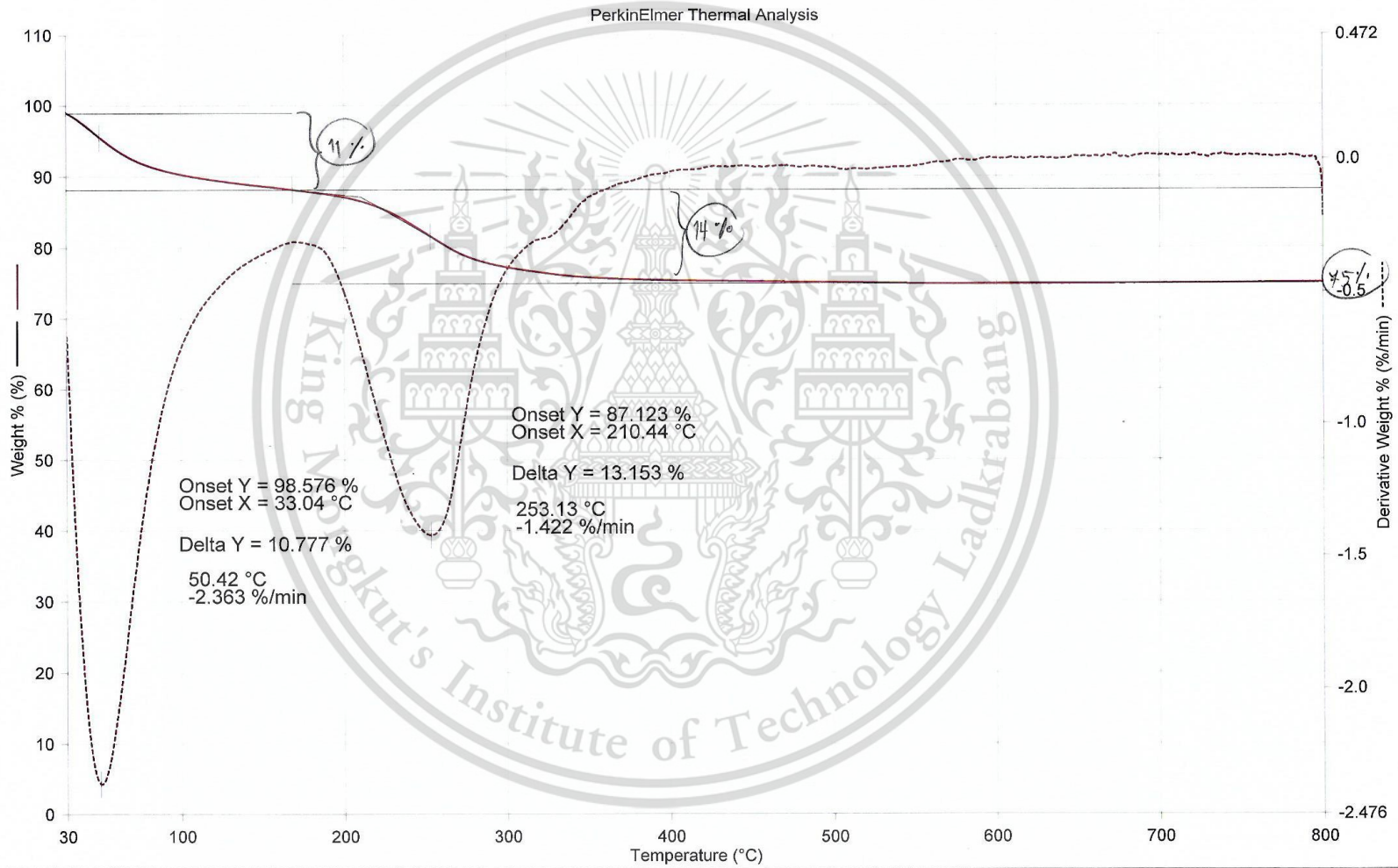
CS0.3/IO-HT75



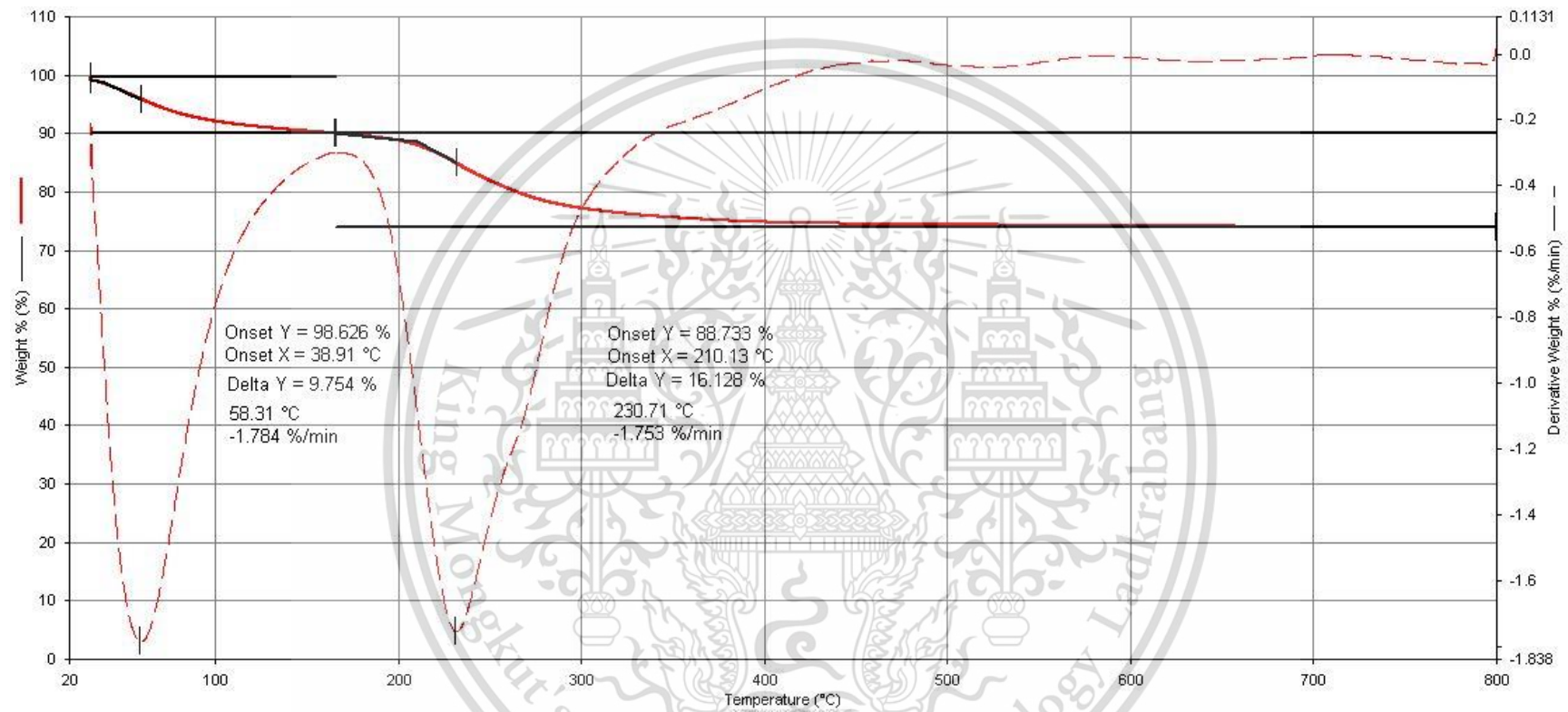


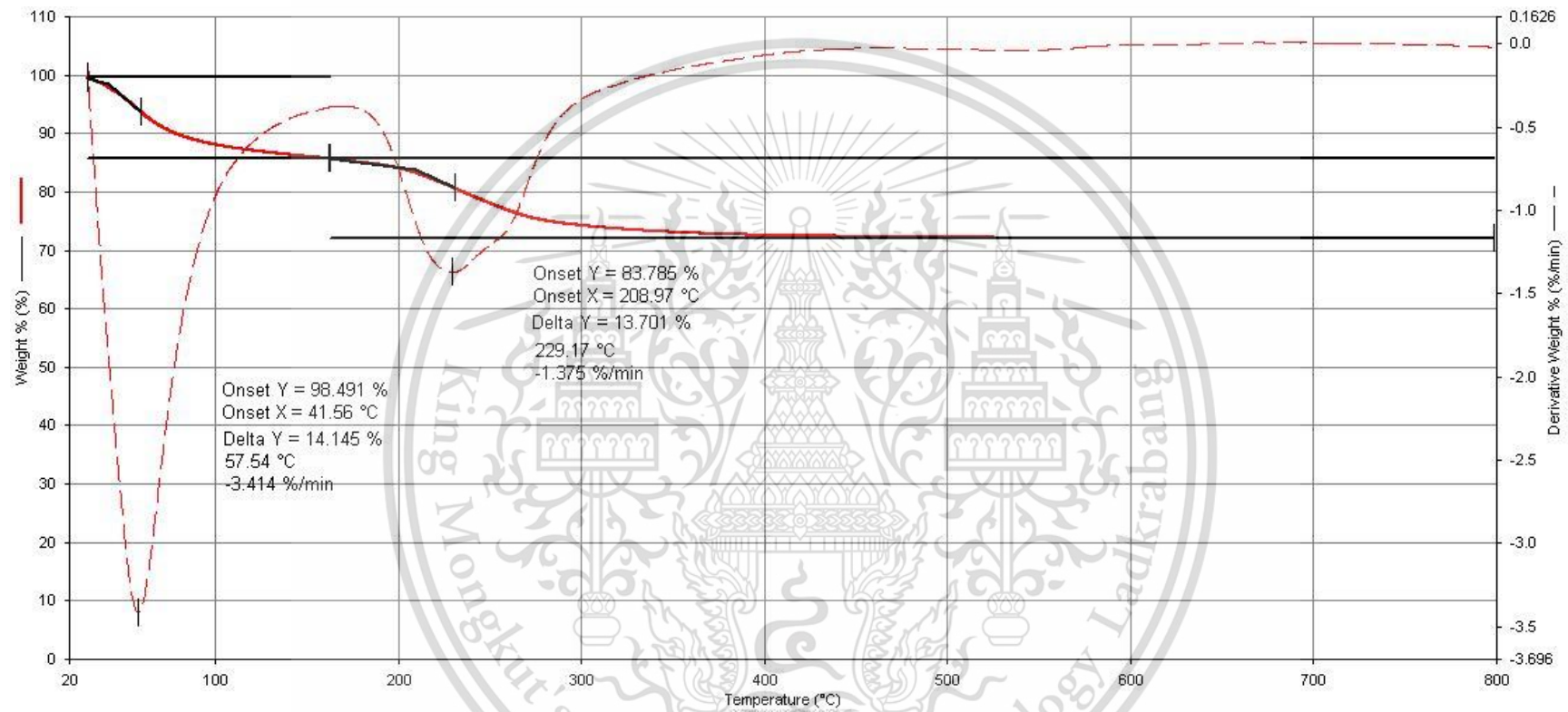
Filename: C:\Program F...\TG60_063_06_HT 1.67_O2.th1d
Operator ID:
Sample ID: HT 1.67_O2
Sample Weight: 4.909 mg
Comment:

CS0.3/IO-HT100



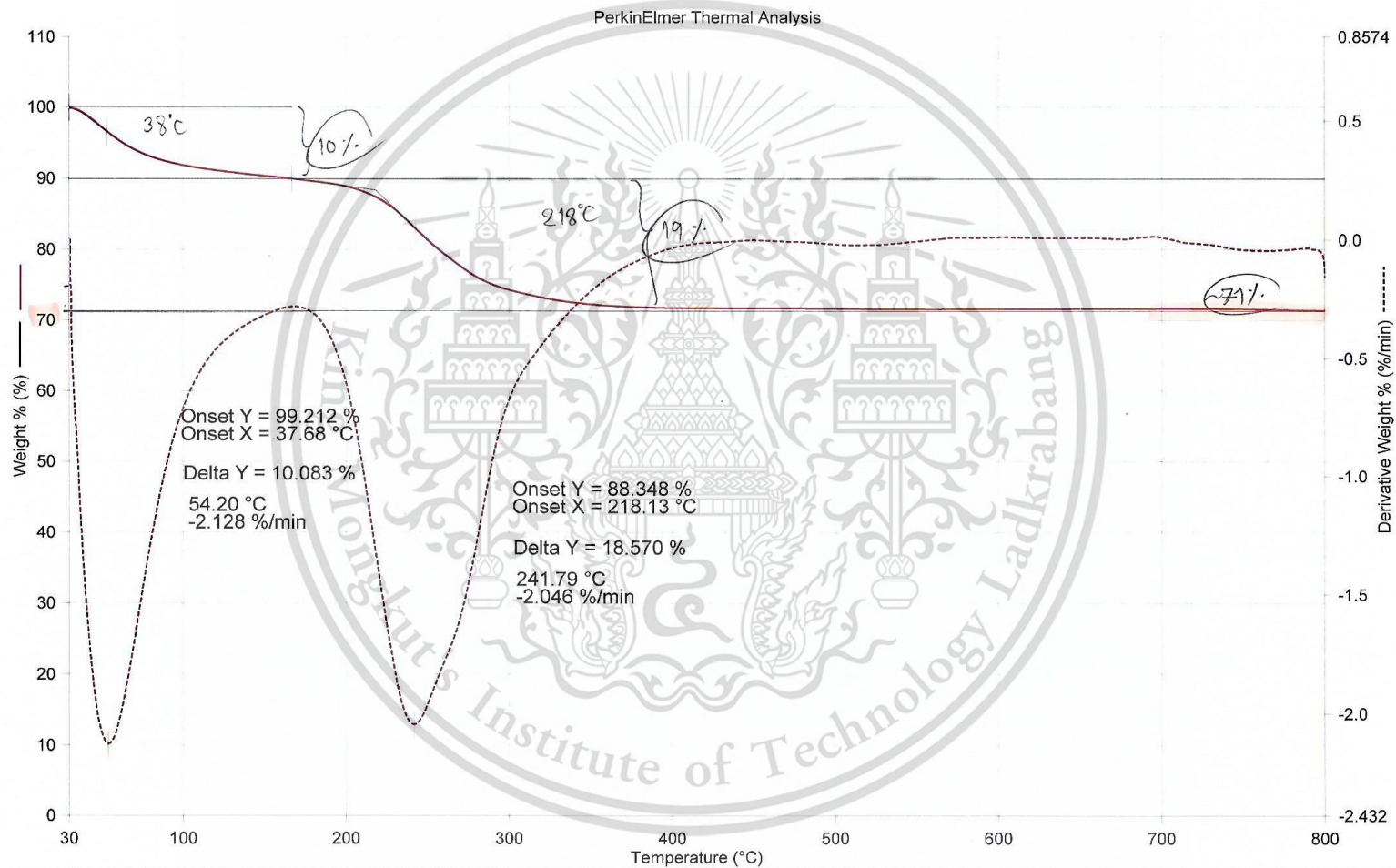
1) Heat from 50.00°C to 800.00°C at 10.00°C/min



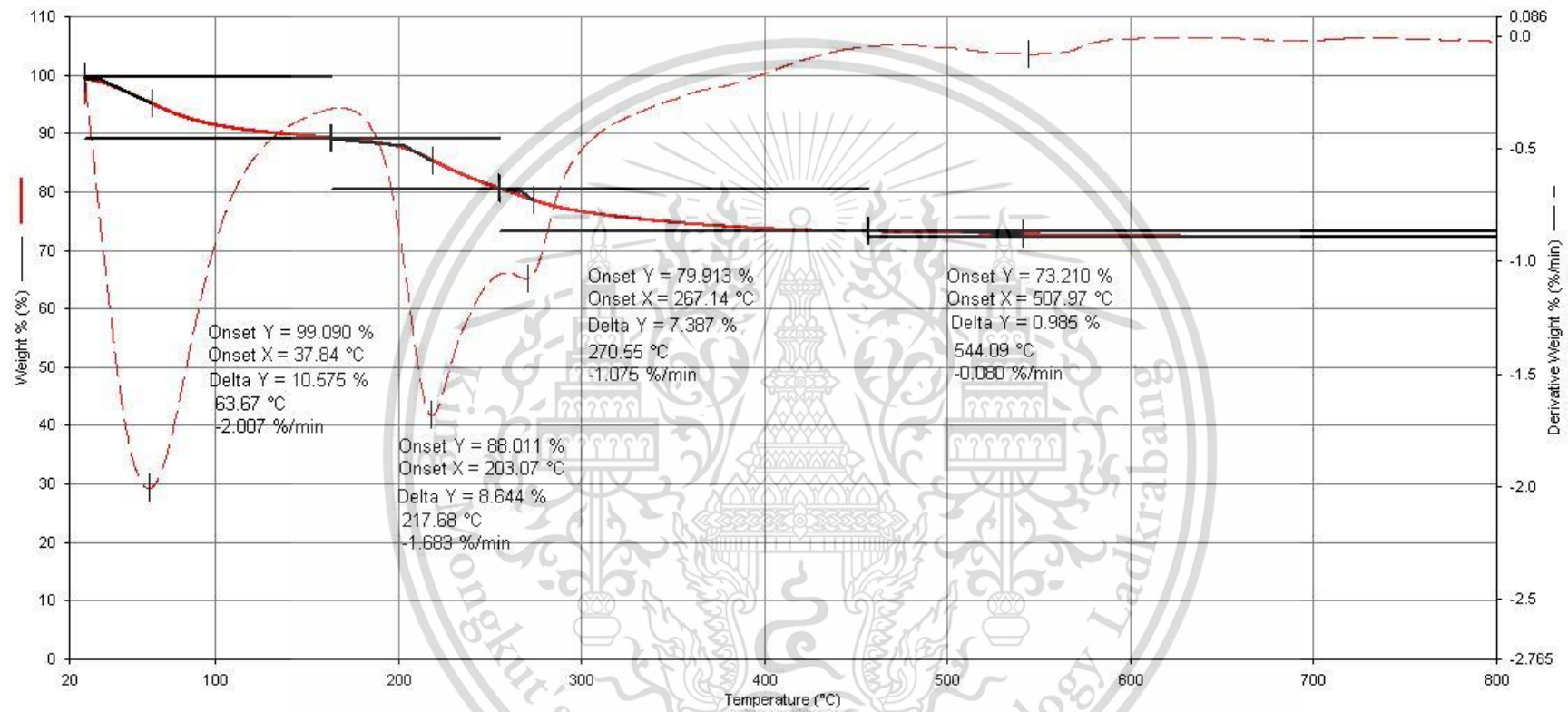


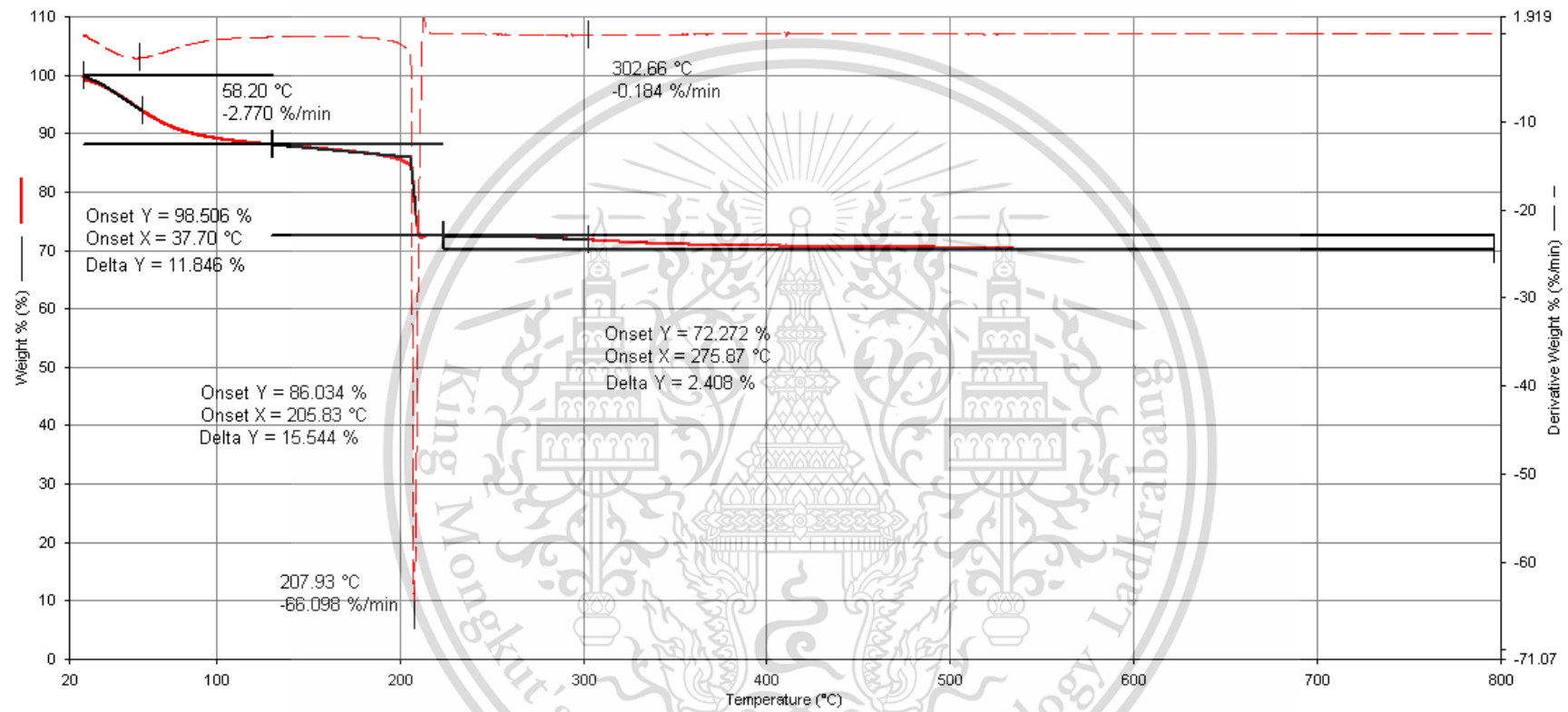
Filename: C:\Program Files\IP...\TG60_015_02_3_O2.th1d
Operator ID:
Sample ID: HT 3
Sample Weight: 3.181 mg
Comment:

CS0.6/IO-HT100



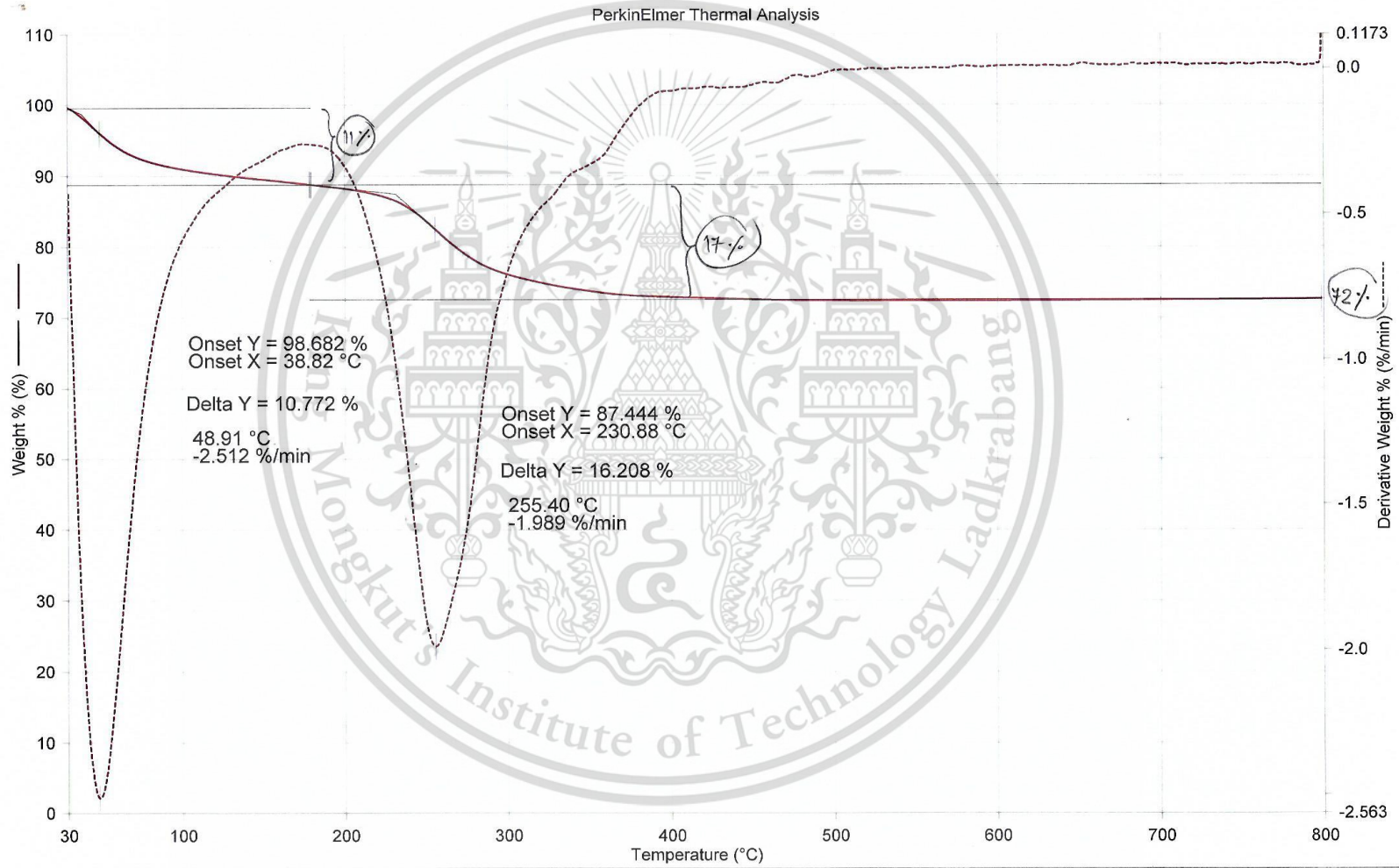
1) Heat from 35.00°C to 800.00°C at 10.00°C/min

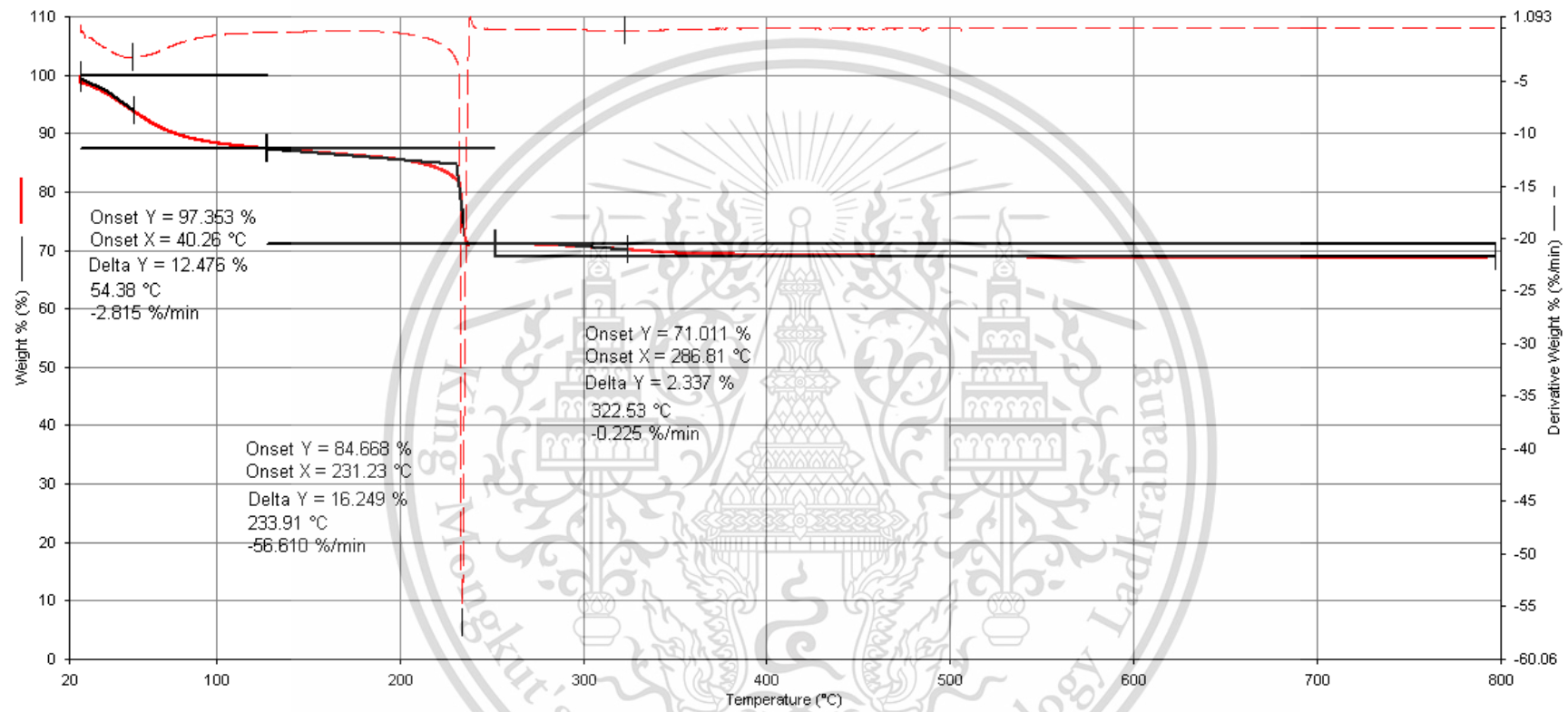


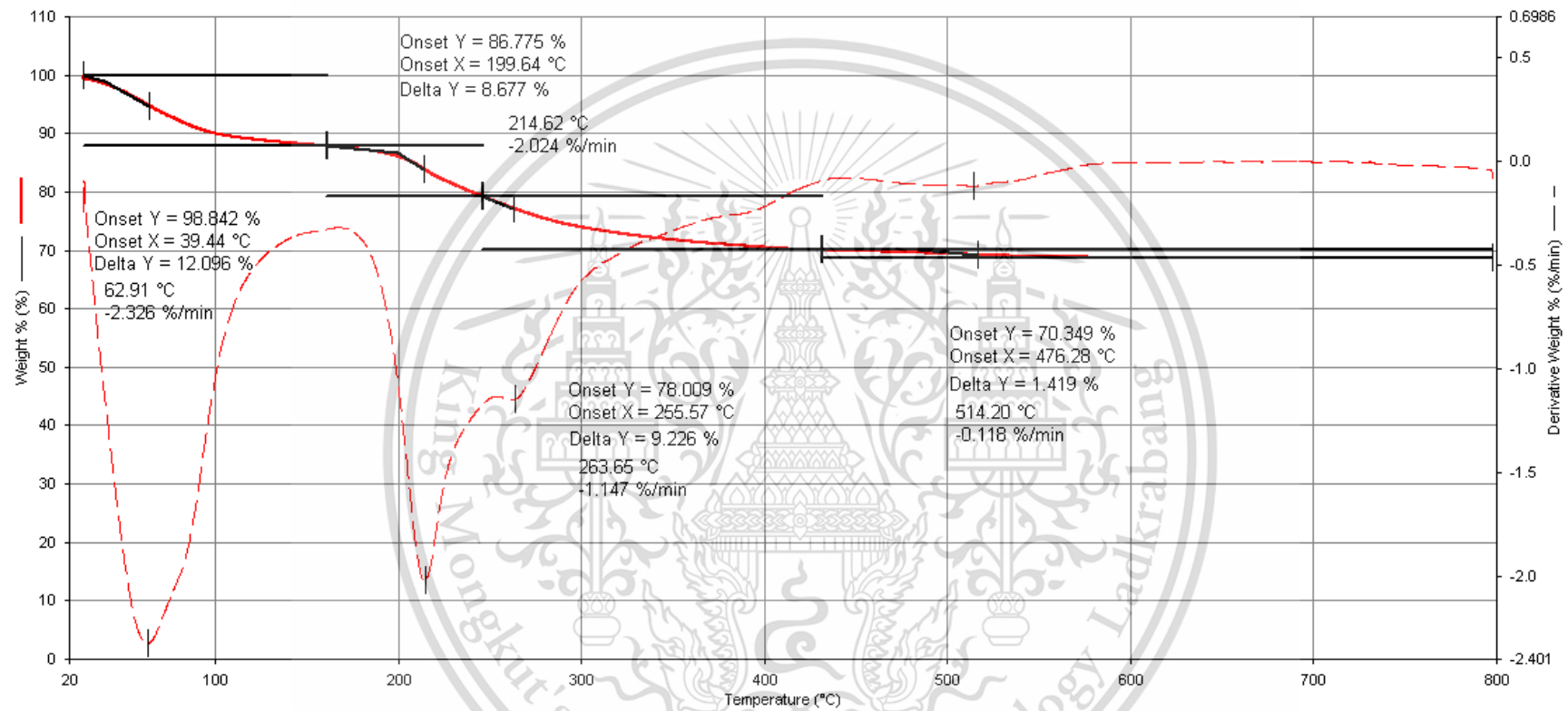


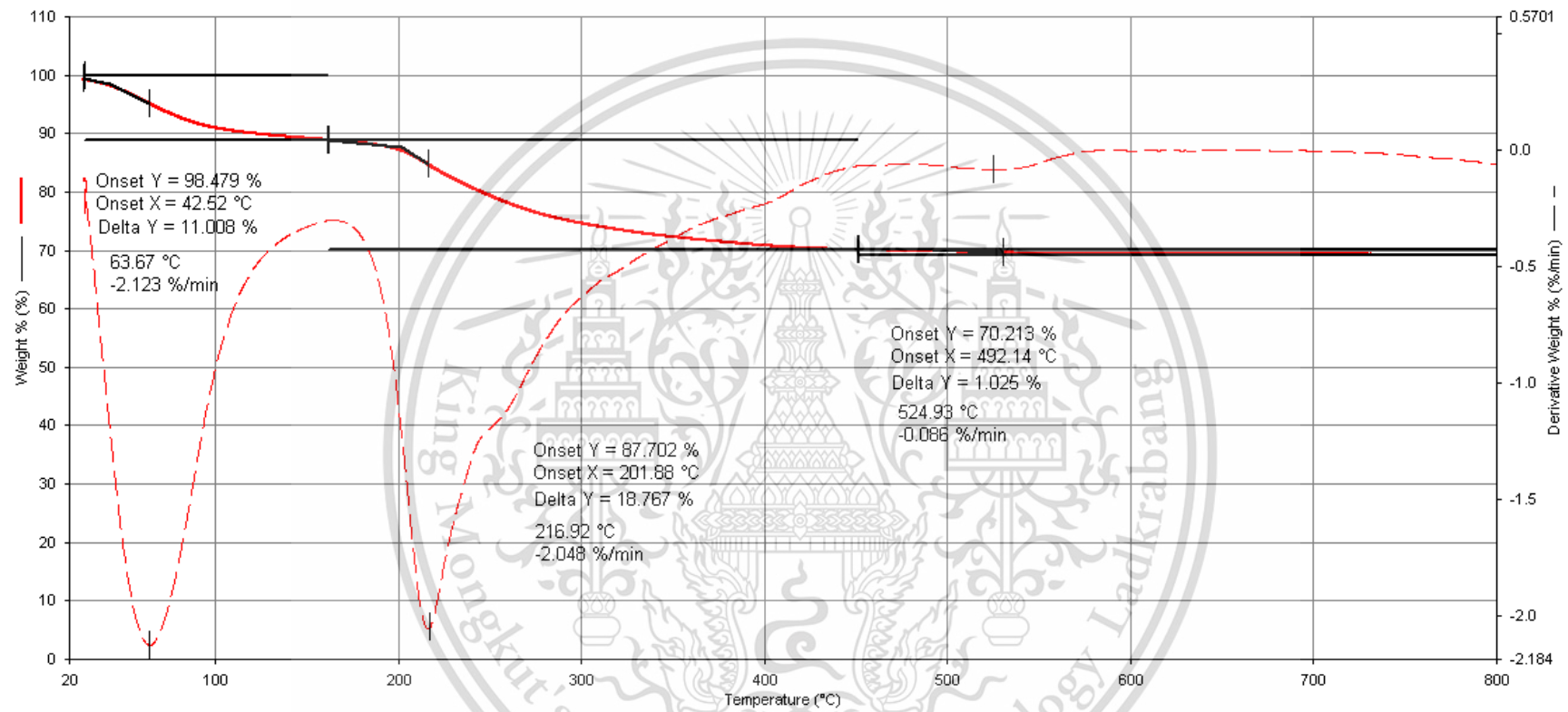
Filename: C:\Program Fi...TG60_063_03_R 1.67_O2.th1d
Operator ID:
Sample ID: R 1.67_O2
Sample Weight: 4.006 mg
Comment:

CS0.3/IO-R



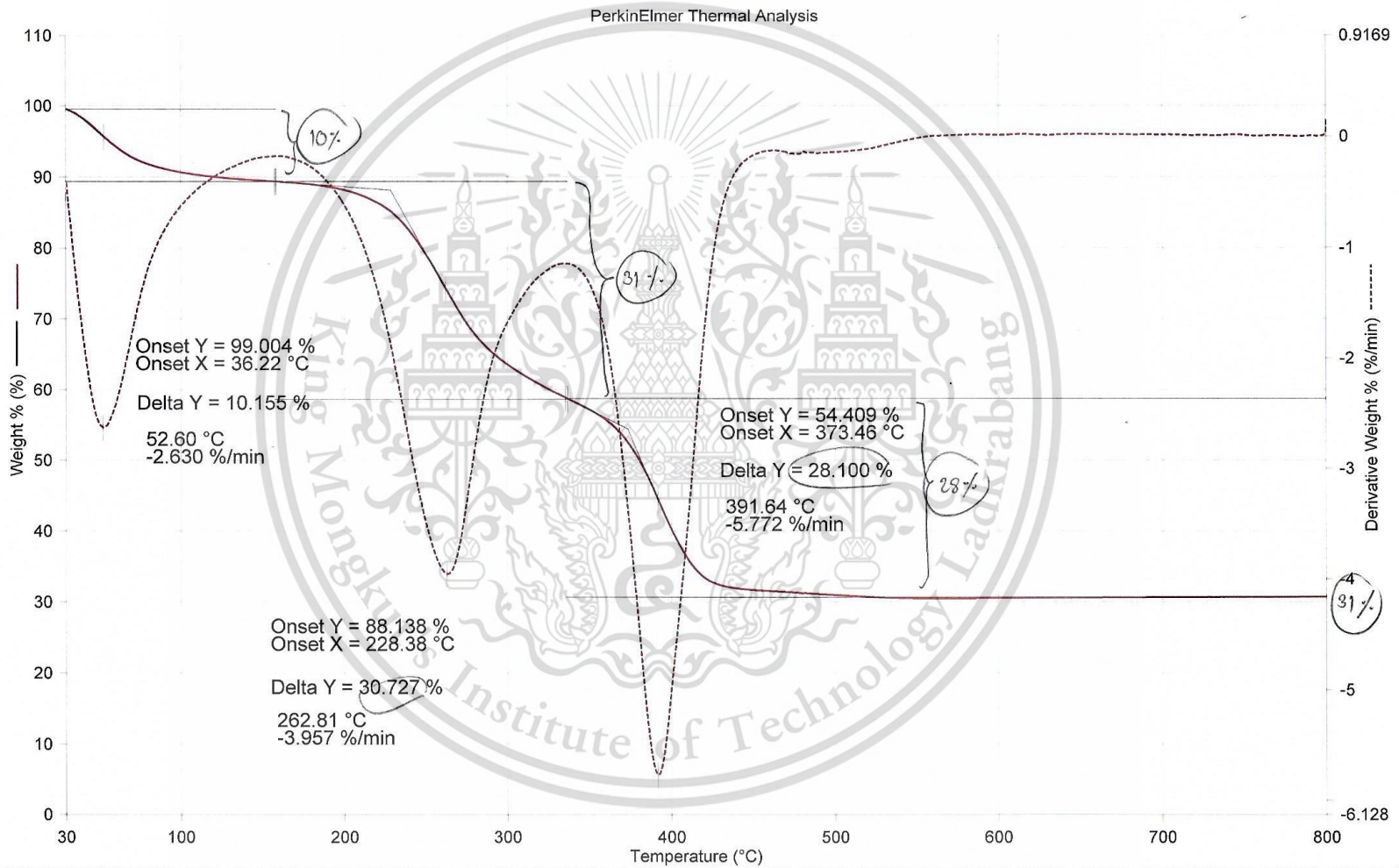


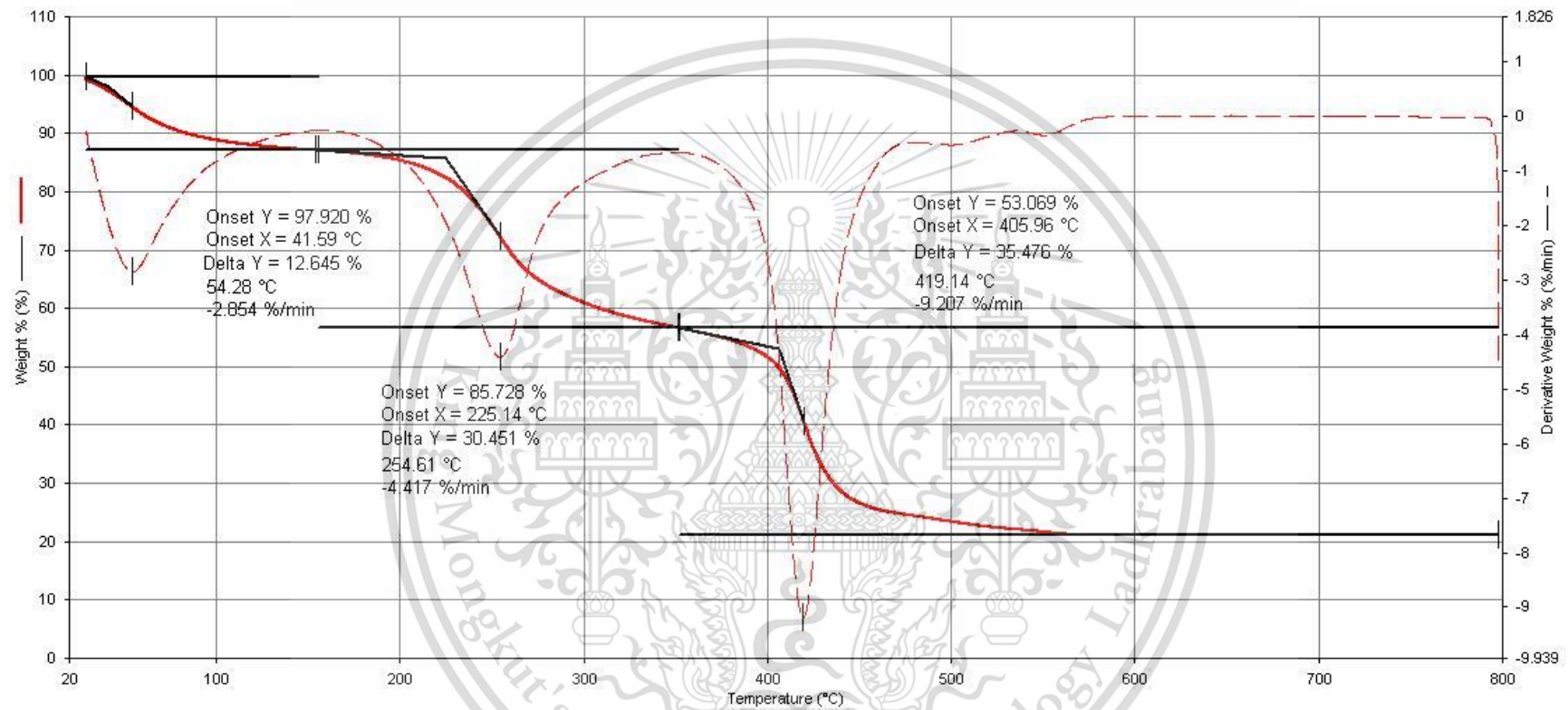


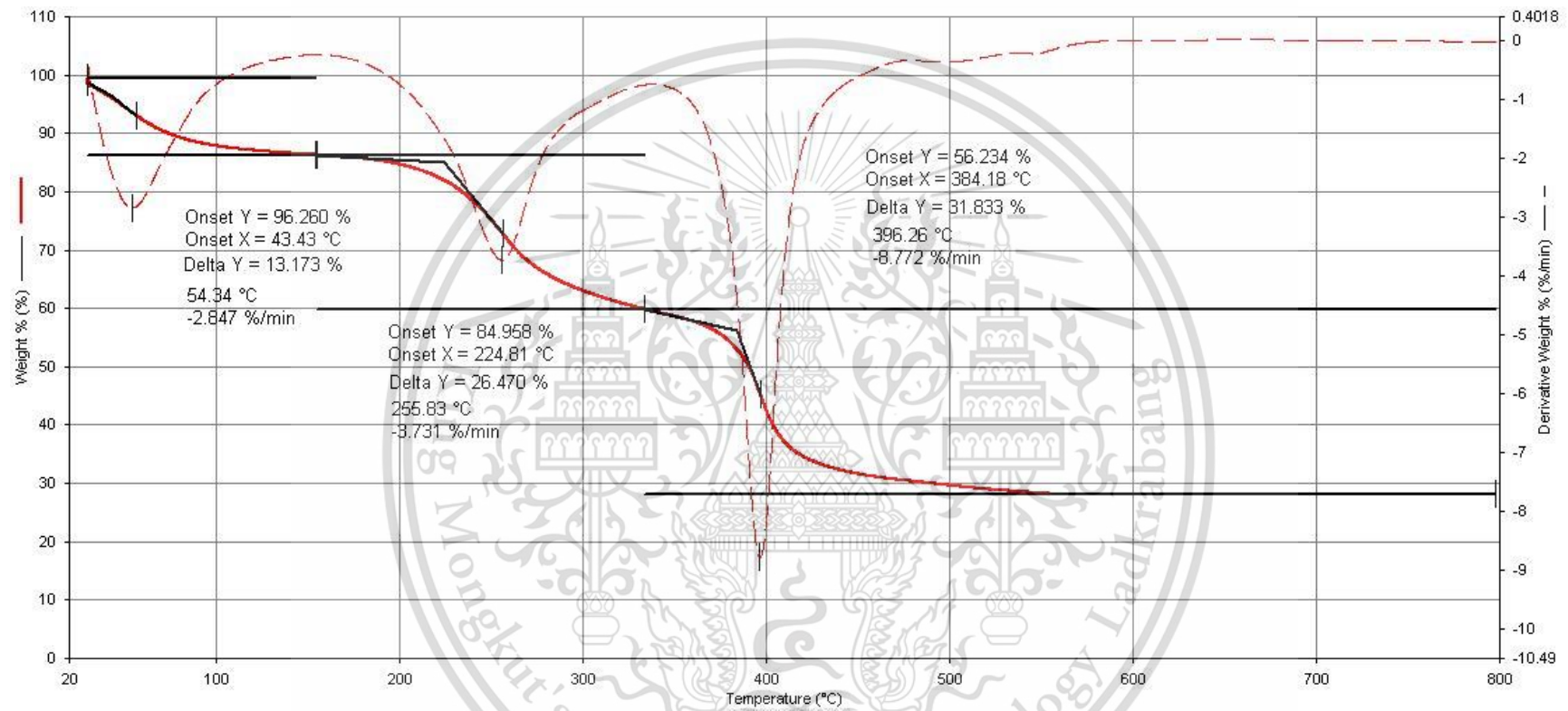


Filename: C:\Program...ITG60_063_05_CCHT 1.67_O2.th1d
 Operator ID:
 Sample ID: CCHT 1.67_O2
 Sample Weight: 3.907 mg
 Comment:

CC0.3/IO-HT100

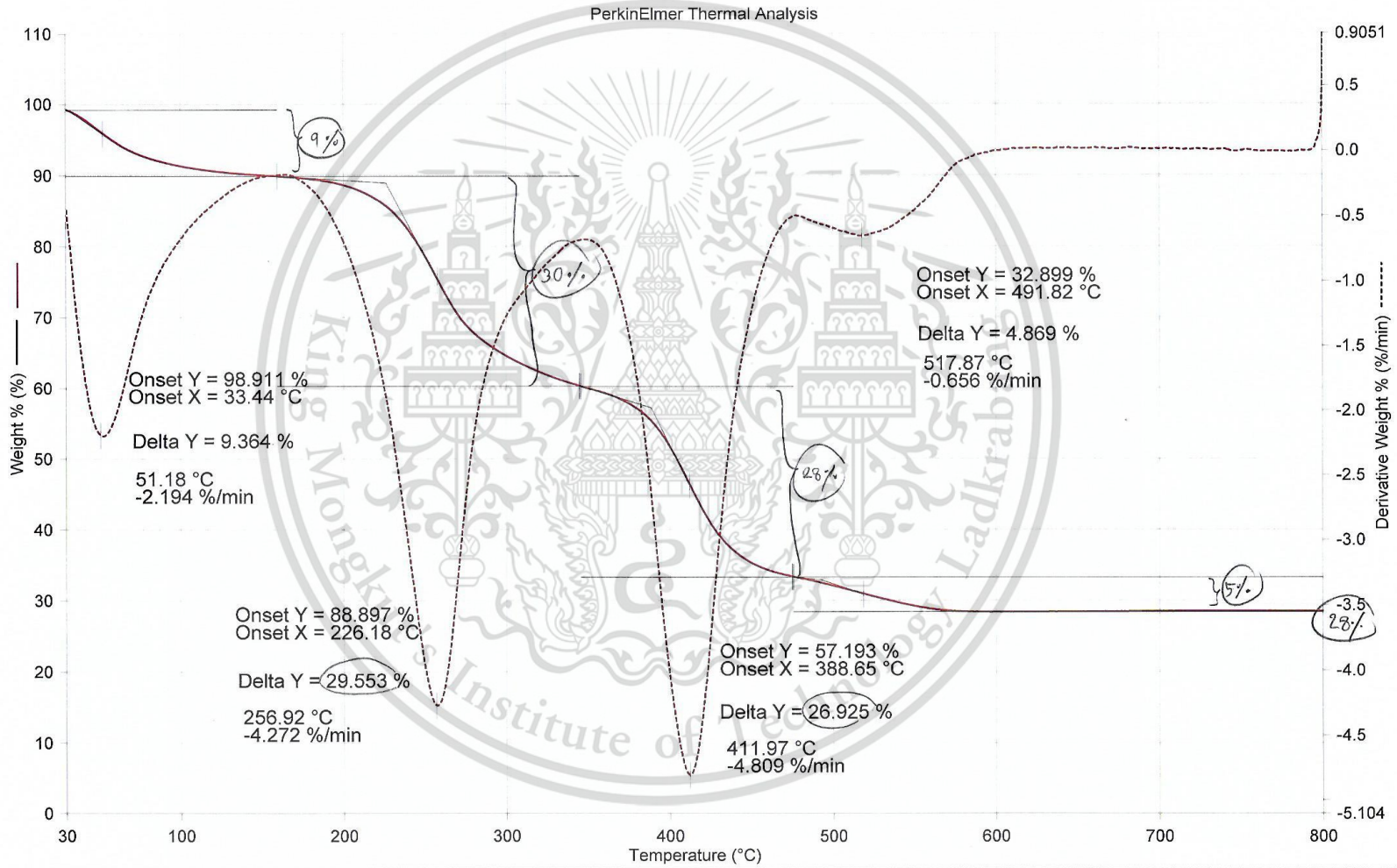


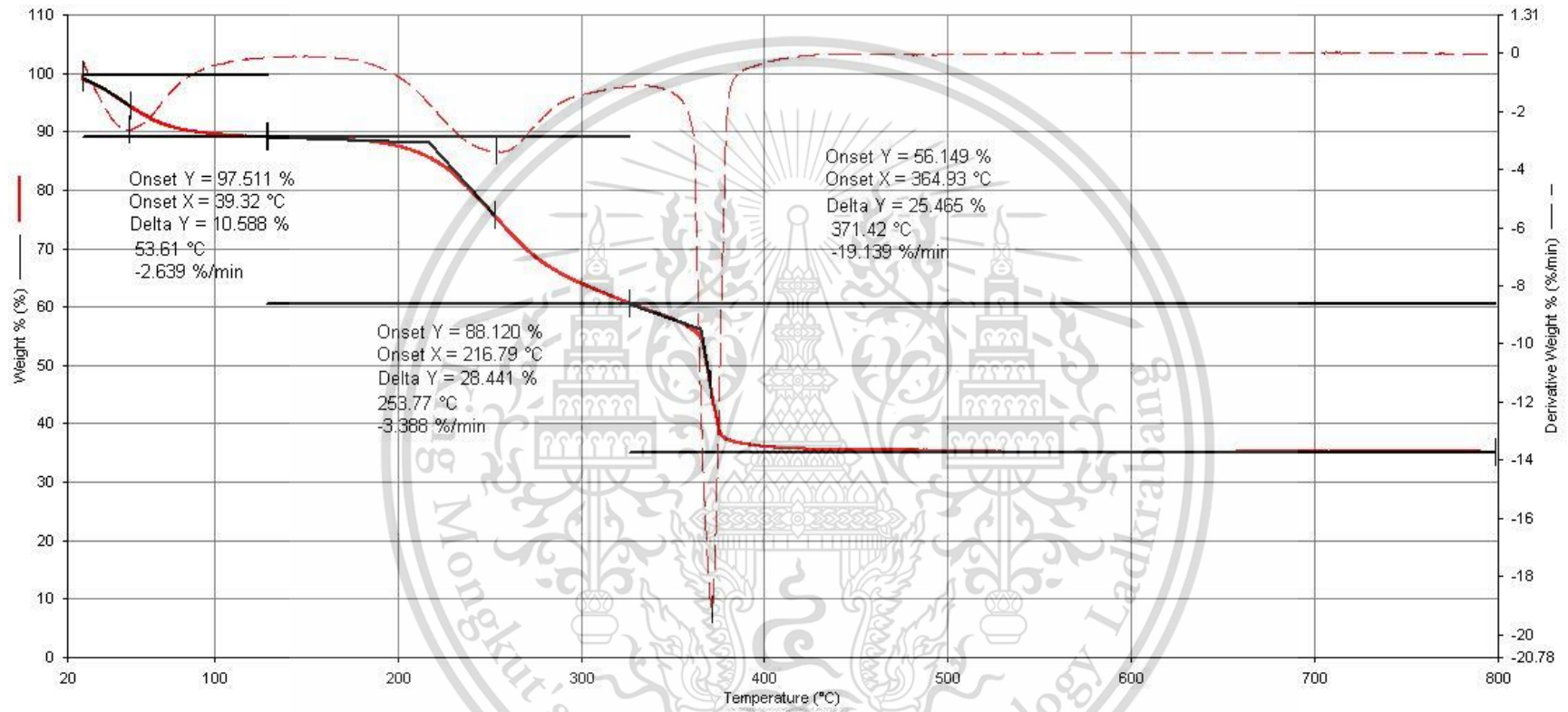


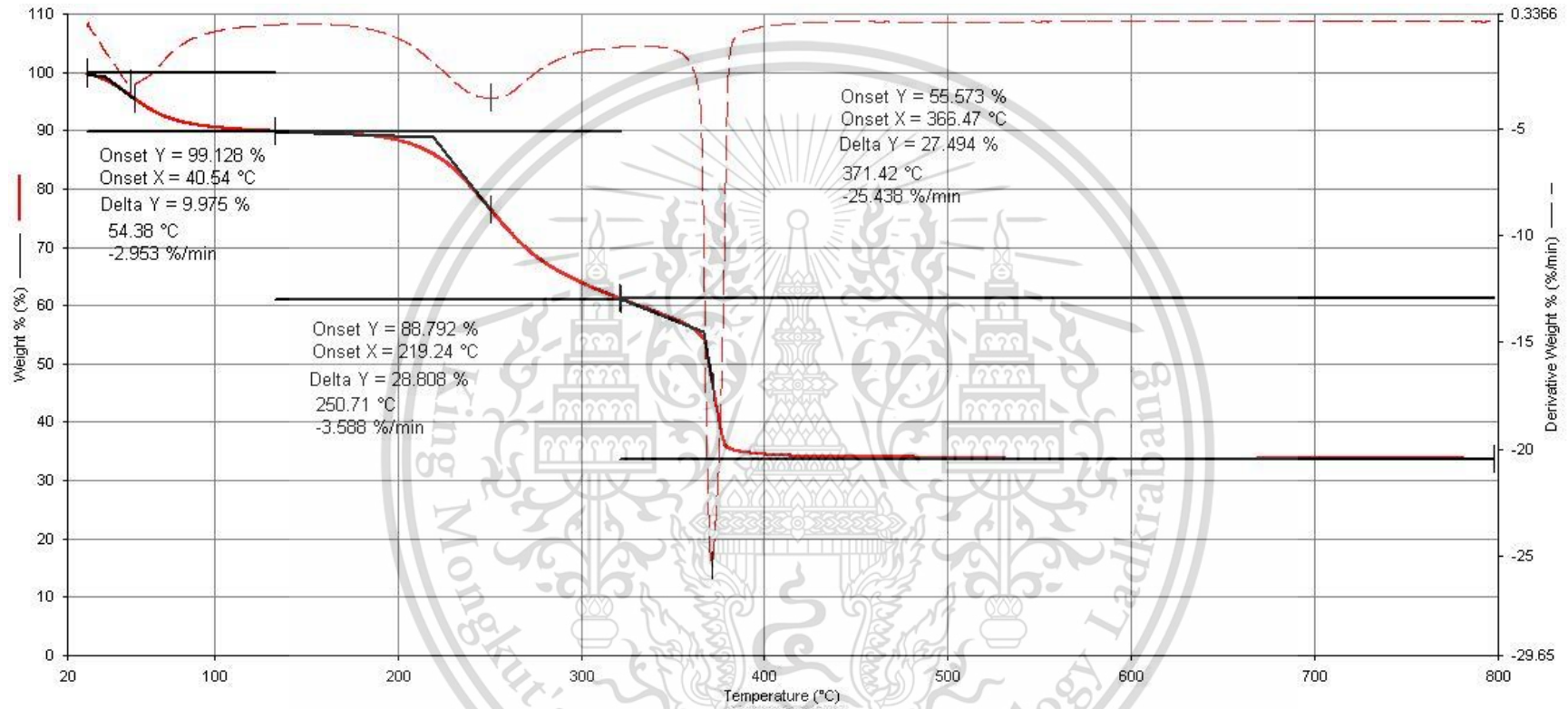


Filename: C:\Program ...TG60_063_04_CCR 1.67_O2.th1d
 Operator ID:
 Sample ID: CCR 1.67_O2
 Sample Weight: 3.780 mg
 Comment:

CC0.3/IO-R

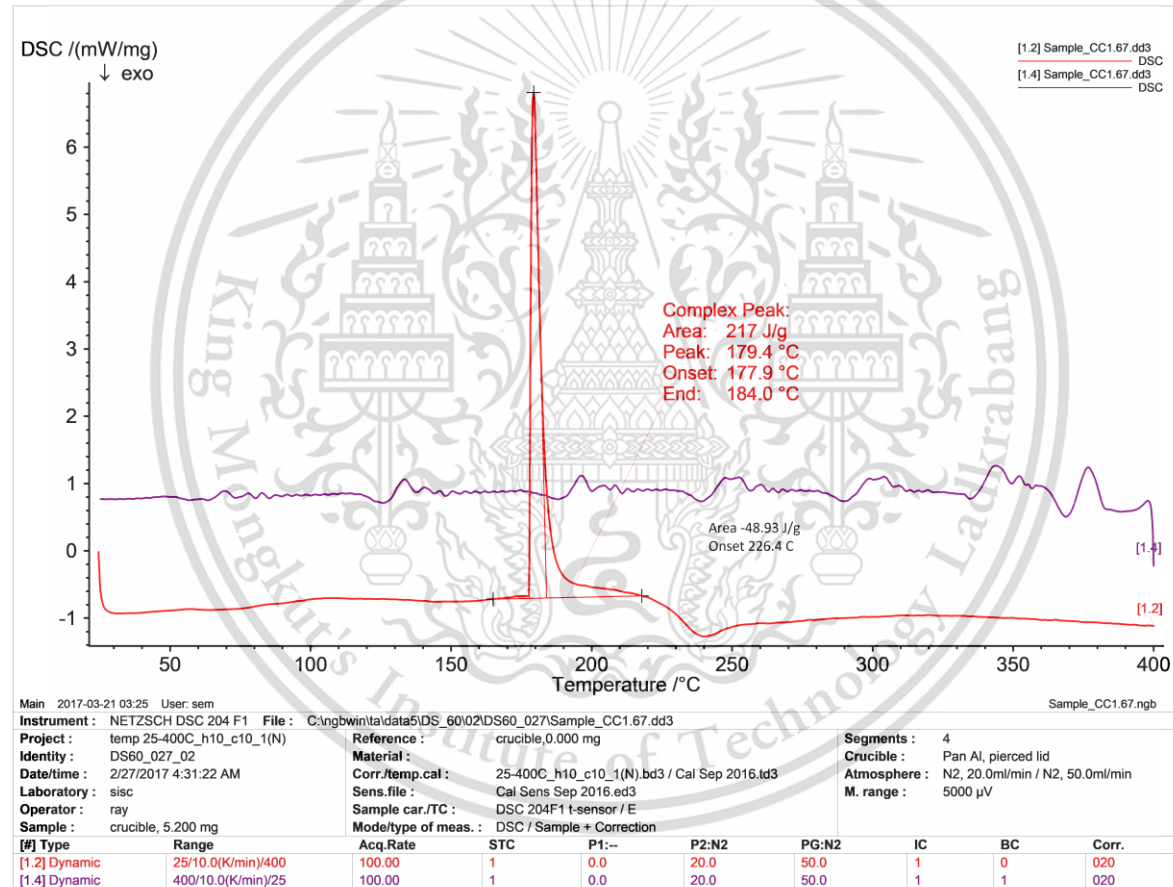


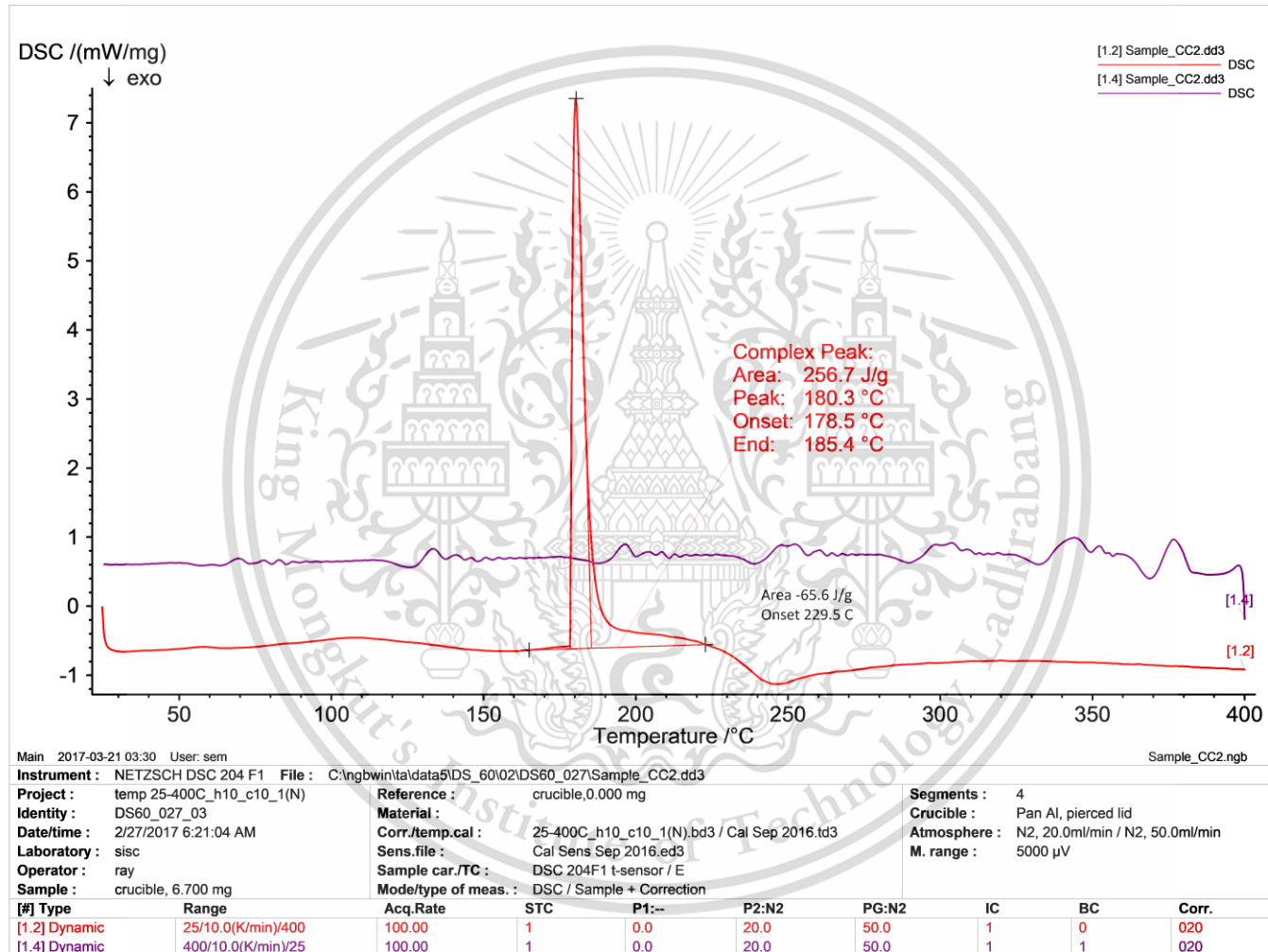


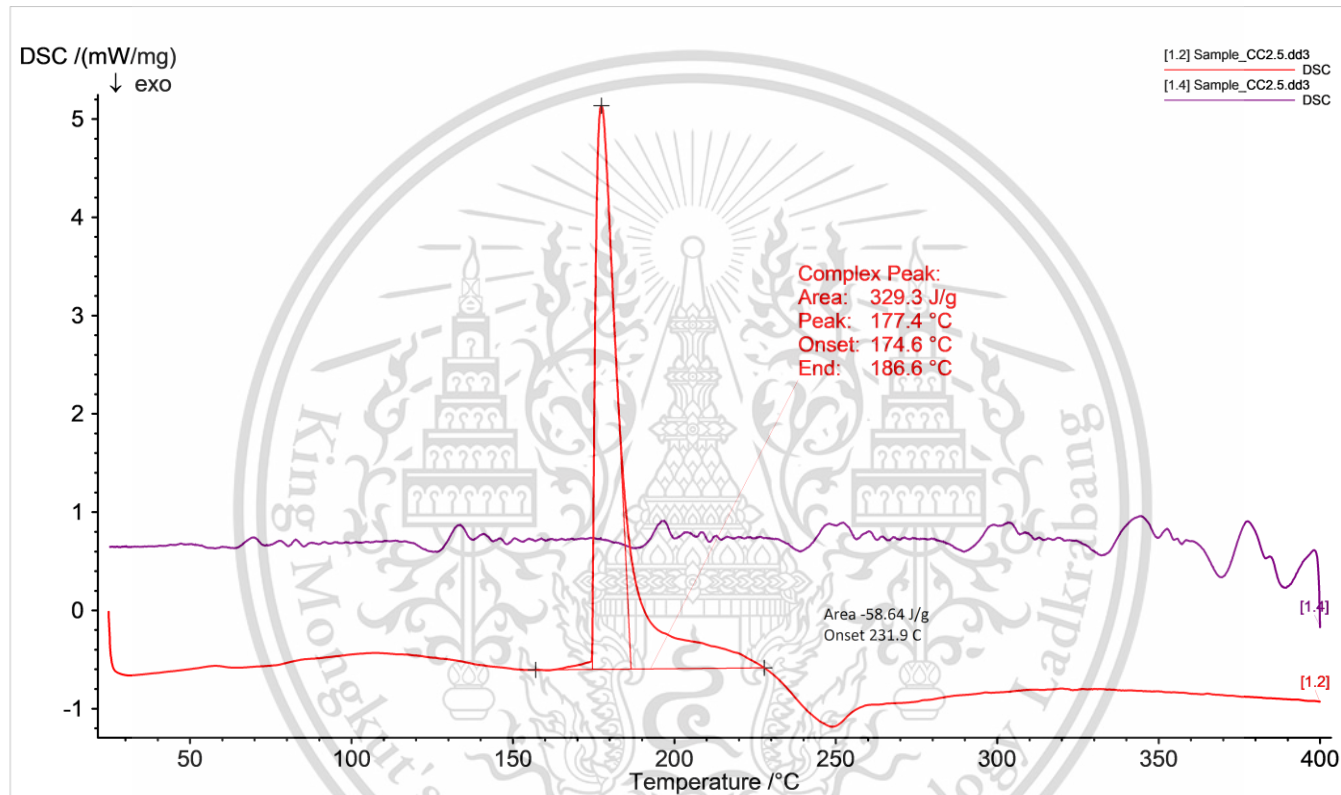


Appendix E

CC0.3





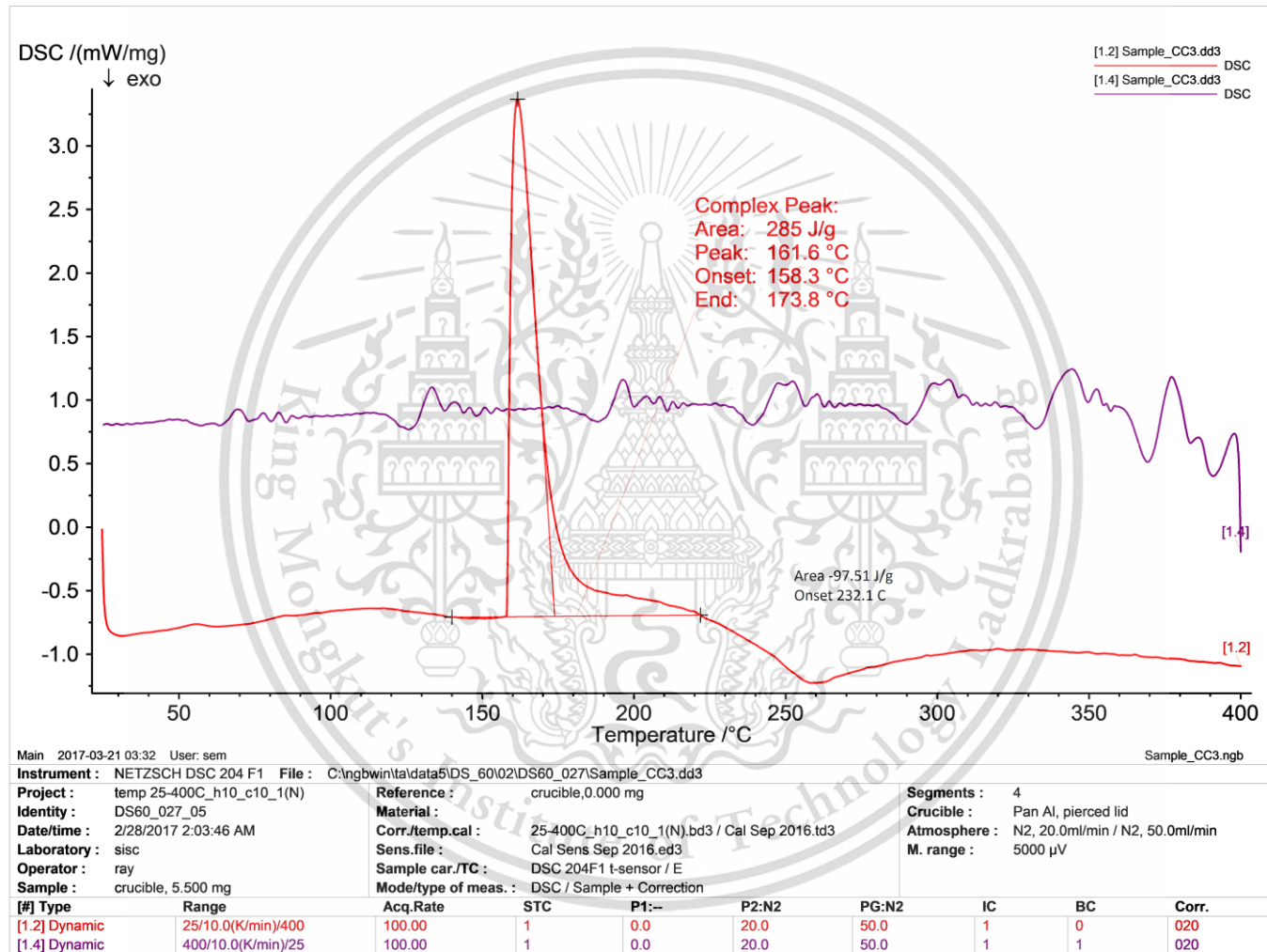


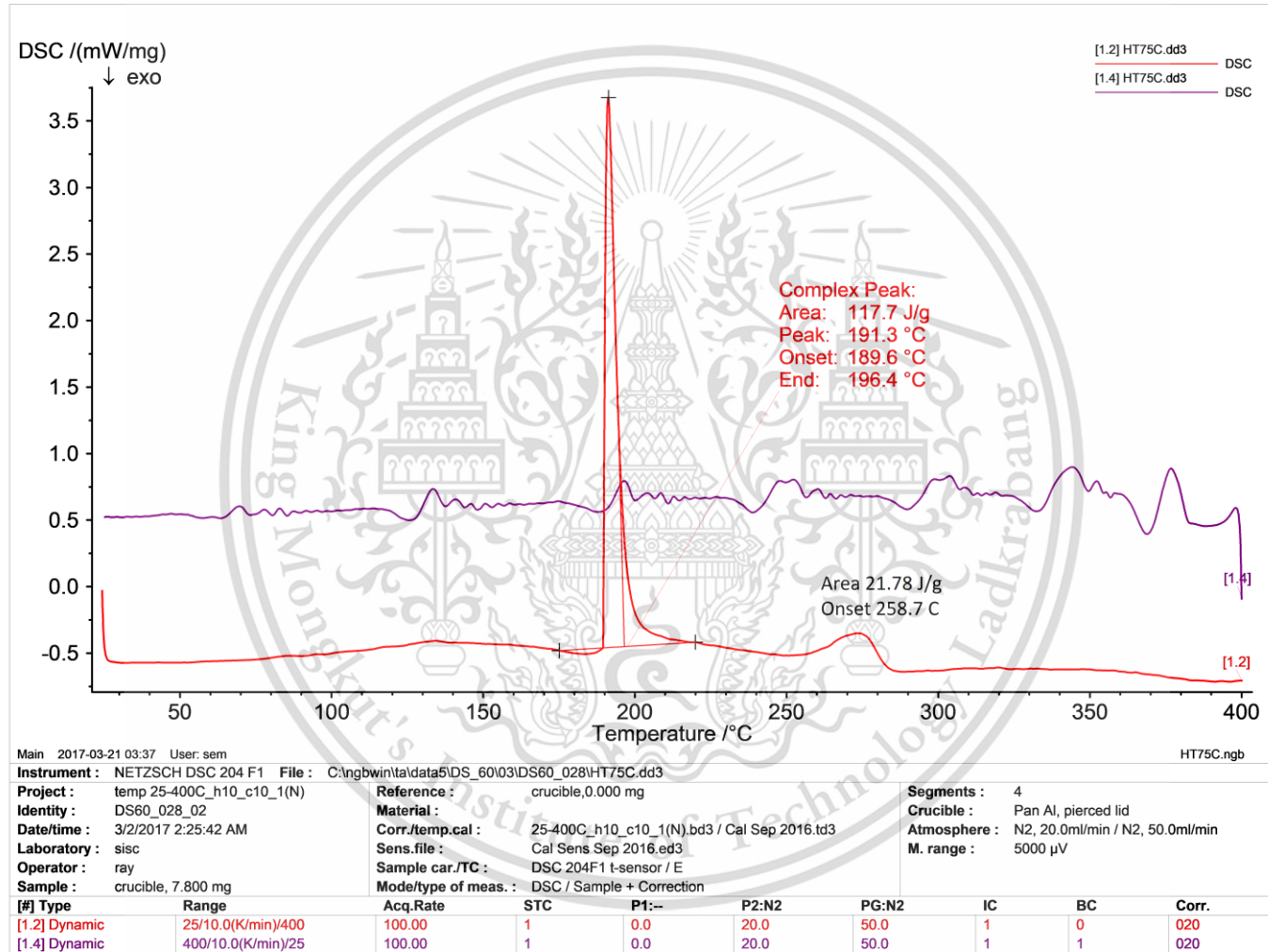
Main 2017-03-21 03:29 User: sem Sample_CC2.5.ngb

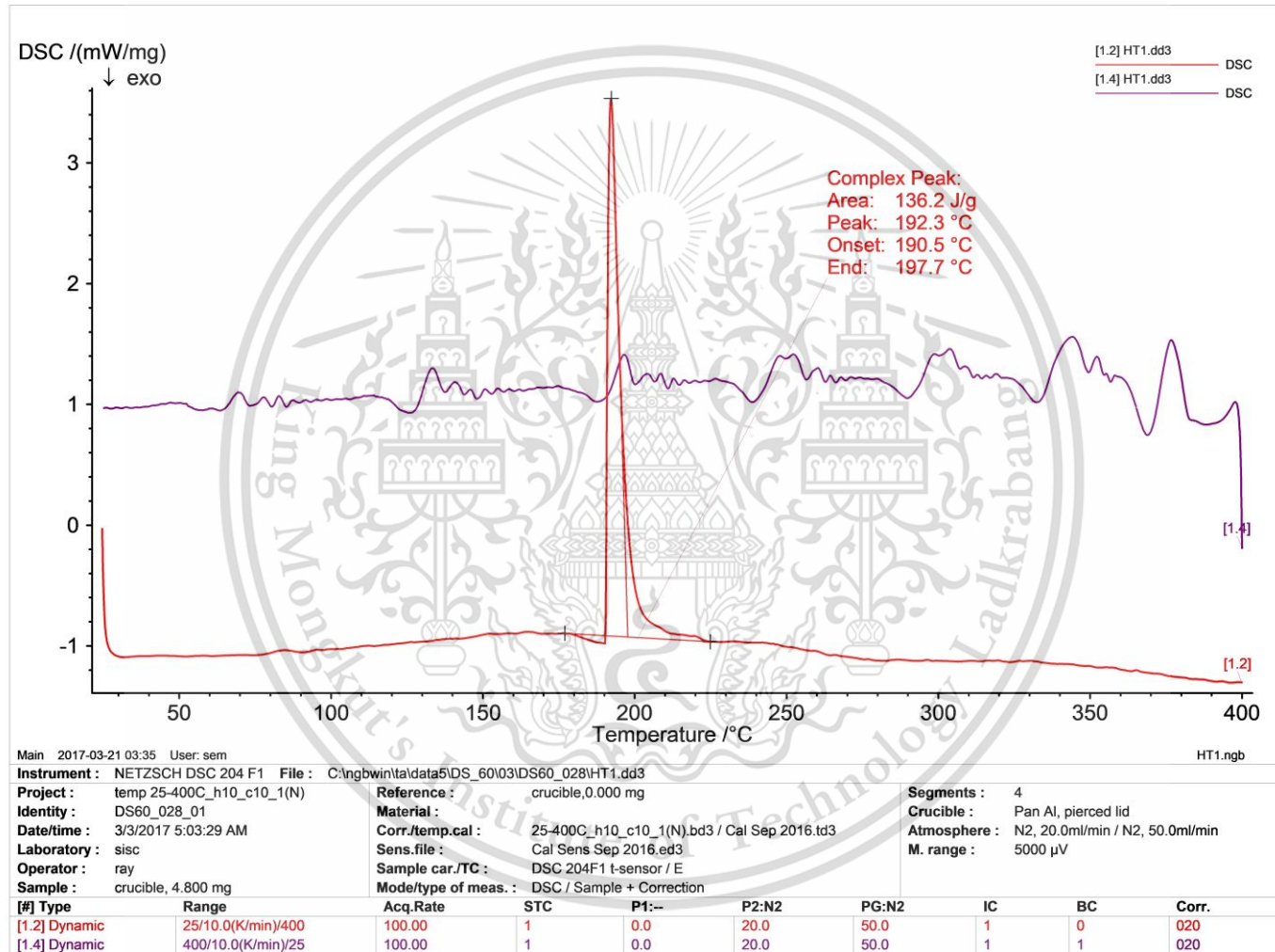
Instrument: NETZSCH DSC 204 F1 **File:** C:\ngbwin\ta\data5\DS_60102\DS60_027\Sample_CC2.5.dd3

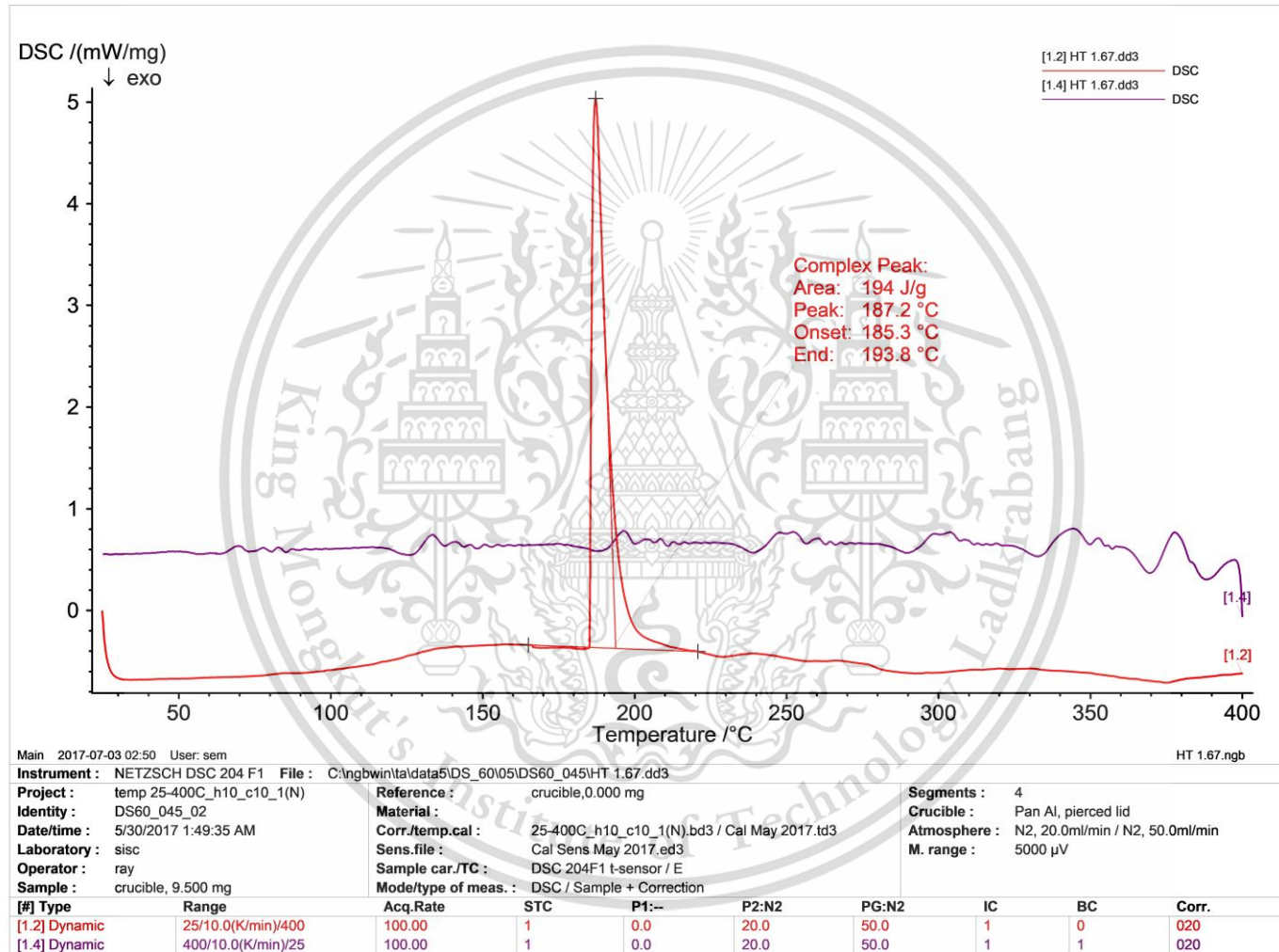
Project: temp 25-400C_h10_c10_1(N)	Reference: crucible,0.000 mg	Segments: 4
Identity: DS60_027_04	Material:	Crucible: Pan Al, pierced lid
Date/time: 2/28/2017 12:19:03 AM	Corr./temp.cal: 25-400C_h10_c10_1(N).bd3 / Cal Sep 2016.td3	Atmosphere: N2, 20.0ml/min / N2, 50.0ml/min
Laboratory: sisc	Sens.file: Cal Sens Sep 2016.ed3	M. range: 5000 µV
Operator: ray	Sample car./TC: DSC 204F1 t-sensor / E	
Sample: crucible, 6.500 mg	Mode/type of meas.: DSC / Sample + Correction	

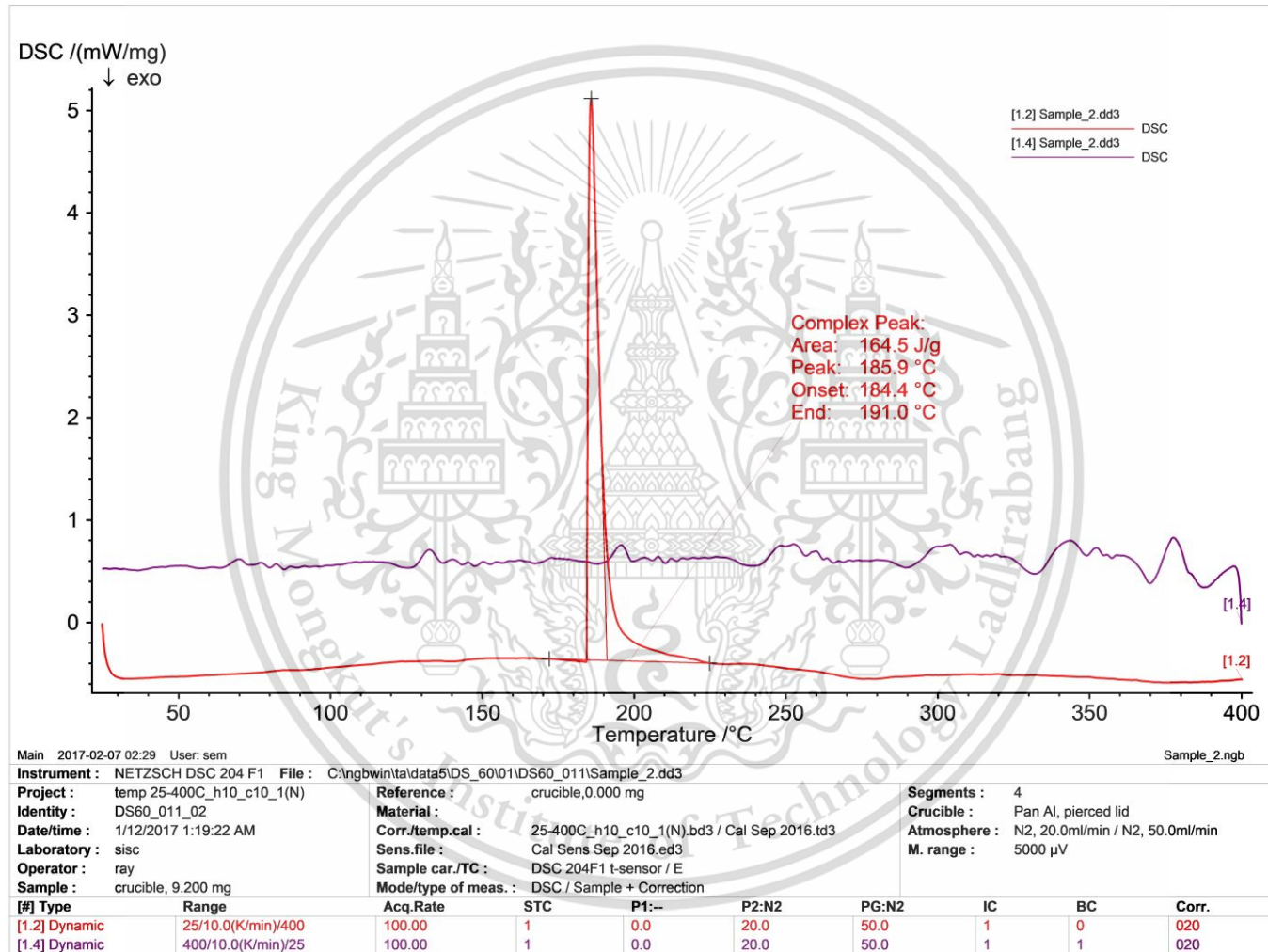
[#]	Type	Range	Acq.Rate	STC	P1:-	P2:N2	PG:N2	IC	BC	Corr.
[1.2]	Dynamic	25/10.0(K/min)/400	100.00	1	0.0	20.0	50.0	1	0	020
[1.4]	Dynamic	400/10.0(K/min)/25	100.00	1	0.0	20.0	50.0	1	1	020

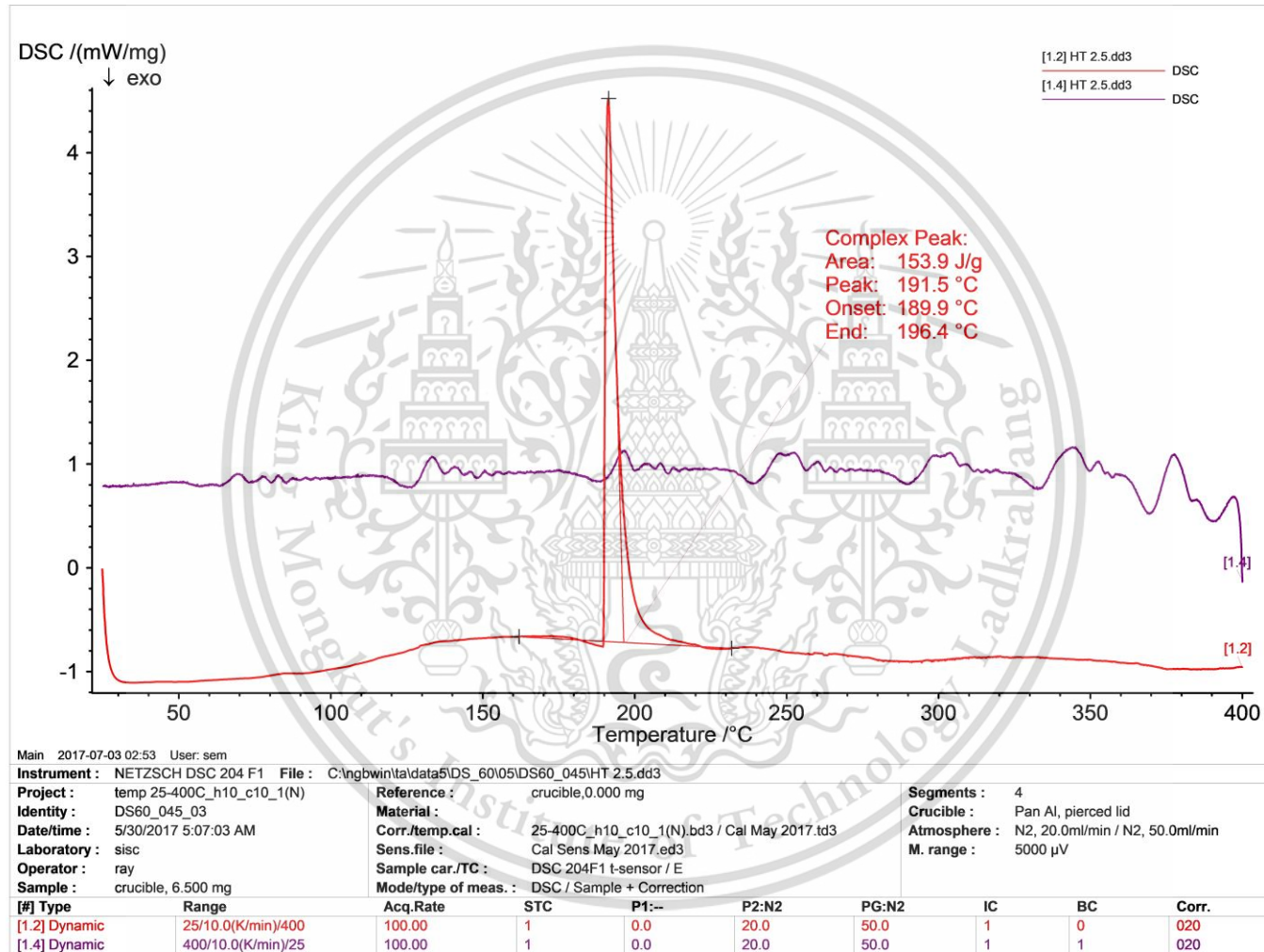


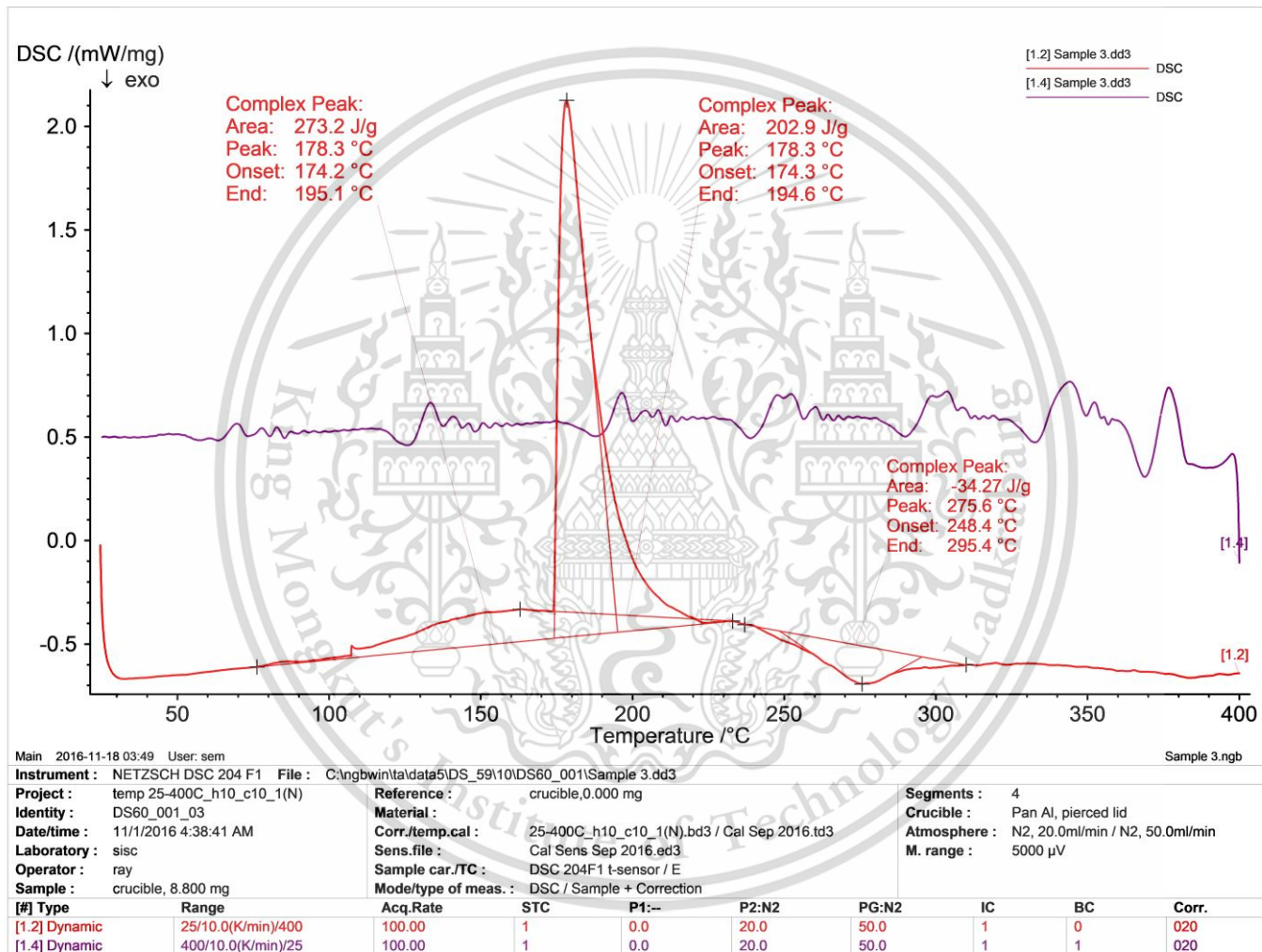


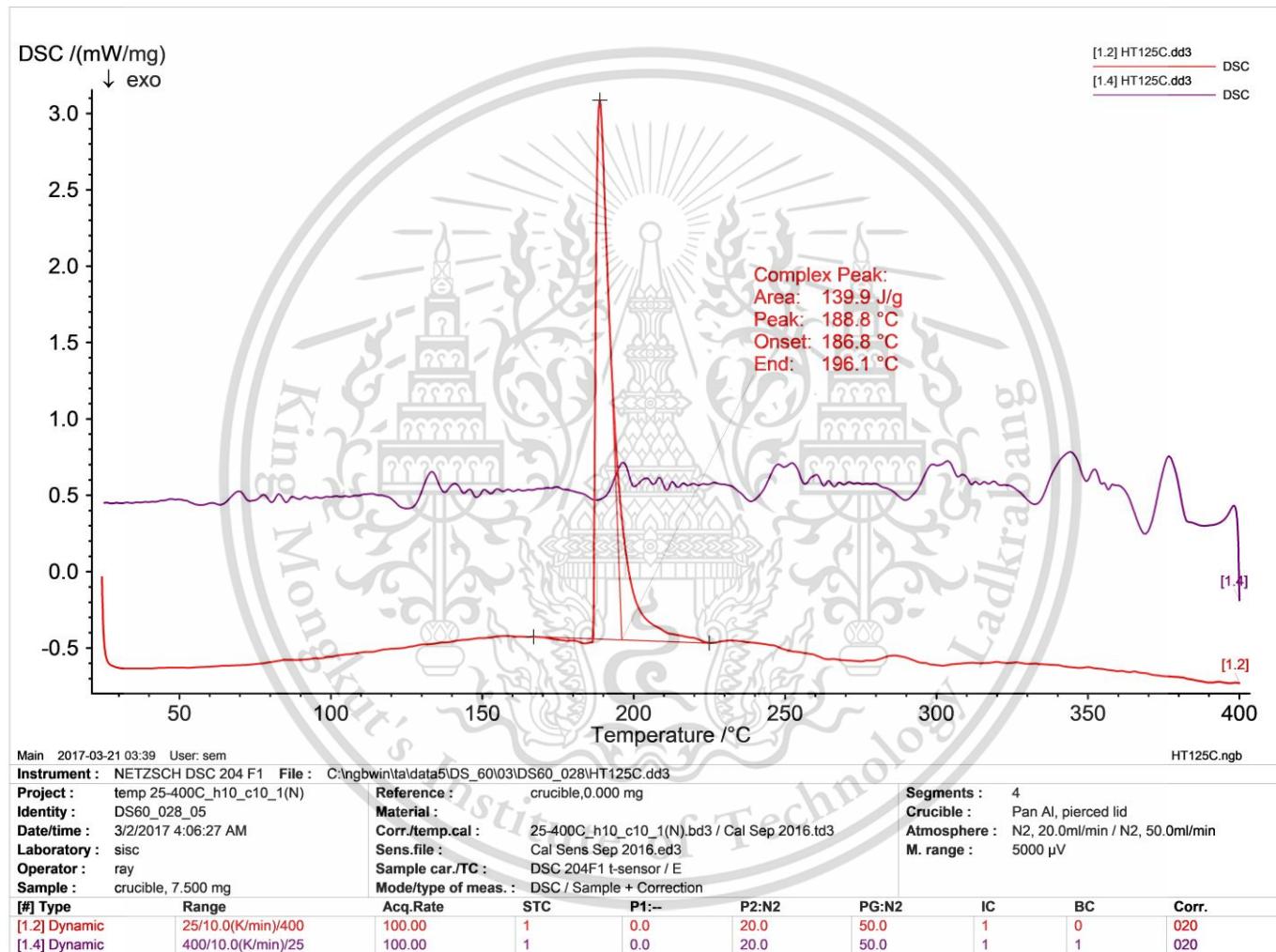


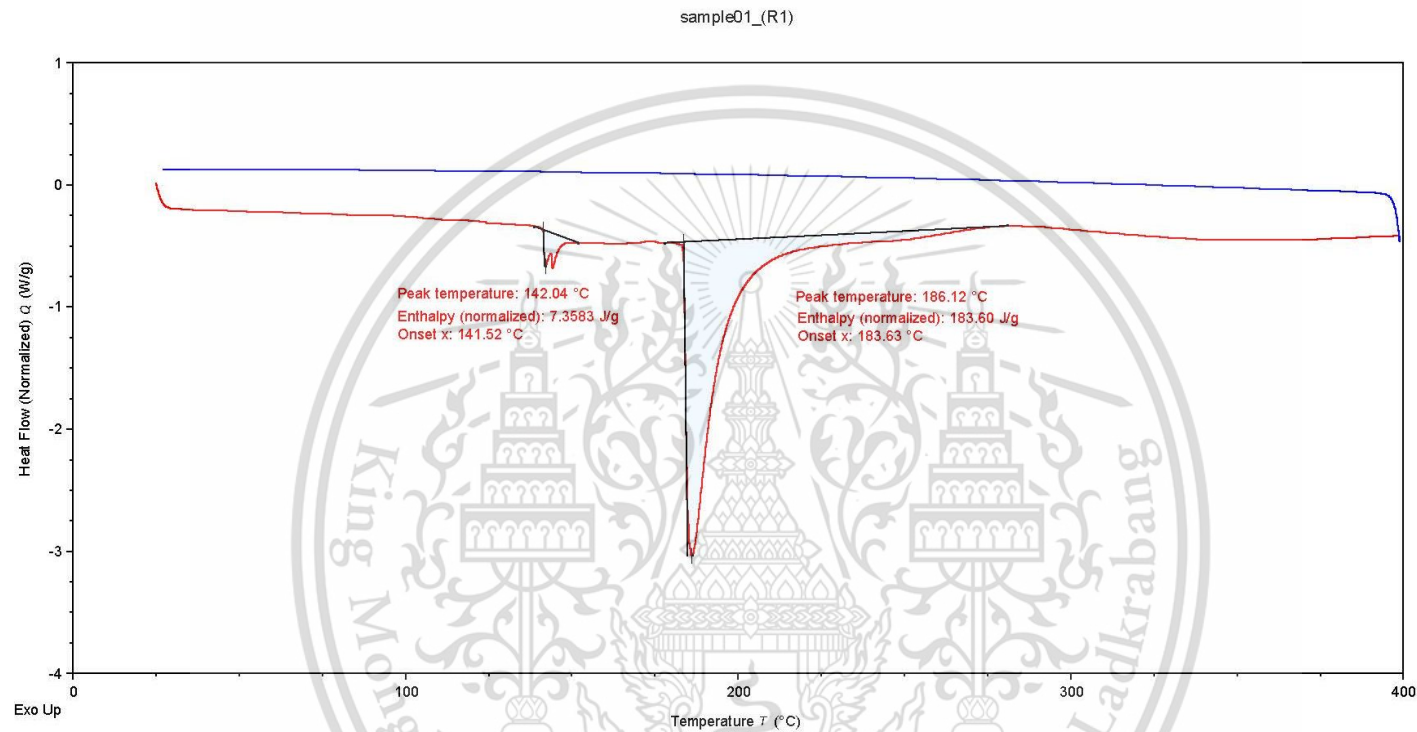




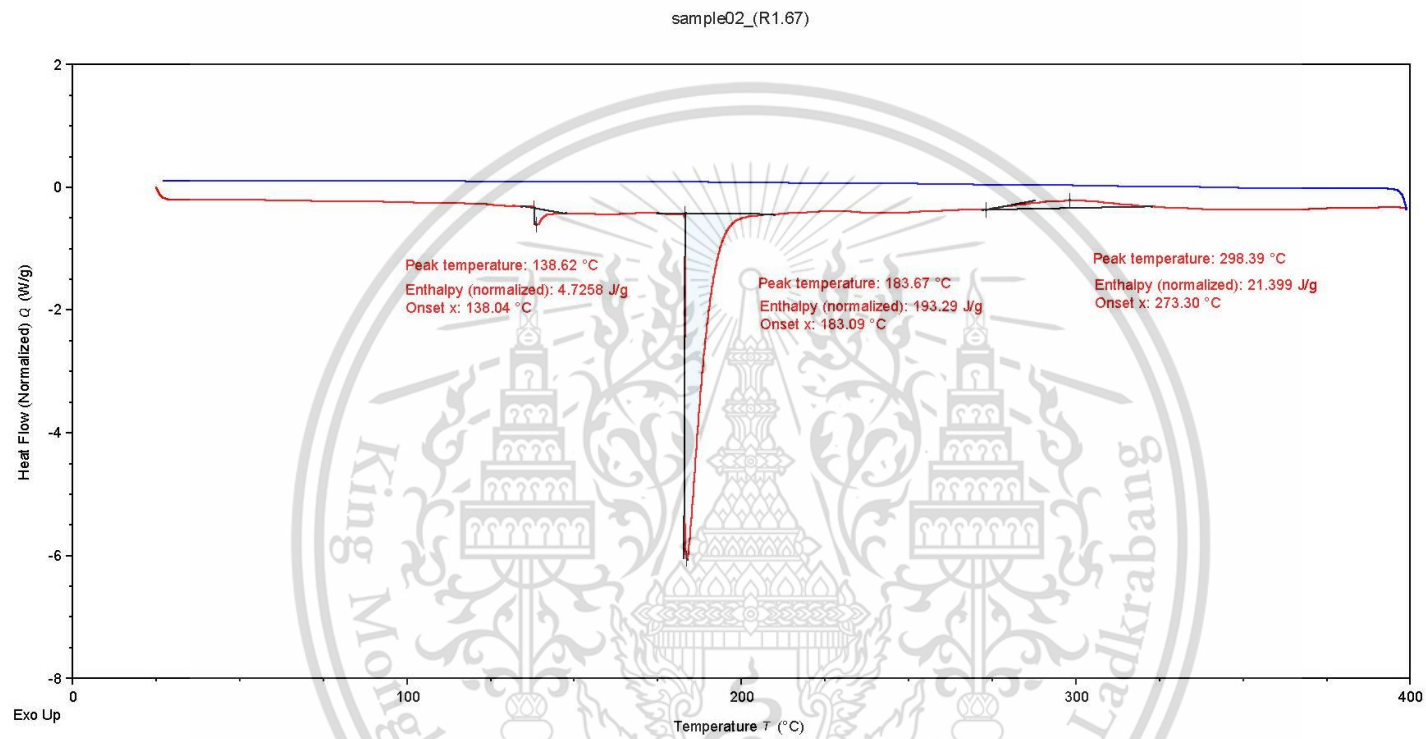






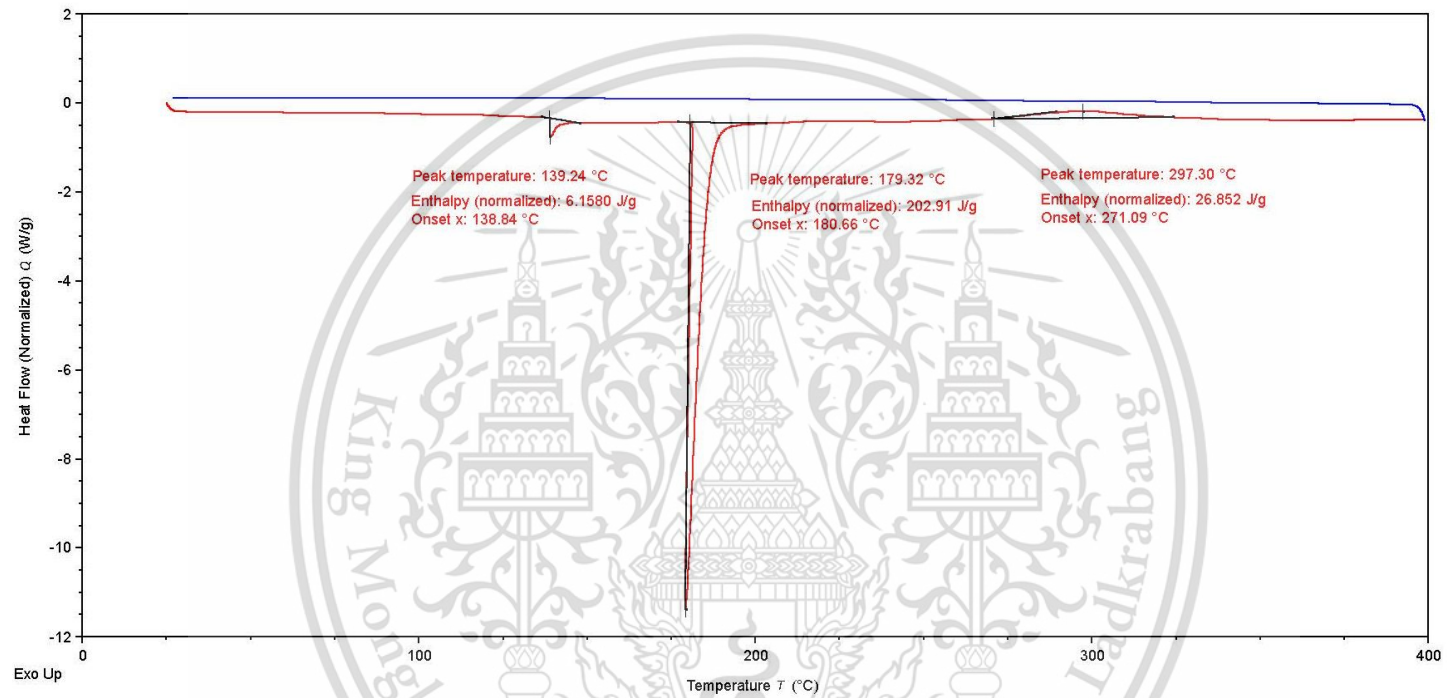


TA Instruments Trios V5.1.1.46572

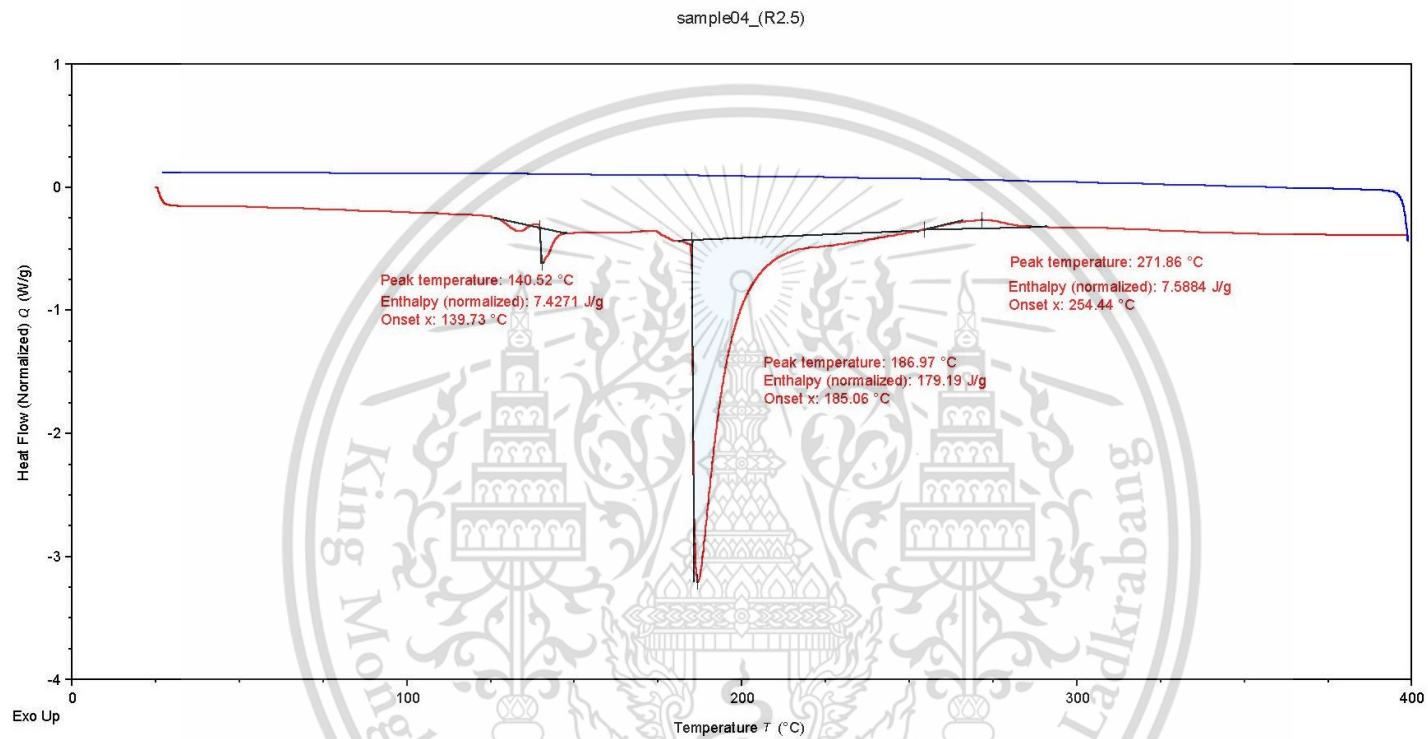


TA Instruments Trios V5.1.1.46572

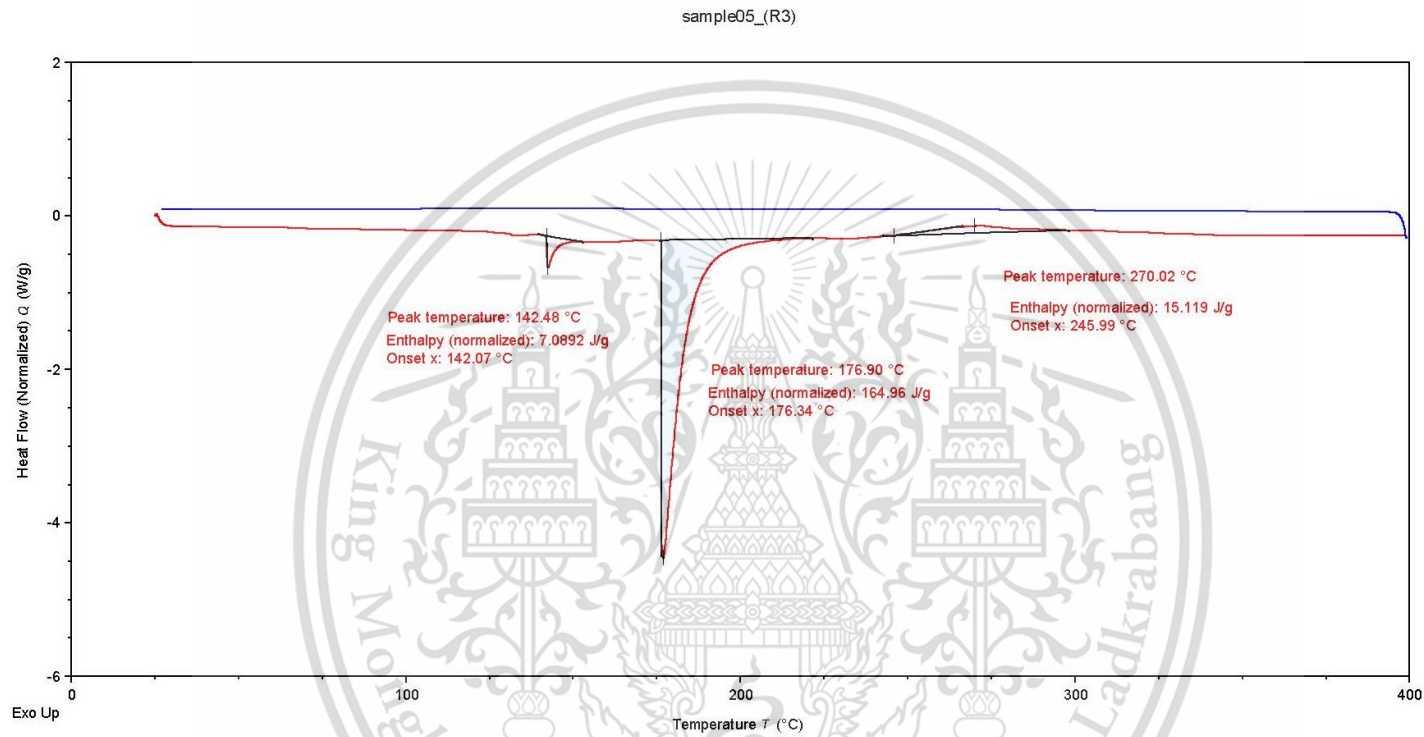
sample03_(R2)

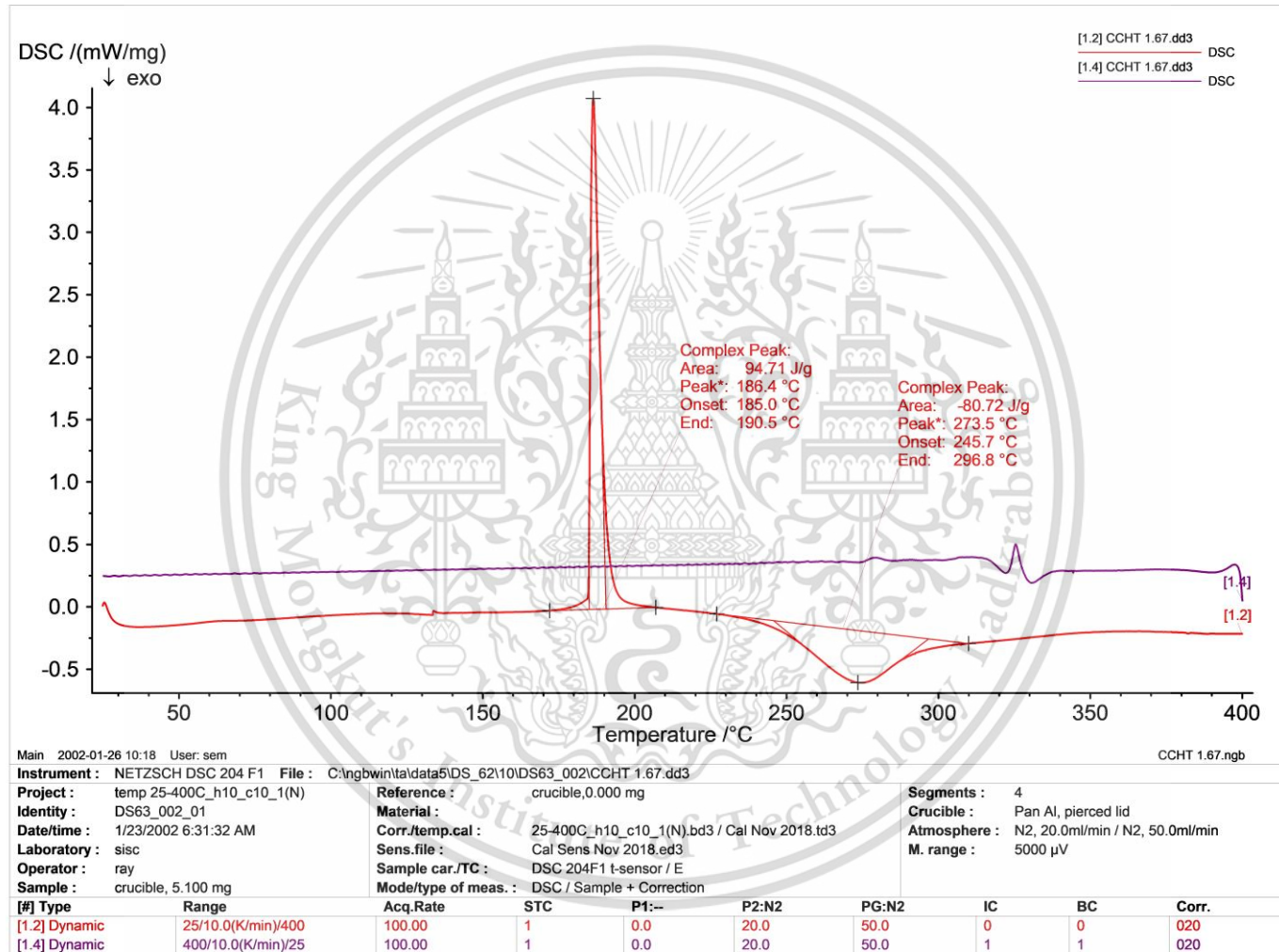


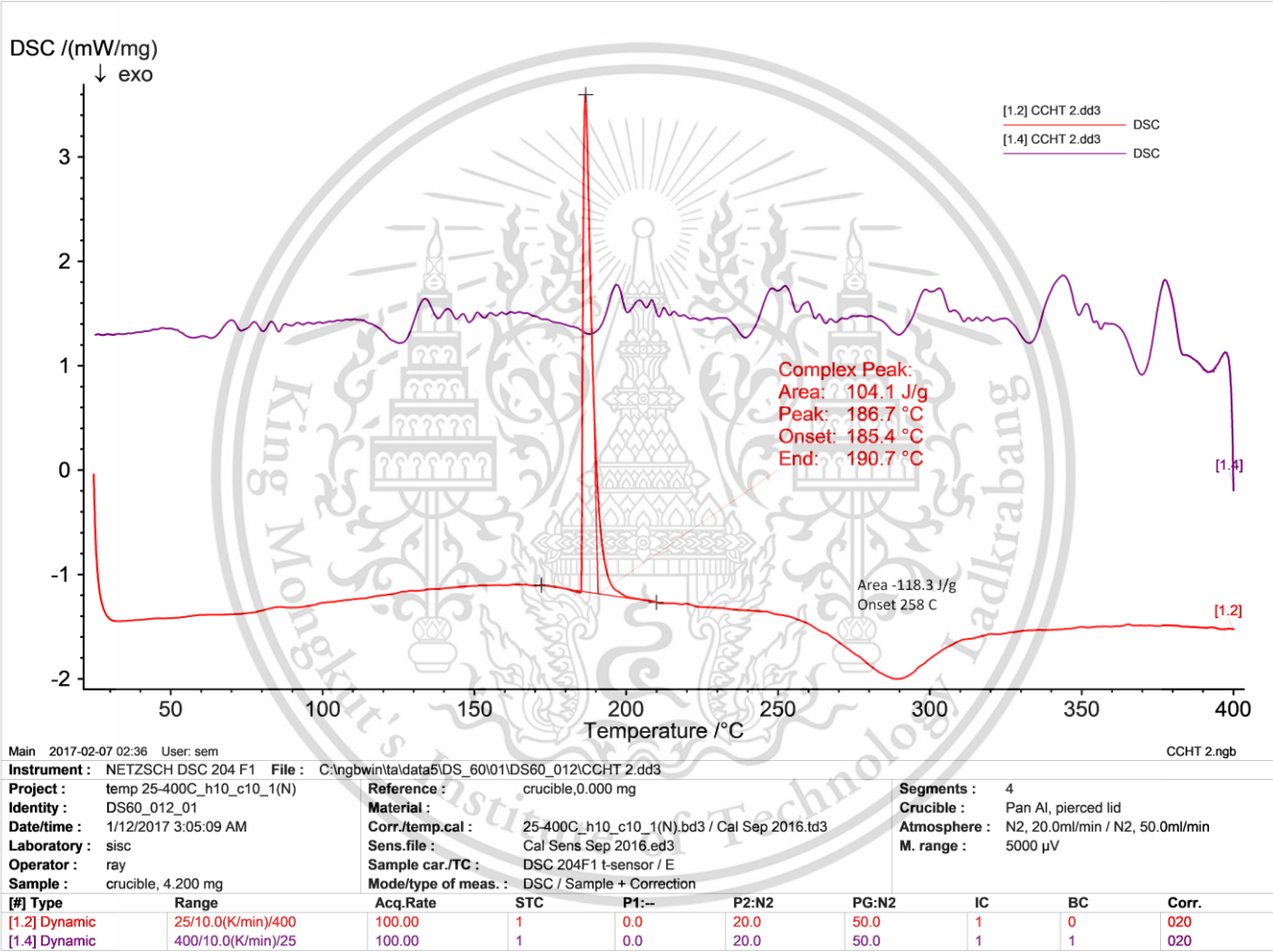
TA Instruments Trios V5.1.1.46572

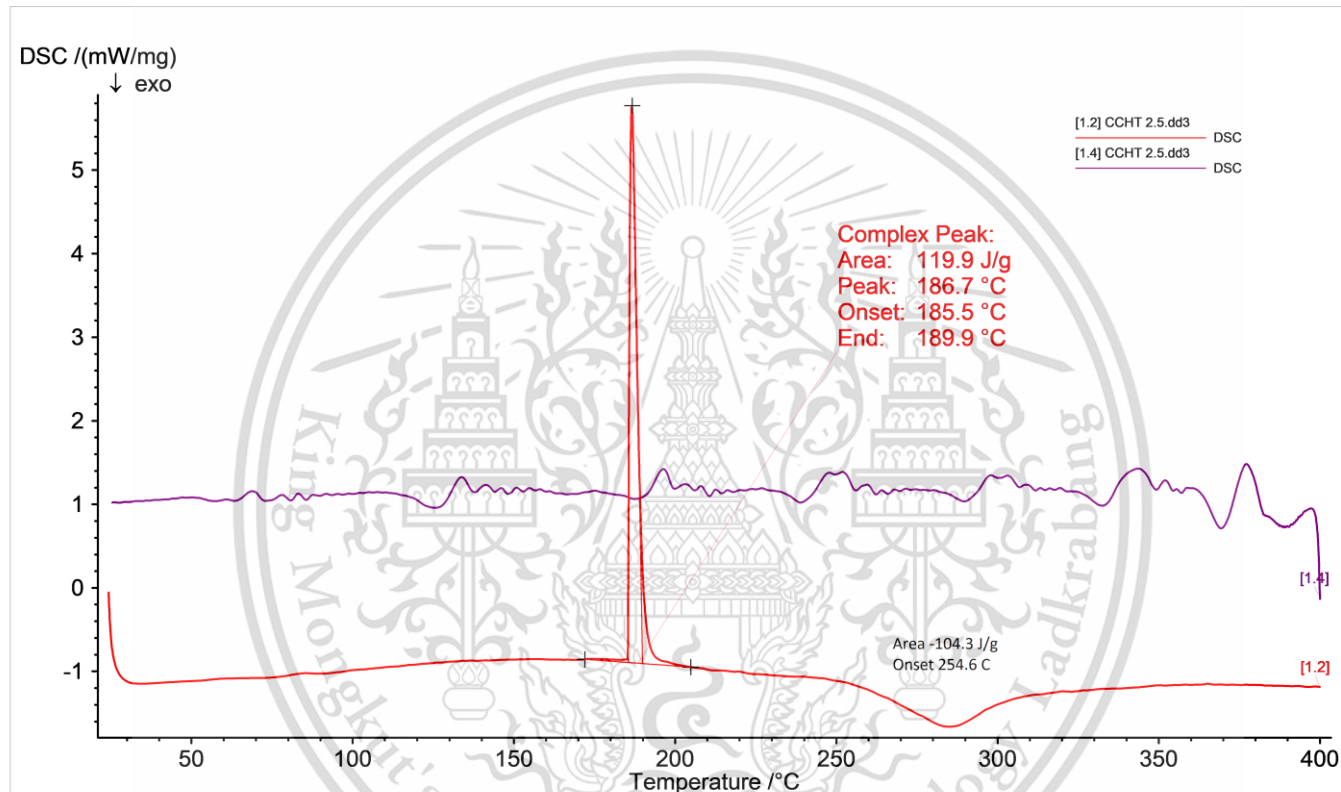


TA Instruments Trios V5.1.1.46572







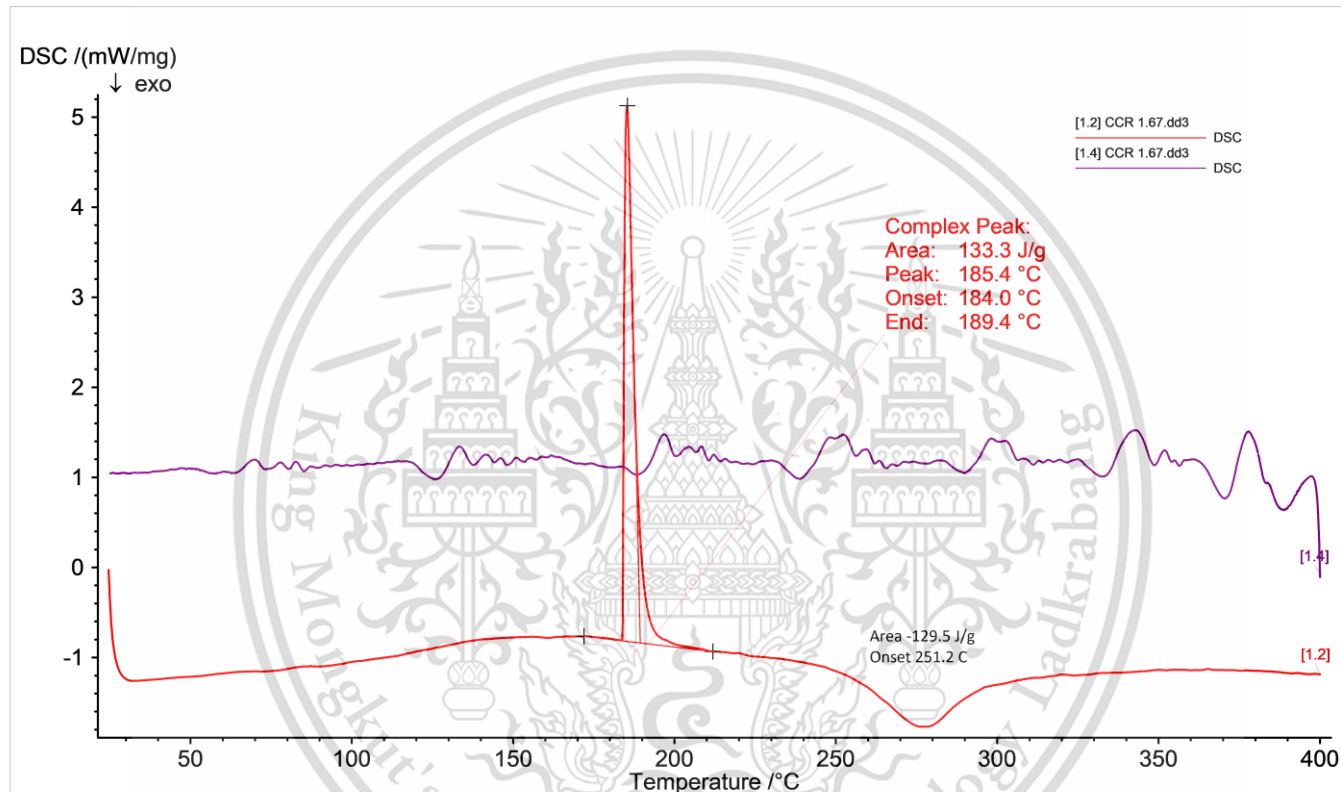


Main 2017-02-07 02:34 User: sem CCHT 2.5.ngb

Instrument: NETZSCH DSC 204 F1 **File:** C:\ngbw\in\ta\data5\DS_60101\DS60_012\CCHT 2.5.dd3

Project: temp 25-400C_h10_c10_1(N)	Reference: crucible,0.000 mg	Segments: 4
Identity: DS60_012_02	Material:	Crucible: Pan Al, pierced lid
Date/time: 1/12/2017 4:36:28 AM	Corr./temp.cal: 25-400C_h10_c10_1(N).bd3 / Cal Sep 2016.td3	Atmosphere: N2, 20.0ml/min / N2, 50.0ml/min
Laboratory: sisc	Sens.file: Cal Sens Sep 2016.ed3	M. range: 5000 µV
Operator: ray	Sample car./TC: DSC 204F1 t-sensor / E	
Sample: crucible, 5.200 mg	Mode/type of meas.: DSC / Sample + Correction	

[#]	Type	Range	Acq.Rate	STC	P1:-	P2:N2	PG:N2	IC	BC	Corr.
[1.2]	Dynamic	25/10.0(K/min)/400	100.00	1	0.0	20.0	50.0	1	0	020
[1.4]	Dynamic	400/10.0(K/min)/25	100.00	1	0.0	20.0	50.0	1	1	020

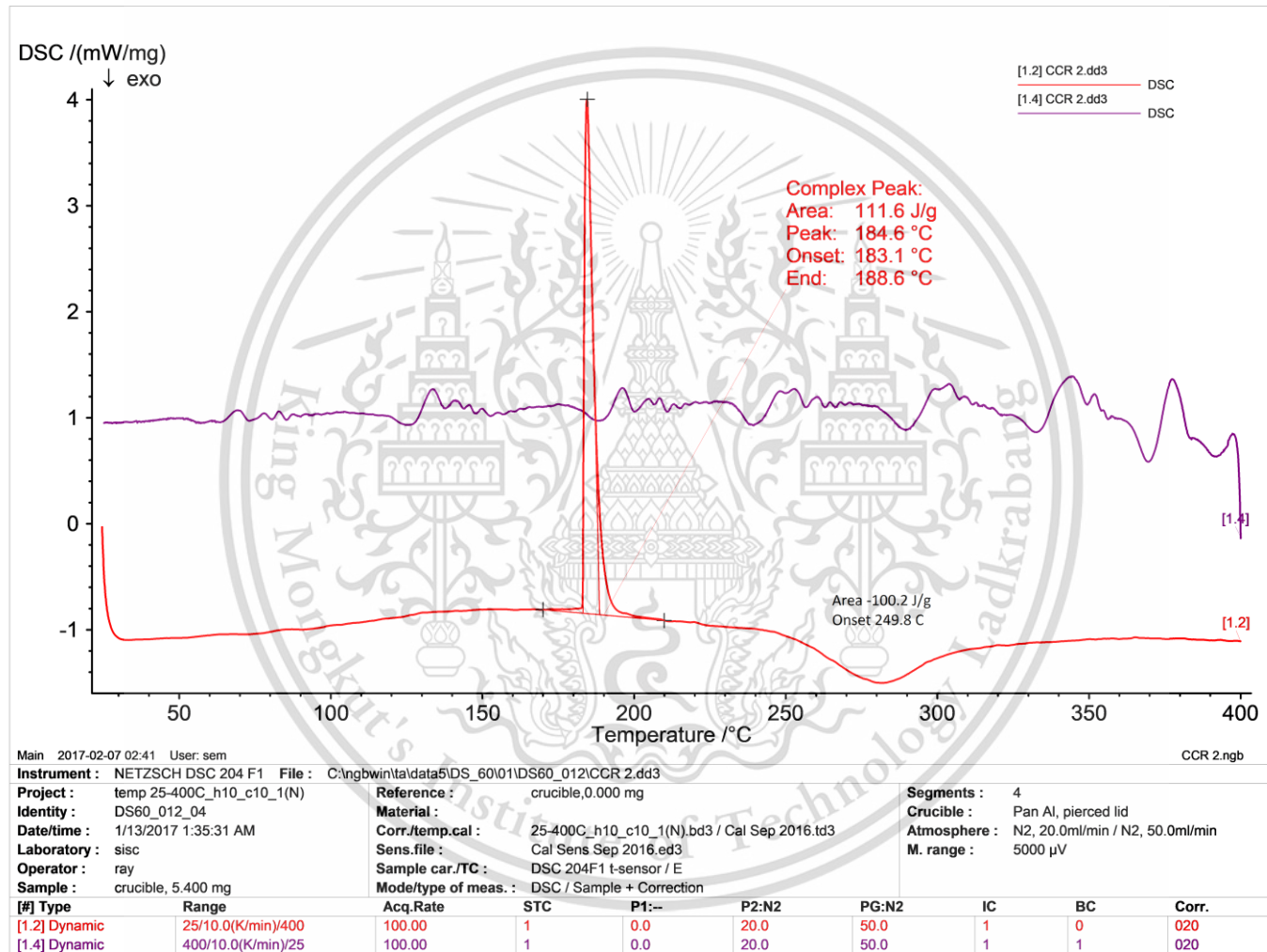


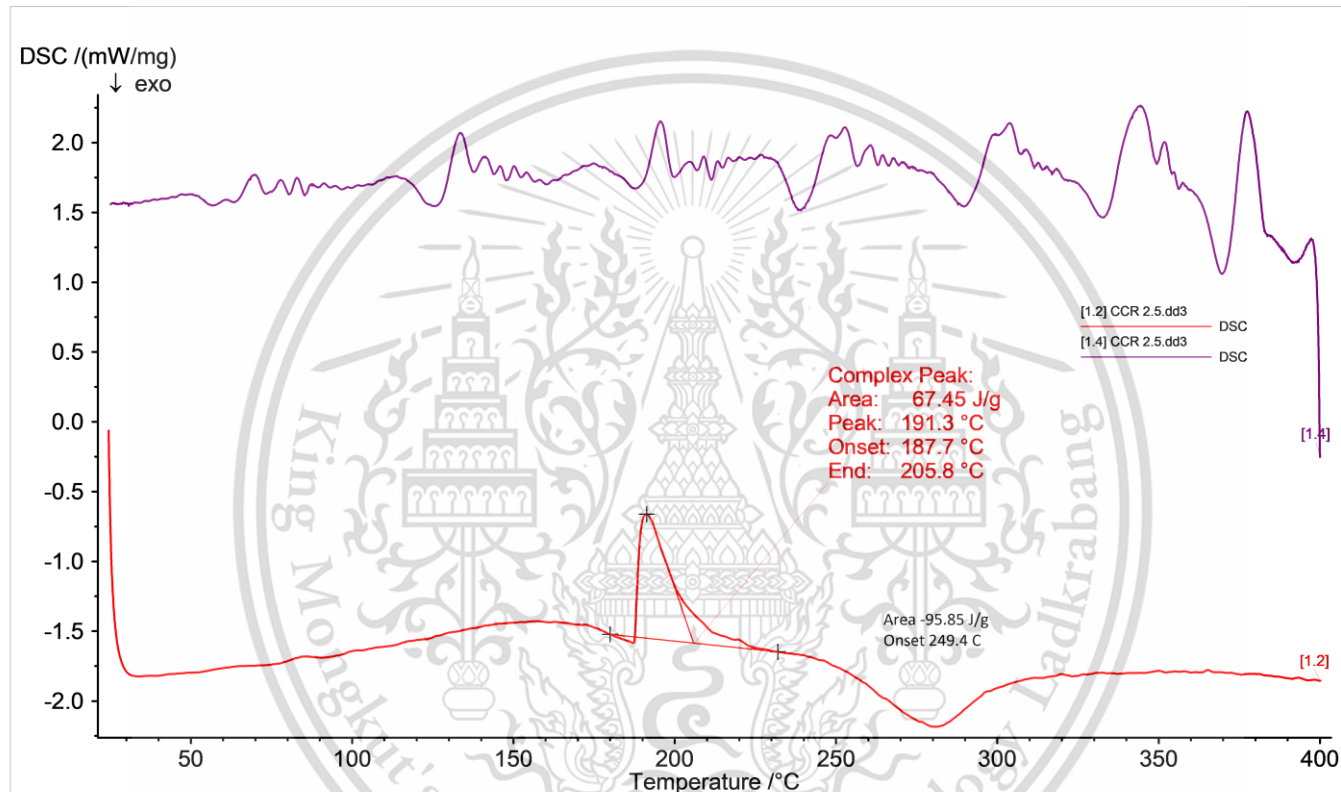
Main 2017-02-07 02:37 User: sem CCR 1.67.ngb

Instrument: NETZSCH DSC 204 F1 **File:** C:\ngbwin\td\data5\DS_60101\DS60_012\CCR 1.67.dd3

Project: temp 25-400C_h10_c10_1(N)	Reference: crucible,0.000 mg	Segments: 4
Identity: DS60_012_03	Material:	Crucible: Pan Al, pierced lid
Date/time: 1/12/2017 11:57:42 PM	Corr./temp.cal: 25-400C_h10_c10_1(N).bd3 / Cal Sep 2016.td3	Atmosphere: N2, 20.0ml/min / N2, 50.0ml/min
Laboratory: sisc	Sens.file: Cal Sens Sep 2016.ed3	M. range: 5000 µV
Operator: ray	Sample car./TC: DSC 204F1 t-sensor / E	
Sample: crucible, 4.700 mg	Mode/type of meas.: DSC / Sample + Correction	

[#] Type	Range	Acq.Rate	STC	P1:-	P2:N2	PG:N2	IC	BC	Corr.
[1.2] Dynamic	25/10.0(K/min)/400	100.00	1	0.0	20.0	50.0	1	0	020
[1.4] Dynamic	400/10.0(K/min)/25	100.00	1	0.0	20.0	50.0	1	1	020





Main 2017-02-07 02:39 User: sem CCR 2.5.ngb

Instrument: NETZSCH DSC 204 F1 **File:** C:\ngbwin\ta\data5\DS_60101\DS60_012\CCR 2.5.dd3

Project: temp 25-400C_h10_c10_1(N)	Reference: crucible,0.000 mg	Segments: 4
Identity: DS60_012_05	Material:	Crucible: Pan Al, pierced lid
Date/time: 1/13/2017 3:13:54 AM	Corr./temp.cal: 25-400C_h10_c10_1(N).bd3 / Cal Sep 2016.td3	Atmosphere: N2, 20.0ml/min / N2, 50.0ml/min
Laboratory: sisc	Sens.file: Cal Sens Sep 2016.ed3	M. range: 5000 µV
Operator: ray	Sample car./TC: DSC 204F1 t-sensor / E	
Sample: crucible, 3.500 mg	Mode/type of meas.: DSC / Sample + Correction	

[#] Type	Range	Acq.Rate	STC	P1:-	P2:N2	PG:N2	IC	BC	Corr.
[1.2] Dynamic	25/10.0(K/min)/400	100.00	1	0.0	20.0	50.0	1	0	020
[1.4] Dynamic	400/10.0(K/min)/25	100.00	1	0.0	20.0	50.0	1	1	020

Author biography

Name	Miss Sukanda Vaewbundit
Date of Birth	10 July 1992
Address	39/4 Moo1, Plai Bang, Bang Kruai, Nonthaburi 11130
Education	(2011) Bachelor of Science in Industrial Chemistry GPA 3.62 (King Mongkut's Institute of Technology Ladkrabang)
Scholarship	The Royal Golden Jubilee PhD program (RGJ) (PHD/0005/2558)

Academic Publications

1. Soft solution *in situ* synthesis of chitosan/iron oxide nanocomposites and their magnetic properties
2. Soft solution growth of magnetite-maghemite nanocrystals in crosslinked chitosan templates and their superparamagnetic properties

